# ESTIMATION OF EVAPOTRANSPIRATION USING

# ADVANCED VERY HIGH RESOLUTION

# RADIOMETER (AVHRR) DATA

By

EDWARD MACDONALD BARNES

Bachelor of Science
North Carolina State University
Raleigh, North Carolina
1988

Master of Science
North Carolina State University
Raleigh, North Carolina
1990

Submitted to the Faculty of the
Graduate College of the
Oklahoma State University
in partial fulfillment of
the requirements for
the Degree of
DOCTOR OF PHILOSOPHY
May, 1996

Thesis
1996D
Bable

# ESTIMATION OF EVAPOTRANSPIRATION USING

# ADVANCED VERY HIGH RESOLUTION

# RADIOMETER (AVHRR) DATA

Thesis Approved:

_____
Thesis Advisor

_____

_____

_____

_____

_____
Dean of the Graduate College

## ACKNOWLEDGMENTS

# TABLE OF CONTENTS

# LIST OF TABLES

# LIST OF FIGURES

# NOMENCLATURE

| | |
|---|---|
| ATN | Advanced TIROS (Television Infrared Operational Satellite)-N |
| AVHRR | Advanced Very High Resolution Radiometer |
| $B(n,T_b)$ | Planck function |
| $C_1$ | Constant in the Planck function, $1.1910659 \times 10^{-5}$ mW m$^{-2}$ sr$^{-1}$ cm$^4$ |
| $C_2$ | Constant in the Planck function, $1.438833$ K cm$^{-1}$ |
| $c_p$ | Specific heat of air at constant pressure |
| DN | Digital Number |
| DOS | Dark Object Subtraction |
| DOY | Day of the Year (1 to 365) |
| Ecc | Eccentricity correction factor for the earth's orbit |
| ET | Actual evapotranspiration |
| $ET_{area}$ | Area weighted evapotranspiration |
| $ET_{ref}$ | Reference evapotranspiration |
| $ET_{point}$ | Point estimate of ET from either a calculated reference ET or the lysimeter measurement |
| ExoAtmo | Extoatmospheric method for calculating reflectance |
| $e^o_z$ | Saturation vapor pressure at a level z above the surface |
| $e_z$ | Actual vapor pressure above the surface |
| F | Integrate solar spectral irradiance (W m$^{-2}$) |
| G | Soil heat flux (W m$^{-2}$) |
| GAC | Global Area Coverage |
| Gain | Sensor gain (W m$^{-2}$ sr$^{-1}$ count$^{-1}$) |
| GCP | Ground Control Point |
| GOES | Geostationary Operational Environmental Satellite |
| H | Sensible heat flux (W m$^{-2}$) |
| HRPT | High Resolution Picture Transmission |
| I | Intercept of the calibration of the AVHRR channels in terms of albedo |
| Iq-NoPath | Atmospheric correction methods adapted from Iqbal (1983) with path radiance assumed equal to 0. |

| | |
|---|---|
| Iqbal | Atmospheric correction methods adapted from Iqbal (1983). |
| IRT | Infrared Thermometer |
| k | von Karman's constant |
| $K_c$ | Crop coefficient |
| | |
| $L_{sat}$ | Radiance received by the satellite's sensor |
| LAC | Local Area Coverage |
| | |
| $M_a$ | Molecular weight of air |
| $M_w$ | Molecular weight of water |
| MAD | Mean Absolute Difference |
| MSAVI | Modified Soil Adjusted Vegetation Index |
| MSS | Landsat Multispectral Scanner |
| m | Total relative air mass from sun to ground to satellite |
| | |
| NCAR | National Center for Atmospheric Research |
| NESDIS | National Environmental Satellite, Data and Information Service |
| NDVI | Normalized Difference Vegetation Index |
| NIR | Near-Infrared |
| NOAA | National Oceanic and Atmospheric Administration |
| | |
| Offset | Value corresponding to 0 radiance (counts) |
| P | Atmospheric pressure |
| P&M | Atmospheric correction method of Paltridge and Mitchell (1990) |
| PRT | Platinum Resistance Thermometer |
| | |
| $Q_0(m)$ | Integrated source function for to molecular scattering |
| $Q_1(m)$ | Integrated source function for aerosol scattering |
| | |
| R | Reflectance |
| $R_c$ | Cover coefficient (ratio between ET from a crop and the ET measured by the lysimeter) |
| $R_n$ | Net radiation ($W\ m^{-2}$) |
| Red | Reflectance in the red region of the spectrum |
| RF | Rainfall |
| RH | Relative Humidity |
| RMSE | Root Mean Squared Error |
| RTM | Radiative Transfer Model |
| r | Correlation coefficient |
| $r^2$ | Coefficient of determination |
| $r_a$ | Aerodynamic resistance |
| $r_c$ | Canopy resistance to moisture transfer |
| | |
| SAA | NOAA's Satellite Active Archive |
| SAVI | Soil Adjusted Vegetation Index |

| Slope | Slope of the calibration for the AVHRR reflective channels in terms of albedo |
| $STD_{err}$ | standard error |
| SWT | Split-Window Technique |
| | |
| $T_a$ | Air temperature |
| $T_b$ | Brightness temperature (K) |
| $T_s$ | Surface temperature |
| TM | Landsat Thematic Mapper |
| | |
| u | Wind velocity |
| USGS | United States Geological Survey |
| | |
| VISSR | Visible and Infrared Spin Radiometer |
| VP | Vapor Pressure |
| VPD | Vapor Pressure Deficit |
| | |
| W | Equivalent width of the spectral response function (um) |
| WS | Daily average wind speed |
| | |
| $\alpha$ | Short-wave surface albedo |
| $\beta$ | Bowen ratio |
| $\gamma$ | Psychometric constant |
| $\Delta$ | Slope of the saturation vapor pressure-temperature curve |
| $\varepsilon_a$ | Average thermal emmissivity of the surface for AVHRR channels 4 and 5 |
| $\varepsilon_{at}$ | Apparent emmissivity of the atmosphere |
| $\varepsilon_s$ | Surface emmissivity |
| $\theta_{sat}$ | Satellite zenith angle as seen from the target |
| $\theta_{sun}$ | Solar zenith angle |
| $\lambda$ | Latent heat of vaporization |
| $\nu$ | Wave number ($cm^{-1}$) |
| $\rho_a$ | Density of air |
| $\sigma$ | Stefan-Boltzman constant |
| $\phi$ | Spectral response function of the AVHRR thermal channels |
| $\psi_{sat}$ | Satellite azimuth angle |
| $\psi_{sun}$ | Solar azimuth angle |

CHAPTER 1

INTRODUCTION

**Organizational Overview**

The main body of this document is divided into 6 chapters (see Figure 1.1). This chapter provides a basic definition of evapotranspiration, explains why regional estimates of evapotranspiration are needed and defines the objective of this study. Chapter 2 is a literature review of studies related to ground-based estimates of ET, image processing and correction procedures and studies using remotely sensed data to measure ET. The third chapter describes the procedures and results relating to ground-based measurements used to validate the remotely sensed estimates. Chapter 4 documents the image correction and processing procedures used and the results of these procedures. The procedures and results of the use of AVHRR data to provide estimates of ET are presented in Chapter 5. The final chapter summarizes this investigation and the associated conclusions.

**Evapotranspiration**

Evapotranspiration (ET) is defined as transpiration from vegetative surfaces plus evaporation from free water bodies and bare soil. ET is a major component of both the hydrologic cycle and the surface energy balance. About 70% of precipitation reaching

1

```
┌─────────────────────────────────┐
│  Chapter 1 -  Introduction      │
│        • Problem                │
│        • Objective              │
│                                 │
└─────────────────────────────────┘
                 │
                 ▼
┌─────────────────────────────────┐
│  Chapter 2 - Literature Review  │
│        • ET Theory              │
│        • Image Processing       │
│        • Previous Studies       │
└─────────────────────────────────┘
```

```
┌──────────────────────────────────┐   ┌──────────────────────────────────┐
│ Chapter 3 - Ground-Based Methods │   │ Chapter 4 -  Image Processing    │
│     • Equipment                  │   │     • Image Selection and        │
│     • Estimation of ET           │   │         Screening                │
│     • Water Balance Model        │   │     • Geometric Correction       │
│     • Infrared Thermometry       │   │     • Radiometric Correction     │
│                                  │   │     • Examination of             │
│                                  │   │         AVHRR channels 1 & 2     │
└──────────────────────────────────┘   └──────────────────────────────────┘
```

```
┌─────────────────────────────────────────────────────────┐
│  Chapter 5 - Comparison of Ground-Based Data            │
│              and Satellite Derived Information           │
│     • Comparison of Satellite Derived Surface Temperature│
│         to Air Temperature                              │
│     • Correlation between AVHRR data and Weather data    │
│     • AVHRR Data and Vapor Pressure                     │
│     • AVHRR Data and Potential Evapotranspiration       │
│     • Vegetation Indices and Soil Moisture              │
│     • AVHRR Data and Actual Evapotranspiration          │
└─────────────────────────────────────────────────────────┘
```

```
┌─────────────────────────────────┐
│  Chapter 6 - Conclusions and    │
│              Recommendations    │
└─────────────────────────────────┘
```

Figure 1.1: Organizational overview of the primary chapters of the dissertation.

the ground in the continental United States returns to the atmosphere, with the remainder eventually entering drainage systems or percolating to groundwater storage (Rosenberg et al., 1983). The rate at which ET occurs is dependent on several factors including atmospheric conditions, soil properties and vegetative cover. Many methods have been developed to estimate the rate of ET assuming there is sufficient moisture at the surface. These methods are typically data intensive, often requiring observations of solar radiation, temperature, wind speed and relative humidity. The data requirements increase in order to obtain a measure of the ET rate for moisture limiting conditions.

## The Need for Regional Estimates of Evapotranspiration

A limitation of ground-based instrumentation is that the measured value of ET is only valid for the point at which the instrumentation is placed. Attempts to extend point estimates of ET over large areas can result in substantial error due to the variation in surface cover and microclimatic conditions (Morton, 1983; Stannard et al., 1994). Methods for estimating ET over larger areas have been a growing concern as efforts to use environmental models at global scales are intensified (Doran, 1993). The need for measurement of ET over large areas is increasing in a variety of scientific disciplines, including environmental management, hydrology and meteorology. Moran et al. (1989) note that the only feasible method of determining the spatial distribution of evaporation on regional scales is through the use of data obtained from sensors on satellite platforms.

The spatial variation of ET over smaller areas has been shown to be an important consideration in irrigation management (Or and Hanks, 1992). Curran and Foody (1994)

3

stress the need to consider spatial scale as a variable in environmental modeling, as detection of various processes is scale dependent. Physical parameters are not always linearly related to surface fluxes; therefore, using a mean value of a parameter to calculate a flux representing a large area may not be appropriate (Crosson and Laymon, 1995). Song and James (1992) observe that the sources of scale effects in hydrologic processes are related to the heterogeneity of the surface. Variations in variables (weather, climate, soils, topography), discontinuities (break between a forest and a field for example) and process all can be linked to the heterogeneity. Morton (1983) presents results from a study showing the rate of pan evaporation across irrigated cotton fields located downwind of a large fallow area. Evaporation rates decreased rapidly across the first 80 m of the upwind side of the cotton field, but approached a constant rate farther into the field.

Mintz and Walker (1993) note that land surface ET is one of the more important physical processes that impacts the global weather system. Efforts are underway to better account for the ET process in general circulation models (Verseghy et al., 1993; Bouttier et al., 1993). While various methods have been attempted to incorporate an estimation of land surface water flux in atmospheric models, the methods are very approximate and typically data intensive (Mitchell, 1993).

A large scale estimate of ET would also be valuable in hydrological applications. Many hydrologic models require estimates of antecedent soil moisture conditions or ET (Anderson, 1993). Additionally, remotely sensed estimates of ET would be very valuable to erosion and nonpoint source simulation models (Leonard et al., 1987). Morton (1983) notes that point estimates of ET can result in substantial error in hydrological estimates if

applied to large areas. Stannard et al. (1994) further state that relating point estimates

spatially over complex terrain is difficult. Such point estimates fail to account for the

spatial interaction between different surface covers and microclimatic conditions.

The effects of prolonged periods of drought on the economic, social and physical

human condition are of significant concern. The early detection of drought conditions

can allow policy makers additional time to direct resources to affected areas. Various

methods have been developed to detect drought conditions such as the Palmer (1965)

drought severity index. The index is based on regional water balance calculations using

meteorological measurements. Such methods have limitations including the need for

extensive amounts of data in order to properly monitor conditions over a large area,

assumptions required to reduce the physical input data, and the effect anomalous

precipitation can have on creating artificial wet spells (Alley, 1985; Guttman, 1991).

Remote sensing observations from satellites can provide the spatial and temporal

resolution needed for global monitoring. Continued low evaporation rates will be

characteristic of drought.

The need to monitor ET at a global scale is becoming realized as an important

matter in studies of global change (Curran and Foody, 1994). ET patterns at a global scale

integrate factors such as change in land use, rainfall distribution and desertification.

**Objective**

While many studies have focused on the derivation of ET from remotely sensed

data, few have been validated using reliable ground measurements of ET over a range of

5

conditions for an extended time period. Oklahoma is in a unique position to evaluate the potential of the remotely sensed data for ET estimation due to the presence of the Oklahoma Mesonet (a network of 111 weather stations) and four precision, weighing lysimeters in key climatic locations of the state. The objective of the current study is to utilize data from the Advanced Very High Resolution Radiometer (AVHRR) to derive daily estimates of ET with minimal ground based measurements. The AVHRR was selected for this study as it has the necessary reflective channels for vegetation monitoring and two thermal channels that can be used to estimate surface temperature (Seguin et al., 1994). Additionally, the AVHRR provides daily global coverage at an approximate pixel resolution of 1.1 km; therefore, the data can be applied across a range of spatial scales.

CHAPTER 2

## LITERATURE REVIEW

A significant amount of research effort has been devoted to the study of evapotranspiration (ET) . This literature review begins by introducing key concepts of the ET process and methods to measure and model ET. Before focusing on specific examples of the role remote sensing has played in estimating ET, an overview of relevant remote sensing techniques is provided. Emphasis is placed on the quantitative application of remotely sensed data. Finally, studies are cited that have utilized remotely sensed data in the prediction of ET. Special emphasis is placed on studies using Advanced Very High Resolution Radiometer (AVHRR) data to estimate ET.

### Evapotranspiration

Jensen et al. (1990), Brutsaert (1982), and Rosenberg et al. (1983) all provide good discussion of the various aspects of estimating ET and the environmental and physical factors that impact the rate at which ET occurs. The following discussion provides an overview of the physical process of ET and methods to measure and model ET.

Physics of the ET Process

There are several physical processes that influence ET. These can be grouped into two broad categories: energy exchange and water transfer. There must be sufficient energy to allow the vaporization of water, and there must be some mechanism to move the vapor from the surface.

Most of the energy received at the earth's surface comes from the sun. Incident energy at the boundary of the earth's atmosphere can be reflected, absorbed, or transmitted to the land surface. The energy balance at the land surface can be expressed as:

$$R_n + G + H + \lambda ET + M = 0 \qquad (2.1)$$

where $R_n$ is the net radiation, G is the soil heat flux, H is the sensible heat flux between the surface and the air, $\lambda$ is the latent heat of vaporization, ET is the amount of water evaporated from the surface and M is miscellaneous energy fluxes including energy used by plants for photosynthesis, and plant canopy heat storage (Rosenberg et al., 1983). For practical purposes, M is generally ignored, representing less than 3% of the total energy balance. Each component of Equation 2.1 represents complex and dynamic processes. For example, heat may be stored in the soil during the day and radiated back to the atmosphere during the night. The rate of transfer is dependent on physical soil properties and the heat distribution within the soil profile. Note that ET can be related to the total amount of energy reaching the surface and the amount transferred to or from the soil and atmosphere. Individual components of the surface energy balance are further described in

Chapter 5.

The amount of water that can be evaporated from a surface is also dependent on

the movement of vapor away from the surface. Air can only hold a specific amount of

water at a given temperature; therefore, it is possible for a saturated surface boundary

layer to form. Turbulent and laminar transfer mechanisms determine how quickly

moisture can be removed. Turbulent transfer is affected by the roughness of the surface

and wind speed (Stone, 1977). Surface roughness is quantitatively defined as the distance

above the soil surface where wind speed becomes effectively zero. Because vegetation

can shelter the surface from the wind, surface roughness can be related to plant height.

Laminar transfer is related to the diffusion resistance of water vapor in air, while in

turbulent transfer, the resistance is also a function of wind speed. In the case of

transpiration, the physiology of the plant and stomatal resistance become of great

importance (Taiz and Zeiger, 1991).

Measurement of ET

Methods for the direct measurement of ET have been reviewed by Teare and Peat

(1983), Rosenberg et al. (1983), and Jensen et al. (1990). One of the earliest methods to

measure potential ET was with pan evaporimeters. A pan of water is placed near or at the

ground surface and the changes in water level are assumed due to evaporation. However,

because of the dissimilarity between the pan and the surroundings, pans typically do not

provide reliable estimates (Rosenberg and Powers, 1970). Additionally, the estimates

provided relate only to how much water vapor can be transferred to the atmosphere, not

what is actually occurring at the surface.

Lysimeters are soil filled bins placed in the ground with their surface at ground level. Lysimeters were originally used to study the percolation of water through the soil, but have been modified to measure actual ET (Pelton, 1961). The two major types of lysimeters used to measure actual ET are floating and weighing lysimeters (Blad, 1983). Floating lysimeters use a bin that floats on a liquid such as water or oil and the displacement of the fluid due to the bin is measured. Weighing lysimeters determine ET by measuring the change in mass of the bin, assuming the change in mass is due to ET. The mass can be measured by mechanical scales or through the use of electronic strain gages. Lysimeters can vary in size, with surface areas ranging from 0.02 to 30 m$^2$ (Martin et al. 1985; Pruitt and Lourence, 1985).

Lysimeters should be constructed so that the soil physical properties are not significantly altered and a sufficient depth is provided for root development. The area over the lysimeter should be managed the same as the surrounding area (Blad, 1983). Pruitt and Lourence (1985) overview several designs and sources of potential measurement error, including wind effects and maintaining the lysimeter conditions which are non-representative of the surrounding area. Despite some potential error, lysimeters are considered the standard for evaluating ET estimates (Dugas et al., 1985). A more complete review of the use of lysimeters for ET measurement is provided by Allen et al. (1991).

The eddy correlation approach for measuring evapotranspiration is based on measuring water vapor flux directly (Swinbank, 1951). The method assumes fully

turbulent flow in which the transport of air and water vapor is dominated by the bulk

mixing of air due to eddy currents. The eddy correlation equation applied directly to

water vapor flux (E) can be expressed as:

$$E = \frac{M_w}{M_a P} \rho_a \overline{w'e'_a}$$

(2.2)

where $M_w$ is the molecular weight of water, $M_a$ is the molecular weight of air, P is

atmospheric pressure, $\rho_a$ is the density of air, w' is the instantaneous departure from the

mean vertical wind speed and $e'_a$ is the instantaneous departure from the mean vapor

pressure. Because instantaneous deviations from the mean are of interest, high precision,

rapid response measurements on the order of 10 Hz are required (Tanner et al., 1985).

A Lyman-alpha hygrometer is an example of an instrument that can be used for

rapid measurement of water vapor (Tanner et al., 1985). The instrument generates

radiation in the far ultraviolet wavelength of the spectrum. The ultraviolet wavelengths

are strongly absorbed by water vapor and thus the density of radiation completely

crossing the sensor is inversely proportional to water vapor. Used with a fast response

anemometer (such as a drag or hot-wire type), eddy correlation measurements can be

made. In order to measure the appropriate correlation between vertical wind velocity and

vapor pressure, the sensors should be placed close together; however, a sufficient distance

between the sensors is needed to prevent a distortion of the wind flow pattern.

The Bowen ratio approach for measuring evapotranspiration provides an estimate

of actual evapotranspiration using only meteorological measurements (Bowen, 1926).

The Bowen ratio ($\beta$) is the ratio between sensible heat flux (H) and latent heat flux ($\lambda$ET)

or,

$$\beta = \frac{H}{\lambda ET} . \tag{2.3}$$

The Bowen ratio is used in ET estimation by rearranging the energy balance equation to solve for $\lambda ET$ such that:

$$\lambda ET = -(\frac{R_n + G}{1 + \beta}) \tag{2.4}$$

Equation 2.4 represents what is sometimes referred to as the Bowen Ratio Energy Balance. The Bowen ratio can be approximated by measuring temperature and vapor pressure at two heights. Measurements can be made every 30 to 60 minutes and integrated over the day to get the total estimate of ET.

The method assumes that the turbulent exchange coefficients for sensible heat and water vapor are equal, which is not always the case. The assumption is valid under conditions of atmospheric neutral stability. Neutral stability occurs when air temperature decreases with elevation at a specific rate (the adiabatic lapse rate). If stable conditions do not exist, there are correction methods based on the temperature gradient and horizontal wind speed. Many studies have found the Bowen ratio model to supply good estimates of ET; however, in conditions of high advection, the equation can under estimate ET (Verma, et al., 1978). The Bowen Ratio method requires precision instrumentation and only supplies a very localized estimate of ET.

## Reference and Potential ET

Numerous studies have been devoted to the estimation of evapotranspiration from meteorological observations. Extensive review of a range of methods is provided by Jensen et al. (1990), Brutsaert (1982), and Rosenberg et al. (1983). Reference ET is defined as ET from a well watered reference crop maintained at some standard height. Reference ET is often measured using irrigated lysimeters; however, several models of reference ET have been developed using meteorological variables as the primary input.

A concept similar to reference ET is potential ET. Shuttleworth (1993) defines potential ET as the quantity of water evaporated from an extensive free water surface as dictated by existing atmospheric conditions. Therefore, potential ET can be defined exclusively from meteorological conditions, while reference ET is dependent on the reference crop selected. Typically grass is used as the reference crop; however, other crops such as alfalfa have been used as well (Jensen et al., 1990).

One of the most well known meteorological methods to estimate potential ET was developed by Penman (1948). This method combines energy balance and aerodynamic transfer concepts to predict the amount of moisture the atmosphere is capable of removing from the surface. A modified form of the original Penman equation for reference evaporation ($ET_{ref}$) can be expressed as:

$$\lambda ET_{ref} = \frac{\Delta}{\Delta + \gamma}(-R_n - G) + \frac{\gamma}{\Delta + \gamma} f(u)(e^o_z - e_z) \qquad (2.5)$$

where $\Delta$ is the slope of the saturation vapor pressure-temperature curve, $\gamma$ is the

psychometric constant, f(u) is a wind function, $e^o_z$ is saturation vapor pressure at a level

z above the surface, and $e_z$ is the actual vapor pressure at that level. Various wind

functions have been defined based on crop type or climatic conditions (Jensen et al.,

1990).

In Equation 2.5, the first group of terms on the right hand side accounts for energy

effects on ET, while the second group of terms is focused on the moisture transfer.

Several other variations of Equation 2.5 can be found in the literature (e.g., van Bavel,

1966; Priestley and Taylor, 1972). It is important to note that all of the "combination

methods" are data intensive and only provide an estimate of reference ET at the location

where the measurements are taken.

Monteith (1981) modified the Penman equation so that aerodynamic resistance to

both heat and vapor transfer, as well as the surface resistance to vapor transfer, is

considered. The resistance terms are a function of the crop's growth stage and moisture

availability. Shuttleworth and Wallace (1985) further modified the resistance approach to

account for soil surfaces below sparse canopies.

Crop Coefficients

Direct, ground-based measurement of ET requires extensive instrumentation;

therefore, it is typically not feasible to measure conditions over every cover or crop type

in an area. The ET from a particular crop at a specified growth stage is often related to

the ET of a reference crop through the use of a dimensionless crop coefficient (Jensen,

1968). The coefficient is dependent on several factors such as the difference in surface

resistance to moisture transfer between the two crops (which in turn is dependent on other variables including leaf area index, crop height, and wind speed) and relative soil moisture conditions (Shuttleworth, 1993). Crop coefficients are based on the assumptions that under conditions of equal evaporative demand, the ET from one crop will be related to another by a factor that is a function of growth stage, and that both crops are under no moisture stress. The reference crop coefficients can be further modified to account for wet soil surface conditions or for conditions of moisture stress (USDA, 1993). The coefficients are typically defined using concurrent lysimeter measurements of a reference crop (such as grass or alfalfa) and the crop of interest. Crop coefficients should be applied under climatic conditions similar to the conditions where they were developed (Hargreaves, 1994). Doorenbos and Pruitt (1977) provide crop coefficients for a variety of crops and climatic conditions.

## Remote Sensing Techniques

This section begins by describing the characteristics of selected earth observing satellites. Next, methods to minimize the effects of sensor calibration, atmosphere and viewing geometry are presented. The section is concluded with a review of spectral indices that have been found useful in monitoring vegetative conditions.

### General Description of Selected Earth Observing Satellites

Several earth observing satellites have been used to obtain estimates of evapotranspiration. In order to facilitate the discussion of how these satellites have been

15

used in the study of ET, an overview of their characteristics is presented. Table 2.1

provides a summary description of the satellites discussed in the following sections.

*NOAA ATN Satellites and the AVHRR*

The NOAA Advanced TIROS-N (ATN) satellites carry several instruments,

including the Advanced Very High Resolution Radiometer (AVHRR), a five channel

multispectral scanner (Everdale, 1985). The satellites are identified by letter prior to

launch and then assigned a number after becoming operational. The satellites operate in a

near-polar, sun-synchronous orbit (the satellite orbits the Earth at the same rate the Earth

rotates about the sun). One orbit requires about 102 minutes, resulting in 14.1 orbits per

day. The orbital altitude ranges from 833 to 850 km (NESDIS, 1985). Odd numbered

satellites are designed for approximately 19:30 and 7:30 Local Solar Time (LST) Equator

crossing times, while even numbered satellites have 13:40 and 1:40 LST crossing times.

McGregor and Gorman (1994) note that, in general, odd-numbered satellites drift later in

time, while even numbered satellites drift earlier in time. The drift also reduces the sun-

synchronism of the orbit.

The radiometer has a 1.3 mrad Field of View (FOV) and scans 55.4 degrees to

each side of nadir (Everdale, 1985). The ground resolution at nadir is about 1.1 km, with

2048 pixels per scan line. For measurements 55 degrees off nadir, the area measured is

about 15.6 km$^2$ (Goward et al., 1993). The scan begins at space view side of the satellite

and scans towards the sun, allowing a record of a "zero" reading for each scan line (Rao

et al., 1990a).

Loveland and Ohlen (1993) summarize the daily processing of AVHRR data and

16

**Table 2.1: Summary description of satellite sensors used in ET studies.**

| | NOAA 11/12 | Landsat 4/5 | | SPOT 1-3 | GOES | METEOSAT |
|---|---|---|---|---|---|---|
| Platform: | | | | | | |
| Sensor: | AVHRR | MSS | TM | HRV/MS | VISRR | |
| Orbit: | Near Polar | Near Polar | | Near Polar | Geostationary | Geostationary |
| adir Resolution (m): | 1,100 | 80 | 30 | 10/20 [a] | 1000/7000 [b] | 2500/5,000 [c] |

| Spectral Region | | | -------[*Channel*] Nominal Band Width (um)------- | | | |
|---|---|---|---|---|---|---|
| Visible | | | | $[p^d]$ 0.51 - 0.73 | [1] 0.55 - 0.70 | [1] 0.40 - 1.1 |
| Blue | | | [1] 0.45 - 0.52 | | | |
| Green | | [1] 0.50 - 0.60 | [2] 0.52 - 0.60 | [1] 0.50 - 0.59 | | |
| Red | [1] 0.58 - 0.68 | [2] 0.60 - 0.70 | [3] 0.63 - 0.69 | [2] 0.61 - 0.68 | | |
| Near Infrared | [2] 0.73 - 1.10 | [3] 0.70 - 0.80 | [4] 0.76 - 0.90 | [3] 0.79 - 0.89 | | |
| | | [4] 0.80 - 1.10 | | | | |
| Mid Infrared | | | [5] 1.55 - 1.75 | | | |
| | | | [7] 2.08 - 2.35 | | | |
| Thermal | [3] 3.55 - 3.93 | | | | [2] 3.9 - 15.0 | [2]  5.7 - 7.1 |
| Thermal | [4] 10.3 - 11.3 | | [6] 10.4 - 12.5 | | | [3] 10.5 - 15.0 |
| Thermal | [5] 11.5 - 12.5 | | | | | |

[a] 10 m resolution in panchromatic mode, 20 m in multispectral mode.

[b] Visible channel resolution 1 km, thermal channel 7 km.

[c] Visible channel 2.5 km, thermal 5 km

[d] Panchromatic mode

the products available. Full resolution data is referred to as High Resolution Picture Transmissions (HRPT) or Local Area Coverage (LAC). In order to reduce storage requirements, a lower resolution product is also available called Global Area Coverage (GAC). GAC images are obtained by storing only every third scan line and then averaging four of every five pixels in that scan line. The resulting resolution is approximately 4 km at nadir. The first level of data typically released by NOAA is 1B-level data (Gutman et al., 1995). The data contains calibration and navigation information appended to each scan line.

AVHRR data is particularly useful for the study of ET as channels 1 and 2 can be used to derive an estimate of vegetative conditions, while two of the thermal channels (4 and 5) allow for an estimate of surface temperature that minimizes the effect of the atmosphere (Seguin et al., 1994). The fact that the AVHRR provides measurements of any location each day is also appealing; however, Goward et al. (1993) point out significant limitations of the AVHRR data for scan angles greater than $40°$ off nadir. If images are limited to scan angles less than $40°$, 3 sequential days are missed in each 9 day orbital cycle.

*Landsat and SPOT*

Other near-polar orbiting earth observing satellites include Landsat and SPOT. Landsat carries two scanning radiometers, the Multispectral Scanner (MSS) with 4 reflective channels having a nominal spatial resolution of 80 m and the Thematic Mapper (TM). The TM has 7 channels, with a spatial resolution of 30 m in the 6 reflective channels and a 120 m resolution in the thermal channel. SPOT carries a High Resolution

Visible (HRV) instrument that can operate in panchromatic or multispectral modes. In the panchromatic mode the instrument has a 10 m resolution, and in the multispectral mode the three reflective channels have a 20 m resolution. Landsat overpasses occur once every 18 days, while SPOT has an overpass frequency of 26 days. Note that by using the off-nadir capability of SPOT, the frequency can be increased to 2 or 3 days (Engman, 1993). The temporal frequency of these satellites can be a limitation for real time ET monitoring (Price, 1990).

*Geostationary Satellites*

GOES and METEOSAT are geostationary, meteorological satellites. They maintain a fixed position relative to the earth and thus can supply images of the same area at a greater frequency than orbiting satellites (typically 30 minutes per channel). Their limitation in monitoring land surface processes is the fact that they only image the surface with one reflective channel and one thermal channel (METEOSTAT does have two thermal channels; however, channel 3 is designed to be sensitive to changes in atmospheric water vapor). METEOSTAT estimates of surface temperature have an uncertainty of at least 5 K without extensive atmospheric correction (Seguin et al., 1994).

Spectral Responses and Vegetative Indices

The reflective properties of the earth's surface can be used to determine many physical characteristics of the surface. Figure 2.1 shows a characteristic spectral response curve for both a bare soil and a vegetative surface (Perry and Lautenschlager, 1984). Vegetation has a reflectance peak in the green area of the spectrum (0.50 to 0.55 μm) and

19
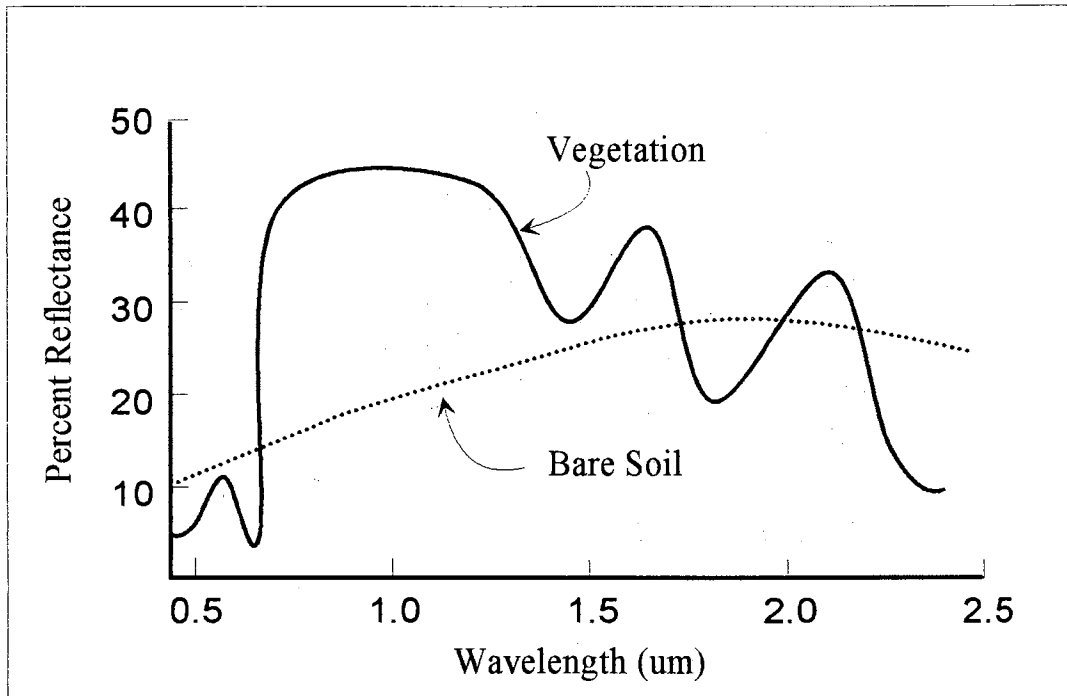
Figure 2.1:Characteristic spectral reflectance curves (after Perry and Lautenschlager, 1984).

much stronger absorption in the red area (0.65 to 0.70 μm) compared to a bare soil due to the presence of chlorophyll. The high reflectance of vegetation in the near-infrared portion of the spectrum (0.7 to 1.3 μm) is mainly due to internal leaf structure (Singh, 1987). These spectral response patterns are used in many applications including detection of plant nitrogen status (Bausch et al., 1994) and automatic detection of weeds in spot spraying (Woebbecke et al., 1994).

The primary application of the spectral characteristics of vegetation occurs through vegetative indices. Perry and Lautenschlager (1984) reviewed several spectral vegetation indices and compared the relationships among them. They note that the indices are typically based on ratios or linear combinations of spectral reflectance, and that functional relationships exist between many of the indices.

*Linear Indices*

An example of a linear combination of multispectral data is the Tasseled Cap Transform, originally developed for Landsat's 4-band MSS (Kauth and Thomas, 1976). The transform is based on the fact that surface features creating variations in one band of a sensor will often create similar variation in other bands. The correlation between the bands will not be perfect and the maximum information in a scene can be captured by a combination of the bands (Crist and Kauth, 1986). For MSS data, 95% of the variation of the image was attributed to two components labeled Brightness (B) and Greenness (G):

$$B = 0.433\ MSS_1 + 0.632\ MSS_2 + 0.586\ MSS_3 + 0.264\ MSS_4 \qquad \textbf{(2.6)}$$

$$G = -0.290\ MSS_1 - 0.562\ MSS_2 + 0.600\ MSS_3 + 0.491\ MSS_4 \qquad \textbf{(2.7)}$$

where MSS$_i$ is a digital number from MSS band i.

High greenness values correspond to areas of increased vegetation, while high brightness values correspond to areas of bare soil. The Tasseled Cap concept has been applied to other sensors such as Landsat TM data (Crist and Cicone, 1984), the Nimbus-7 Coastal Zone Color Scanner (Cicone and Metzler, 1984) and the AVHRR (Ferencz et al., 1993).

*Ratio Indices*

The normalized difference vegetation index (NDVI) is defined as:

$$NDVI = \frac{NIR - Red}{NIR + Red} \qquad \textbf{(2.8)}$$

where NIR is the reflectance in the near-infrared region of the spectrum and Red is the reflectance in the red region of the spectrum (Tarpley, 1990). Referring again to Figure 2.1, vegetation has a higher reflectance in the NIR region of the spectrum compared to bare soil, while the inverse is true in the red region. Since plants produce more chlorophyll and the mesophyll structure of the leaves is more developed under favorable growth conditions, NDVI is correlated to plant vigor as well as density (Singh, 1989).

The NDVI has been used for applications such as sorghum yield modeling (Potdar, 1993), derivation of crop coefficients (Bausch and Neale, 1987), biomass estimation (Christensen and Goudriaan, 1993), soil heat flux estimation (Xinmei et al., 1993), estimation of leaf area index (Nemani and Running, 1989a), fire danger rating (Burgan and Hartford, 1993), global land cover (DeFries and Townshend, 1994) and

incorporation into general circulation models (Dedieu, 1990). Specific applications of the NDVI in estimating evapotranspiration are included in a later section.

Several studies have found that the NDVI is not independent of soil background conditions. Huete (1988) found that darker soils resulted in higher NDVI values than lighter soils with the same amount of vegetation. In an attempt to reduce soil background effects, Huete (1988) developed a soil-adjusted vegetation index (SAVI):

$$SAVI = \frac{NIR - Red}{NIR + Red + L}(L+1)$$  (2.9)

where L is the soil correction term. Huete (1988) found a constant value of 0.5 for L was appropriate for a wide range of conditions.

Clevers (1988) estimated L by:

$$L = 1 - 2\,[(NDVI)\,(NIR - 1.06\ Red)]$$  (2.10)

and found this relationship to minimize soil background effects. Qi et al. (1994) also found that a combination of Red and NIR reflectance could be used to replace the L term of equation 2.9. Moran et al. (1994b) found that the SAVI was less sensitive to soil background effects than NDVI over a semiarid range land. However, Duncan et al. (1993) found that NDVI had a higher correlation with the fraction of an area under shrub cover than did the SAVI.

A similar index used with AVHRR data is the ratio vegetation index (RVI). RVI is simply the ratio between the NIR and red reflectance. Gupta (1993) found that RVI was more sensitive than NDVI to changes in wheat growth both during early formation

and maturation; however, the RVI was more susceptible to atmospheric interference. Korobov and Railyan (1993) also found a high correlation between RVI from an aircraft mounted sensor and the growth stage of wheat.

Geometric Correction

Satellite images are spatially distorted due to influences such as the movement of the satellite, the earth's curvature, variations in the satellite's altitude, and the scanning motion of the sensor. Images may be geometrically corrected by either modeling the sources of distortion or by correlating image coordinates to map coordinates using ground control points (Richards, 1986). Ground control points (GCPs) are points of a known location that can be easily identified on the image of interest. Accurate geometric correction is important when ground-based observations are to be related to remotely sensed data (Duncan et al., 1993).

Moreno and Melia (1993) present a method to geometrically correct AVHRR data by combining an orbital model with data extracted from recent ephereris data and a few ground control points (GCP's). A Keplerian orbital model is used, with the orbital parameters updated from the ephereris data as the data becomes available. Using an iterative approach, the model parameters are adjusted to fit a minimum of 6 GCP's. Moreno and Melia (1993) have applied the method to AVHRR data with sub-pixel accuracy.

Rosborough et al. (1994) have also developed a method to geometrically correct AVHRR data based on an orbital model and an attitude model, with the option included

24

of determining attitude from GCP's. The method is capable of correcting images to accuracies within 1 km.

Di and Rundquist (1994) note that AVHRR data may also be corrected by the direct correlation of the map coordinates GCP's to the image coordinates using polynomials. Because of the time involved in determining GCP's, the correction of AVHRR images strictly by a polynomial fit is often not possible for real time processing. However, with the increased data available from geographic information systems (GIS), the application of GCP corrections may become more feasible (Mather, 1994).

## Radiometric Calibration of the AVHRR Reflective Channels

The AVHRR images transmitted from the TIROS ATN satellites are received as 10 bit digital numbers (Everdale, 1985). In order to convert the digital numbers to radiance, the calibration coefficients of the sensor must be known. Conversion of the digital numbers to radiance is necessary if radiances obtained from one satellite are to be compared to another, even if the satellites are from the same series. Further calculation to some expression of reflectance is necessary, as each detector will have a different spectral response function (Campos-Marquetti and Rockwell, 1989).

The reflective channels (channels 1 and 2) of the AVHRR sensor are silicon detectors designed to have a linear relationship to radiance. Direct calibration of the AVHRR reflective channels is only conducted under prelaunch conditions using radiation from integrating spheres (Planet, 1988). NOAA presents the calibration results in terms of albedo, defined as the effective radiance seen by the channel divided by the

exoatmospheric irradiance in the same wave band. Albedo (A) is related to the digital

numbers from the sensor by:

$$A_i = Slope_i * DN_i + I_i \qquad (2.11)$$

where i indexes the channel number, $Slope_i$ is the calibration slope, $DN_i$ is the digital

number, and $I_i$ is the intercept. The albedo can be converted to radiance, $L_i$ (W m$^{-2}$ μm$^{-1}$

sr$^{-1}$), by:

$$L_i = A_i \frac{F_i}{100\pi\, W_i} \qquad (2.12)$$

where $F_i$ is the integrated solar spectral irradiance (W m$^{-2}$), and $W_i$ is the equivalent width

of the spectral response function (Kidwell, 1991).

In-flight calibration of the AVHRR reflective channels must be determined

indirectly, as there is no on-board calibration source for these channels. Several methods

have been used for the in-flight calibration of the AVHRR, including the use of desert

targets as areas of known reflectance (Wu and Zhong, 1993), aircraft sensor

measurements (Abel et al., 1993), and ocean glint (Kaufman and Holben ,1993).

Che and Price (1992) summarize several studies conducted to determine the in-

flight gain of AVHRR channels 1 and 2. All of the studies indicate a degradation of both

of the reflective channels, with the highest degradation rate occurring immediately after

launch. Offset values for the AVHRR sensor show little variation with time and can be

estimated from the sensor response when viewing deep space (Kaufman and Holben,

1993). Mekler and Kaufman (1995) analyzed the degradation of the AVHRR instruments

on NOAA-7 and NOAA-9 and concluded the degradation was primarily due to the collection of interplanetary dust on the scanning mirror.

Kaufman and Holben (1993) found that sensor degradation could result in a change in the NDVI value of 0.09. Changes in NDVI due to sensor degradation can make comparison between years or satellites unreliable (Los, 1993). The change in NDVI results from the fact that degradation does not occur at equal rates for channels 1 and 2.

## Brightness Temperature Determination of the AVHRR Thermal Channels

Radiometric calibration and determination of brightness temperature are described by both Planet (1988) and Kidwell (1991). The thermal channels (3, 4 and 5) all contain on-board calibration sources. The sensor takes readings of both free space and then an on-board calibration target during each scan. The temperature of the calibration target is measured by four platinum resistance thermometers (PRTs). Both the sensor output in digital counts and the PRT readings are transmitted with the video data. Once received, the deep space sensor reading is assumed to represent zero radiance, and the radiance for the calibration source is determined from a weighted average of the PRT readings. This data provides two points for a linear calibration between digital counts and radiance.

Channel 3 uses an indium antimonide (InSb) detector and its calibration is highly linear; however, channels 4 and 5 use mercury cadmium telluride (HgCdTe) detectors, with slightly nonlinear calibrations (Rao et al., 1990a). Non-linear corrections are applied to these channels after conversion to brightness temperature. McGregor and

Gorman (1994) note that the thermal calibration coefficients vary with the temperature of the satellite, but conclude that the on-board calibration procedure is sufficient to correct for these variations.

Conversion from radiance to brightness temperature is accomplished by the use of the Planck function. The radiance N sensed in a particular channel from a black body at temperature T is the weighted mean of the Planck function over the spectral response function of the channel:

$$N(T) = \frac{\int_{v_1}^{v_2} B(v,T)\phi(v)dv}{\int_{v_1}^{v_2} \phi(v)dv} \tag{2.13}$$

where $v$ is the wave number ($cm^{-1}$), $\phi$ is the spectral response function, $v_1$ and $v_2$ are the response function lower and upper limits, and $B(v,T)$ is the Planck function. The only unknown in Equation 2.13 is T. The Planck function is given by:

$$B(v,T) = \frac{C_1 v^3}{\exp((C_2 v / T) - 1)} \tag{2.14}$$

where $C_1$ and $C_2$ are constants equal to $1.1910659 \times 10^{-5}$ $mW^{-1}$ $m^{-2}$ $sr^{-1}$ $cm^4$ and 1.438833 $K$ $cm^{-1}$, respectively.

Once a channel's response has been converted to brightness temperature, non-linearity corrections are applied for channels 4 and 5 as a function of the base plate temperature of the satellite and the uncorrected brightness temperature (Planet, 1988). Beginning with NOAA 14, a different nonlinearity correction procedure is being

implemented that does require a repeated reference to the PRT temperature (Brown, 1995). Sullivan (1995) presents an alternative method to calculate brightness temperatures that does not require sensor specific response functions.

Atmospheric Correction of Remotely Sensed Data

The quantitative interpretation of remotely sensed data requires that variables introduced by atmospheric conditions are considered. Teillet (1992) reported error in the NDVI of 0.01-0.02 due to ozone absorption, 0.02-0.06 due to molecular scattering, 0.03-0.06 due to water vapor and 0.02-0.04 due to aerosol scattering.

Many efforts have been devoted to removing atmospheric effects from remotely sensed data including radiative transfer models, empirically based models, dark object subtraction, and direct measurement of optical thickness. A recent comprehensive review of atmospheric correction techniques is given by de Haan et al. (1991). Both Iqbal (1983) and McCartney (1976) provide a good introduction to radiative transfer methods.

*Atmospheric Influences on Remotely Sensed Data*

Foster (1984) discusses the factors that impact the radiance that is viewed by the satellite beyond the actual radiance of the target under consideration. Figure 2.2 illustrates several of the variables that can impact the radiance reaching a sensor. The radiance reflected by a target viewed by a satellite is partly a function of the incoming exoatmospheric irradiance from the sun (Io). This incoming irradiance is reduced by atmospheric absorption and scattering and supplemented by diffuse sky irradiance (Id).
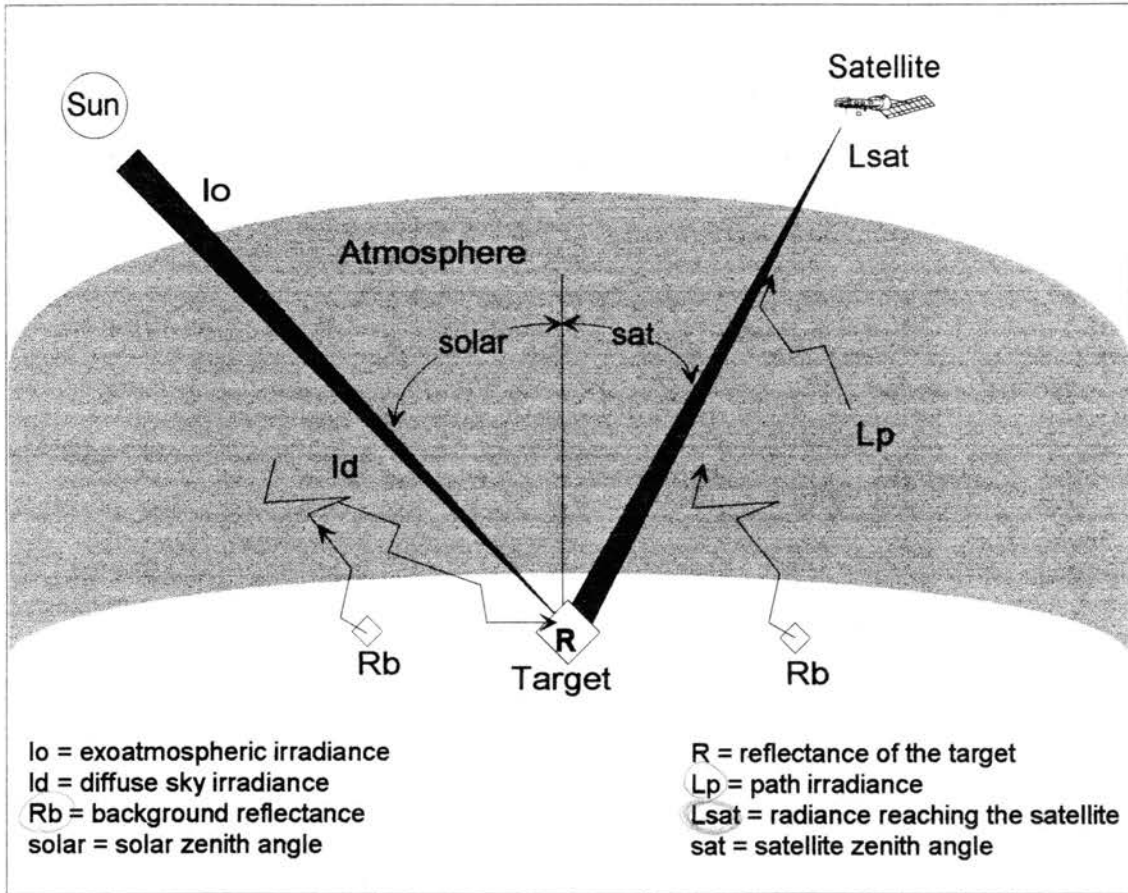
Figure 2.2: Illustration of atmospheric interferences on remotely sensed data (after Foster, 1984).

The irradiance reaching the target may be reflected, absorbed or transmitted (Lillesand and Kiefer, 1994). The reflected energy is then attenuated by the atmosphere and supplemented by both scattered radiation (path radiance, Lp) and background reflectance (Rb). Reflectance is the only parameter that is solely a function of the surface.

Atmospheric scattering and attenuation do not affect all wavelengths equally (Turner et al., 1971). Rayleigh scattering (molecular scattering) is inversely proportional to the 4th power of the wavelength of light; however, the effect of mie scattering due to aerosol particles (particles with radii in the range from 0.1 to 1 $\mu$m) is more complex. The amount of scattering is a function of both the wavelength of light and the particle's size. Because the concentration of aerosols varies throughout the atmospheric profile, describing Mie scattering is very difficult (Iqbal, 1983). Additionally, both incoming and reflected radiances are attenuated by absorption due to atmospheric gases. This attenuation only occurs at specific wavelength intervals and is often referred to as selective absorption.

*Radiative Transfer Models*

Radiative transfer models (RTMs) attempt to quantitatively describe the amount of scattering and attenuation in the atmosphere as a function of profile measurements or standard climatic conditions (Turner and Spencer, 1972). LOWTRAN is a popular model, capable of calculating transmittance and radiance based on either climatological or measured atmospheric profiles (Kneizys et al., 1988). Another model often used in the atmospheric correction of satellite data is the 5S code (Tanre et al., 1990). The code accounts for the effects of selective absorption, molecular and aerosol scattering, and

31

background reflectance. Ferencz et al. (1993) note that even with RTMs using detailed input data, the data still only represent point measurements. The atmospheric conditions can vary significantly depending on surface conditions. This is particularly true for sensors with a large swath width such as the AVHRR. Furthermore, the atmospheric measurements required as input to these models are extensive and can only be obtained from radiosonde data or by measuring optical depth (Moran and Jackson, 1991).

RTMs also require extensive computational time that limits their usefulness for real-time image processing. To overcome this limitation, look-up tables are generated from the models. Teillet (1992) presents a method to correct the reflective channels of the AVHRR using look-up table results from the 5S Code. Both Paltridge and Mitchell (1990) and Mitchell and O'Brien (1993) present a parameterization method to correct AVHRR data. The parameterization is based on physically observable variables related to the atmosphere, albedo of the surface and viewing geometry. An atmospheric profile is used to determine albedo and optical thickness profiles for molecular atmospheres using LOWTRAN 6. Error in total radiance was found to be less than 5% for satellite zenith angles up to $70^{\circ}$.

Moran and Jackson (1991) compared Landsat TM data to aircraft measurements in order to evaluate atmospheric correction techniques. Using radiative transfer models with measurements of Mie, Rayleigh, and ozone optical depths, remotely sensed measurements were within ± 0.01 reflectance of ground observations. Using LOWTRAN 7 with a Standard U.S. Atmospheric profile rather than atmospheric measurements, the resulting values were within ±0.013 reflectance. Hanan et al. (1995) also found that

climatic conditions used with RTMs may be sufficient for the correction of remotely sensed data for many applications.

*Other Correction Methods*

A simpler method of atmospheric correction is haze compensation. An area that is known to have a low reflectance in a particular wavelength is assumed to have near 0 reflectance, and all other pixels are reduced accordingly.

A second method for correcting NDVI images is that of compositing. A composite image is created on a one to two week time scale, using the maximum NDVI derived from the daily images of an area (D'Iorio, 1990; Burgan and Hartford, 1993). The assumption is that both clouds and atmospheric attenuation will reduce the NDVI and that the maximum NDVI for a given area is the least contaminated.

The difference in channels 4 and 5 of the AVHRR has been shown to be a useful measure of atmospheric moisture, which is an important variable in the attenuation of near-infrared radiation (Eck and Holben, 1994). Justice et al. (1991) propose a method to atmospherically correct AVHRR derived NDVI values using the difference in channels 4 and 5. While the method appears promising, it has not been evaluated for a range of temperature and water profiles.

Ferencz et al. (1993) examine methods to atmospherically correct Landsat MSS and NOAA AVHRR images using Tasseled Cap-type indices. The least correlated component of the image (called nonsuch) is assumed to contain information on atmospheric conditions. Using an inverted RTM, normal optical thickness is derived from the component, assuming that the surface is vegetated. The method improved yield

33

forecast from a growth model based on remotely sensed data.

*Influences of Viewing Geometry on Remotely Sensed Data*

While some of the variation due to atmospheric influences cancels in a ratio index such as the NDVI, the NDVI has also been found to be sensitive to solar zenith angle and look angle (Singh, 1989; Verstraete and Pinty, 1990). Paltridge and Mitchell (1990) note these differences are partially due to the unequal atmospheric interference in the red and NIR bands. They corrected for these effects by using a parameterization for atmospheric effects using solar zenith and look angles as key inputs.

Different viewing angle and illumination conditions can add variation to surface reflectance due to the geometric features of the surface (Cierniewski, 1989). In many remote sensing applications, surfaces are assumed to be Lambertian (having a reflected radiance that is uniformly distributed); however, for most agricultural surfaces this is not the case (Pinter et al., 1990). Shadowing and orientation of the cover to the sensor can impact the reflected radiances. Additionally, investigations have shown that red and NIR reflectance values behave differently with varying viewing geometries (Huete et al., 1992). Moran et al. (1990) found that the wavelength dependence of viewing geometry was limited to vegetative surfaces, but not present over bare soil areas. Cihlar et al. (1994) note that the use of ratio spectral indices minimizes the impact of the geometric influences.

Chehbouni et al. (1994) overview two approaches that are used to account for the effects of viewing geometry. The first approach is the utilization of directional reflectance models. These physically based models typically require information such as

34

canopy height, leaf orientation and leaf area index. The data requirements of these

models limit their usefulness. The second approach is to develop empirical corrections

calibrated to the cover of interest based on solar and viewing angles. Cihlar et al. (1994)

were able to minimize viewing geometry effects on AVHRR imagery using an empirical

model requiring solar and satellite zenith and azimuth angles and cover type.

## Thermal Remote Sensing

The thermal infrared spectral region of 8 to 13 μm is typically used for thermal

remote sensing. This spectral range contains the maximum thermal emission for

temperatures in the range found at the earth's surface and is less subject to absorption by

atmospheric gases (Becker and Li, 1990a). The most common application of

observations in the thermal region of the spectrum is for the retrieval of land surface

temperature.

### *Remotely Sensed Surface Temperature*

The retrieval of land surface temperatures from sensors on remotely sensed

platforms requires knowledge of both atmospheric conditions and the surface emissivity

(Li and Becker, 1993). Atmospheric attenuation can result in up to 10 K error in surface

temperature estimates if no correction is performed, while an error of 0.01 in emissivity

can result in errors greater than 1 K (Rao et al., 1990b).

It is possible to correlate ground based temperature measurements directly to

remotely sensed DN values for application over a specific area (Moran et al., 1989).

RTMs have been used to atmospherically correct thermal data (Wilson and Anderson,

1986; Perry and Moran, 1994); however, little error in the measured radiance can be tolerated, as an error of less than 1% in radiance can result in errors of 1 K (Houghton, 1986). Perry and Moran (1994) found that errors of 2 K were still possible even after correction of the thermal data using LOWTRAN 7 with observed atmospheric profiles. Reutter et al. (1994) were able to obtain surface temperatures within approximately 1.6 K from a single AVHRR channel using a RTM with measured atmospheric profiles.

*Split-window Techniques for Surface Temperature Determination*

Correction for atmospheric attenuation can be accomplished using a split-window technique (SWT) for radiometers with more than one channel in the thermal spectral region. Thermal wave bands for sensors are usually chosen to minimize the amount of atmospheric attenuation. These spectral areas are often referred to as "atmospheric windows". The SWT is based on the idea that the difference in surface temperatures derived from two channels in close, but different, wave bands is due to atmospheric interference. A linear combination of the brightness temperatures derived from two channels is used to derive an atmospherically corrected surface temperature (Kerr et al., 1992).

Rao et al. (1990b) summarize studies utilizing the SWT to determine sea-surface temperatures. Reported accuracies of 0.4 to 0.6 K were found when comparing drifting buoy data and sea surface temperatures derived from the SWT with AVHRR data. The sea has a fairly constant and known emissivity of about 0.97 (Rosenberg et al., 1983); however, land surface emissivity may range from 0.99 for forest to 0.93 for sandy, bare soils (Humes et al., 1994; Lagouarde and Brunet, 1993). Cooper and Asrar (1989)

evaluated several SWT equations for sea surface temperature over land surfaces. They found a resulting uncertainty in the surface temperature of ±3.0 °C after an approximate correction of the brightness temperatures for surface emissivity. Price (1984) concluded that surface temperatures within 2 to 3 K can be determined for land surfaces, using the SWT of the AVHRR and assuming a surface emissivity of 0.96. Prata (1994) was able to calibrate a split window equation to ±1.5 °C for a specific site using ground-based measurements of surface temperature.

*Surface Emissivity*

The calculation of brightness temperature is accomplished by use of the Planck function; by definition, brightness temperature assumes the surface behaves as a black body (emissivity = 1). However, for most surfaces, emissivity is less than 1 and can vary with wavelength (Humes et al., 1994). For a surface with an emissivity less than 1, the relationship between temperature and radiance then becomes:

$$T = f(\varepsilon(\lambda)B(\lambda,T)) \tag{2.15}$$

where $\varepsilon(\lambda)$ is the thermal emissivity at wavelength $\lambda$ and $B(\lambda,T)$ is the radiance corresponding to temperature T at wavelength $\lambda$. When integrating across a short wavelength range, the emissivity is typically assumed constant in that range. Both Becker and Li (1990b) and Coll et al. (1994) present SWTs that account for both the variable land surface emissivity and the difference in channel 4 and 5 emissivities. Coll et al. (1994) were able to obtain accuracies of 0.7 K by accounting for emissivity differences.

Li and Becker (1993) present a method to determine emissivity using both day and night time AVHRR thermal images. Li and Becker proposed that the emissivity for each of the AVHRR thermal channels could be calculated from brightness temperatures corrected with a RTM using a climatic atmosphere. Using their satellite derived emissivities, they were able to estimate land surface temperature to within 0.5 K.

Kerr et al. (1992) propose a land surface temperature retrieval method that provides an accuracy better than 1.5 K. For each pixel, "soil" and "vegetative" surface temperatures are determined using a SWT from Becker and Li (1990a). "Soil" and "vegetative" surface temperatures are defined as the surface temperature derived assuming the emissivity for a bare soil and vegetative surface, respectively, in the SWT. The actual surface temperature is calculated as a linear combination of the vegetative ($T_v$) and bare soil ($T_{bs}$) temperatures by:

$$T_s = C(T_v) + (1 - C) T_{bs} \tag{2.16}$$

where C is defined as:

$$C = \frac{(NDVI - NDVI_{bs})}{(NDVI_v - NDVI_{bs})} \tag{2.17}$$

where NDVI is the actual NDVI of the pixel, $NDVI_v$ is the NDVI corresponding to the maximum NDVI for a fully vegetative pixel in the region of interest, and $NDVI_{bs}$ is the NDVI corresponding to the minimum NDVI (typically a bare soil) expected for a region of interest.

Other influences that can introduce error to remotely sensed surface temperatures include angular effects from both the atmosphere and surface (Dergileva, 1995). The

atmospheric angular effects are not significant when the SWT is applied; however, shadowing of the surface can introduce variability between satellite passes (Kerr et al., 1992).

*Split-Window Technique and Atmospheric Water Vapor*

The primary source of attenuation that results in differences between the brightness temperatures retrieved from channels 4 and 5 of the AVHRR is water vapor (Justice et al., 1991). There is greater water vapor attenuation in the spectral region of channel 5, thus the brightness temperature derived from this channel is typically lower than that of channel 4. The transmittance in AVHRR channels 4 and 5 has been linearly related to precipitable water, a measure of the total amount of moisture in the atmosphere (Becker and Li, 1990b).

Eck and Holben (1994) developed site specific equations to determine precipitable water from the differences in the brightness temperatures of channels 4 and 5. They speculated that the primary reason a general relationship between sites was not possible is due to differences in surface emissivity. Dalu (1986) also used the difference in channels 4 and 5 and was able to determine precipitable water with an uncertainty of 0.5 cm.

Kleespies and McMillin (1990) provide a mathematical derivation which indicates the transmission ratio between channels 4 and 5 can be expressed as:

$$\frac{\tau_5}{\tau_4} = \frac{\Delta T_{b5}}{\Delta T_{b4}} \tag{2.18}$$

where $\tau_4$ and $\tau_5$ are the transmittances in the spectral regions of AVHRR channels 4 and 5

and $\Delta T_{bi}$ represents the difference in brightness temperatures of channel i for two contrasting conditions. The difference in brightness temperature may be obtained by two measurements over the same surface in a short time period or by using two contrasting surfaces with similar emissivities (such as a water body and a vegetated surface). The ratio of the transmittances is then correlated with precipitable water. Using AVHRR data from NOAA 7, a standard error of 0.3 cm resulted when using the method to estimate precipitable water. Jedlovec (1990) also found the method to provide acceptable results when applied with sensors other than the AVHRR.

Goward et al. (1994) related absolute humidity at the surface to the least squares regression slope of channel 5 versus channel 4 brightness temperatures in a 9x9 pixel array of an image. The implied assumptions of this approach are that there is strong vertical mixing of the atmosphere, the horizontal atmospheric vapor distribution is fairly uniform and the emissivity of the surface in question does not vary significantly over time. A coefficient of determination ($r^2$) of 0.56 was found between the slope and absolute humidity.

Cloud Screening

A significant problem in obtaining surface observations from satellite platforms is cloud obstruction (Tarpley, 1988). For most quantitative applications, cloud contaminated pixels must be excluded from the analysis. The most popular method to identify cloud contaminated pixels is gray level thresholding. Clouds generally have a higher reflectance in short-wave channels and a lower thermal emission than the earth's

surface. Therefore, a certain digital number threshold can be set by manually observing pixels containing clouds and classifying all pixels exceeding the threshold as cloud contaminated (Di and Rundquist, 1994). This procedure is most effective in the thermal spectrum, as cirrus clouds are often invisible in the reflective spectral range (Price, 1990). While thermal thresholding is easily implemented over surfaces of uniform temperature with thermal sensors, the heterogeneity of land surface temperatures can make accurate detection difficult (Rao et al., 1990c). Additionally, for sensors with large pixel areas, the presence of small, scattered clouds may not dominate the pixel sufficiently to exceed the threshold.

Saunders and Kriebel (1988) provide tests that can be applied to AVHRR data to detect cloud contaminated pixels. The tests include thresholding the thermal channels, test of uniformity in 3x3 pixel blocks, histogram analysis, and examining the ratio between channels 2 and 1 which approaches unity for cloudy pixels.

Cihlar and Howarth (1994) present a method to detect cloud contamination in composites of NDVI images. Their method is based on the assumptions that NDVI increases from the beginning of the season until peak conditions are reached and that the true NDVI will be as high or higher than a previously measured NDVI for the same location.

Yhann and Simpson (1995) note that accurate cloud detection is affected by atmospheric water vapor, aerosol levels, variable path length, variable land surface and sub-pixel clouds. They have developed two semi-automatic cloud detection methods using a neural network.

# ET Estimates from Remotely Sensed Data

Several studies have been made to examine the relationship between ET and remotely sensed data. An overview of several approaches to apply remotely sensed measurements to estimate ET is provided by Hatfield (1983) and more recently by Choudhury (1994). Engman and Gurney (1991) and Engman (1993) provide a summary of methods to utilize remotely sensed data to estimate ET as well as other hydrologic parameters.

The following discussion begins by summarizing selected studies that have used remote sensing data from ground and aerial platforms to estimate ET. This is followed by an overview of efforts to use data from various earth observing satellites for the estimation of regional ET. The discussion is concluded with a more comprehensive review of studies utilizing AVHRR data to obtain estimates of ET.

## ET Estimation Using Remote Sensing Data from Ground and Aerial Platforms

Two approaches using remotely sensed data from ground and aerial platforms are reviewed here. The first approach is to use remotely sensed surface temperatures and ground-based measurements of air temperature. The second approach involves relating the spatial distribution of surface temperature and NDVI to ET.

### Surface Temperature Techniques

Outcalt (1972) noted that only one surface temperature can satisfy the energy balance at the surface (Equation 2.1). As water evaporates from a surface, energy is used

in the process, resulting in a cooling of the surface, and thus decrease in surface temperature. Davidoff and Selim (1988) showed that soil moisture is inversely correlated to surface temperature. The difference between surface and air temperature has been used to estimate water requirements for crops (Jackson et al., 1977).

Ben-Asher et al. (1992) showed that canopy temperatures obtained from ground-based infrared thermometers can be used to derive good estimates of actual evapotranspiration at a daily time scale. The temperature version of the Penman-Monteith formula (Jackson et al., 1981) is used to determine the amount of moisture transfer resistance. The use of remotely sensed canopy temperature has also been shown to be highly correlated with actual ET by Stone and Horton (1974), Blad and Rosenberg (1976), Shuttleworth and Gurney (1990) and Diaz et al. (1983) for a variety of crops and conditions. A popular form of the relationship is given by Jackson et al. (1977) as:

$$ET = A - B(T_s - T_a) \tag{2.19}$$

where A and B are empirical coefficients, $T_s$ is surface temperature and $T_a$ is air temperature. In some cases, the A coefficient is replaced with daily net radiation.

Thunnissen and Nieuwenhuis (1990) use thermal infrared images taken from aircraft to estimate ET at an hourly time step. In addition to the infrared data, wind velocity, crop type and height, and hourly reference ET values must also be known for the site of interest. The actual ET rate ($ET_a$) is related to reference ET ($ET_{ref}$) by:

$$\frac{ET_a}{ET_{ref}} = 1 - B^r (T_c - T_c^*) \tag{2.20}$$

where $T_c$ is the actual canopy temperature, $T_c^*$ is the canopy temperature under potential ET conditions, and $B^r$ is an empirical coefficient.

The $B^r$ coefficient was found to be sensitive to wind velocity, crop type and crop height. Good estimates of actual ET could be obtained for areas of complete vegetative cover; however, forested areas and areas of incomplete cover could not be accurately determined. Other studies using aircraft-based remote sensing measurements (Reginato et al., 1985; Jackson, 1985) have found that the main limitation to the application of remote sensing observations to determine ET is the extrapolation of point measurements of wind speed and air temperature across the entire area considered. Despite the limitations, aircraft-based observations coupled with ground measurements have estimated ET to within 15% of measured values (Kustas et al., 1994) with coefficients of determination as high as 0.77 (Reginato et al., 1985).

*NDVI and Surface Temperature Relationships with ET*

Gillies et al. (1995) used a relation between NDVI and surface temperature derived from multispectral aircraft measurements to define surface fluxes. Over a large area, a plot of NDVI versus surface temperature forms a triangular distribution that is due to the distribution of soil moisture and vegetative cover. An idealized distribution is pictured in Figure 2.3a. Pixels in the image having the lowest surface temperature and highest NDVI correlated to well watered, vegetative surfaces. Pixels with higher surface temperatures and lower values of NDVI were found to correspond to dry, bare soil surfaces. Instantaneous ET was estimated to within 38.2 W m$^{-2}$ with a r$^2$ of 0.98 using data from 2 sites (N=30). Schmuggee and Becker (1991) also observed the NDVI and
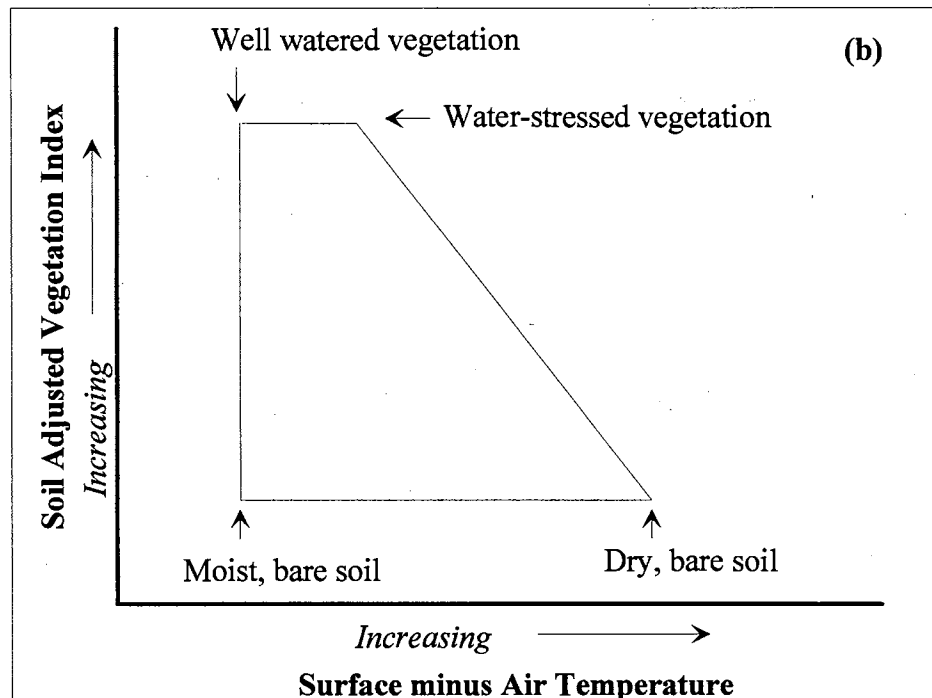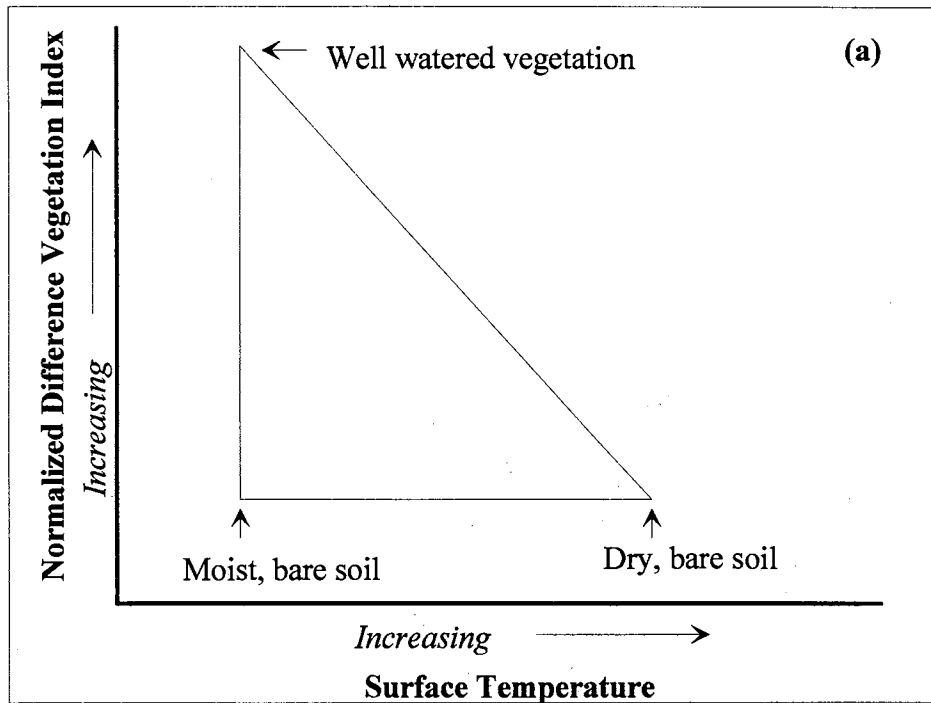
Figure 2.3: Surface conditions as indicated by the distribution of vegetation indices and temperatures within an image: (a) triangular distribution of Gillies et al. (1995) and (b) trapezoidal distribution of Moran et al. (1994c).

surface temperature relationship with ET. Humes et al. (1995) showed that points of both low NDVI and surface temperature correspond to areas of high soil moisture. It was also noted that the variability of the relationship decreased as pixel area increased (6.2 m to 200 m).

Moran et al. (1994c) defined a vegetation index and surface minus air temperature trapezoid for deriving a water deficit index (WDI) from remotely sensed measurements. Surfaces with the minimum value of surface minus air temperature and high index values were found to correspond to well watered vegetation. The physical significance of the other points of the trapezoid are illustrated in Figure 2.3b. WDI is defined as the ratio between actual and potential ET. The method to define the trapezoid requires several input variables including net radiation, vapor pressure deficit, maximum possible plant height, maximum and minimum possible stomatal resistance, and maximum possible LAI. Evaluated with a backpack yoke mounted sensor with red, NIR and thermal channels, the method was found to provide accurate estimates of ET rates.

Estimation of ET Using Sensors on Various Satellite Platforms

The following sections review selected studies that use data from sensors on various platforms to estimate ET. Because satellite sensors are able to provide data over large areas, there is a great interest in developing regional ET estimates from this data. A more detailed review of efforts to estimate ET using AVHRR data is reserved for the next section.

46

*Geostationary Satellites and ET Estimation*

Wetzel et al. (1984) present a method to relate Geostationary Operational Environmental Satellite (GOES) infrared data to soil moisture. In a sensitivity study, mid-morning slope (change in surface temperature with respect to the short wave radiation flux absorbed by the soil) was found to have the strongest relation to soil moisture.

Using METEOSAT observations, Feddes et al. (1993) found resistance and transfer coefficients by calibration with ground based data, while regional empirical relations were developed for the remaining data. Once calibrated, only remotely sensed data (surface reflectance and surface temperature) were needed to estimate ET. Using METEOSAT data over Egypt (6.5 km x 6.5 km resolution), ET estimates were made within 5 to 7% of observed rates. Rosema (1993) also presented an energy balance method to estimate ET and biomass using METEOSAT data. A comparison of rainfall measurements from 15 stations in West Africa showed reasonable correlation with ET estimates.

Estimates of large scale monthly evapotranspiration using an energy balance approach have been developed by Tarpley (1994). An energy balance is applied at the surface, with the only required input data coming from GOES VISSR (Visible and Infrared Spin Radiometer) and AVHRR observations. Rather than attempting to estimate the resistance terms in the energy equations, Tarpley applied several assumptions and an iterative, simultaneous solution technique.

GOES VISSR data are analyzed to determine surface morning heating rates and to

estimate incoming short-wave solar radiation. AVHRR channels 1 and 2 are used to determine NDVI. The aerodynamic roughness is related to monthly NDVI values by:

$$z_0 = z_m [1 + \frac{NDVI - V_{min}}{V_{max} - V_{min}}]$$ (2.21)

where $z_m$ is the minimum roughness, $V_{max}$ is the maximum monthly NDVI, and $V_{min}$ is the minimum monthly NDVI.

The model requires some variables that are not typically measured. Atmospheric temperatures were specified at 300 meters above the surface. The wind speed was defined as the mean value, without turbulent fluctuations and assumed to be 4 m/sec at all sites and times in the model. For each month, the air temperature was assumed to be $2^\circ$ C lower than the surface mean for that month at that site and the specific humidity was assumed to equal the mean monthly surface humidity. Soil thermal properties were adjusted assuming no ET in winter in west Kansas. The soil temperature at the 30 cm depth was assumed to be the previous month's average air temperature.

While there were large assumptions in the model regarding input parameters, the model was able to provide reasonable monthly ET estimates using satellite information as the primary input. However, the only ground-based data used in the evaluation procedure were rainfall amounts at each site.

Seguin et al. (1989) applied procedures similar to Tarpley's (1994) with METEOSAT surface temperature estimates and AVHRR derived NDVIs. They found a high correlation between the surface temperature and rainfall, but had trouble correlating the measurements to ET. They speculated that AVHRR derived surface temperature

48

estimates may allow for improvement of the method.

*Landsat and ET Estimation*

The use of Landsat Thematic Mapper (TM) data has also been considered in determining regional ET. Because of the spatial resolution of TM data (30 m, 120 m thermal), it is possible to characterize surface vegetative and soil features which have a large influence on ET. Lindsey et al. (1993) used Landsat TM data and a digital elevation model to characterize the surface characteristics of a watershed. A fuzzy-c classification system was applied to the TM data set to separate the watershed into different classes. Once the classes were distinguished, empirical parameters were determined for each class that allowed a simple water balance model to be applied, with the model including estimates of ET. Comparison of predicted and measured soil moisture content at 29 sites showed good correlation.

Shih and Jordan (1993) also used TM data to classify land use, but additionally used the thermal channel (channel 6) to provide estimates of regional soil moisture conditions. They found a direct correlation between surface temperature and soil moisture content of the top 24 cm of the soil profile ($r^2$=0.72).

Moran et al. (1989) used Landsat TM data to estimate actual ET using an energy balance approach. Aerodynamic parameters were estimated for specific land cover types and then assigned to image pixels using a classification procedure. Wind speed and air temperature were extrapolated from ground stations, with actual measurements of surface temperature from the satellite. TM ET estimates differed by less than 12% from Bowen-ratio measurements over fields of cotton, wheat and alfalfa.

had a higher correlation with monthly actual evaporation than either the red or NIR

reflectance alone; however, the relationship still contained a large amount of unexplained

variation. Annual comparisons of NDVI and ET showed a stronger relationship than the

monthly values.

Chong et al. (1993) also reported success in estimating annual ET amounts from

the NDVI. NDVI values were in the form of weekly maximum value composites from

GAC data. The composite values were further averaged to a grid projection system,

resulting in a 16 km resolution at the equator. In order to make a climatic comparison,

the 16 km weekly NDVI data were averaged over a four year period. Actual climatic ET

was determined using a monthly water balance method. Input data to the water balance

were monthly rainfall totals and average temperature obtained from 305 weather stations

distributed over the African continent . The correlation between monthly values of

NDVI and ET was low; however, a relationship was found between annually integrated

NDVI and annual ET. Annually integrated NDVI ($NDVI_{an}$) was defined as:

$$NDVI_{an} = \sum_{i=1}^{52} (NDVI_i - 0.05) \qquad (2.22)$$

where i is week of the year and $NDVI_i$ is the weekly composite NDVI for week i. The

relationship determined between NDVI and actual ET was:

$$NDVI_{an} = \frac{A}{1 + \exp(-B(ET - C))} - D \qquad (2.23)$$

where A, B, C and D are fitting parameters. The distribution of the data suggested

slightly different parameters were required for the northern and southern areas of the

continent. Resulting correlation coefficients (r) were 0.85 and 0.91 for two continental zones.

Nicholson and Santos (1995) used AVHRR derived NDVI to parameterize evapotranspiration for use in a land surface process model. Energy balance calculated ET and NDVI at four sites in Africa showed similar trends over six years at a monthly time step. It was speculated that transpiration would show an even stronger trend with NDVI.

Diak et al. (1995) found NDVI to correlate with Bowen ratio measurements over an 8 state region in the north central United States. They also noted an inverse relationship between NDVI and a change in surface temperature during the day derived from the GOES satellite. The relationship between high NDVI and lower changes in surface temperature was attributed to evapotranspiration and increased surface roughness. The relationship was weaker for lower values of NDVI.

*Process Based Models Utilizing AVHRR Data to Determine ET*

Xinmei et al. (1993) used the surface energy balance approach to determine ET with much of the input information derived from NOAA AVHRR data. Satellite derived albedo and surface temperature are used in the calculation of net radiation, while NDVI is used in the determination of soil heat flux. Surface temperature is also used to calculate sensible heat flux. Wind speed, air temperature and surface roughness are required from ground observations. Using results of images on 4 clear days at 5 sites, they found their model provided results similar to those obtained with Bowen ratio measurements. The largest error in ET estimates occurred when the surface roughness was high and there was a large difference between surface and air temperatures.

Price (1990) presents a method to utilize AVHRR derived surface temperature and NDVI with independent estimates of evaporation from both a vegetative and bare soil surface to estimate actual ET. Surface temperature is determined using a split window technique with channels 4 and 5, while NDVI is calculated based on sensor radiances. Using a numerical simulation model with measured inputs such as wind speed, air temperature, and humidity and assumed values for surface roughness, diurnal heat capacity and albedo, ET is calculated for vegetated, moist soil and dry soil conditions. Noting that vegetative surfaces with high evaporation rates occur at one extreme of this relationship (higher NDVI, lower surface temperature) and dry, bare soils at the other, actual ET for the other surfaces is partitioned between these two limits as a function of surface temperature and NDVI.

Nemani and Running (1989b) plot AVHRR-derived NDVI versus surface temperature. The slope of the line is used to estimate surface resistance to evapotranspiration. Using eight images acquired in a two month period, they found a strong correlation between the satellite derived resistance terms and evapotranspiration ($r^2$ = 0.92) over a 20 by 25 pixel area of forest. Nemani and Running (1989a) used the satellite derived resistance values in a simulation model, coupled with a topographic, soils and vegetation geographic information system (GIS). Simulated ET from the model ranged from 40 to 49 cm per year compared to 43 cm for the area determined from the difference of annual precipitation and stream discharge.

Running (1991) extended the estimation of the satellite derived resistance term to a complete ET model as:

$$ET = NDVI_t (\sigma\ NDVI)\varepsilon_w \qquad\qquad\qquad \textbf{(2.24)}$$

where $NDVI_t$ is a seasonal NDVI which excludes days with surface temperatures less

than 10 °C, $\sigma$ is the resistance term defined by the slope of the NDVI and surface

temperature relationship and $e_w$ is a conversion efficiency term (mm water/NDVI).

Taconet et al. (1986) used AVHRR derived surface temperature with a canopy

resistance model to estimate evapotranspiration (ET) over dense vegetation. The canopy

model requires vegetation height, density and soil hydraulic conductivity. At two sites in

France they were able to estimate daily ET within 100 W m$^{-2}$ (~1.5 mm d$^{-1}$) and 10 W m$^{-2}$

(~0.15 mm d$^{-1}$) when compared to surface flux measurements at each site over a three day

period.

To estimate ET at the basin scale, Kustas et al. (1994) used AVHRR derived

surface temperatures to spatially partition point estimates of ET determined from flux

stations. ET for each pixel was scaled to a reference measurement utilizing the difference

in surface temperature at the reference site and the AVHRR derived surface temperature.

NDVI was used to partition soil heat flux components. Qualitative evaluation found that

the estimated values of ET matched recent rainfall patterns in the area for the two days

evaluated. Additionally, basin averages computed by averaging the ET rates determined

for each pixel in the basin were very close to the averages obtained from flux stations

distributed across the basin.

*Use of Crop Coefficients with AVHRR Data*

Caselles and Delegido (1987) estimated reference evapotranspiration ($ET_{ref}$) from

AVHRR using the expression:

$$ET_{ref} = a + b\,R_g + c\,R_g\,T_{max} \qquad\qquad (2.25)$$

where $R_g$ and $T_{max}$ are global radiation and maximum air temperature derived from

AVHRR data and a, b, and c are regional, empirical coefficients that depend on wind

speed and relative humidity. Solar radiation was estimated as a function of

extraterrestrial radiation and satellite derived surface albedo. Maximum air temperature

was derived by a regression of AVHRR derived surface temperatures obtained near mid

day with point measurements of air temperature in the region. They found that their

method provided reference ET rates that were correlated with class A pan evaporation.

They also noted that using a vegetation map and corresponding crop coefficients,

estimates of actual ET can be obtained.

Seevers and Ottman (1994) developed a method to relate NDVI values to crop

coefficients. Two NDVI values were associated with crop coefficients based on a

knowledge of the crops in the area and a NDVI frequency distribution. A linear

relationship was then used to assign crop coefficients to the remaining NDVI values. ET

calculated from these crop coefficients was found to provide estimates consistent with ET

estimated from gauging station data.

*Application of AVHRR Data with A Simplified Energy Balance Model*

Several studies have focused on using the relationship previously described by

Equation 2.19 to estimate ET with AVHRR derived surface temperatures. Vidal and

Perrier (1990) analyzed the A and B coefficients independently. They concluded that A

is sensitive to irrigation levels, but that it remains essentially constant with time. B was found to be independent of climatic conditions, and could be related to crop height and leaf area index (LAI).

Sandholt and Anderson (1993) were able to obtain a $r^2$ of 0.74 between flux measurements and ET estimated from Equation 2.19 with AVHRR surface temperature using 18 daily values in northern Senegal (NW Africa). They concluded that the B coefficient is a function of NDVI due to its relationship to surface roughness.

Hurtado et al. (1994) calibrated the B parameter of Equation 2.19 for maize and replaced the A parameter with measured net radiation. Using the calibrated equation with AVHRR derived surface temperature, they were able to obtain an estimate of ET that differed by 0.7 mm d$^{-1}$ from ET estimated from Penman's equation. Based on an error analysis, they concluded that the method can estimate daily ET within 0.9 mm d$^{-1}$ assuming the equation has been calibrated to the site of interest.

## Conclusions

Several methods exist to determine ET from ground-based measurements; however, these methods require extensive instrumentation. The instrumentation requirements prevent these methods from being feasible for measurements over large areas.

Remotely sensed data from satellite platforms is subject to several uncertainties, including sensor calibration, atmospheric attenuation and variation due to viewing geometry. Any quantitative application of this data requires that these uncertainties be

minimized.

The application of remotely sensed data has been investigated using several

sensors and platforms. Many of these studies are either limited to short time periods or

use very approximate relationships to derive the ground-based estimate of ET.

Additionally, several of the ET estimates obtained using remotely sensed inputs still

require significant surface measurements or site specific calibration.

# CHAPTER 3

# GROUND-BASED PROCEDURES AND RESULTS

This chapter summarizes measurements taken at the surface used to develop and verify the AVHRR-ET relationships. The first sections describe the equipment used to obtain measurements of both ET and weather conditions. The procedures used to relate these point measurements to represent the larger areas measured by the satellite are then described. Also included in this chapter is a description of a water balance model used at each of the lysimeter sites. The water balance was used to derive daily estimates of soil water during the study period. Finally, procedures and results are presented for a comparison between infrared thermometer measurements of surface temperature and temperatures recorded by the Oklahoma Mesonet.

## Ground-Based Measurements

This section describes the ground-based equipment used to take meteorological and flux measurements. First, a brief description of the observations available from the Oklahoma Mesonet is given. Next, the lysimeter design and sites are described. The concluding section provides a description of additional measurements of surface conditions available for the area surrounding the Apache lysimeter site for select time periods during the study.

58

## Mesonet Meteorological Measurements

The Oklahoma Mesonet is an automated network of 111 weather stations, with a minimum of one station per county in the state. Brock et al. (1995) provide a summary of the technical operation of the Mesonet stations. These stations measure rainfall, temperature and relative humidity at 1.5 m, wind speed and direction at 10 m, solar radiation, barometric pressure, and soil temperature. All measurements are reported and stored at intervals of 15 minutes or less. Measurements of air temperature at 9 m and wind speed at 2 m are available at about half of the sites (including the lysimeter sites). The data can be retrieved in many forms, including 15 minute interval time series for a particular site and day, conditions at every site for a particular time, and daily summaries for every site.

For each lysimeter site, daily summaries for each day of 1994 were retrieved and total rainfall and solar radiation, average wind speed at 2 m, and average / maximum / minimum temperatures and relative humidity at 1.5 m were extracted. Additionally, 15 minute averages were obtained for the time closest to the satellite overpass for images that were used in this study.

## Lysimeter Measurements

In order to have reliable point estimates of actual ET, four weighing lysimeters were used. The lysimeter sites were chosen to represent different climatic, soil and vegetation conditions present across Oklahoma. The locations of the lysimeters are pictured in Figure 3.1. Elevation and average annual precipitation at each of the sites are

**Goodwell**

⊙

Elevation: 995 m
Avg. P[a] : 430 mm

[a]Avg. P is average annual precipitation.

⊙

**Marena**

Elevation: 330 m
Avg. P: 820 mm

⊙

**Wister**

Elevation: 150 m
Avg. P: 1140 mm

⊙

**Apache**
Elevation: 440 m
Avg. P: 640 mm

N
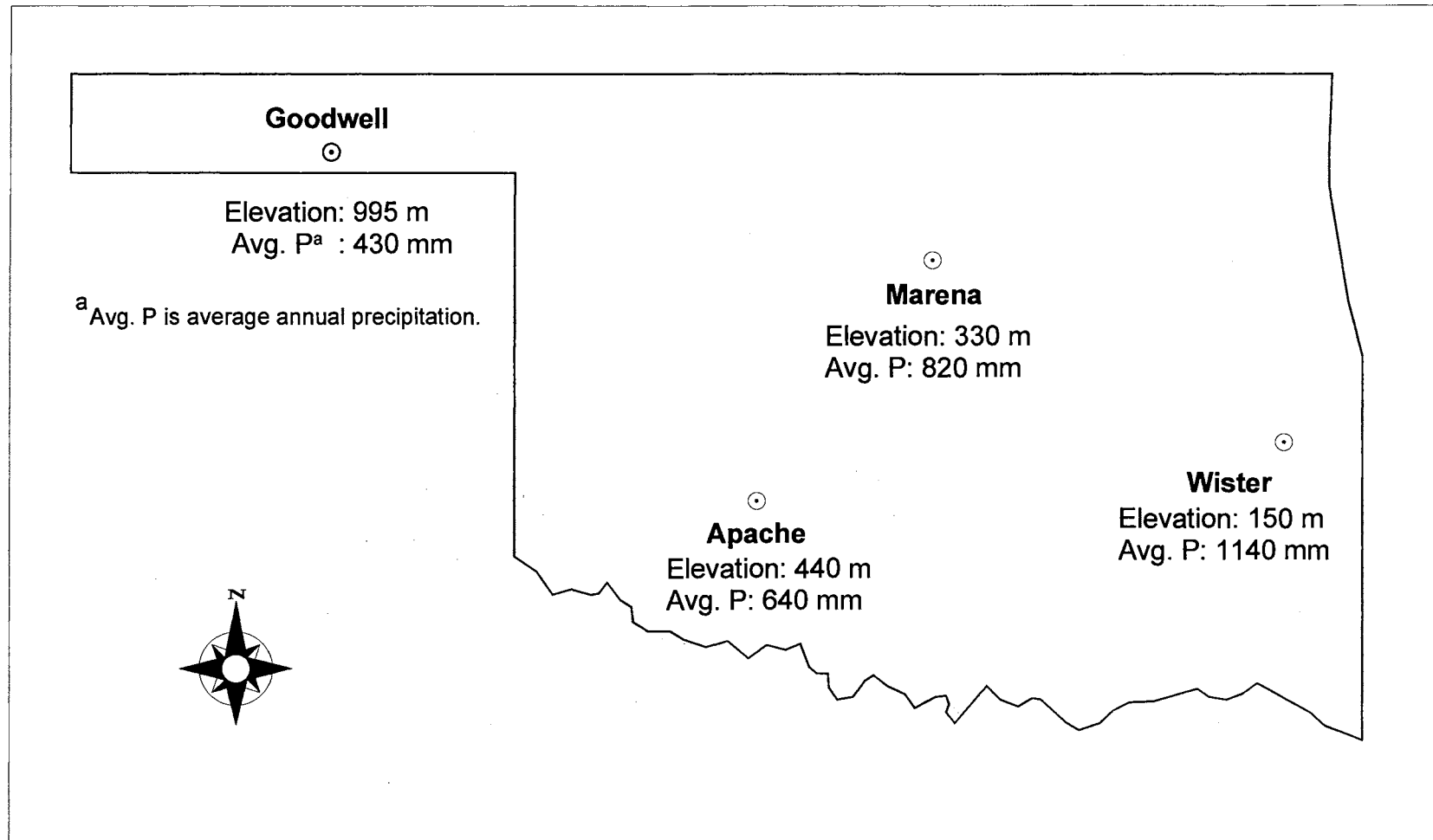
Figure 3.1: Location, elevation, and average annual precipitation for each lysimeter site.

also presented in the figure. The sites range from the semi-arid High Plains of the Oklahoma Panhandle to the high rainfall area of the Ouachita Highlands in the east. Each lysimeter is co-located with an automated weather station that is part of the Oklahoma Mesonet.

Fisher and Elliott (1994) and Fisher (1995) provide a detailed presentation of the lysimeter design, installation and operation. The following site descriptions are taken from their discussion. The vegetation at Goodwell consists of buffalograss (a native, warm-season, perennial short grass), six-weeks fescue (a native, warm-season, annual grass) and little barley (a native, cool-season, annual grass). The soil is a Ulysses clay loam, a deep, moderately fine textured, calcareous soil. At Apache, the vegetation is primarily bermudagrass (a warm-season perennial), with some Japanese brome (a cool-season, annual grass) and little barley also present. Vegetation at Marena consists of a mixture of warm-season grasses such as little blue stem and switch grass and cool-season grasses such as little barley and Japanese brome. The soil is a Grainola-Lucien complex, a silty clay loam with underlying shale and sandstone layers at depths greater than 0.6 m. Tall fescue ( a cool-season, perennial grass) is the primary vegetation at Wister, with some white clover (a perennial legume) also present. The soil is a Wister silt loam, with a silty clay subsoil and underlying shale layers.

The lysimeters are composed of a soil filled inner tank suspended from an outer tank by four load cells. The inner tank has a 0.95 m$^2$ surface area and a depth of 1.5 m. The load cells are sampled every 30 seconds and the readings averaged and reported every 15 minutes. The total weight of the lysimeter is found by summing the four

individual load cell readings and evapotranspiration is estimated from the change in weight with time. In order to minimize any temperature effects on the load cells and data logging equipment, daily ET is determined by the difference in weight from sunrise one day to sunrise on the next day.

Flux Station Measurements

In addition to the lysimeter measurements of ET, the USDA-ARS and NASA conducted two field campaigns in the area of the Apache lysimeter site. As part of these campaigns, flux stations were set up over different cover types from April 6 to April 13 and August 17 to August 23, 1994 by John Prueger (USDA, ARS National Soil Tilth Laboratory, Ames, IA). In the April campaign, ET estimates were from Bowen ratio energy balance stations, with stations located in a wheat field, native pasture, cool season grazed pasture and bermudagrass pasture. In the August campaign, eddy correlation flux measurements were taken over native pasture, short cool season pasture, bare soil and bermudagrass pasture. In addition to the flux measurements, each station was also equipped with an infrared thermometer. Note that in both the April and August campaigns, the bermudagrass pasture is the same pasture containing the Apache lysimeter.

Data composed of 30 minute averages from the stations were obtained from Prueger (1994). Daily estimates of ET were determined from the Bowen ratio measurements, summing only ET values while net radiation is positive. The eddy correlation systems were operated from approximately sunrise to sunset. Daily ET

estimates were obtained by the summation of 30 minute average ET rates. While these estimates only consider the day light hours, it was assumed that significant ET does not occur after sunset.

## Site Characterization and Crop Coefficients

In order to expand the point measurements of the lysimeter to the larger area measured by the AVHRR, the areas occupied by different surface covers in a 9 km$^2$ area centered on the lysimeter sites were determined. Using portions of United States Geological Survey (USGS) 1:24,000 topographic maps, a ground survey was made of the area around the lysimeter. Topographic features and section lines were used to locate cover types on the maps. General field patterns were verified by viewing 1:63,360 color infrared photographs of the areas taken during 1984 by the Soil Conservation Service. While some land use and fields had changed, the field patterns in the photographs were in good agreement with the ground survey. The cover types were digitized and the total area of each cover type determined using GRASS 4.0 (GRASS, 1991). The cover types and percentage of the area occupied are shown in Table 3.1. Covers surrounding Marena and Wister sites were primarily pasture and woodland. The areas surrounding Apache and Goodwell were more diverse, containing both crop and pasture covers.

To estimate the ET over the 9 km$^2$ area, an area weighted ET ($ET_{area}$) was defined at each site as:

$$ET_{area} = \sum_{1}^{n} A_i R_{ci} ET_{point} \qquad (3.1)$$

63

**Table 3.1: Distribution of the major land cover types in a 9 km$^2$ area centered on the lysimeter site.**

| Site | Cover Description | Percent of area |
|------|-------------------|-----------------|
| Apache | Native Pasture | 12 % |
| | Cool Season Pasture | 12 % |
| | Warm Season Pasture | 24 % |
| | Wheat/Fallow | 52 % |
| Goodwell | Pasture | 55 % |
| | Wheat/Fallow | 25 % |
| | Irrigated Corn | 20 % |
| Marena | Pasture | 77 % |
| | Woodland | 23 % |
| Wister | Pasture | 68 % |
| | Woodland | 32 % |

where $A_i$ is the fraction of the 9 km$^2$ area occupied by cover i, $R_{ci}$ is the ratio of ET from cover i to $ET_{point}$, and $ET_{point}$ is the point estimate of ET from either the lysimeter or a calculated reference ET.

Calculated Reference ET

For woodland and irrigated areas, lysimeter measurements were not used to partition the area weighted ET, as ET rates over these areas are not under the same soil water conditions as the lysimeters. Instead, a daily grass reference ET, for use with standard crop coefficients, was calculated using the Penman-Monteith equation found in REF-ET (Allen, 1990). The Penman-Monteith equation can be expressed as:

$$ET_{ref} = \frac{1}{1 - r_c / r_a} \frac{\Delta}{\Delta + \gamma} (-R_n - G + K0.622 \frac{\lambda \rho_a}{P r_a} (e^o_z - e_z)) \qquad (3.2)$$

where $ET_{ref}$ is the calculated reference evapotranspiration, $r_c$ is canopy resistance, $r_a$ is the aerodynamic resistance to moisture and heat transfer, $\Delta$ is the slope of the saturation vapor pressure-temperature curve, $\gamma$ is the psychrometric constant, $R_n$ is net radiation, G is soil heat flux, K is a units conversion factor, $\lambda$ is the latent heat of vaporization, $\rho_a$ is the density of air, P is atmospheric pressure, $e^o_z$ is saturation vapor pressure at a level z above the surface, and $e_z$ is the actual vapor pressure at that level. REF-ET estimates the resistance terms as a function of grass height. Daily Mesonet weather data (temperature, relative humidity, solar radiation and wind speed) served as inputs to the REF-ET program.

A limitation of the Mesonet data for use in the calculation of a reference ET is that

the stations are not maintained at reference conditions (well watered and vegetation at a standard height). This limitation was a particular concern at the Goodwell location due to the arid conditions. Therefore, minimum/maximum temperature and relative humidity were adjusted for the non-reference conditions using procedures from Allen (1995) at the Goodwell site.

## Standard Crop Coefficients

The calculated reference ET was related to the woodland areas at Marena and Apache and irrigated crops at Goodwell using standard crop coefficients. Trees typically have a more developed root system that extends deeper into the soil, and thus can utilize soil water at greater depths. Therefore, a calculated reference ET is used rather than the lysimeter measurements. However, the canopy height of the woodland areas is much greater than that of grass and thus there is a higher canopy resistance. Considering discussions of both Shuttleworth (1993) and Calder (1993), a crop coefficient of 0.9 was assumed for the woodland areas when not dormant. Under conditions of dormancy, the ET rate was assumed to be 0.9 of the ET measured by the lysimeter to continue to reflect the increased canopy resistance of the woodland areas.

For the irrigated corn in the area of the Goodwell lysimeter, grass crop coefficients for an arid Mediterranean climate reported by Jensen et al. (1990) were used. The climatic conditions under which these coefficients were developed are similar to the conditions at the Goodwell site. During a site visit on July 13, most corn in the area was nearing full canopy conditions. This observation is in agreement with the reported

coefficients.

Both dryland and irrigated wheat are grown in the Goodwell area. Therefore, point estimates of wheat are based on the average of the lysimeter measured ET and the Penman-Monteith calculated reference ET. The wheat crop coefficients used are from Doorenbos and Pruitt (1977) for low relative humidity and high wind speeds that are appropriate to the Goodwell location. A summary of the wheat and corn crop coefficients is shown in Table 3.2. Coefficients for days between those shown in the table were determined by linear interpolation.

To account for increased soil surface evaporation near the time of rainfall, the coefficients were adjusted by procedures from Wright (1981). For times within 7 days (time selected based on elevated lysimeter ET rates after a rainfall) of a rainfall, the crop coefficient was calculated as:

$$K_{crf} = K_c + (1 - K_c)(1 - (t / 7)^{0.5}) \qquad (3.3)$$

where $K_{crf}$ is crop coefficient adjusted for the increased evaporation due to rainfall, $K_c$ is the standard crop coefficient, and t is the time in days since the rainfall occurred. Note that the increase in ET resulting from the adjustment was not allowed to exceed the amount of rainfall.

## Derived Cover Coefficients

The flux measurements during April and August were used to determine the relationship between ET from the various cover types and the lysimeter measurements at the Apache site. The cover coefficients (the $R_c$ term of Equation 3.1) are similar to a

**Table 3.2: Standard crop coefficients used with the calculated reference ET.**

| Day of the Year | Crop Coefficients Corn [a] | Crop Coefficients Wheat [b] |
|---|---|---|
| 106 | NA | 1.20 |
| 123 | NA | 1.20 |
| 139 | 0.12 | 0.84 |
| 144 | 0.13 | 0.71 |
| 150 | 0.15 | 0.59 |
| 155 | 0.20 | 0.47 |
| 160 | 0.29 | 0.34 |
| 165 | 0.45 | 0.22 |
| 170 | 0.81 | 0.20 |
| 176 | 0.99 | 0.20 |
| 181 | 1.08 | 0.20 |
| 186 | 1.13 | 0.20 |
| 196 | 1.17 | 0.20 |
| 206 | 1.17 | 0.20 |
| 216 | 1.17 | 0.20 |
| 226 | 1.14 | 0.20 |
| 236 | 1.03 | 0.20 |
| 246 | 0.87 | 0.20 |
| 256 | 0.67 | 0.20 |

[a] Based on information from Table 6.8 of Jensen et al. (1990).

[b] Based on information in Doorenbos and Pruitt (1977) for low relative humidity and windy conditions.

standard crop coefficient; however, in this case the reference condition is non-irrigated.

The $R_c$ values determined from the flux measurements are shown in Table 3.3.

**Table 3.3: Cover coefficients ($R_c$) derived for the Apache lysimeter from flux measurements over the other cover types.**

| Time Period | Cover | Average $R_c$ | Standard Deviation [a] | N |
|---|---|---|---|---|
| April | Wheat | 1.38 | 0.21 | 5 |
| April | Native Pasture | 0.66 | 0.11 | 5 |
| August | Native Pasture | 1.24 | 0.30 | 6 |
| Both [b] | Cool Season | 0.60 | 0.33 | 11 |
| | Warm Season [c] | 1.00 | ----- | --- |

[a] Standard deviation of the $R_c$ measurements over the period of N days.
[b] Most cool season pastures had low plant densities. The $R_c$ values for the two time periods were similar; therefore, the data was combined.
[c] Warm season pastures are assumed to have the same ET rate as the lysimeter.

For cool season pasture, a constant coefficient of 0.60 was used for all days. The low value of the coefficient reflects the fact that most of the cool season pastures in the area had low plant densities. The native pasture was assumed to be 0.66 of the lysimeter measured ET before May 15, as both covers were dormant. The increased height of the native pasture insulates the surface and decreases evaporation relative to that of the lysimeter; however, during times of active growth the increased height will decrease surface resistance to transpiration. Therefore, after May 15, a $R_c$ value of 1.24 was used.

The wheat growth stage was determined both by observations during site visits to Apache in April and discussion by Kirkham and Kanemasu (1983). For times prior to active growth of the wheat (approximately March 1), the wheat ET rates were assumed equal to those of the lysimeter, as neither the Bermudagrass in the lysimeter nor the wheat

is actively growing. Between the dates of March 1 (DOY = 60, $R_c$ = 1) and April 6

(DOY = 96, $R_c$ = 1.4) when the Bermuda grass is primarily dormant, a linear relationship

for the cover coefficient of wheat was derived from the flux data as:

$$R_{cwheat} = \frac{0.4}{36}DOY + 0.33 \qquad (3.4)$$

where DOY is the day of the year. After April 6 and before harvest (approximately June

15), when the bermudagrass grass in the lysimeter is no longer dormant, cover

coefficients are based on information from Doorenbos and Pruitt (1977) shown in Table

3.2.

During the August study a 25 mm rainfall event occurred on the 17th and one of

the flux stations was in a tilled field. Therefore, it was possible to determine a

relationship between lysimeter ET and bare soil evaporation,

$$R_{cbare} = \frac{1.58}{\sqrt{t}} - 0.55 \qquad (3.5)$$

where $R_{c\,bare}$ is the ratio of bare soil evaporation to lysimeter ET, and t is time in days

since the rainfall occurred ($r^2$ of 0.997 and standard error of 0.037). The relationship

between soil evaporation and the square root of time since a rainfall is discussed by

Ritchie (1972).

Area Weighted ET Results

A complete presentation of the area weighted ET estimates is included in

Appendix A for days that cloud free AVHRR images were obtained and the lysimeters

were operating. Also included in the appendix are the corresponding measurements of ET from the lysimeters and Penman-Monteith calculated ET for each site.

A summary comparison of the area weighted ET, lysimeter ET and Penman-Monteith calculated reference ET is shown in Table 3.4. The Apache and Goodwell sites are listed independently, while the Marena and Wister sites are combined as there were only 4 days at Marena when the lysimeter was operating and clear images were available.

**Table 3.4: Summary statistics of calculated Penman-Monteith reference ET ($ET_{pmon}$), lysimeter measured ET ($ET_{lys}$) and area weighted ET ($ET_{area}$).**

| Statistic | $ET_{pmon}$ | $ET_{lys}$ | $ET_{area}$ |
|---|---|---|---|
| | | Apache | |
| Average (mm d$^{-1}$) | 6.1 | 4.0 | 3.0 |
| Standard Deviation (mm d$^{-1}$) | 1.9 | 2.3 | 1.7 |
| Coefficient of Variation | 31% | 58% | 57% |
| Number of Days | 19 | | |
| | | Goodwell | |
| Average (mm d$^{-1}$) | 8.0 | 2.9 | 3.1 |
| Standard Deviation (mm d$^{-1}$) | 1.1 | 1.4 | 0.9 |
| Coefficient of Variation | 14% | 47% | 30% |
| Number of Days | 15 | | |
| | | Marena/Wister | |
| Average (mm d$^{-1}$) | 5.7 | 4.9 | 4.6 |
| Standard Deviation (mm d$^{-1}$) | 1.3 | 2.1 | 1.5 |
| Coefficient of Variation | 23% | 43% | 32% |
| Number of Days | 16 | | |

At each site the calculated reference ET showed less variation than did the lysimeter estimate of ET. Additionally, at both the Apache and Goodwell sites, the lysimeter measured ET was considerably lower on average than the reference ET. Both

71

are an indication that soil water availability was influencing the rate of evaporation. The cover distribution at the Apache site explains why the average area weighted ET is lower than the lysimeter ET. Early in the year when the wheat is actively growing, a majority of the other covers are primarily dormant. After the wheat has been harvested the other cover types are actively growing. There is only a limited time period when all covers are actively growing.

At Goodwell, the fact that the estimate of area ET is on average slightly higher than the lysimeter ET is a result of the presence of irrigated corn and wheat. In the more humid regions of the Marena and Wister sites, average lysimeter ET rates are closer to the calculated reference ET. As much of the area at these two sites was assumed to have the same ET as the lysimeter, the average ET for the lysimeter and area weighted ET's are comparable.

Uncertainty Analysis of the Area Weighted ET Estimates at Apache

The use of cover coefficients to extend the point estimates of ET to a larger area does introduce error into the area weighted ET estimates. First Order Analysis (Dettinger and Wilson, 1981) was used to estimate the effect the combined uncertainties in the $R_c$ values have on the area weighted ET at the Apache site. The standard deviations of the $R_c$ values in Table 3.3 were used to represent the uncertainty in the cover coefficients. The errors in the $R_c$ values are assumed to be uncorrelated and no error is assumed in the lysimeter measurements. A further assumption is that the uncertainty in the $R_c$ for the warm season pastures is 0.1. Applying these assumptions, the uncertainty in the area

72

weighted ET estimate from equation 3.1 can be expressed as:

$$S_{ETarea} = \sqrt{\sum_{i=1}^{n} (STD_i \, A_i \, ET_{point})^2}$$  (3.6)

where $s_{ETarea}$ is the uncertainty in the area weighted ET, n is the number of cover types, $STD_i$ is the standard deviation of $R_c$ from Table 3.3 for cover i, $A_i$ is the fraction of area occupied by cover i and $ET_{point}$ is the point estimate of ET.

Since $ET_{point}$ is always the lysimeter for all the covers during the time of the April and August flux measurements, it can be factored out of the Equation. Therefore, Equation 3.6 can be rearranged as:

$$\frac{S_{ETarea}}{ET_{point}} = \sqrt{\sum_{i=1}^{n} (STD_i A_i)^2}$$  (3.7)

From the data in Table 3.3, the uncertainty in the area weighted ET estimate was 11% of the point estimate of ET for the April time period, and the uncertainty was 6% for the August time period. These uncertainty estimates are only explicitly valid for the time periods surrounding the actual flux measurements; however, this analysis does provide a quantification of the potential error in the area weighted ET estimates. While no data is available to conduct such an analysis at the other sites, it is assumed that the error would not be any greater at Marena and Wister, as a majority of the areas surrounding these sites are pastures with similar vegetation. A higher uncertainty is expected at Goodwell due to the irrigated agriculture.

73

## Water Balance Model

In order to have an estimate of soil water at the lysimeter sites, a daily water balance model was used. The objective of deriving these estimates is not to obtain precise estimates of the soil water, but to provide some measure of relative dry and wet periods during the study. The following is a description of both the model and a comparison of predicted to observed soil water contents.

Model Description

The water balance equation used was:

$$\theta_i = \theta_{i-1} + RF_i - ET_i - LOST_i \tag{3.8}$$

where $\theta_i$ is the average water content in the top 1.2 m of the soil profile (mm), RF is total daily rainfall (mm) from the Mesonet station, ET is the daily actual evapotranspiration (mm), LOST is the amount of moisture lost as runoff or deep percolation, and i is an index of the day of interest.

At the Apache and Goodwell sites, ET was determined from the lysimeter measurements, as there were only limited time periods when lysimeter data was not available. For the intermediate times the lysimeter was not available, the ratio of lysimeter ET to reference ET from Equation 3.2 was calculated for the day before lysimeter data was not available. This ratio, similar to a crop coefficient, was then multiplied by the reference ET on days the lysimeter was not working in order to provide an estimate of actual ET. As the time periods considered ranged from 1 to 3 days, the effect of changes in moisture availability on the ratio was ignored. Additionally, at the

74

Apache and Goodwell sites the LOST term of Equation 3.8 was assumed equal to 0 for all days.

Lysimeter data was less consistent at the Marena and Wister sites, usually due to flooding of the outer tank. Therefore, there were longer periods when lysimeter data was not available. For these time periods, the $ET_i$ of Equation 3.8 for days lysimeter data was not available at Marena and Wister was calculated as:

$$ET_i = K_s\, K_{lys}\, ET_{ref} \qquad\qquad (3.9)$$

where $K_s$ is a soil availability coefficient, $K_{lys}$ is an apparent crop coefficient and $ET_{ref}$ is the reference ET from Equation 3.2. A ratio of the lysimeter ET to reference ET was used to establish $K_{lys}$. The soil availability coefficient was calculated as:

$$K_s = AW^x \qquad\qquad (3.10)$$

where AW is available water, and x is a fitting parameter. Available water was defined as:

$$AW = \frac{\theta_{i-1} - \theta_{dry}}{\theta_{FC} - \theta_{dry}} \qquad\qquad (3.11)$$

where $\theta_{i-1}$ is the soil water content on day i-1, $\theta_{FC}$ is the water content at field capacity and $\theta_{dry}$ is the water content corresponding to dry conditions. Field capacity was defined based on neutron probe readings soon after a rainfall. Anytime the predicted soil water exceeded the field capacity parameter, the additional moisture was assumed lost to runoff or deep percolation. The x parameter of Equation 3.10 and $\theta_{dry}$ of Equation 3.11 were used as calibration parameters. The parameters were selected by comparison of the resulting prediction of soil water with soil water data obtained from neutron probe

readings made by Fisher (1995).

Estimates of Soil Water from the Water Balance

Based on the neutron probe readings early in the season, field capacities of 320

mm and 480 mm were assigned for Marena and Wister, respectively. A value of 1.5 for

the x parameter of Equation 3.10 resulted in reasonable predictions of soil water at both

Marena and Wister. Final adjustment of the model resulted in a $\theta_{dry}$ value of 140 mm,

again the same for both Marena and Wister.

Figure 3.2 is a comparison of the predicted and measured soil water at the

lysimeter sites. In general, the soil water estimates of the water balance are in good

agreement with the measured soil water. At Marena, the soil water was under predicted

during the time period from day 150 to 300; however, the difference is typically less than

10 mm. During the same time period, soil water was slightly over predicted at the

Marena site. Any effort to further adjust the fitting parameters decreased the accuracy of

the predictions at earlier and later time periods. Better overall results were obtained at the

Apache and Goodwell sites compared to the results at Wister and Marena. At Goodwell,

there is a definite under prediction of soil water by the water balance model on day 230.

It is possible that the tipping bucket rain gage under estimated rainfall for an intense

storm or there was an error in the neutron probe reading.

At all of the sites, there is a definite drying trend beginning near day 150 (May

30). The soil water content is consistently lower for the time period from day 160 to day

300 (June 9 to October 27) compared to the other time periods. Further discussion of the

implications of the soil water conditions will be discussed in Chapter 5.
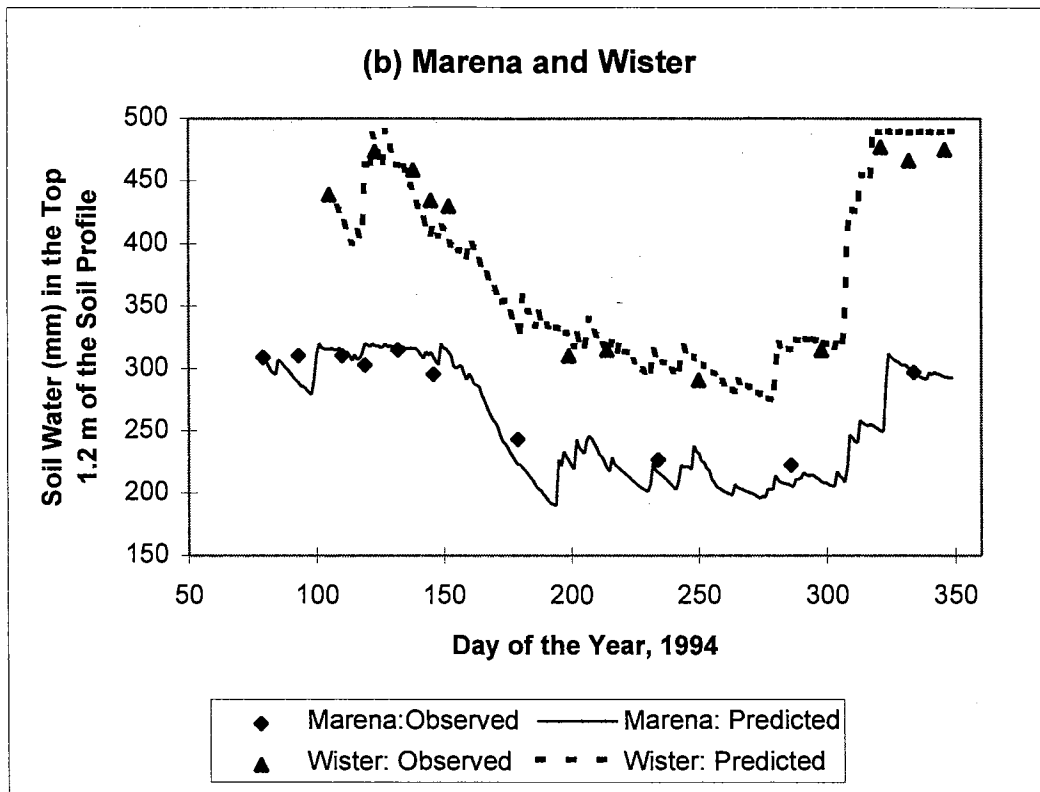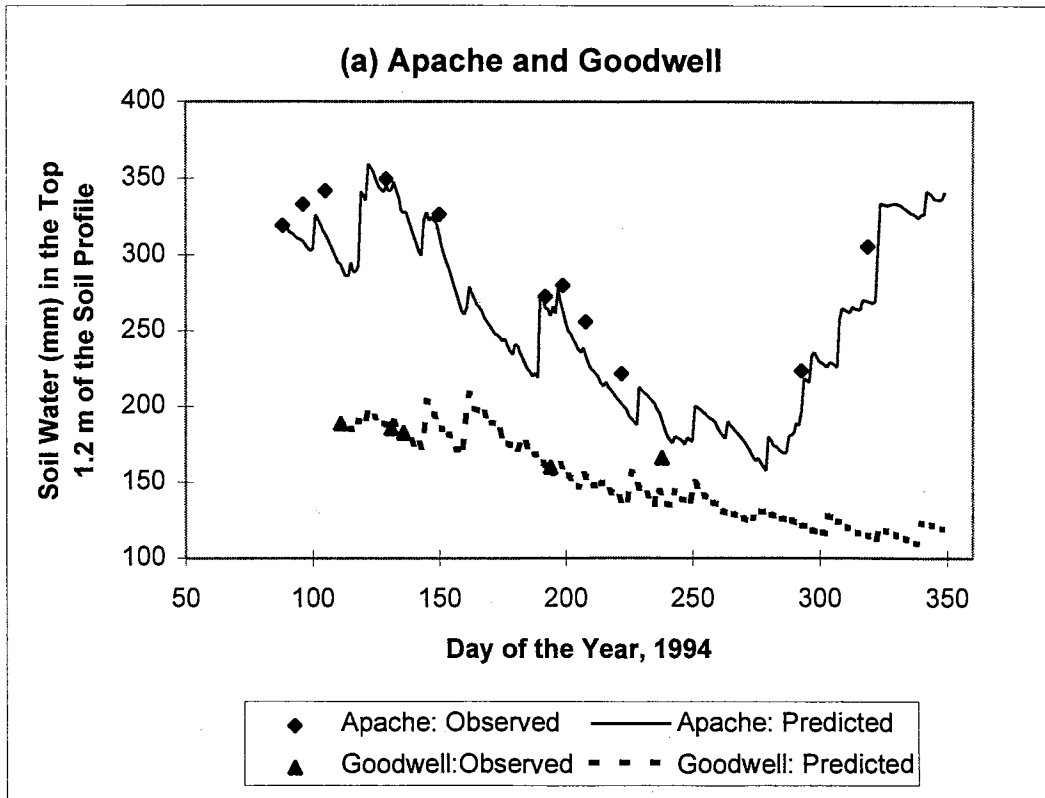
Figure 3.2: Predicted and observed soil water content in the top 1.2 m of the soil profile at (a) Apache and Goodwell and (b) Marena and Wister lysimeter sites.

## Infrared Thermometry

The Mesonet weather stations do not provide a direct measurement of the surface temperature; however, a method to evaluate AVHRR derived surface temperatures was needed for this study as will be further discussed in Chapter 5. The following is a description of a comparison made between measurements from the Mesonet and available infrared thermometer data. The objective of the comparison is to determine which Mesonet temperature (1.5 m, 9 m air temperature, or 5 cm soil temperature) best represents surface temperature.

### Measurements

For the period of September 15 to October 3, surface temperature was measured at the Marena Mesonet site using an Everest Model 4000 LCS infrared thermometer (IRT) with a 15° field of view. The IRT was sampled every 30 seconds and the readings averaged and stored by a Campbell data logger. Additionally, readings of surface temperature were taken using a Telatemp AG42 hand held IRT with a 4° field of view at the different lysimeter sites between April and August of 1994. Readings were taken using a tripod holding the IRT at 1 m above the surface with a 90° look angle. The surface emissivity was set at 0.98 for all readings.

The surface temperatures at Marena were compared to Mesonet reported 1.5 m and 9 m air temperature, and 5 cm bare and sod soil temperatures. Using data from the Marena site while the IRT was in operation, the relationship between the IRT measured surface temperature and Mesonet temperatures was evaluated at times corresponding to

typical AVHRR overpass times (11:15 and 22:15 GMT). IRT measurements taken at the flux stations in the Apache area were also evaluated to examine the relationship between air and surface temperature over different cover types.

Evaluation Statistics

The following evaluation statistics were used to evaluate which Mesonet temperature most closely represented surface temperature. Note that these evaluation statistics are also used in Chapters 4 and 5. The least squares linear regression coefficients between the calculated and measured values were determined for the equation:

$$\text{Predicted} = A_r + B_r \text{Measured} \tag{3.12}$$

where Predicted is the value of the predicted variable, Measured is the measurement of interest, and $A_r$ and $B_r$ are the least squares regression parameters (intercept and slope, respectively). For the ideal case, where the estimated and measured values are equal, $A_r$ will have a value of 0 and $B_r$ will equal 1. If the slope of the relationship is 1, average over prediction will be indicated by $A_r$ having a positive value.

The coefficient of determination ($r^2$) was used as a measure of the relative amount of variation explained by the regression relationship. The standard error of the regression relationship was calculated as:

$$\text{STD}_{err} = \sqrt{\frac{\sum_{i=1}^{N} (\text{Predicted} - \text{Measured})^2}{N-2}} \tag{3.13}$$

where $STD_{err}$ is the standard error, and N is the number of observations. The standard

error has the same units as the measurements and provides a measure of the accuracy of

the relationship. All regression calculations were conducted using the Excel 5.0

spreadsheet program.

Comparison of IRT Measurements to Soil and Air Temperatures

Table 3.5 is a presentation of the results for the regression relationships between

IRT measured surface temperature and 1.5 and 9 m air temperature, 5 cm soil temperature

under vegetative (sod) and bare surface for typical AVHRR over pass times. To aid in

interpretation of the statistics, sample plots of surface versus 1.5 m air temperatures for

both 11:15 and 22:15 GMT are shown in Figure 3.3. For morning observations, the 1.5

m air temperature has a higher coefficient of determination ($r^2$) and lower standard error

when compared to surface temperature predictions using the other temperatures. The

coefficient of determination is decreased with the evening measurements. This is not

unexpected, as energy exchanges are at a minimum in the early morning without solar

radiation to drive the process. In the evening, the effect of solar heating of the surface is

still creating a vertical temperature gradient. The magnitude of this gradient will vary

depending on soil water conditions and transpiration rates. As 1.5 m air temperature

consistently has the highest $r^2$ and lowest standard error for a given time period, it is

concluded this temperature is the best for later comparison with AVHRR derived surface

temperatures.

Regression results of the comparison between IRT measured surface temperatures

over different cover types in the Apache area and Mesonet air temperature at 1.5 m are

**Table 3.5: Results from the least squares relationship [a] between surface temperature ($T_s$) and Mesonet air or soil temperatures evaluated at the Marena lysimeter site from August 25 to October 3, 1994.**

| Statistic [b] | Temperature used as the independent variable. [c] | | | |
|---|---|---|---|---|
| | $T_a$ 1.5m | $T_a$ 9m | $T_{sod}$ | $T_{bare}$ |
| **Morning (11:15 GMT)** | | | | |
| n | 35 | 35 | 35 | 35 |
| $A_r$ | 2.09 | 1.73 | -10.89 | -3.32 |
| $B_r$ | 0.90 | 0.92 | 1.29 | 1.01 |
| $STD_{err}$ | 0.76 | 1.36 | 1.45 | 1.76 |
| $r^2$ | 0.97 | 0.91 | 0.90 | 0.85 |
| **Evening (22:15 GMT)** | | | | |
| n | 34 | 34 | 34 | 34 |
| $A_r$ | 2.67 | 3.62 | -3.42 | 0.61 |
| $B_r$ | 1.03 | 1.03 | 1.27 | 0.96 |
| $STD_{err}$ | 1.77 | 1.91 | 3.34 | 2.11 |
| $r^2$ | 0.90 | 0.89 | 0.65 | 0.86 |

[a] Regression equation: $T_s = A_r + B_r$ T? where T? is temperature used as the independent variable.

[b] n is the number of observations, $STD_{err}$ is the standard error of the regression relationship, and $r^2$ is the coefficient of determination.

[c] $T_a$ 1.5m is the air temperature at a height of 1.5 m, $T_a$ 9m is the air temperature at a height of 9 m, $T_{sod}$ is the soil temperature at a depth of 5 cm under sod cover and $T_{bare}$ is the soil temperature at a depth of 5 cm under bare soil. All temperatures are °C.
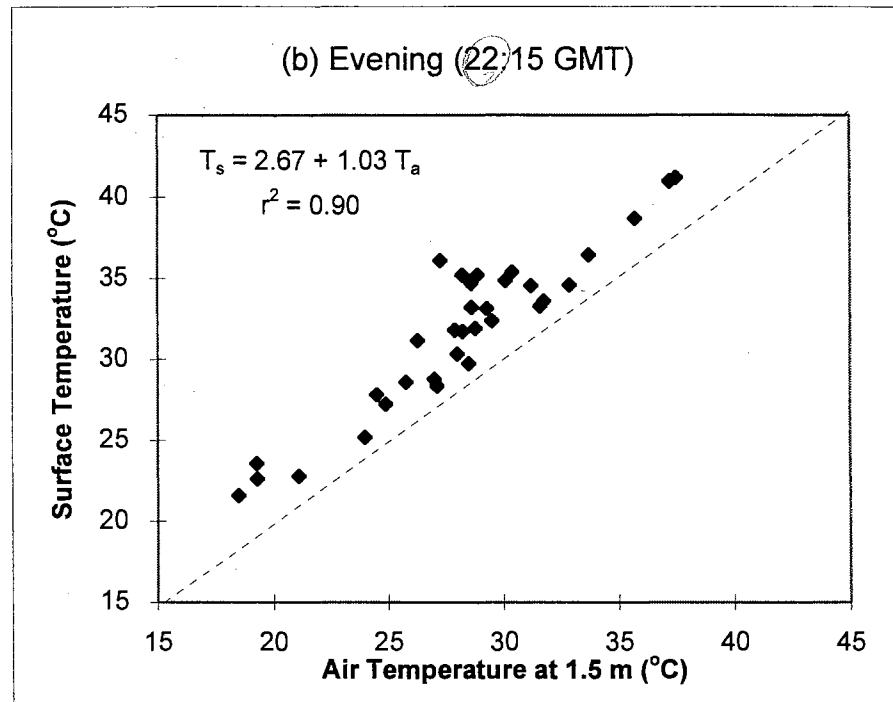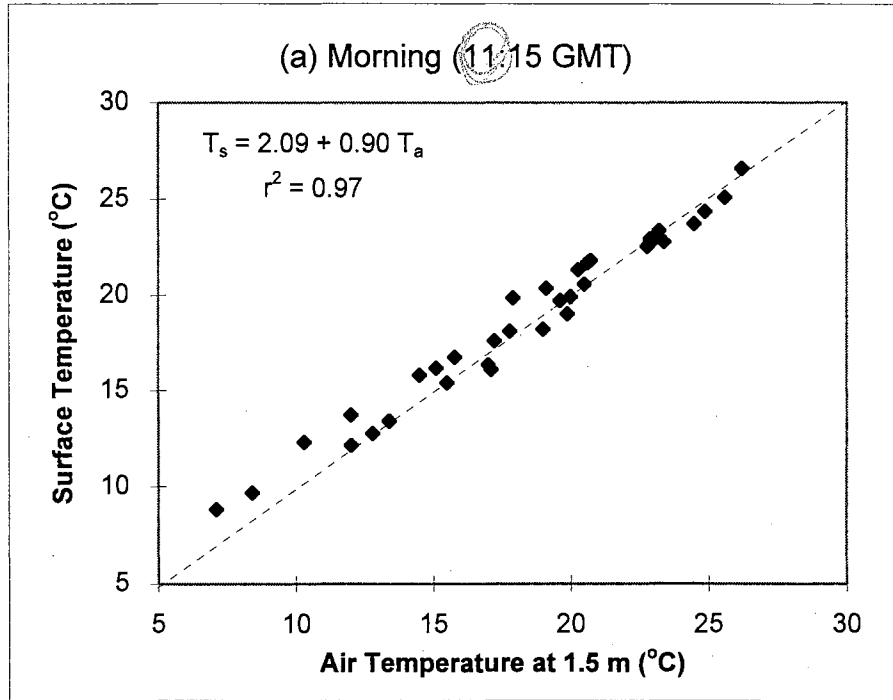
Figure 3.3: Surface versus 1.5 m air temperature at the Marena lysimeter site at (a) 11:15 GMT and (b) 22:15 GMT from August 25 to October 3, 1994.

presented in Table 3.6. Sample plots for the morning and evening surface versus air temperature over the native pasture are shown in Figure 3.4. For most of the cover types, the relationship between morning 1.5 m air temperature and surface temperature had standard errors under 1 °C. Again, the relationship was not as strong with the evening measurements. The poor relationship over bare soil for evening times is related to the rainfall event that took place on August 17, the beginning of the observation period. When the soil was wet, the surface temperature was close to the air temperature; however, as the soil dried, the surface temperature was up to 10 °C higher than the air temperature. These results support the Marena data, in that morning air temperature provides a reasonable estimate of surface temperature. Meaningful comparisons will be possible between the AVHRR derived surface temperature and 1.5 m air temperature for a variety of surface covers. Comparisons between evening surface and air temperatures will require more careful interpretation, especially over sparsely vegetated surfaces. From Figure 3.3 (b), note that evening surface temperatures were consistently higher than air temperatures at the Marena site. Surface temperatures measured with the hand-held IRT were also found to be higher than air temperature at the other lysimeter sites and time periods. Surface temperature was approximately 4 °C higher than air temperature on May 23 at the Wister lysimeter site (20:00 GMT). On July 13, surface temperature was 21 °C higher than air temperature at the Goodwell site (20:15 GMT). For irrigated crops, surface temperature is typically less than air temperature; however, this is not necessarily the case for these dryland conditions.

**Table 3.6:** Results from the least squares relationship[a] between surface temperature ($T_s$) and air temperature at a height of 1.5 m ($T_a$) evaluated for different cover types near the Apache lysimeter site from April 6 to 13 and August 17 to 22, 1994.

| Statistic[b] | Bermuda-grass | Cool Season Grass | Native Pasture | Wheat[c] | Bare Soil[d] |
|---|---|---|---|---|---|
| | | | | | |

**Morning**
**(Based on average temperatures from 11:00 to 11:30 GMT)**

| Statistic[b] | Bermuda-grass | Cool Season Grass | Native Pasture | Wheat[c] | Bare Soil[d] |
|---|---|---|---|---|---|
| n | 12 | 10 | 11 | 7 | 4 |
| $A_r$ | -1.66 | -2.47 | -2.23 | 0.02 | -1.96 |
| $B_r$ | 0.99 | 1.10 | 1.08 | 0.91 | 0.97 |
| $STD_{err}$ | 0.91 | 0.99 | 0.82 | 0.75 | 1.13 |
| $r^2$ | 0.99 | 0.99 | 0.99 | 0.99 | 0.95 |

**Evening**
**(Based on average temperatures from 22:00 to 22:30 GMT)**

| Statistic[b] | Bermuda-grass | Cool Season Grass | Native Pasture | Wheat[c] | Bare Soil[d] |
|---|---|---|---|---|---|
| n | 12 | 12 | 11 | 6 | 5 |
| $A_r$ | -0.11 | -0.75 | 0.97 | 2.69 | 30.67 |
| $B_r$ | 1.01 | 1.07 | 0.95 | 0.75 | 0.10 |
| $STD_{err}$ | 2.14 | 1.85 | 1.91 | 0.65 | 5.85 |
| $r^2$ | 0.95 | 0.96 | 0.94 | 0.98 | 0.01 |

[a] Regression equation: $T_s = A_r + B_r\,T_a$, temperatures in °C.

[b] n is the number of observations, $STD_{err}$ is the standard error of the regression relationship, and $r^2$ is the coefficient of determination.

[c] Wheat measurements were only available in April.

[d] Bare soil measurements were only available in August.
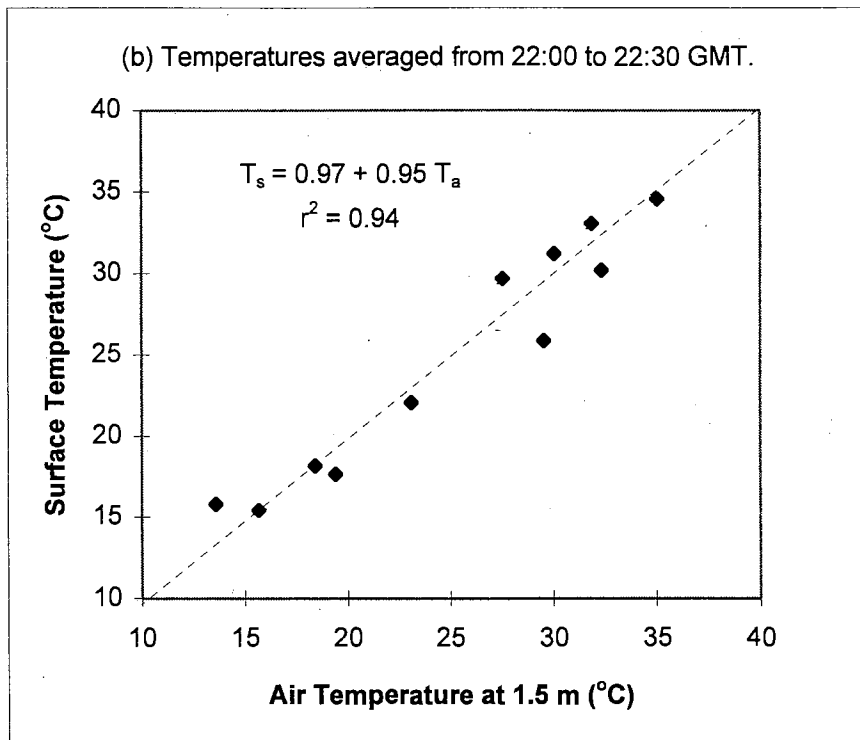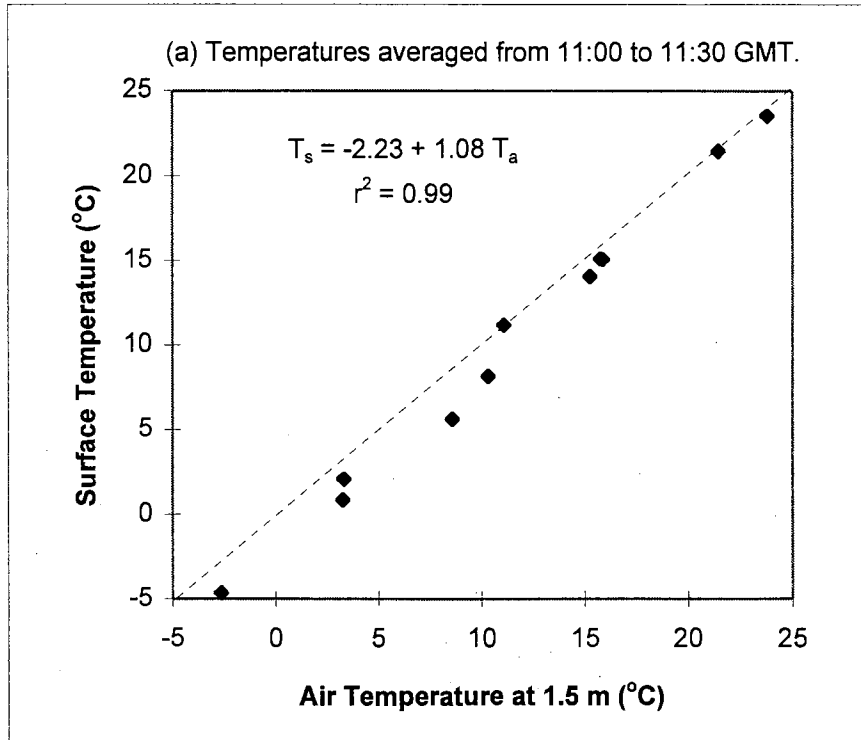
Figure 3.4: Surface versus 1.5 m air temperatures over a native pasture near Apache during (a) morning and (b) evening time periods for April 6 to 13 and August 17 to 22.

## Chapter Summary

A combination of data from the Oklahoma Mesonet, weighing lysimeters, supplemental flux measurements and cover types surrounding the lysimeter sites was used to provide estimates of ET corresponding to the area measured by the satellite. A simple water balance model was also used to provide an estimate of soil water content during the time of the study. In 1994, there were relatively dry conditions from early June to the end of October. Air temperature at 1.5 m was found to be highly correlated with surface temperature, particularly during the early morning hours. The relationship between air and surface temperature appears sufficient for the evaluation of AVHRR derived surface temperatures.

CHAPTER 4

IMAGE PROCESSING PROCEDURES AND RESULTS

This chapter describes the steps taken to process the satellite derived information. A flow diagram summarizing the image processing steps is shown in Figure 4.1. The chapter begins with a description of the methods used to select and retrieve images, including cloud screening procedures. Then a description and evaluation of the geometric correction procedures are presented. Next, radiometric calibration techniques for both the reflective and thermal channels are discussed. Methods to derive estimates of reflectance from channels 1 and 2 are then explained and evaluated. Finally, the temporal variations in three spectral indices are examined. Note that a discussion of the split-window surface temperature procedures and results is included in Chapter 5.

**Image Selection and Retrieval**

This section begins by describing the process used to identify days on which cloud cover would be least likely. Next, a description is provided of the archive systems used to obtain images. Finally, the cloud screening procedures are described.

The time period of this study was from February to September 1994. Prior to February, only the Marena lysimeter site was in full operation, and high solar zenith angles limited the usefulness of the AVHRR's reflective channels in January and part of
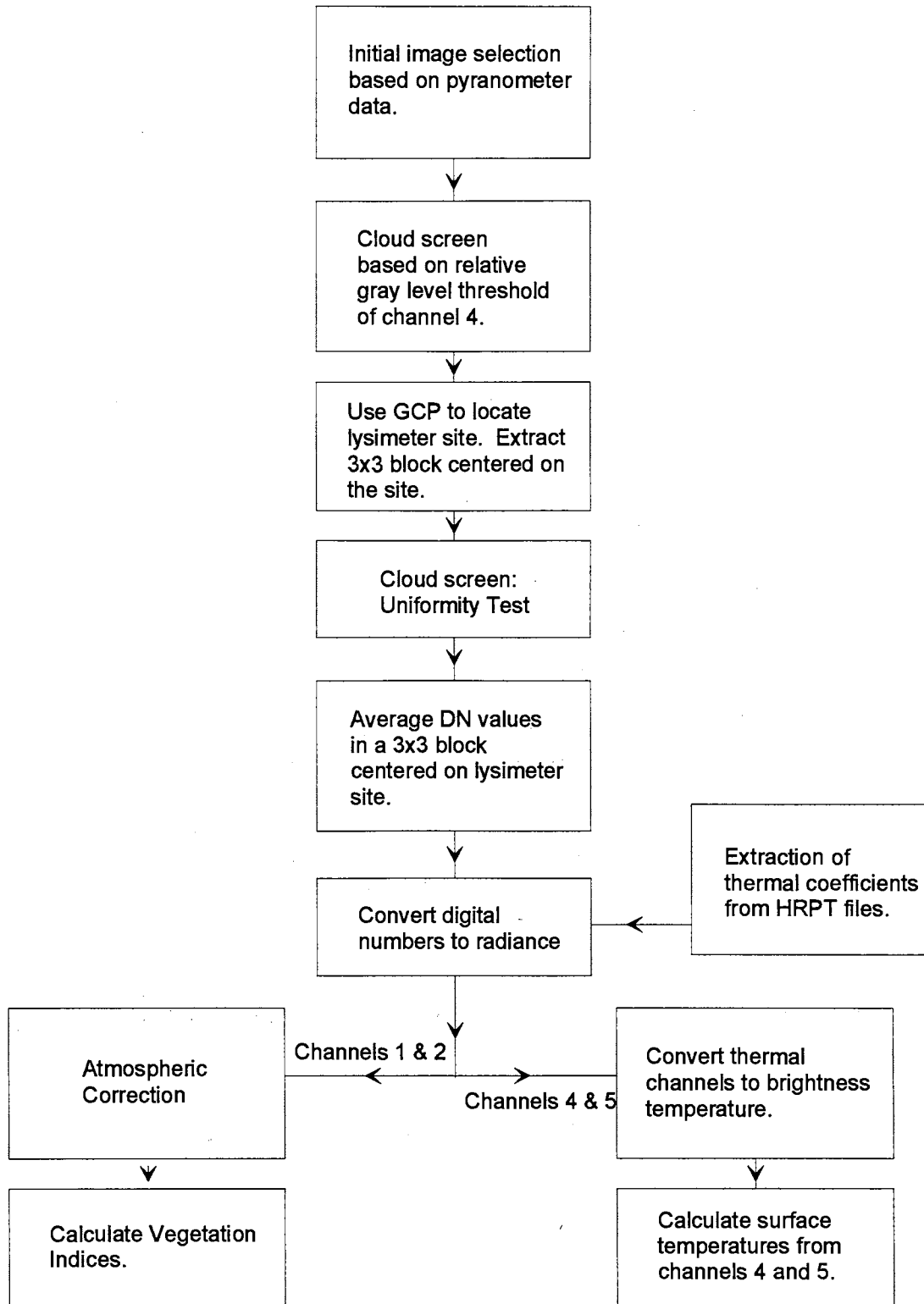
Figure 4.1: Flow diagram of the image processing steps.

February. On September 13, the AVHRR on NOAA 11 ceased transmitting meaningful data.

## Initial Image Selection

In order to identify days with minimal probability of cloud cover over the lysimeter sites, Mesonet pyranometer data was used. The first procedure was to give priority to days with the highest ratio of total measured to extraterrestrial solar radiation. Extraterrestrial radiation was calculated as a function of the day of the year and latitude of each site using equations from Iqbal (1983). The equations are included as part of Appendix H. Days with high ratios of actual to extraterrestrial solar radiation were assumed to be days on which cloud contamination would be least likely. However, it was found that for some of these days, there would still be scattered clouds at the time of satellite overpass.

To further identify clear days at the lysimeter sites, solar radiation at each site was plotted versus the time of day at a 15 minute interval. Any deviation from the smooth diurnal trend was assumed to be an indication of clouds. On average, only 6 days per month between March and August were found to be cloud free at the time of overpass by viewing the solar radiation data at a particular lysimeter site. Priority was given to days when no deviation from the diurnal trend was observed near the time of overpass and the lysimeter was functioning properly.

<u>Archive Systems</u>

Images were initially retrieved from the Earth Observing System Disk Test Bed System located at the National Center for Atmospheric Research (NCAR) in Boulder, Colorado. The AVHRR archive system allowed for a latitude, longitude range to be entered, and the corresponding portion of the image selected was extracted. In order to retrieve data over the Apache, Marena and Wister sites, a $5^{\circ}$ range was extracted, centered on the coordinates $36^{\circ}$ North, $97^{\circ}$ West. For the Goodwell site, images were centered on $36.5^{\circ}$ North, $101.5^{\circ}$ West, with a $2.5^{\circ}$ range. The extracted images were geometrically corrected by the NCAR system for deterministic error following the procedures of Rosborough et al. (1994). Each channel was extracted individually to a 2 byte binary format and retrieved electronically.

At the time these image retrievals were made, the NCAR system did not provide the thermal calibration information transmitted by the satellite, only the video data. In order to accurately determine the brightness temperatures, it was necessary to obtain the thermal coefficients for the same images from NOAA's Satellite Active Archive (SAA). Images from this system were also used to supplement the images from the NCAR system.

The SAA system contains an archive of both High Resolution Picture Transmission (HRPT) images and Global Area Coverage (GAC) images. The SAA system allows areas along the satellite's ground track to be extracted; however, the full swath of the AVHRR is included in the extracted image. Calibration information, earth location data and telemetry data are appended to each scan line. Both HRPT and GAC

data are in the same format with the exception of the video data. Details on HRPT and GAC file formats are given by both Kidwell (1991) and Planet (1988). GAC data was only used to obtain the thermal coefficients.

A total of 51 unique AVHRR images containing the Apache, Marena and Wister sites were downloaded from ascending (evening) overpasses of NOAA 11, while 24 images were initially retrieved for the Goodwell site. Six images containing a majority of the state (with the exception of the Panhandle) were also retrieved for descending (morning) overpasses. An additional 15 days were identified when at least one of the lysimeter sites appeared cloud free (as indicated by the pyranometer data), but images were not available from either archive.

Cloud Screening

The use of the solar radiation data in the selection of the images provided a first step in the cloud screening process. However, the pyranometer data only provides an indication that there were no cloud shadows directly over the lysimeter site at the time of satellite overpass. Additional cloud screening was accomplished using gray level thresholding and uniformity testing. Channel 4 images were viewed and a corresponding gray scale threshold was selected for each image. Portions of the images failing the threshold test were omitted from further analysis.

Uniformity tests were applied to a range of pixels centered on the lysimeter sites. If any of the following tests were true, the image was labeled as potentially cloud contaminated:

$$T_{bmax} - T_{bmin} > 1.5 \ ? \tag{4.1}$$

$$|\ DN_{c9x9} - DN_{c3x3}\ | > 5\ ? \tag{4.2}$$

$$T_s - T_a < -3\ ? \tag{4.3}$$

where $T_{bmax}$ and $T_{bmin}$ are the maximum and minimum brightness temperatures (K) in a 3x3 block centered on the lysimeter site, $DN_{c9x9}$ is the average of the sensor counts in a 9x9 block centered on the lysimeter site from channel c (1 or 2) and $DN_{c3x3}$ is the average of a 3x3 block centered on the lysimeter site. Equation 4.1 was limited to a 3x3 block centered on the lysimeter and performed using brightness temperatures from both channels 4 and 5. While there is variation in brightness temperatures between adjacent pixels, variations greater than 1.5 K were not common and attributed to cloud contamination. Equation 4.2 is based on the assumption that the distribution of cover types surrounding the lysimeter sites is fairly uniform. At the Goodwell site, this assumption is not valid and the test was not used. As discussed in Chapter 3, there are few times when the dryland vegetation had a surface temperature much lower than air temperature, thus surface temperatures more than 3 K below air temperature were assumed to be due to cloud cover (Equation 4.3).

The final step in the cloud screening was accomplished by viewing plots of the NDVI values versus time for each lysimeter site. If the NDVI was significantly lower than other values for the same time period and one of the uniformity tests failed for that day, the image was assumed to be cloud contaminated and omitted from further analysis. After these procedures, the following number of days were identified as cloud free: Apache, 29; Goodwell: 15; Marena, 27; and Wister, 21.

# Geometric Correction

This section is a presentation and evaluation of the methods used to determine the geographic location of image pixels. As noted, files retrieved from the two archives were in different formats. Software called "Sho" was obtained from NCAR for displaying the images as received. The software also displays the latitude and longitude for each pixel based on the initial geometric registration procedure. Additional processing steps were required in order to approximate locations in the files from the SAA system and to precisely locate the lysimeter sites.

## Geometric Correction Procedures

### *Navigation of HRPT and GAC Image Files*

The earth location information appended to the HRPT and GAC files was used to approximate locations of interest. Bytes 309 to 448 contain latitude/longitude information for every 40 pixels of each scan line, starting at pixel 25. Following a procedure similar to that of Di and Rundquist's (1994), pixels between the reference points were assigned a latitude and longitude by linear interpolation between the reference points of a scan line. The latitude and longitudes were converted to a three dimensional Cartesian coordinate system by:

$$x = R \cos(lat) \cos(long) \qquad\qquad (4.4)$$

$$y = R \cos(lat) \sin(long) \qquad\qquad (4.5)$$

$$z = R\sin(lat) \qquad\qquad (4.6)$$

where x, y, z are the Cartesian coordinates of a pixel (km), lat and long are the latitude and longitude of given pixel, respectively, and R is average polar and equatorial radius of the earth (6367 km, Fogiel, 1992). The distance between the pixel and a location of interest was then determined by:

$$D = \sqrt{(x - x_L)^2 + (y - y_L)^2 + (z - z_L)^2} \qquad\qquad (4.7)$$

where D is distance from the pixel to the location (km), and $x_L$, $y_L$, $z_L$ are the coordinates (km) of the location. The algorithm applied evaluates the distance between each pixel and specified location for an image and returns the scan line and column number containing the pixel closest to a specified location. Appendix B contains source code that utilizes the algorithm.

*Location of Pixels Surrounding the Lysimeter Sites*

In order to precisely determine the locations of the lysimeter sites in the images, the locations of 24 ground control points (GCPs) were determined from 1:24,000 USGS maps. The majority of these points are the centers of dams of lakes that are clearly visible in the AVHRR channel 2 images. For images containing the Marena, Apache and Wister lysimeter sites, 21 GCPs were used, with the remaining 3 used for the Goodwell site. In the area of the Goodwell site, only 1 lake was clearly visible in the images. The other two GCPs corresponded to stream intersections that were difficult to locate in many of the images.

The row and column as indicated by either Sho or from the navigation procedure were determined for each GCP and lysimeter site. The row and column locations of the GCP's were then manually determined by viewing channel 2 images. The procedures used to view the HRPT files are described in Appendix C. The differences between the navigated coordinates and those manually determined were consistent within an image, especially for locations in close proximity. Therefore, the pixel containing the lysimeter site was determined as:

$$RC = RC_{nav} + Corr \qquad (4.8)$$

where RC is the actual pixel row or column in the image containing the lysimeter site, $RC_{nav}$ is the row or column containing the lysimeter pixel as indicated by the navigation procedures, and Corr is the difference noted between the actual and navigated row or column for a GCP near the lysimeter site.

Once each image had the X, Y coordinates of the lysimeter pixels identified, a 9x9 area centered on the lysimeter pixel was extracted and converted to ASCII format. The source code used to implement this procedure for the NCAR files is included in Appendix D. A modification of the program in Appendix C was used to extract the data from HRPT files.

While this geometric correction procedure should accurately locate pixels corresponding to the lysimeter sites, the areas represented by these pixels will not be identical for each satellite overpass. For example, the lysimeter site may be in the center of a pixel in one overpass and in the corner of the pixel on the next. Additionally, the

actual area represented by a pixel is a function of the distance the area is from the satellite. Therefore, a 3x3 average of the raw sensor output is used in the remaining processing steps. Averaging the readings before or after processing did not result in significantly different results, which is consistent with the discussion of Ferencz et al. (1993).

Evaluation of the Geometric Correction Procedures

In order to illustrate the geometric distortion in the AVHRR images, sample images with the initial geometric correction performed by the methods of Rosborough et al. (1994) and no geometric correction are presented. Figure 4.2 is a gray scale representation of the digital numbers for channels 1, 2, 4 and 5 on March 15, 1994 over Oklahoma (excluding the Panhandle area) using geometrically corrected images. Lighter shades of gray correspond to higher relative response in the channel. Note that the in the thermal channels, lower values correspond to higher temperatures. Figure 4.3 is a set of gray scale AVHRR images of the Panhandle area on May 29, 1994, also geometrically corrected. Note that the only clear feature in the Panhandle image is Lake Meredith in Texas, visible in the lower, center portion of the image. Adjacent pixels in the Panhandle area consistently showed more contrast than the rest of the state. This increased variation can be ascribed to the presence of irrigated fields in the area.

Figure 4.4 is a channel 2 image without geometric correction which includes the full swath width of the AVHRR on August 27, 1994 for an ascending (evening) pass. The far Northwest edge of the image corresponds to approximately 34.1 latitude, 109.6
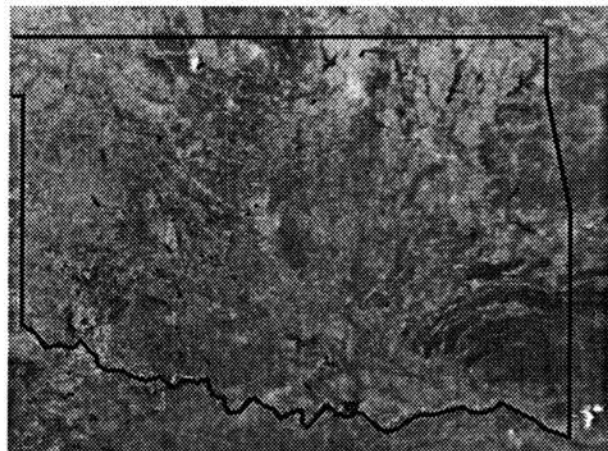
Channel 1: Red
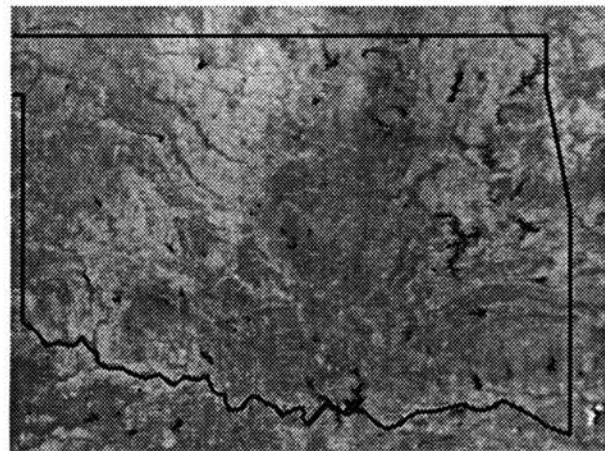
Channel 2: NIR
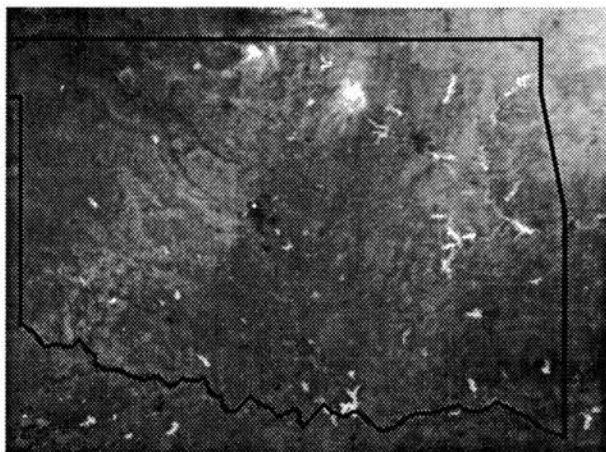
Channel 4: Thermal
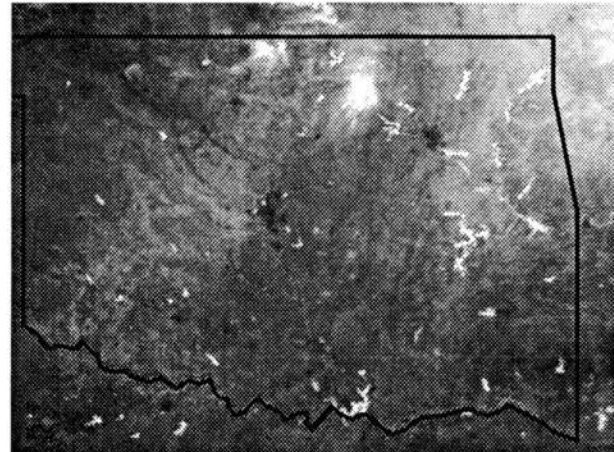
Channel 5: Thermal

Figure 4.2: Gray-scale images of Oklahoma from AVHRR channels 1, 2, 4 and 5 for an ascending pass of NOAA 11 on March 15, 1994 with geometric registration.

Channel 1

Channel 2
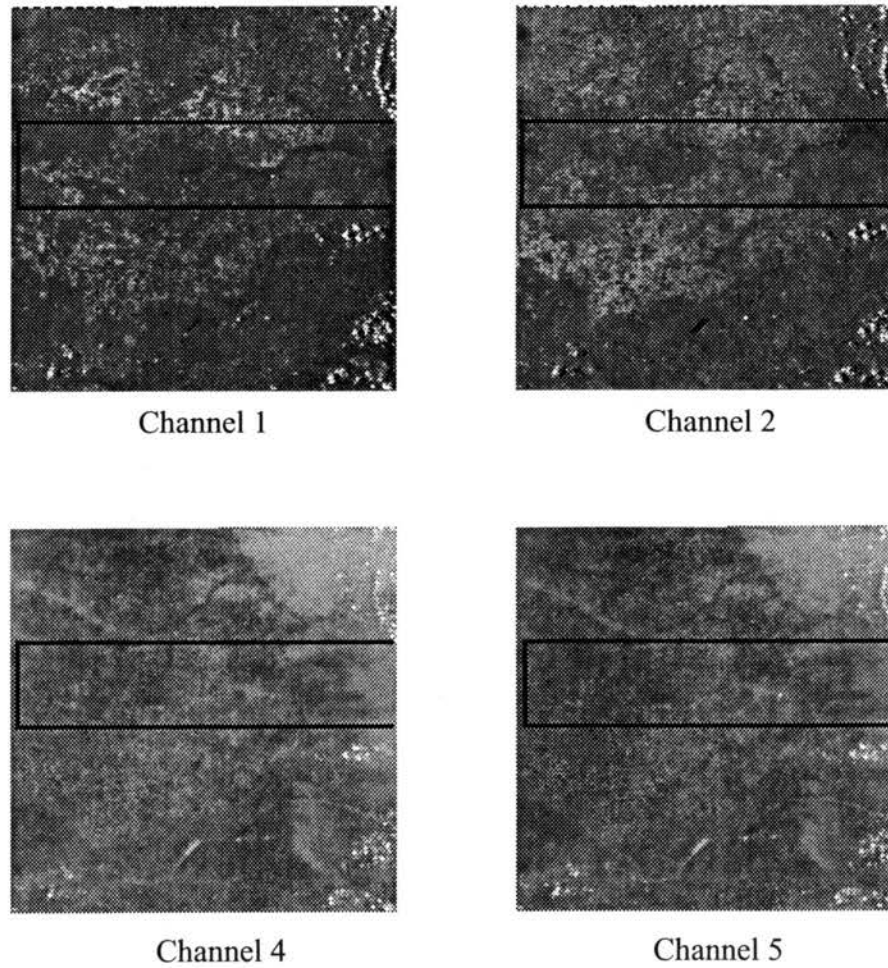
Channel 4

Channel 5

Figure 4.3: Gray-scale images including the Oklahoma Panhandle from AVHRR channels 1, 2, 4 and 5 for an ascending pass of NOAA 11 on May 29, 1994 with geometric registration.
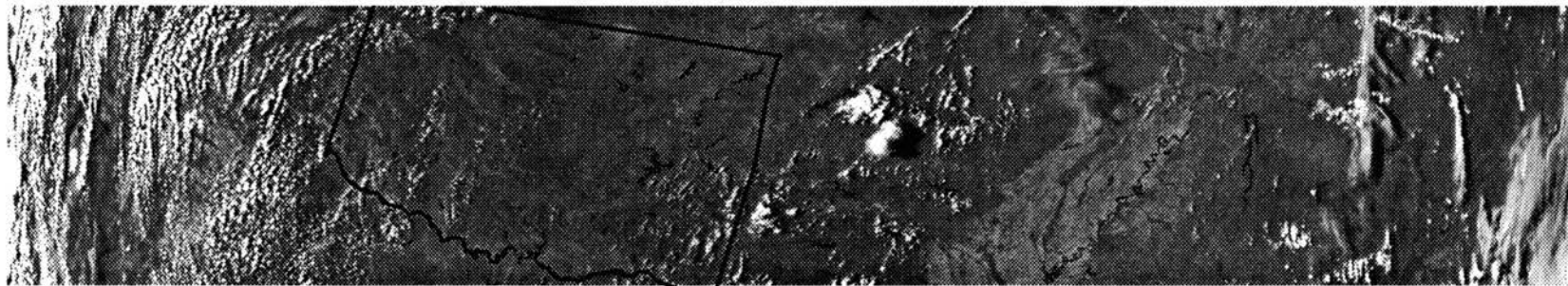
Figure 4.4: Full swath image of AVHRR channel 2 from an ascending pass of NOAA 11 on August 27, 1994 without geometric correction.

longitude and the Northeast corner is at 39.1°W, 78.6°N. The total ground distance along the swath is approximately 2,800 km.

The obvious differences between the corrected and non-corrected image is the orientation of features relative to the North and South. Additionally, features appear "compressed" towards the outside edges of the swath due to the increase in actual ground area represented by a pixel off nadir. Figure 4.5 shows both the instantaneous field of view (IFOV) and pixel resolution in terms of width along the scan line verses the satellite zenith angle. Derivation of the equations used to obtain the results in Figure 4.5 is presented in Appendix E. The IFOV is a representation of the ground area contributing radiance to the sensor while the resolution represents the area between samples of the sensor reading. The fact that the resolution is lower than the IFOV indicates that there is an overlap in the areas contributing to the radiance in a single pixel. The increase in area corresponding to the increase in satellite zenith angle can be attributed to both the increased distance from the satellite and the curvature of the earth. Note that for satellite zenith angles greater than 45°, the area represented by a single pixel exceeds 4 km$^2$. At this satellite pixel size, it is possible the 3x3 1 km$^2$ grid centered on the lysimeter site could be represented by a single pixel based on nearest neighbor resampling. In the case of averaging a 3x3 set of the satellite pixels, the area represented corresponds to 36 km$^2$. Therefore, preference was given to satellite zenith angles less than 40° (other limitations imposed by large off nadir viewing angles are discussed in later sections). Due to the orbital pattern of the satellite, data for a particular location is only available at satellite zenith angles less than 40° about every 6 of 9 consecutive days.

100
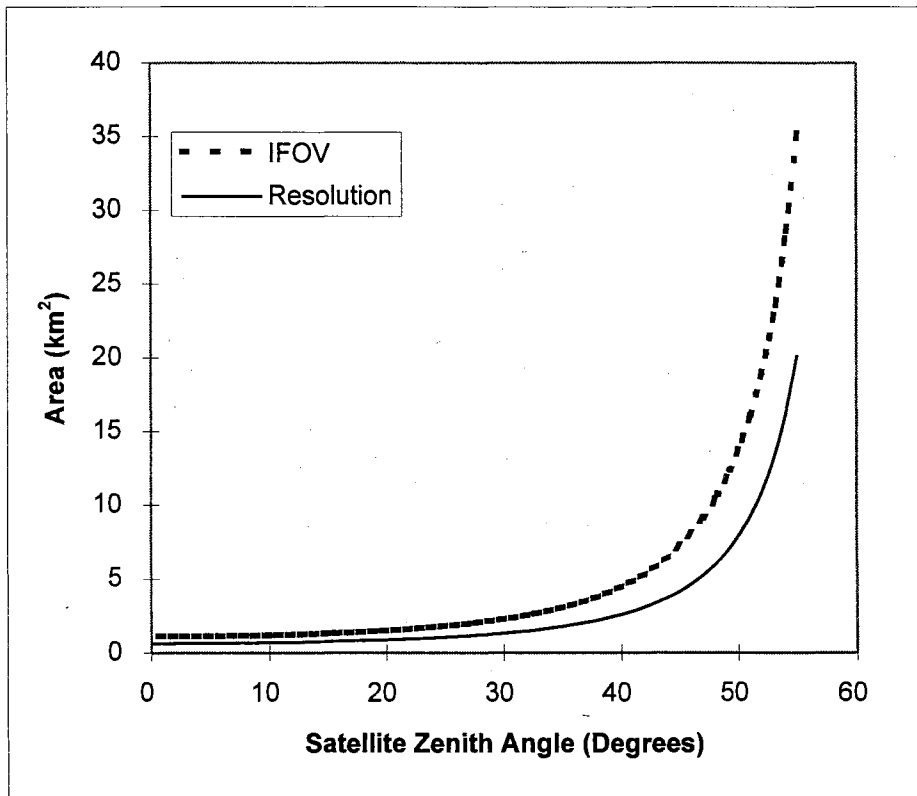
Figure 4.5: Instananeous field of view (IFOV) measured by the AVHRR and resolution corresponding to a image pixel versus the satellite zenith angle.

*Evaluation of the NCAR Navigation Procedures*

A comparison of the GCP locations predicted by the NCAR navigation procedure and the locations determined manually is shown in Table 4.1. The values in the table correspond to the difference between the manually determined row or column and the predicted row and column. The latitude and longitude of the GCPs are also included in the table. Note that the errors are fairly consistent within a particular geographical area. The primary error is that of a constant row and column offset as indicated by the low standard deviations within an image. Considering these results, it is concluded that once the location of a lysimeter is determined with respect to a nearby lake, no further correction is required. To account for possible error in identifying a particular GCP, three GCPs are used to locate a lysimeter site. In case these GCPs do not all point to the same location, the row and column values closest to the average of the three are used.

*Evaluation of the HRPT Navigation Procedure*

In order to determine the accuracy of the HRPT navigation procedure, the error between the interpolated and observed row and column locations is summarized by:

$$D_e = \frac{\sum_{i=1}^{N} \sqrt{X_e^2 + Y_e^2}}{N} \tag{4.9}$$

where $D_e$ is the average distance error in terms of pixels, $Y_e$ and $X_e$ are the difference between the observed and calculated row and column position in the image, respectively, and N is the number of points evaluated.

**Table 4.1: Latitude (Lat) and Longitude (Lon) of Ground Control Points (GCP) and the error in the predicted coordinates from the NCAR navigation procedure.**

| GCP (Lake)[a] | Lat | Lon | A Xe[c] | A Ye[d] | B Xe | B Ye | C Xe | C Ye | D Xe | D Ye |
|---|---|---|---|---|---|---|---|---|---|---|
| Altus | 34.89 | 99.30 | 3 | 0 | 1 | -3 | 1 | -3 | -5 | 4 |
| Foss | 35.56 | 99.18 | 3 | -2 | 1 | -2 | 0 | -2 | -7 | 4 |
| Tom Steed | 34.74 | 98.99 | 2 | 0 | 1 | -2 | 1 | -3 | -6 | 3 |
| Canton | 36.09 | 98.59 | 2 | 0 | 0 | -2 | 0 | -3 | -7 | 4 |
| Lawtonka | 34.74 | 98.50 | 3 | 0 | 1 | -3 | 1 | -3 | -5 | 4 |
| Fort Cobb | 35.16 | 98.45 | 4 | -1 | 3 | -4 | 2 | -2 | -5 | 3 |
| Ellsworth | 34.80 | 98.37 | 4 | -1 | 3 | -3 | | | -5 | 3 |
| Salt Plain | 36.74 | 98.14 | 3 | 0 | 1 | -3 | 0 | -2 | -7 | 4 |
| Chickasha | 35.13 | 98.13 | 3 | 0 | 1 | -3 | 1 | -3 | -6 | 3 |
| Waurika | 34.23 | 98.07 | 4 | -1 | 2 | -4 | 4 | -3 | -4 | 2 |
| Blackwell | 36.13 | 97.19 | 4 | -1 | 2 | -3 | 2 | -3 | -5 | 3 |
| McMurty | 36.16 | 97.18 | 3 | -1 | 1 | -3 | 1 | -3 | -6 | 2 |
| Kaw | 36.70 | 96.92 | 3 | 0 | 2 | -3 | 2 | -3 | -5 | 3 |
| Texoma | 33.82 | 96.57 | 5 | -1 | 2 | -3 | 2 | -4 | -5 | 2 |
| Keystone | 36.15 | 96.26 | 5 | -1 | 4 | -7 | 3 | -3 | -2 | -3 |
| Oologah | 36.42 | 95.68 | 6 | -1 | 3 | -4 | 3 | -3 | -4 | 2 |
| Hugo | 34.01 | 95.38 | 5 | -1 | 3 | -4 | 2 | -5 | -5 | -1 |
| Sardis | 34.63 | 95.32 | 5 | -1 | 1 | -3 | 0 | -4 | -6 | 1 |
| Ft. Gibson | 35.87 | 95.23 | 1 | -2 | 1 | -2 | 1 | -2 | -8 | 2 |
| Wister | 34.94 | 94.72 | 6 | 0 | 2 | -2 | 2 | -2 | -6 | 2 |
| Kerr | 35.36 | 94.78 | 3 | -1 | 3 | -1 | 2 | -2 | -6 | 3 |
| Tenkiller | 35.59 | 95.04 | 4 | -3 | 4 | -3 | 3 | -3 | -5 | 1 |
| Eufaula | 35.31 | 95.36 | 3 | -3 | 3 | -3 | 2 | -4 | -5 | 2 |
| Average: | | | 3.7 | -0.9 | 2.0 | -3.0 | 1.6 | -3.0 | -5.4 | 2.3 |
| Standard Deviation | | | 1.3 | 0.9 | 1.1 | 1.1 | 1.1 | 0.8 | 1.2 | 1.7 |

[a] Coordinates correspond to the center of the dam for the corresponding lake.

[b] Images: A-March 15; B-April 1; C-June 13; D-July 18. All ascending passes of NOAA 11.

[c] Column position of GCP manually determined minus predicted column position

[d] Row position of GCP manually determined minus predicted row position

The average error in the navigation procedure for HRPT images was 6.1 pixels calculated by Equation 4.9 for 126 GCPs compared in 15 images. At nadir, this corresponds to approximately 6.7 km. The standard deviation of the error was 1.43 pixels. While the error is not acceptable for identification of lysimeter sites, it is considered sufficient to identify pixels located in the proximity of Mesonet sites for later use in evaluation of satellite derived surface temperatures. As with the NCAR procedure, the error between the predicted and actual locations was consistent within a geographic region. Therefore, the lysimeters were located using the predicted coordinates plus a correction term derived from the GCP's.

## Radiometric Correction

The data transmitted from the satellite is received as digital numbers (DN), which have no explicit physical meaning. As noted in Chapter 2, the DNs are converted to units of radiance through the use of calibration coefficients. In this section, the procedures used to convert the digital numbers to radiance are presented. Because the AVHRR has no on-board calibration for the reflective channels (channels 1 and 2), methods used to determine the degradation in these channels with time are discussed. Finally, the procedures used to convert the output of the thermal channels to brightness temperature are presented.

Radiometric Correction of Channels 1 and 2

*Conversion Equation*

The prelaunch calibration data for channels 1 and 2 of the NOAA 11 AVHRR are

presented in Table 4.2 (Kidwell, 1991). The radiance coefficients relate radiance

received at the satellite to the sensor output in counts by:

$$L_{sat_i} = Gain_i (DN_i + Offset_i)$$  **(4.10)**

where $L_{sat_i}$ is the radiance received at the satellite (W m$^{-2}$ sr$^{-1}$), Gain is the sensors gain in

channel i (W m$^{-2}$ sr$^{-1}$ count$^{-1}$), DN is the raw digital number received from the satellite

(counts) and Offset is the DN corresponding to zero radiance (counts). The reflective

calibration values appended to the HRPT files are also included in Table 4.2. Los (1993)

reports that the prelaunch coefficients for NOAA 11 were updated on September 27,

1990. The values appended to the HRPT files agree with those reported by Los (1993).

Also included in Table 4.2 are the spectral band width and integrated solar irradiance

corresponding to each channel. The spectral band width is the wavelength range the

sensor responds to, while the integrated solar irradiance is the irradiance received at the

top of the earth's atmosphere weighted according to the spectral response function of the

sensor.

*Determination of Calibration Parameters*

Selection of offset values in Equation 4.10 for channels 1 and 2 of the NOAA 11

AVHRR was determined from the sensor's reading when viewing free space. The

**Table 4.2: Prelaunch and HRPT updated AVHRR channel 1 and 2 radiance calibration values.**

| Source | Channel 1 | | Channel 2 | |
|---|---|---|---|---|
| | Gain (W m$^{-2}$ sr$^{-1}$ um$^{-1}$ count$^{-1}$ | Offset (Counts) | Gain (W m$^{-2}$ sr$^{-1}$ um$^{-1}$ count$^{-1}$) | Offset (Counts) |
| Prelaunch [a] | 0.470 | -41.2 | 0.277 | -41.0 |
| HRPT [b] | 0.493 | -39.8 | 0.302 | -40.0 |
| | W [c] | F [d] | W | F |
| Neckel and Labs (1984) | 0.113 | 184.14 | 0.229 | 241.14 |

[a] Prelaunch values from Planet (1988).

[b] Values appended to HRPT files in 1994.

[c] Spectral band width of the channel (um).

[d] Integrated solar irradiance weighted according to the sensor's spectral response function (W m$^{-2}$).

values were very constant between images, almost always having a value of 40 counts for both channels 1 and 2.

Reflective gain values for NOAA 11 were determined by analyzing the summary of degradation studies compiled by Che and Price (1992) as a function of time. Linear and semi-log (ln[time]) least squares regression fits of gain versus time were considered. Figure 4.6 is a plot of the gain values for both channels 1 and 2 versus the months after launch as summarized by Che and Price (1992). Points labeled with common letters are gain values from the same study. The first point labeled O corresponds to the updated prelaunch gains. There is fairly consistent agreement between studies for the gain of channel 1; however, there appear to be two groupings of results for channel 2. Therefore, the gain values for channel 2 were placed into two sets for analysis. The first set contained points labeled GR, G, C1 and C2, while the second set contained the remaining points. The gains were also analyzed as a complete group.

Table 4.3 shows the results of the regression analysis of the gain values for NOAA 11. While the $r^2$ values were not extremely high for any of the methods, expressing gain as a linear function of the natural log of time consistently provided the highest $r^2$. Also included in Table 4.3 is the gain value determined by extrapolating the degradation functions to June of 1994 (months after launch = 69, the midpoint of the study period). For channel 2, there is little difference in the extrapolated gain value using all observations and that using only set 2. Based on these results, a gain value of 0.599 W $m^{-2}$ $sr^{-1}$ $\mu m^{-1}$ $count^{-1}$ was selected for channel 1, while a gain value of 0.408 was selected for channel 2 in the remainder of the analysis. The 95% prediction intervals associated
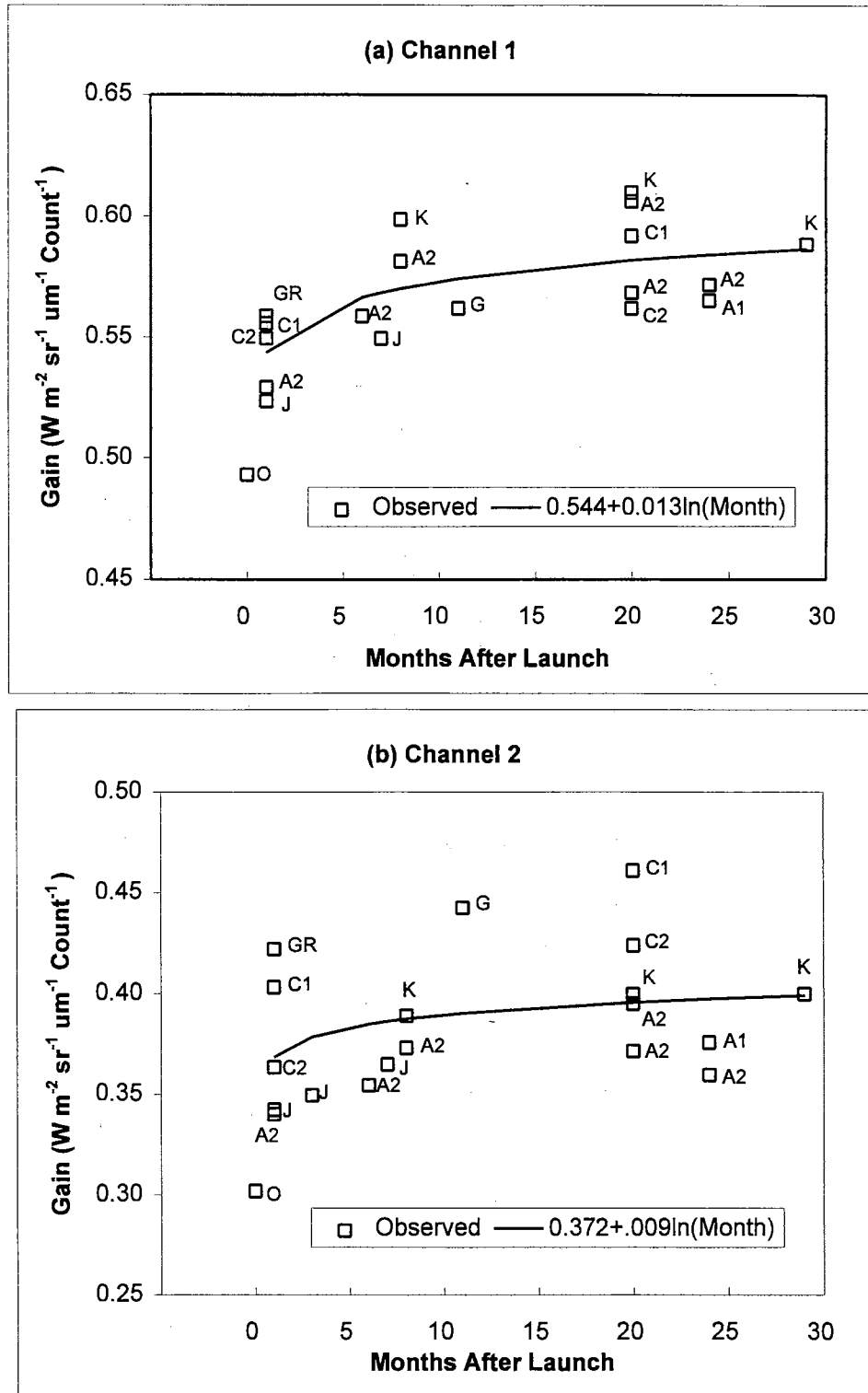
Figure 4.6: Gain values for NOAA 11 AVHRR channels (a) 1 and (b) 2 reported from studies summarized by Che and Price (1992). Points with the same notation were measured by the same investigator. The results of the regression analysis are also shown.

**Table 4.3: Summary of results from the regression analysis of Che and Price (1992) gain degradation data for the NOAA 11 AVHRR.**

| Statistic | Channel 1 | |
| --- | --- | --- |
| | Linear [a] | $\ln(mn)$ [b] |
| $A_r$ | 0.549 | 0.544 |
| $B_r$ | 0.002 | 0.013 |
| $r^2$ | 0.386 | 0.482 |
| Standard Error | 0.019 | 0.018 |
| Number of Observations | 18 | 18 |
| redicted Gain (month = 69) [c] | 0.668 | 0.599 |

| Statistic | Channel 2 | | | | | |
| --- | --- | --- | --- | --- | --- | --- |
| | All Observations [d] | | Set 1 | | Set 2 | |
| | Linear | $\ln(mn)$ | Linear | $\ln(t)$ | Linear | $\ln(t)$ |
| $A_r$ | 0.372 | 0.369 | 0.397 | 0.397 | 0.351 | 0.340 |
| $B_r$ | 0.001 | 0.009 | 0.003 | 0.016 | 0.001 | 0.014 |
| $r^2$ | 0.118 | 0.121 | 0.494 | 0.552 | 0.496 | 0.617 |
| Standard Error | 0.033 | 0.033 | 0.027 | 0.025 | 0.016 | 0.014 |
| Number of Observations | 19 | 19 | 6 | 6 | 13 | 13 |
| Predicted Gain (month = 69) | 0.465 | 0.408 | 0.591 | 0.467 | 0.466 | 0.402 |

[a] Linear regression model: Gain = $A_r$ + $B_r$ (Months after launch), with gain in units of $W\ m^{-2}\ sr^{-1}\ um^{-1}\ count^{-1}$.

[b] Semi-log regression model: Gain = $A_r$ + $B_r$ ln(Months after launch), with gain in units of $W\ m^{-2}\ sr^{-1}\ um^{-1}\ count^{-1}$.

[c] Gain predicted by the regression model for 69 months after launch.

[d] The gain data for channel 2 was analyzed in three groupings: all the data; a set of gain values from two studies that appear to show a different trend than the other data points (Set 1); and all the data excluding Set 1 (Set 2).

with these gain values are ± 0.039 for channel 1 and ± 0.077 for channel 2.

While there is considerable scatter between methods used to determine the gain, a majority of the degradation appears to occur immediately after launch and then the gain stabilizes. For the purpose of this study, the uncertainty in the gain value has limited impact. Based on the small slopes in any of the degradation functions, the gain values will not change significantly during the time period considered (assuming no change in the process contributing to the degradation rate). Therefore, the change in sensor gain should not introduce much variability in the data over limited time periods. The uncertainty in the gain values could impact the results if measurements from another sensor were considered. Additionally, uncertainty in the gain will have some impact when the atmospheric correction methods are applied to the radiance values.

Calculation of Brightness Temperature

The relevant thermal calibration information was then extracted from the HRPT or GAC data for the scan line nearest the lysimeter. Calibration coefficients for each channel are contained in bytes 13-52 of each scan line, with 4 bytes per slope or offset. Slope values were divided by $2^{30}$ and offsets by $2^{22}$ to provide the proper units for radiometric calibration (Kidwell, 1991). Base plate temperatures needed to account for nonlinearities were extracted from 10 bit words within the telemetry information. The average base plate temperature was determined from 4 individual PRT readings.

Brightness temperatures for each thermal channel were determined following methods suggested by Planet (1988). The brightness temperature ($T_b$) in Kelvin of a

110

corresponding radiance was first estimated by the inverse of Planck's function in the form:

$$T_b = \frac{C_2\, \nu_c}{\ln(1 + \frac{C_1\, \nu_c^3}{L_{sat}})} \qquad (4.11)$$

where $\nu_c$ is central wave number chosen to optimize accuracy over a given temperature range (cm), $L_{sat}$ is the radiance received by the sensor (mW m$^{-2}$ sr$^{-1}$ cm) and $C_1$ and $C_2$ are constants. Wooster et al. (1995) report that the central wave numbers of the AVHRR reported in the prelaunch data were specified incorrectly. The error is reported to have little effect on channels 3 and 4, but will result in higher brightness temperatures in channel 5. While the updated values were not incorporated at the time of this analysis, the central wave numbers are only used to provide a starting point for the iterative procedure to be discussed. Therefore, the reported errors should have no impact on the procedures used here.

The estimate of brightness temperature from equation 4.11 is then used as a first approximation in a numerical solution of the Planck function, expressed as:

$$L_{sat}(T_b) = \frac{\sum_{i=1}^{n} B(\nu_i, T_b)\phi(\nu_i)\Delta\nu}{\sum_{i=1}^{n} \phi(\nu_i)\Delta\nu} \qquad (4.12)$$

where n is the number of discrete wave lengths, $\nu_i$ is the wave number, $\Delta\nu$ is the incremental wave number, and $\phi(\nu_i)$ is a channel and sensor specific spectral response function. Response function information was taken from the amendments from Planet

111

(1988) for the NOAA 11 AVHRR.

Brightness temperatures were adjusted through an iterative procedure until the radiance calculated by Equation 4.12 was within a specified tolerance with respect to the radiance measured by the sensor. Tolerance values were selected to insure that brightness temperatures were determined to within 0.05 K for each channel.

Once the initial brightness temperature was determined, channels 4 and 5 were corrected for nonlinearities using correction tables presented by Planet (1988). The tables provide corrections as a function of the initial brightness temperature and average PRT temperature. The source code used to calculate brightness temperature is provided in Appendix F. Use of these brightness temperatures in the estimation of surface temperature is discussed in Chapter 5.

## Analysis of AVHRR Channel 1 and 2 Data

As noted in Chapter 2, several atmospheric correction procedures have been developed for remotely sensed data. Many of these procedures do not account for off nadir viewing or require measurements of the atmospheric profile at the time of satellite overpass. Several correction procedures specific to the AVHRR require extensive look up tables generated from complete radiative models.

Three correction methods were evaluated for use in the atmospheric correction of channels 1 and 2. Additionally, radiance values were converted to exoatmospheric reflectance. A complete description of each of the procedures is included in Appendix G, while the final correction equation is presented below. Also included in this section is a

112

comparison of the reflectance values from each of the methods and the impact the different methods have on the NDVI and SAVI. The section is concluded with an examination of the effect of viewing geometry on data derived from channels 1 and 2.

## Exoatmospheric Reflectance

A method to account for the variation in the incoming solar radiation is to convert radiances to exoatmospheric reflectance (Schiebe et al., 1992). Exoatmospheric reflectance ($R_{ex}$) is defined as:

$$R_{ex} = \frac{\pi L_{sat}}{I_o (Ecc) \cos(\theta_{sun})} \qquad (4.13)$$

where $I_o$ is the top of the atmosphere irradiance in the spectral band of the channel considered, Ecc is the eccentricity correction factor for the earth's orbit, and $\theta_{sun}$ is the solar zenith angle. Exoatmospheric reflectance represents the reflectance at the surface if there were no atmospheric interference and the surface is Lambertian. Reflectance calculated according to Equation 4.13 will be abbreviated as ExoAt. Calculation of the eccentricity correction factor is described in Appendix H.

## Atmospheric Correction Methods

### Iqbal Methods

Iqbal (1983) provides methods to calculate atmospheric attenuation due to molecular and aerosol single scattering and selective absorption. Using these calculated transmittances, the atmospherically corrected reflectance ($R_{iq}$) was determined by:

$$R_{iq} = \frac{\pi(L_{sat} - L_p) / T_{sat}}{\cos(\theta_{sun})(I_o \, Ecc \, T_{sun} + I_d)} \qquad (4.14)$$

where $T_{sat}$ is the transmittance of the atmosphere from the ground to the satellite, $T_{sun}$ is the transmittance of the atmosphere along the optical path from the sun to the ground, $L_p$ is path radiance, and $I_d$ is diffuse sky irradiance. A measure of selective absorption due to water vapor is based on surface observations of relative humidity and air temperature at the time of satellite over pass. While not shown in equation 4.14, the view angle of the satellite is accounted for in the transmittance calculations (see Appendix G).

Path radiance ($L_p$) was calculated by two methods. The first method is similar to the methods presented by Paltridge and Mitchell (1990); however, the level of atmospheric scattering was calculated from relationships provided by Iqbal (1983). In the second method, dark object subtraction (DOS) is used. This was accomplished by:

$$L_{sat} - L_p = Gain(DN - DO) \qquad (4.15)$$

where DO is the minimum sensor count in the 512x512 image.

To further assess the impact of path radiance, a "reflectance" value was also calculated from Equation 4.14 assuming no path radiance. Reflectance values calculated by this method are denoted Iq-No Path.

*Paltridge and Mitchell Method*

The final atmospheric correction method evaluated was a parameterization procedure from Paltridge and Mitchell (1990). This atmospheric correction scheme was selected as it is not computationally or data intensive, while still accounting for

114

differences in solar and viewing angles. The procedure assumes molecular optical depths from Lowtran-6 transmittance code using a U.S. Standard Atmosphere. Reflectance corrected by this method ($R_{pm}$) was calculated by:

$$R_{pm} = \frac{A(1-M) - \sec(\theta_{sat})(\Phi_0 Q_0(m) + \Phi_1 Q_1(m))}{4\cos(\theta_{sun})g(m)e^{-m\tau_{aer}}(1 + m\tau_{aer})} \qquad (4.16)$$

where A is the satellite measured albedo, M is fraction of radiance at the satellite contributed by molecular multiple scattering (wavelength dependent), $\theta_{sat}$ is satellite zenith angle relative to the area measured, $F_0$ is the scattering phase function for molecular scatter, $F_1$ is the scattering phase function for aerosol scatter, $Q_0(m)$ is the integrated source function for molecular scattering, $Q_1(m)$ is the integrated source function for aerosol scattering, $\tau_{aer}$ is aerosol vertical optical depth, $g(m)$ is a parameterization function of air mass defined by the model atmosphere, and m is total relative air mass from sun to ground to satellite. Note that each of the parameters in Equation 4.16 is channel dependent. Additionally, the parameters for equation 4.16 are based on the response functions of the AVHRR on NOAA 9; however, channels 1 and 2 of NOAA 11 have response curves very similar to those of NOAA 9 (based on a comparison of the response functions presented by Kidwell, 1991).

Paltridge and Mitchell found the method to provide results consistent with a complete radiation transfer model for satellite zenith angles up to $40^{\circ}$. This method assumes atmospheric conditions remain equal to climatic conditions, with the aerosol optical depth as the only variable in addition to the viewing geometry. Optical depths were approximated from daily average visibility data reported by the NWS and retrieved

from NOAA's National Climatic Data Center.

The Paltridge and Mitchell method differs from that of Iqbal's by including an estimate of multiple scattering and background reflection. However, a close review of the terms in Equation 4.16 reveals that it is theoretically similar to Equation 4.14 (see Appendix H for details). The Paltridge and Mitchell method will be referred to as P&M.

Calculation of Solar and Satellite Angles

From the previous discussion, angles representing the location of both the sun and satellite relative to the target of interest must be known to perform the atmospheric correction procedures. Solar zenith and azimuth angles were calculated based on methods presented by Iqbal (1983) as a function of latitude, longitude and time of day. Details on these calculations are included in Appendix H. The satellite azimuth and zenith angle for each lysimeter site was obtained from the satellite tracking program TrakStar (Kelso, 1992). An illustration of these angles is included in Figure 4.7. The tracking program uses North American Air Defense Command (NORAD) two-line orbital element sets to calculate the path of a satellite. Two-line element files were obtained electronically from the Air Force Institute of Technology and were always within 7 days of the satellite pass of interest. Kelso (1992) indicates that the satellite zenith and azimuth angles predicted by the program are within $1^{\circ}$ of actual values if current orbital elements are used.

For full swath images from the SAA system, it was possible to calculate the satellite zenith angle based on the position of the pixel of interest in the image and the

116

**Three Dimensional View**

**y-x Plane**

**z-x Plane**
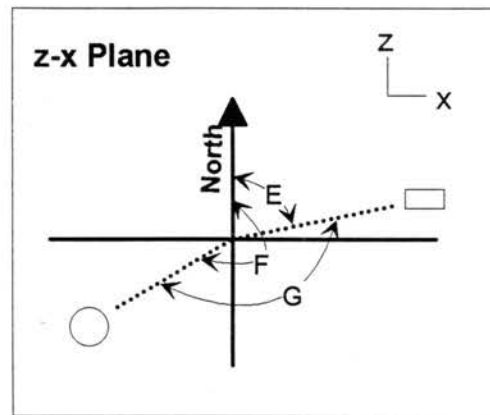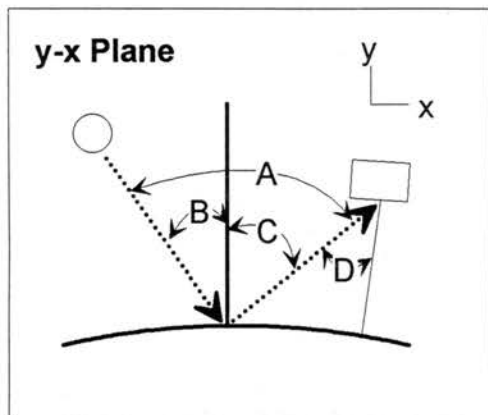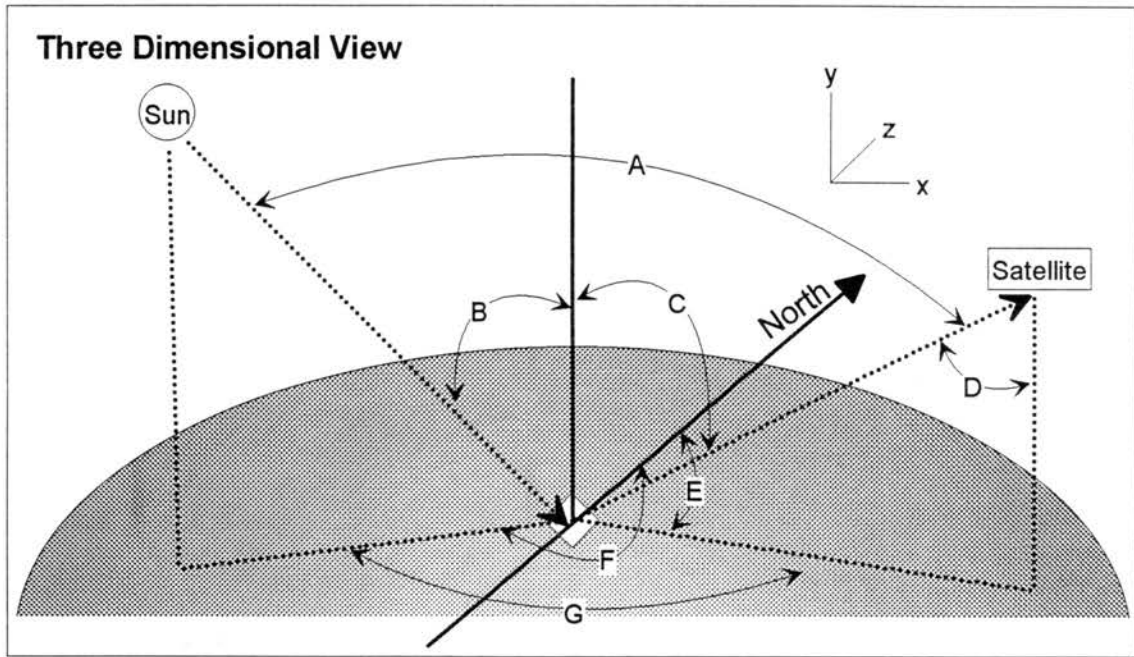
A - 180 degrees - scattering angle
B - Solar zenith angle
C - Satellite zenith angle from the
     location of the target.
D - Satellite zenith angle

E - Satellite azimuth angle
F - Solar azimuth angle
G - Relative azimuth angle
     between the sun and satellite

Figure 4.7: Illustration of satellite and solar angles.

altitude of the satellite by:

$$\theta_{sat*} = \frac{|X - 1024|}{1024} 55.4°$$ 
(4.17)

where $\theta_{sat*}$ is the satellite zenith angle (degrees) to pixel X along the swath of the satellite

(0 to 2048), and 55.4 is the maximum zenith angle of the satellite (degrees). However,

due to the Earth's curvature, the satellite zenith angle is not equal to the zenith angle

relative to the point of observation as illustrated in Figure 4.7. From the Law of Sines, it

can be shown that:

$$\theta_{sat} = \sin^{-1}\left[ \sin(\theta_{sat*})(1 + \frac{alt}{R}) \right]$$ 
(4.18)

where $\theta_{sat}$ is the satellite zenith angle relative to the point of observation, alt is the altitude

of the satellite (approximately 850 km) and R is average polar and equatorial radius of

the earth (6367 km). Note that $\theta_{sat}$ is the angle needed for the atmospheric correction

procedures. Further mention of satellite zenith will refer to the angle from the

perspective of the point of observation.

Evaluation of the Reflectance Calculation Methods

*Comparison of the Atmospheric Correction Methods Over Lake Texoma*

One method used to evaluate the various atmospheric correction methods was to

examine the predicted reflectances over Lake Texoma. A lake is used as the reflectances

of lakes experience less temporal change as compared to those of vegetated land surfaces

(Teillet, 1992). Lake Texoma, located in south central Oklahoma at the Texas border,

was selected as it is the largest lake contained in the images and there were more cloud free images of Texoma available compared to lakes in eastern Oklahoma. Images retrieved for use in the evaluation of the lysimeter data were examined to identify those with no apparent cloud contamination over Lake Texoma.

Channel 2 images were used to locate the lake and select a "pure" water pixel, assuming this corresponded to the lowest sensor output. Daily average visibility observations were retrieved from the National Climatic Data Center (NCDC) and reports of visibility from Ardmore were used. Temperature, relative humidity and solar radiation measurements at Madill for the time of satellite overpass were obtained from the Oklahoma Mesonet.

Figure 4.8 is a plot of the reflectance derived from the different atmospheric correction methods for AVHRR channels 1 and 2 for various dates during 1994 over lake Texoma. Much of the temporal variation in the reflectance can be ascribed to the viewing angle, as water surfaces have both specular and diffuse reflective characteristics (Lenoble, 1993; Davies-Colley et al., 1993). Further discussion of the effect of viewing will be presented. While the directional dependence of the reflectance makes the interpretation of the following results more difficult, water reflectances were typically the lowest in the images considered. Due to the low reflectance, the path radiance for these images was a large percentage of the radiance received at the satellite and the accuracy of the predicted path radiances could be qualitatively considered.

The reflectances are within the range of reflectances reported over lakes in the literature. Teillet (1992) reports average atmospherically corrected reflectances of 1.28 ±
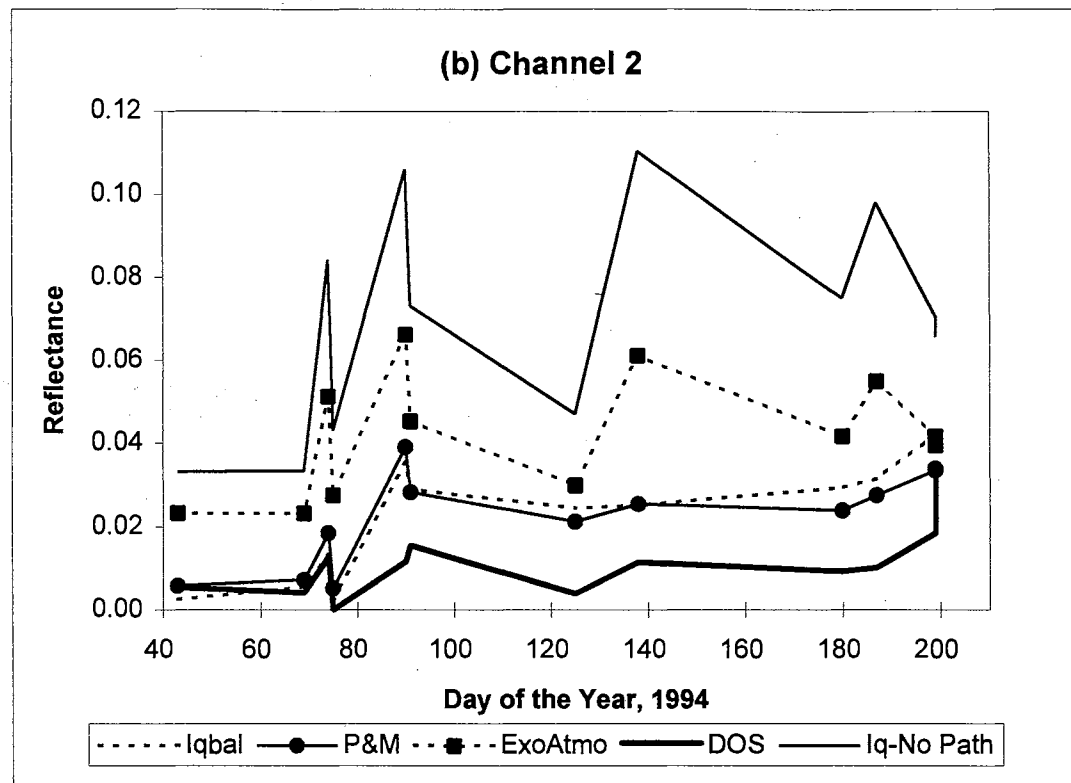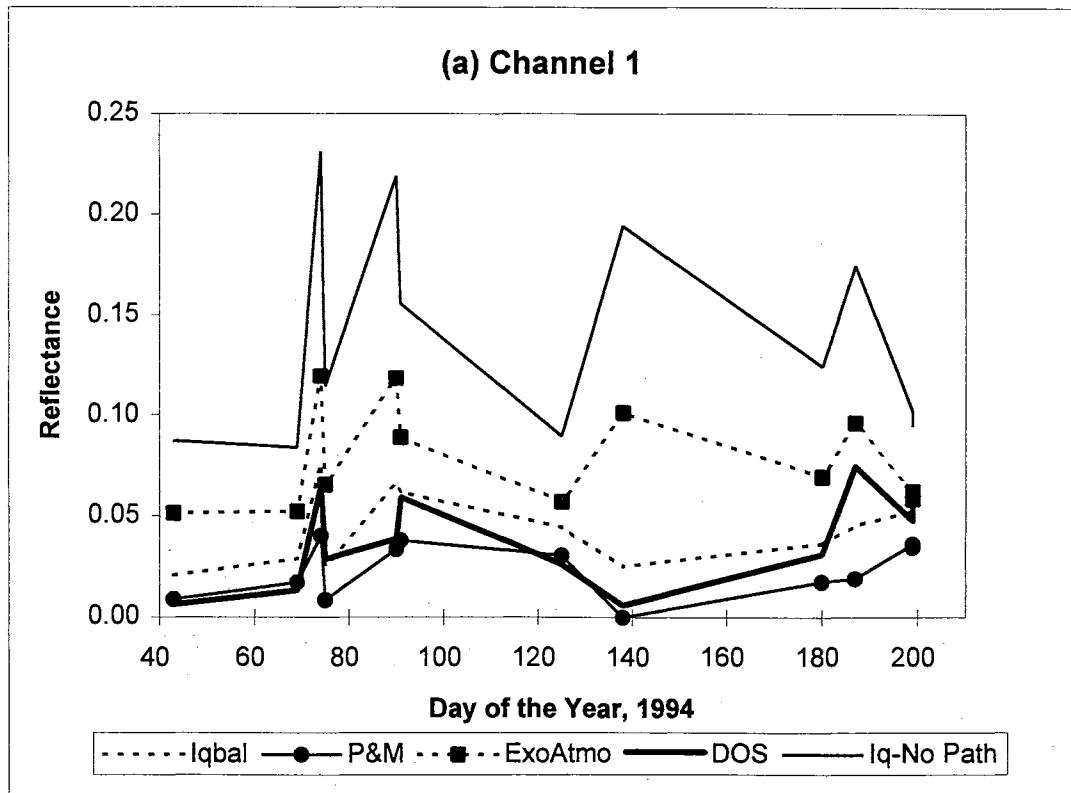
Figure 4.8: Reflectance values for AVHRR channels (a) 1 and (b) 2 derived from various methods for different dates over Lake Texoma.

0.68% and 1.88 ±0.87% for channels 1 and 2 of the NOAA 11 AVHRR over a lake for 10 days spanning a 3 year period. While the reflectances obtained by Teillet are within the range predicted by both Iqbal and P&M methods, a greater reflectance in the NIR is not characteristic of most water surfaces (Paltridge and Platt, 1976). For a solar zenith angle of 34°, Paltridge and Platt (1976) reported reflectance values of 7.5% and 2.5% in the spectral regions corresponding to AVHRR channels 1 and 2. Schiebe et al. (1992) report exoatmospheric reflectances in Landsat's MSS channel 2 ranging from 0.04 to 0.25 (similar spectral region to AVHRR channel 1), with most of the readings concentrated around 0.08 for a small lake in Oklahoma. MSS channel 4 (similar spectral region to AVHRR channel 2) exoatmospheric reflectances ranged from 0.02 to 0.17, with the values concentrated around 0.04.

For the days represented in Figure 4.8, atmospheric correction methods accounting for path radiance (DOS, P&M, Iqbal) typically reduced the predicted reflectance in both channels compared to that of the exoatmospheric reflectances. The comparative reduction is entirely due to predicted path radiance as is evident by comparing the reflectances corrected by Iqbal methods with and without the path radiance term. In general, accounting for atmospheric attenuation and scattering will yield a net decrease in predicted irradiance received at the earth's surface compared to the exoatmospheric irradiance. Additionally, adjustment for the attenuation of the radiance from the surface to the satellite will result in a predicted increase in radiance received at the satellite. The only term that will consistently reduce the corrected reflectance is the subtraction of the path radiance.

The variation in reflectances from any of the methods is higher than might be expected over the lake, especially for consecutive dates (day 69 versus 70 and day 90 versus 91). Table 4.4 includes a summary of the atmospheric conditions for each of the dates considered as well as the viewing geometry. While there is some variation in the precipitable water and visibility between these short time periods, none of the variation is of the magnitude to account for the variation in reflectance.

Figure 4.9 shows the relative position of the sun and satellite to the lake for the dates considered. Comparison between the reflectances shown in Figure 4.8 and angles illustrated in Figure 4.9 shows that the lower exoatmospheric reflectances correspond to times when the satellite zenith angle with respect to the lake is smaller. Also note from Table 4.4 that the relative azimuth angles between the sun and the satellite indicate the satellite and sun were in approximately the same horizontal plane.

Correlation coefficients between the viewing geometry parameters and reflectances are shown in Table 4.5. Also included in Table 4.5 are the correlation between solar/viewing angles and the NDVI (Equation 2.8) and SAVI (Equation 2.9, L = 0.5) derived from the reflectances. From Table 4.5, note that the null hypothesis that the correlation between the exoatmospheric reflectances and satellite viewing angles is 0 cannot be rejected at the 95% confidence level. However, the correlation of the reflectances corrected for path radiance is typically less than that of the other methods.

While some of the increase in apparent reflectance can be attributed to atmospheric scattering, an increase is also expected due to the specular reflectance from the lake. The general variation of the Iqbal and P&M correction methods also tends to

**Table 4.4: Viewing geometry and weather data for times of the satellite overpass on dates in 1994 considered in the evaluation of atmospheric correction methods with Lake Texoma images.**

| Date | Day of the Year | Time of Over-pass (GMT) | Satellite Azimuth Angle | Satellite Zenith Angle | Solar Azimuth Angle | Solar Zenith Angle | Visibility[a] (km) | Station Pressure[b] (mb) | Air Temperature (°C) | Precipitable Water (cm) |
|------|------|------|------|------|------|------|------|------|------|------|
| | | | ---------------- ( Degrees ) ---------------- | | | | | | | |
| 02/13 | 43 | 22:29 | 68 | 4 | 239 | 72 | 40 | 1004 | 13.3 | 0.50 |
| 03/10 | 69 | 22:23 | 74 | 18 | 246 | 66 | 31 | 996 | 17.7 | 0.89 |
| 03/15 | 74 | 23:03 | 260 | 42 | 255 | 72 | 28 | 986 | 24.3 | 1.11 |
| 03/16 | 75 | 22:50 | 258 | 26 | 253 | 70 | 28 | 991 | 23.1 | 1.27 |
| 03/31 | 90 | 23:08 | 260 | 45 | 261 | 71 | 33 | 999 | 20.1 | 1.18 |
| 04/01 | 91 | 22:56 | 258 | 29 | 260 | 68 | 25 | 992 | 24.9 | 1.83 |
| 05/05 | 125 | 22:41 | 74 | 3 | 270 | 60 | 23 | 992 | 25.8 | 3.02 |
| 05/18 | 138 | 23:23 | 261 | 51 | 279 | 67 | 25 | 991 | 28.5 | 2.89 |
| 06/29 | 180 | 23:10 | 258 | 30 | 280 | 61 | 16 | 985 | 34.2 | 4.48 |
| 07/06 | 187 | 23:24 | 260 | 46 | 281 | 64 | 23 | 984 | 32.3 | 3.80 |
| 07/18 | 199 | 22:37 | 73 | 27 | 273 | 55 | 18 | 988 | 27.1 | 4.64 |
| 07/18 [c] | 199 | 14:17 | 281 | 10 | 85 | 57 | 18 | 988 | 33.1 | 4.33 |

[a] Observations from the National Weather Service station in Ardmore, Oklahoma.

[b] Station pressure, air temperature and precipitable water based on data from the Madill Mesonet station.

[c] NOAA 12. All other times correspond to NOAA 11 overpasses.
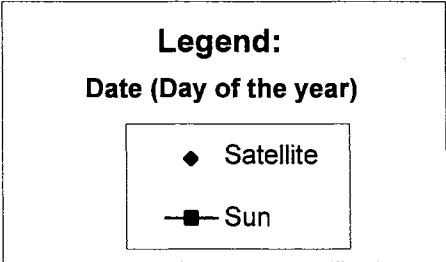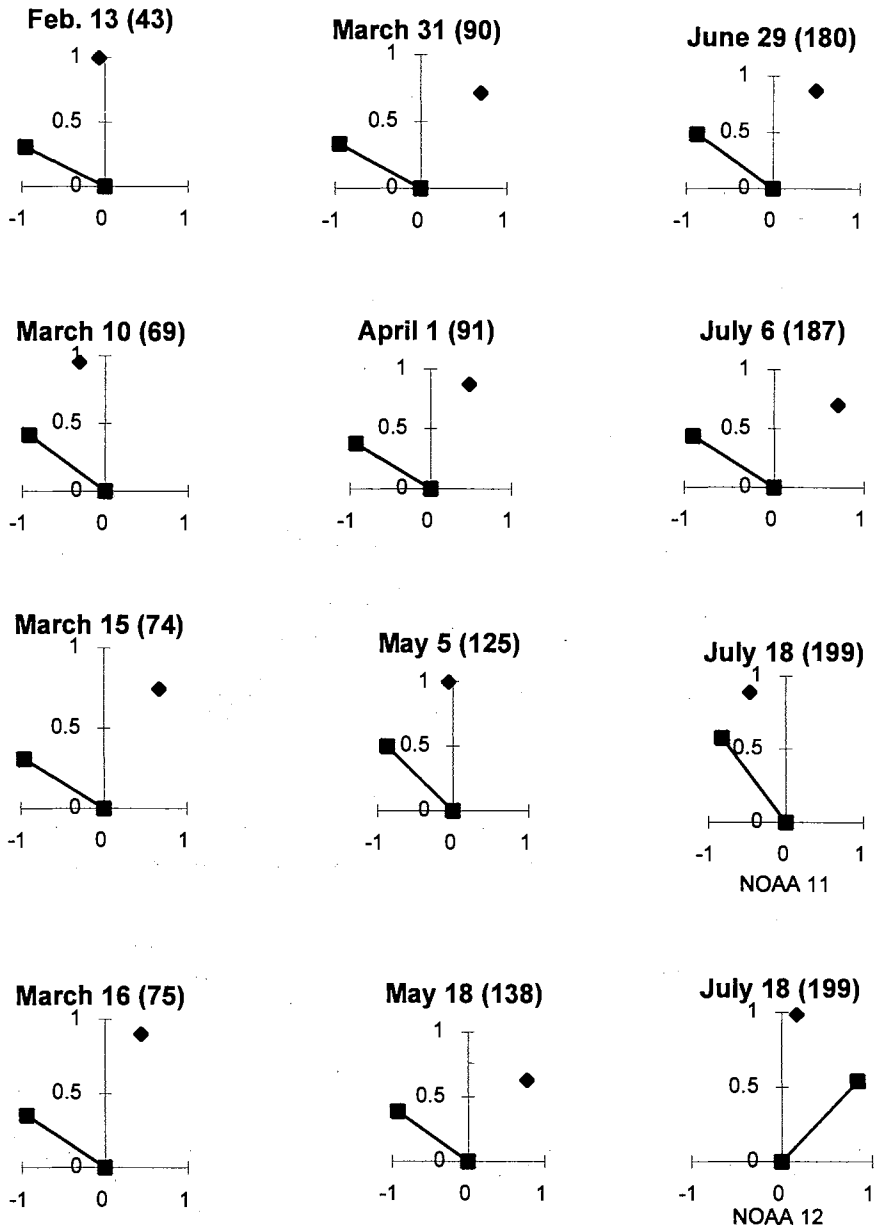
Figure 4.9: Illustration of relative sun and satellite zenith angles for dates used in the evaluation of atmospheric correction methods at Lake Texoma.

**Table 4.5:** Correlation between solar/viewing angles and data derived from AVHRR channels 1 and 2 for dates in Table 4.4 using different atmospheric correction methods. Values in bold face indicate a correlation significantly different than 0 at the 95% confidence level.

| Angle | Correction Method | | | | |
|---|---|---|---|---|---|
| | ExoAtmo | Iq-No Path | P&M | Iqbal | DOS |

Correlation between angle and channel 1 reflectance:

| Angle | ExoAtmo | Iq-No Path | P&M | Iqbal | DOS |
|---|---|---|---|---|---|
| Satellite Azimuth | **0.639** | **0.679** | -0.007 | 0.286 | 0.473 |
| Satellite Zenith | **0.860** | **0.887** | -0.184 | 0.276 | 0.311 |
| Solar Azimuth | 0.304 | 0.273 | -0.274 | -0.088 | -0.176 |
| Solar Zenith | 0.482 | 0.041 | -0.484 | -0.028 | -0.193 |

Correlation between angle and channel 2 reflectance:

| Angle | ExoAtmo | Iq-No Path | P&M | Iqbal | DOS |
|---|---|---|---|---|---|
| Satellite Azimuth | **0.639** | 0.492 | 0.395 | 0.257 | 0.338 |
| Satellite Zenith | **0.858** | **0.633** | 0.392 | 0.207 | 0.008 |
| Solar Azimuth | 0.202 | 0.070 | -0.137 | -0.222 | **-0.722** |
| Solar Zenith | 0.125 | -0.455 | -0.431 | -0.678 | -0.485 |

Correlation between angle and NDVI:

| Angle | ExoAtmo | Iq-No Path | P&M | Iqbal | DOS |
|---|---|---|---|---|---|
| Satellite Azimuth | 0.168 | 0.081 | **0.599** | 0.263 | -0.068 |
| Satellite Zenith | 0.143 | 0.024 | **0.626** | 0.300 | 0.054 |
| Solar Azimuth | -0.244 | -0.256 | 0.075 | -0.051 | -0.192 |
| Solar Zenith | **-0.757** | **-0.872** | -0.154 | **-0.655** | -0.003 |

Correlation between angle and SAVI:

| Angle | ExoAtmo | Iq-No Path | P&M | Iqbal | DOS |
|---|---|---|---|---|---|
| Satellite Azimuth | -0.447 | **-0.611** | 0.485 | -0.054 | -0.383 |
| Satellite Zenith | **-0.601** | **-0.797** | **0.716** | -0.082 | -0.340 |
| Solar Azimuth | -0.350 | -0.389 | 0.199 | -0.100 | -0.138 |
| Solar Zenith | -0.776 | -0.580 | 0.115 | **-0.584** | 0.003 |

show the same trend in apparent reflection as the exoatmospheric reflectances, with the exceptions of May 18 and July 6. Both of these days correspond to the maximum satellite zenith angles for the images considered. It is likely that the path radiance is over predicted for these larger zenith angles. This is definitely the case on May 18, as the predicted path radiance in channel 1 from the P&M method exceeded the radiance received at the satellite. The reflectance is reported as zero since a negative radiance is not physically possible.

The reflectances predicted using dark object subtraction (DOS) to estimate the path radiance show much more variation in channel 1 than do the other methods. On March 16, April 1, May 5 and July 18, the lowest radiance measured in channel 1 corresponded to cloud shadows, while on other dates the minimum values correspond to lakes in the image. In channel 2, the minimum value consistently corresponded to lakes. Since the minimum value in both channels often corresponds to lake reflectances, the minimum values are subject to variation induced by specular reflectance from the lake and not only atmospheric interference. A better use of the DOS method may have been to select pixel values that were low in both channels; however, the only surfaces that would consistently meet that requirement are lakes.

NDVI and SAVI derived from the reflectances over Lake Texoma are shown in Figure 4.10. The NDVI derived from exoatmospheric reflectances shows much less variation than those derived from the atmospherically corrected reflectances. With the exception of the DOS method, the remaining methods tend to show a general increase in the NDVI over time. Also note that the correlation between NDVI and satellite zenith
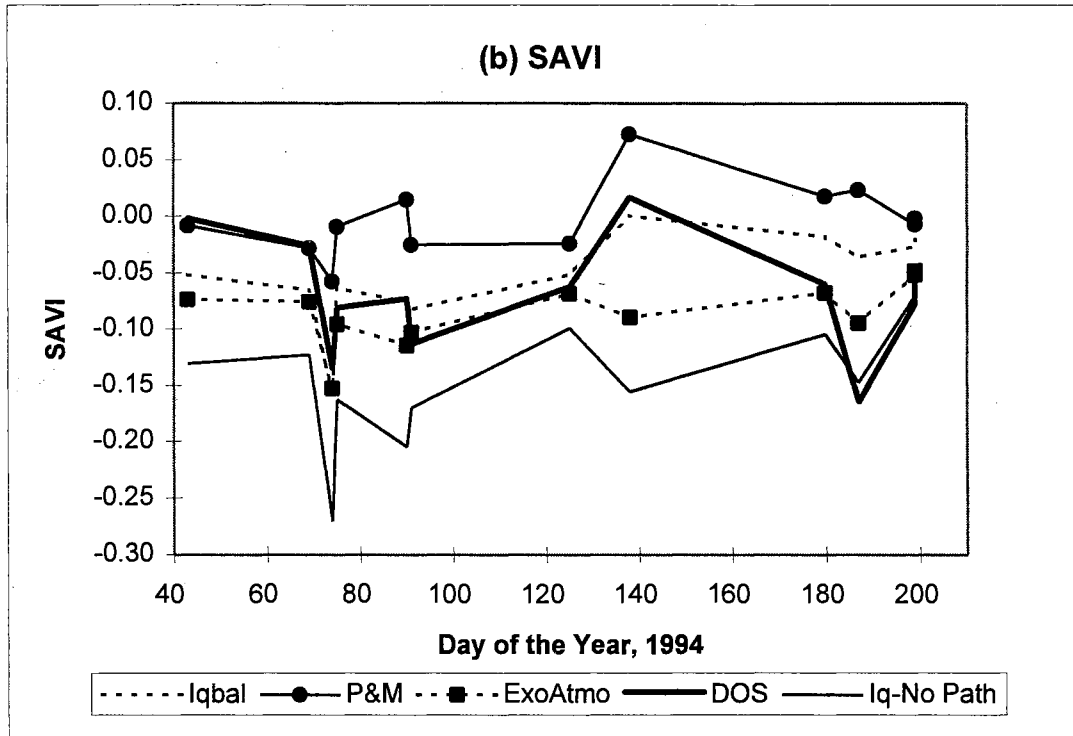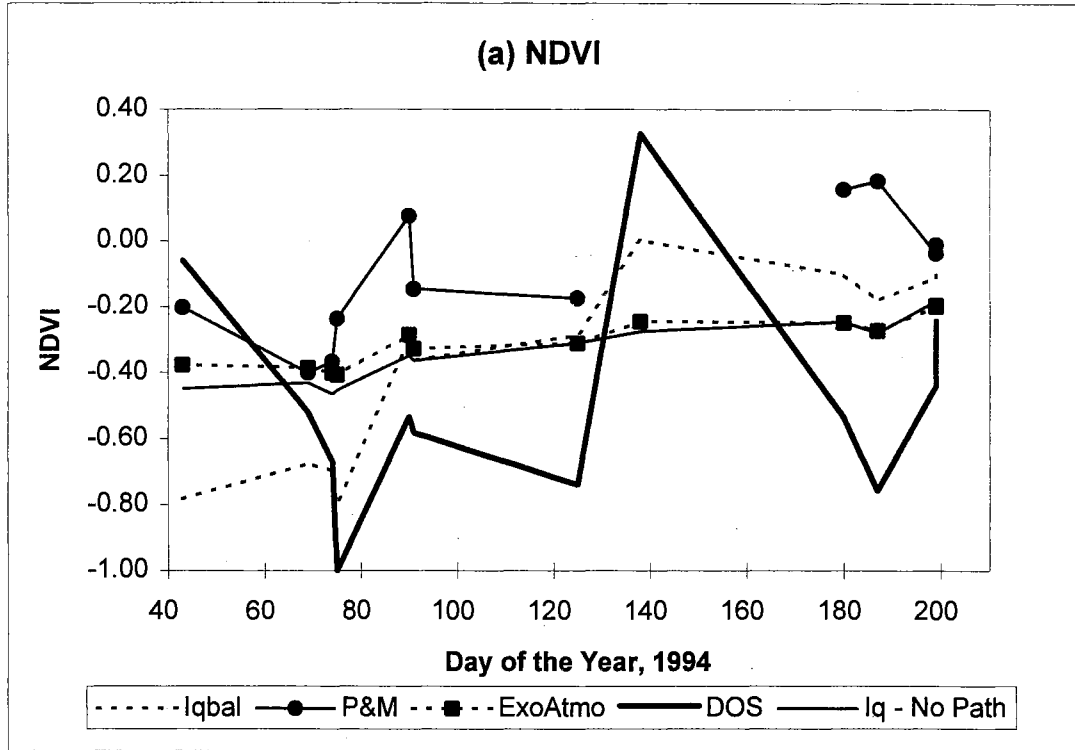
Figure 4.10: (a) NDVI and (b) SAVI derived from reflectance values using different atmospheric correction methods on different dates over Lake Texoma.

127

angle has been greatly reduced (see both Figure 4.10 and Table 4.5) compared to that of the original reflectances. However, there is still evidence of the variation with the satellite zenith angle in the SAVI. In the SAVI, the multiplication of the numerator by (L+1) and addition of L in the denominator prevents the effects of the variation in viewing angle from completely canceling.

Part of the increased variation in the NDVI derived from both the P&M and Iqbal reflectances can be attributed to the increased sensitivity of the NDVI for very low reflectances. Both methods predicted much lower reflectances in both channels 1 and 2 compared to the exoatmospheric reflectances, as a large percentage of the radiance received at the satellite is predicted to be due to path radiance (see Table 4.6). Therefore, the denominator is much smaller and the sensitivity to changes in the numerator is increased. However, it is apparent that the predicted difference in channel 1 and 2 was greater for Iqbal's method on the dates prior to March 31 than the differences from the P&M method. Because the NDVI derived from methods without correction for path radiance is more consistent with time than the NDVI derived from methods accounting for path radiance, the accuracy of the estimates of path radiance may be questionable.

Table 4.6 includes the percent difference between pyranometer measured irradiance from the Madill Mesonet site and the predicted irradiance using Iqbal's method in the spectral range of the pyranometer. The transmission functions discussed in Appendix G were used to calculate the amount of atmospheric attenuation in the spectral response range of the pyranometer (0.4 to 1.1 μm). The spectral range of the pyranometer encompasses the spectral range of both channels 1 and 2 of the AVHRR.

128

**Table 4.6: Percent of radiance received at the satellite due to path radiance as predicted by Iqbal's relationships and a comparison of measured and predicted (Iqbal's methods) solar radiation received at the earth's surface for dates corresponding to the Lake Texoma images.**

| Date | Day of the Year | Percent of radiance received at the satellite due to path radiance (predicted) Channel 1 | Channel 2 | Solar Radiation Measured [a] ------- ( W m$^{-2}$ )--------- | Predicted | Percent Difference Between Measured and Predicted Solar Radiation |
|---|---|---|---|---|---|---|
| 02/13 | 43 | 76% | 93% | 301 | 277 | 8% |
| 03/10 | 69 | 67% | 85% | 406 | 426 | -5% |
| 03/15 | 74 | 69% | 86% | 287 | 272 | 5% |
| 03/16 | 75 | 80% | 95% | 359 | 331 | 8% |
| 03/31 | 90 | 71% | 68% | 305 | 325 | -6% |
| 04/01 | 91 | 62% | 62% | 343 | 316 | 8% |
| 05/05 | 125 | 52% | 49% | 435 | 444 | -2% |
| 05/18 | 138 | 89% | 79% | 349 | 362 | -4% |
| 06/29 | 180 | 73% | 63% | 388 | 397 | -2% |
| 07/06 | 187 | 76% | 70% | 359 | 358 | 0% |
| 07/18 | 199 | 50% | 41% | 453 | 474 | -5% |
| 07/18 [b] | 199 | 49% | 37% | 540 | 549 | -2% |

[a] From the pyranometer at the Madill Mesonet site.

[b] NOAA 12. All other dates are for NOAA 11 overpasses.

129

While this evaluation does not provide information on the accuracy of estimates of path radiance, it does provide some assessment of the accuracy of the transmission functions used to calculate atmospheric attenuation. Typically, the predicted solar irradiance is within 10% of the radiance measured by the pyranometer. A further comparison of predicted solar irradiance at the earth's surface and pyranometer data is included in Appendix G.

In conclusion, it does appear that the Iqbal and P&M methods over predicted path radiance for satellite zenith angles greater than 40 degrees. This limitation for higher zenith angles can be related to the assumptions made in deriving the estimate of the path radiance based on modeling the atmosphere as a flat slab (see Appendix G). Much of the variation in reflectance due to the viewing angle cancels in the NDVI; however, it is still evident in the SAVI. The method used to implement dark object subtraction does not appear to reduce the variation in reflectances because lakes are often the dark object, and because they are subject to variation with satellite zenith angle that is not associated with atmospheric scattering. Additionally, the fact that different pixels were used in each channel for the same image can increase the variation in the NDVI.

Comparison of the Atmospheric Correction Methods at the Marena Lysimeter Site

In addition to examination of the reflectances over Lake Texoma, each of the atmospheric correction methods was applied to the data at each of the lysimeter sites and the time series of the reflectances examined. Figure 4.11 shows the reflectance values predicted from each of the methods at the Marena site, with the NDVIs and SAVIs

derived from the reflectances shown in Figure 4.12. Figures are not presented for the other sites, as the various methods demonstrated the same relationships as shown at the Marena site. The reflectance values corresponding to each of the lysimeter sites under cloud free conditions are provided in Appendix I. The impact of viewing geometry on reflectance noted in the Lake Texoma data is also present in the data at Marena, as indicated by the sharp changes in reflectance over short time periods. Again, the variation is decreased in the vegetation indices (Figure 4.12). Further consideration of the impact of viewing geometry is presented later in this chapter.

The atmospheric correction methods that account for path radiance typically predicted a slight decrease in channel 1 compared to the exoatmospheric reflectances, while corrected reflectances in channel 2 were increased. The differences are related to the fact that channel 1 corresponds to lower wavelengths where Rayleigh and Mie scattering are greater. Therefore, there is higher path radiance in this channel and because the reflectance is lower, the path radiance is a higher percentage of the total radiance received by the satellite. Additionally, radiance in channel 2 is more subject to water vapor absorption, thus the increase.

The consistent decrease in channel 1 and increase in channel 2 of the correction methods relative to the exoatmospheric reflectance results in a predicted increase in the NDVI. While the NDVIs derived from the P&M method are consistently higher than those from Iqbal's method, they appear to change by the same relative amounts with time. This implies that the impact of changes in the atmospheric variables does not have a strong impact on the NDVI as Iqbal's method accounts for variation in atmospheric water
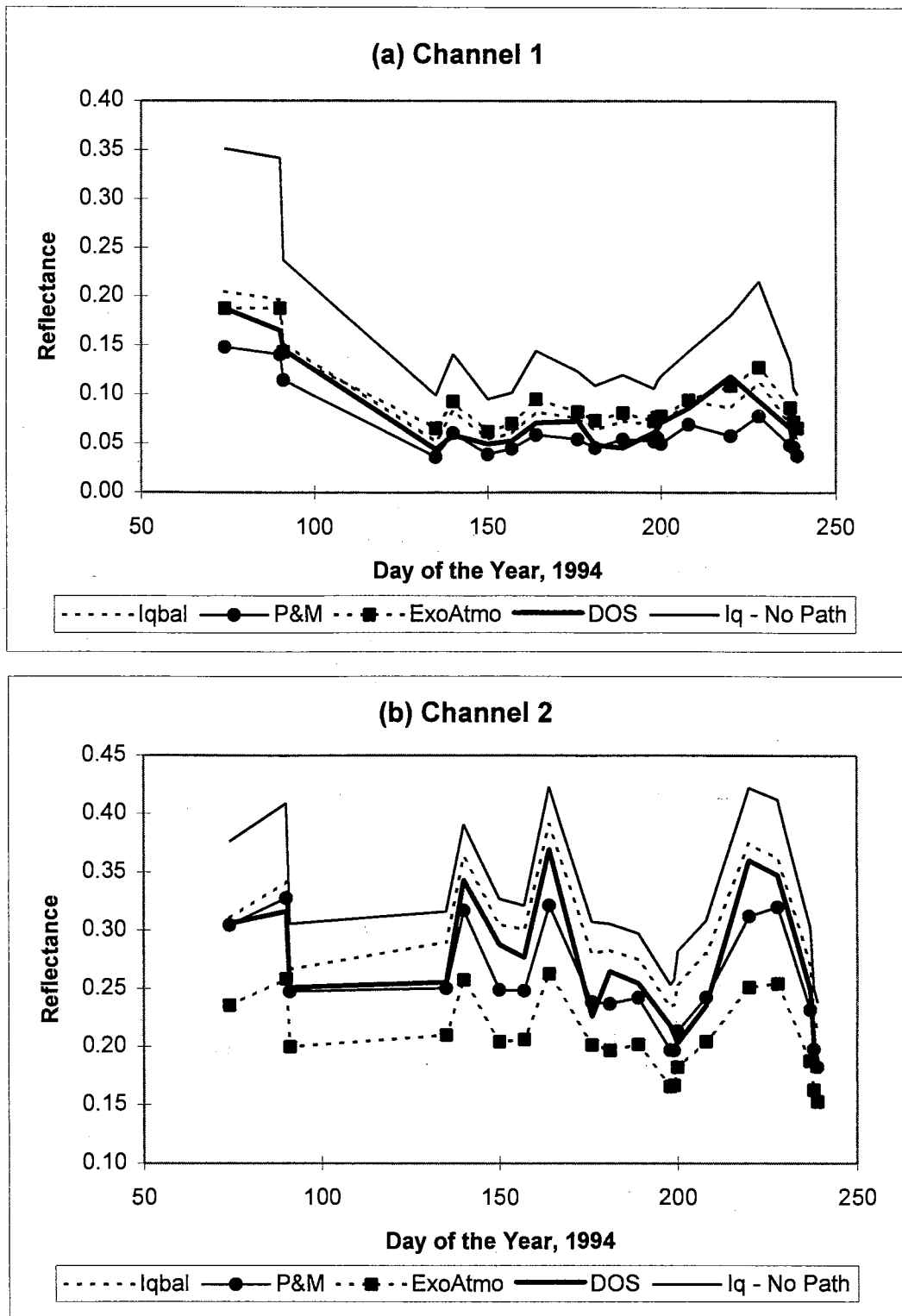
Figure 4.11: Comparision of the reflectance values from five atmospheric correction approaches for (a) channel 1 and (b) channel 2 over the area of the Marena lysimeter site for different dates in 1994.
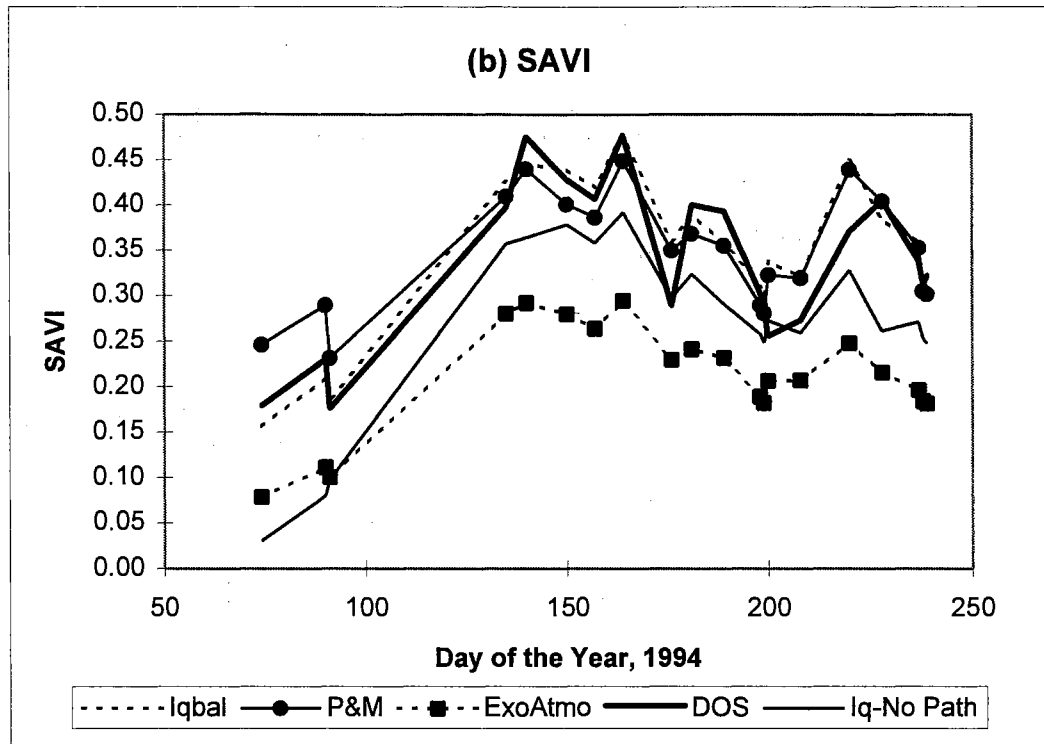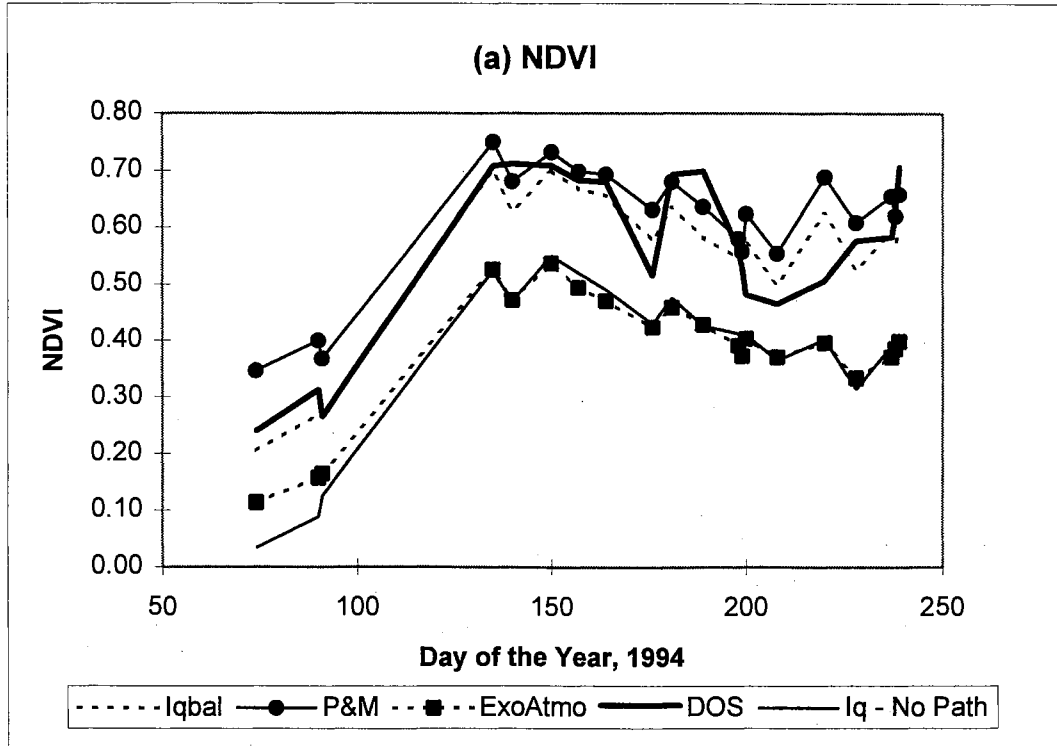
Figure 4.12: Comparison of (a) NDVI and (b) SAVI derived from reflectance values based on different atmospheric correction methods over the area of the Marena lysimeter site for different dates in 1994.

133

vapor and pressure, while the P&M assumes a standard atmosphere for all dates. Additionally, the reflectance values from all of the methods vary in the same manner with time. While atmospheric correction is necessary if the reflectance values are used to estimate physical quantities such as albedo, exoatmospheric reflectance should be sufficient to describe temporal changes for empirical applications.

There is very little difference in the NDVIs from Iqbal's method without the path radiance term and NDVIs from exoatmospheric reflectance. The differences early in the season arise from the impact of differences in the attenuation of the irradiance in the red and NIR channels at high solar zenith angles. However, SAVI is consistently higher for Iqbal's correction without the path term compared to the exoatmospheric calculated SAVI. There also appears to be more variation in the SAVI over short time periods compared to the NDVI. This is probably due to the directional nature of the reflectance as was seen in the Lake Texoma data.

Relationships Between Solar/Viewing Geometry and Reflectance

In order to assess how much of the variation in apparent reflectance over the areas of the lysimeter sites could be explained by solar and viewing geometry, a relationship from Walthall et al. (1985) was used. The relationship is expressed as:

$$R_i = A_{bi}\theta_{sat}^2 + B_{bi}\theta_{sat}\cos(\Delta\psi) + C_{bi} \qquad (4.19)$$

where $R_i$ is the reflectance in channel i, $\theta_{sat}$ is the satellite zenith angle (radians), $\Delta\psi$ is the relative azimuth angle between the satellite and the sun (radians), and $A_{bi}$, $B_{bi}$, and $C_{bi}$ are regression parameters. Cihlar et al. (1994) found Equation 4.19 to describe the bi-

directional variation in cropland and forested areas for AVHRR data. The regression

parameters for Equation 4.19 were determined for both exoatmospheric reflectance and

Iqbal atmospherically corrected reflectance in channels 1 and 2. Regression parameters

for the corresponding NDVIs were also determined.

Table 4.7 shows the results of fitting the reflectances to Equation 4.19. As

indicated by the coefficient of determination ($r^2$), much of the variation in both channels 1

and 2 reflectance could be explained by Equation 4.19. Exact directional correction

equations cannot be derived from this analysis, as the measurements from each site used

to determine the regression parameters were taken over an extended time period and

conditions were not constant. However, the high amount of variation in reflectance that

can be explained by the viewing angle does indicate that viewing geometry is impacting

the measurements, even with correction for atmospheric effects.

In general, the effect of solar and viewing geometry is decreased for the NDVI as

indicated by the lower $r^2$ values compared to the individual channels; however, there is

still evidence of a viewing geometry effect. There is a clearer impact of viewing

geometry on the NDVI for large satellite zenith angles as illustrated in Figure 4.13. In

this figure, overpasses at both Marena and Apache with satellite zenith angles greater

than $50°$ are indicated by arrows (note that data corresponding to satellite zenith angles

greater than $50°$ were not used in the analysis of the regression coefficients of Equation

4.19). As previously mentioned, the area measured by the sensor is larger for greater

zenith angles. Additionally, at these larger viewing angles, the reflected radiance is more

subject to atmospheric interference and the effects of shading are at their

**Table 4.7: Results of the regression analysis between viewing/solar geometry and reflectance or NDVI with reflectance derived as exoatmospheric or by Iqbal's method for data from the area of each of lysimeter site.**

| Site | Regression Coefficients * | | | $r^2$ | Standard Error | Regression Coefficients | | | $r^2$ | Standard Error | Number of Observations |
|---|---|---|---|---|---|---|---|---|---|---|---|
| | $A_{bi}$ | $B_{bi}$ | $C_{bi}$ | | | $A_{bi}$ | $B_{bi}$ | $C_{bi}$ | | | |
| **Exoatmospheric Reflectance** | | | | | | | | | | | |
| | | Channel 1 | | | | | Channel 2 | | | | |
| Apache | 0.08 | 0.05 | 0.10 | 0.76 | 0.01 | 0.15 | 0.08 | 0.19 | 0.81 | 0.02 | 20 |
| Goodwell | 0.06 | 0.05 | 0.12 | 0.74 | 0.01 | 0.07 | 0.03 | 0.19 | 0.31 | 0.02 | 16 |
| Marena | 0.12 | 0.05 | 0.06 | 0.84 | 0.02 | 0.08 | 0.04 | 0.19 | 0.59 | 0.02 | 21 |
| Wister | 0.02 | 0.03 | 0.09 | 0.42 | 0.02 | 0.16 | 0.08 | 0.21 | 0.70 | 0.03 | 17 |
| **Iqbal Corrected Reflectance** | | | | | | | | | | | |
| | | Channel 1 | | | | | Channel 2 | | | | |
| Apache | 0.08 | 0.06 | 0.10 | 0.69 | 0.02 | 0.23 | 0.13 | 0.25 | 0.88 | 0.02 | 20 |
| Goodwell | 0.06 | 0.06 | 0.13 | 0.79 | 0.01 | 0.12 | 0.07 | 0.26 | 0.51 | 0.03 | 16 |
| Marena | 0.13 | 0.06 | 0.05 | 0.73 | 0.02 | 0.09 | 0.06 | 0.27 | 0.44 | 0.04 | 21 |
| Wister | 0.00 | 0.03 | 0.09 | 0.17 | 0.02 | 0.26 | 0.11 | 0.29 | 0.65 | 0.05 | 17 |
| | NDVI derived from Exoatmospheric Reflectance | | | | | NDVI derived from Iqbal Reflectance | | | | | |
| Apache | 0.02 | -0.03 | 0.31 | 0.09 | 0.06 | 0.04 | -0.04 | 0.43 | 0.10 | 0.08 | 20 |
| Goodwell | -0.05 | -0.11 | 0.23 | 0.37 | 0.06 | 0.00 | -0.09 | 0.32 | 0.33 | 0.06 | 16 |
| Marena | -0.30 | -0.12 | 0.46 | 0.50 | 0.09 | -0.35 | -0.13 | 0.64 | 0.44 | 0.11 | 21 |
| Wister | 0.19 | -0.02 | 0.39 | 0.07 | 0.12 | 0.30 | -0.01 | 0.52 | 0.34 | 0.11 | 17 |

* See Equation 4.19.
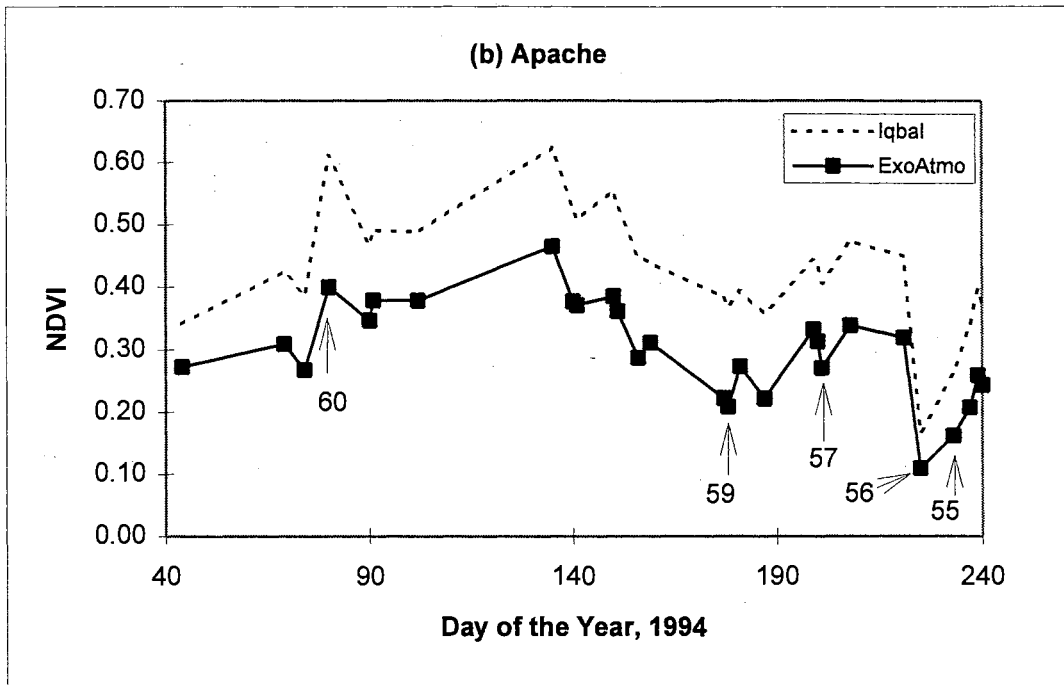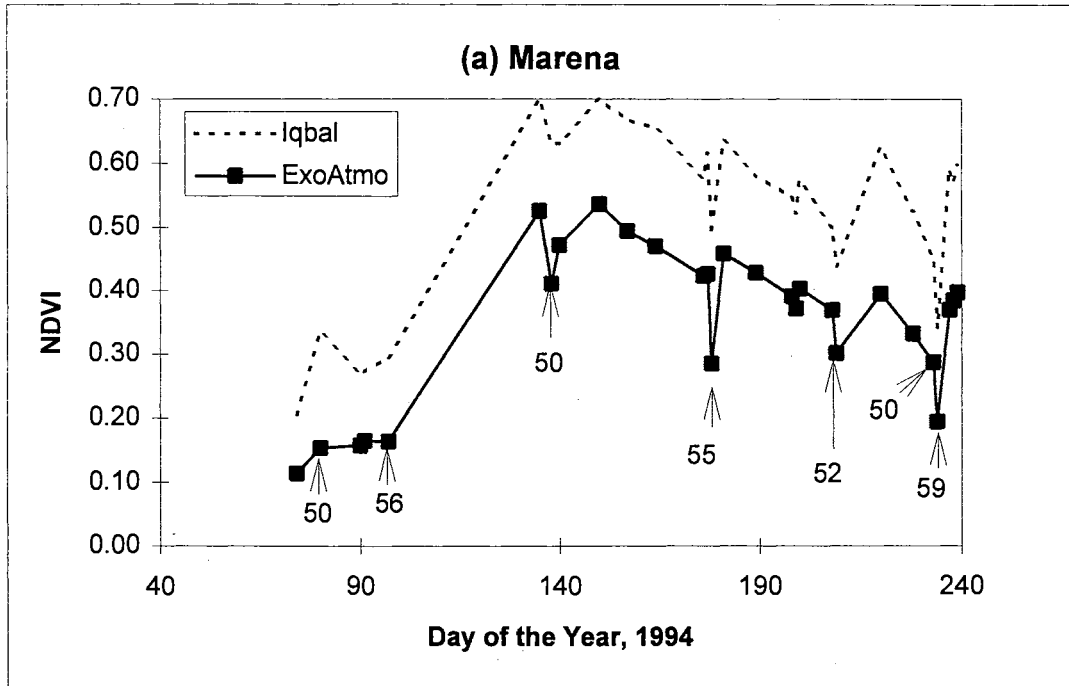
Figure 4.13: NDVI derived from both reflectance adjusted for atmospheric effects by Iqbal's methods (Iqbal) and from exoatmospheric reflectance (ExoAtmo) at the (a) Marena and (b) Apache lysimeter sites with data for satellite zenith angles from the point of observation greater than or equal to 50 degrees indicated.

maximum. For the lower reflectances, the atmospheric correction of Iqbal appears to over compensate for the points near day 90 at both Marena and Apache. For viewing angles greater than $50°$, the combinations of these factors prevent any quantitative interpretation of the data. To minimize both the geometric and viewing angle uncertainties, only images with less than a 45 degree zenith angle (from the point of observation) were used for the analysis described in Chapter 5.

Spectral Indices

After atmospheric correction, the reflectance data from channels 1 (Red) and 2 (NIR) were used to calculate three spectral indices: NDVI (Equation 2.8), SAVI (Equation 2.9) and a Modified Soil Adjusted Vegetation Index (MSAVI) from Qi et al. (1994). For the SAVI, a value of 0.5 is assumed for the soil correction term (L) in Equation 2.9. The MSAVI considered here is based on an inductive solution for the soil adjustment term by Qi et al. (1994). The index is expressed as:

$$MSAVI = \frac{2NIR + 1 - \sqrt{(2NIR + 1)^2 - 8(NIR - RED)}}{2} \qquad (4.20)$$

where NIR and RED are the reflectances in the near infrared and red regions of the spectrum.

NDVI, SAVI and MSAVI were computed for each of the lysimeter sites on different dates. Figure 4.14 shows example plots of the three indices calculated from exoatmospheric reflectance for the Marena and Apache lysimeter sites. At both sites, the trends in SAVI and MSAVI are very similar. The two indices only differ in magnitude
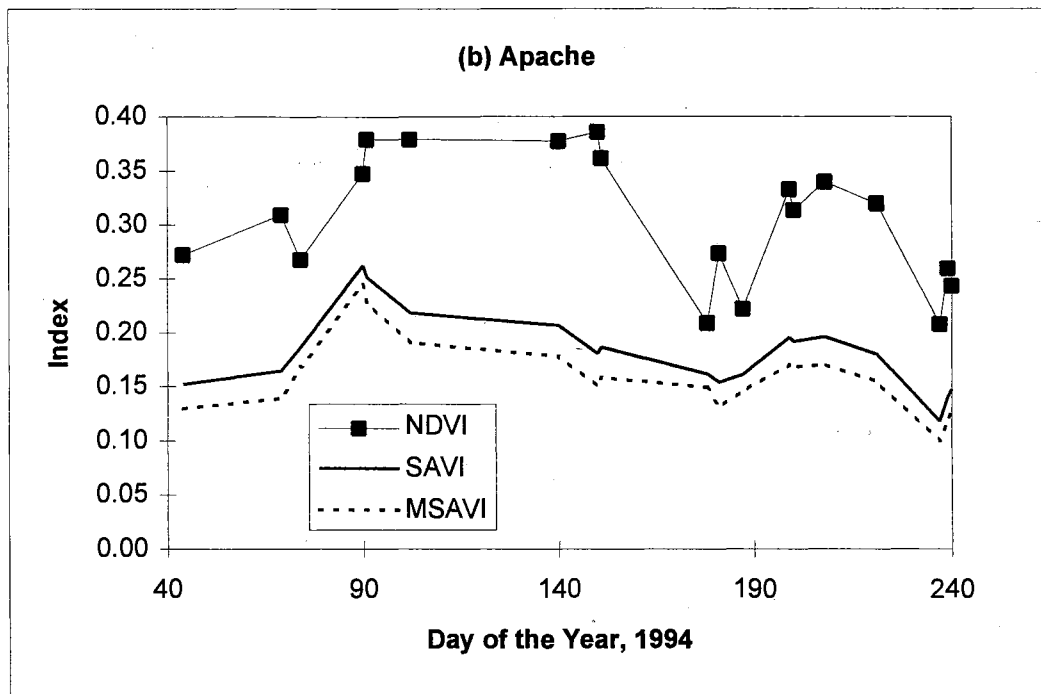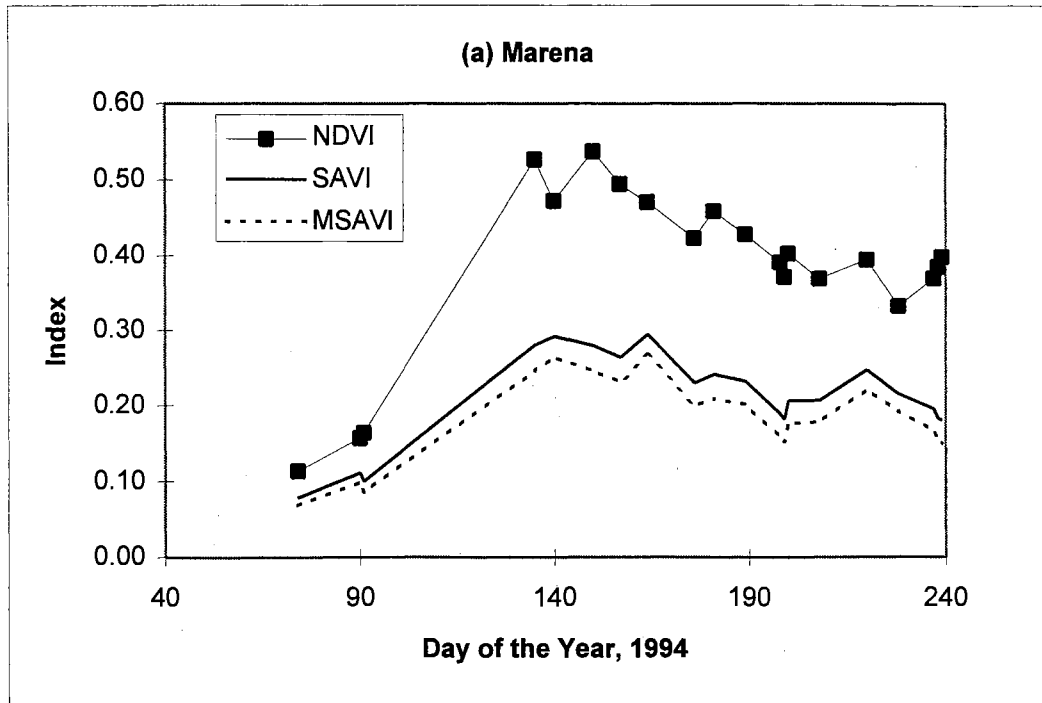
Figure 4.14: Comparison of NDVI, SAVI, and MSAVI derived from exoatmospheric reflectance for the area of the (a) Marena and (b) Apache lysimeter sites for different dates in 1994.

139

by a small amount for any particular day. The similarity between SAVI and MSAVI was also noted at the Wister and Goodwell sites. Due to this similarity, only SAVI and NDVI are considered in the remaining analysis.

The trend in NDVI and SAVI with time at the Marena site is consistent with the seasonal change in vegetation. At Apache, the seasonal trend is not as clear due to the mixture of winter wheat and pasture in the area. Additional discussion of NDVI and SAVI at all of the lysimeter sites is presented in Chapter 5.

## Chapter Summary

Images were initially selected by examining pyranometer data at the lysimeter sites to identify potentially cloud free conditions. Further cloud screening was conducted by examining the images once downloaded from the archives. Geometric correction was initially performed based on the orbital parameters of the satellite and then locations of the lysimeter sites were accurately located using ground control points (GCPs). The final geometric correction should locate the sites to within 1 pixel. This error may be higher at the Goodwell site, where only 1 of the 3 GCPs was easily located.

Conversion of the digital numbers from AVHRR channels 1 and 2 to radiance was accomplished by considering the degradation in the gain of these channels with time. A constant offset value of 40 was determined for these channels by noting their reading while viewing deep space. The thermal channels were converted to brightness temperatures using the onboard calibration values and accounting for nonlinearities in the sensors.

Three primary methods of atmospheric correction were examined for channels 1 and 2. Compared to a standard climatic atmosphere, the use of variable weather data in estimating the transmission provided similar results in the temporal trend of the reflectances. Atmospheric correction consistently resulted in an increase in the spectral indices; however, the relative variation in time of the indices from atmospherically corrected reflectances were to those with no correction. Viewing and solar geometry did have an influence on the apparent reflectances, even when atmospheric correction was applied. Quantitative application of the AVHRR data corresponding to satellite zenith angles greater than 50 degrees does not appear feasible. The impact of viewing geometry will also affect other off-nadir images and add variation to data from the reflected channels not attributed to changes in conditions at the surface. The effect was lessened in the NDVI and SAVI, with the SAVI appearing more sensitive than the NDVI. MSAVI and SAVI had very similar trends in time and there appears to be no advantage in using the MSAVI over the SAVI for the purposes of this study.

A summary of the image selection process is given in Figure 4.15. Cloud contamination limited the number of images available for this study. Restricting images to satellite zenith angles of less than 45 degrees further limited the number available. For completeness, the number of quality images with corresponding lysimeter data is also shown in the figure.

```
┌─────────────────────────────────────────────────────────────────┐
│              Total number of images retreived based             │
│                 primarily on  pyranometer data.                 │
│                                                                 │
│   Images containing the           Images containing the         │
│   Apache, Marena and              Goodwell lysimeter            │
│   Wister lysimeter sites:         site:                         │
│              51                              24                  │
└─────────────────────────────────────────────────────────────────┘
                                    │
                                    ▼
┌─────────────────────────────────────────────────────────────────┐
│              After removing cloud contaminated images:          │
│                                                                 │
│   Apache  Marena  Wister                    Goodwell           │
│    29       27      21                          18             │
└─────────────────────────────────────────────────────────────────┘
                                    │
                                    ▼
┌─────────────────────────────────────────────────────────────────┐
│              After eliminating images with satellite zenith     │
│                     angles ≥ 45 degrees:                        │
│                                                                 │
│   Apache  Marena  Wister                    Goodwell           │
│    23       20      18                          15             │
└─────────────────────────────────────────────────────────────────┘
                                    │
                                    ▼
┌─────────────────────────────────────────────────────────────────┐
│    Both quality image and lysimeter providing reliable data:    │
│                                                                 │
│   Apache  Marena  Wister                    Goodwell           │
│    18       5       10                          13             │
└─────────────────────────────────────────────────────────────────┘
```

Figure 4.15: Summary of the image selection process for data at the lysimeter sites.

CHAPTER 5

EVALUATION OF RELATIONSHIPS BETWEEN GROUND-BASED DATA

AND SATELLITE DERIVED INFORMATION

This chapter evaluates the relationships between the AVHRR derived data and ground-based observations. The chapter begins with an investigation of five split-window parameter sets for surface temperature estimation. The motivation for the comparison is to determine the split-window equation most appropriate for the surface and climatic conditions in Oklahoma. Next, the satellite derived information and Mesonet observations are examined in an effort to determine any relationships that may be useful in developing a satellite-based ET equation. The results of these comparisons are then used to derive estimates of potential ET from the AVHRR data. The chapter is concluded with a description and evaluation of methods to estimate actual ET from the satellite observations.

**Comparison of Satellite Derived Surface Temperature with Air Temperature**

Surface temperature is an important part of the energy balance and has been shown to be useful in obtaining remotely sensed estimates of ET. As noted in Chapter 2,

several recent studies have focused on the use of split-window relationships with AVHRR brightness temperatures to determine surface temperature. In order to select a split-window method appropriate for the climatic and surface conditions in Oklahoma, five methods were compared with Mesonet 1.5 m air temperatures. This section begins with a description of the surface temperature equations selected for evaluation and the evaluation procedures. The section is concluded with the results of the comparison between surface and air temperature.

Split-Window Surface Temperature Equations and Evaluation Methods

Five split-window temperature (SWT) equations were selected for evaluation. The first is from Becker and Li (1990b) and was selected because it accounts for variable surface emissivity. The equation is expressed as:

$$T_s = A + P\frac{T_{b4} + T_{b5}}{2} + M\frac{T_{b4} - T_{b5}}{2} \tag{5.1}$$

where $T_s$ is the satellite derived surface temperature (K), $T_{b4}$ and $T_{b5}$ are the brightness temperatures of channels 4 and 5 (K), A is a constant (1.274 K), and P and M are variables which are a function of the thermal emissivity of the surface. P and M were calculated as:

$$P = 1 + 0.15616\frac{1 - \varepsilon_a}{\varepsilon_a} - 0.482\frac{\Delta\varepsilon}{\varepsilon_a^2} \tag{5.2}$$

$$M = 6.26 + 3.98\frac{1 - \varepsilon_a}{\varepsilon_a} + 38.33\frac{\Delta\varepsilon}{\varepsilon_a^2} \tag{5.3}$$

where $\varepsilon_a$ is the average thermal emissivity in channels 4 and 5, and $\Delta\varepsilon$ is the difference in emissivity for the spectral range of AVHRR channels 4 and 5.

$(2)$ Price (1984) also presents a split-window equation allowing a variable emissivity that can be expressed as:

$$T_s = [T_{b4} + 3.33(T_{b4} - T_{b5})](\frac{3.5 + \varepsilon_4}{4.5}) + 0.75 T_{b5} \Delta\varepsilon) \qquad (5.4)$$

where $\varepsilon_4$ is the surface emissivity in the spectral range of channel 4. Two average thermal emissivity values where considered for use in equations 5.2, 5.3 and 5.4. Price (1984) suggested an average surface emissivity of 0.96 for land surfaces while Humes et al. (1994) found a composite emissivity of 0.98 for both grass-dominated and shrub-dominated areas of an arid watershed. For each of the average emissivity values, differences of -0.017, 0.0 and 0.017 were used. These values were selected based on the discussion of Li and Becker (1993).

$(3)$ Kerr et al. (1992) empirically derived parameters for the equation:

$$T_s = A + B T_{b4} + C T_{b5} \qquad (5.5)$$

over two sites with different vegetative cover conditions. The first site was a native grass land containing large patches of bare soil in southeast France (parameters associated with this site will be referred to as Kerr1). The second site was composed of primarily millet, and tiger brush in Niger (referred to as Kerr2). The coefficients of Equation 5.5 for both sites are included in Table 5.1.

Equation 5.5 with parameters from McClain et al. (1983) was chosen for evaluation because it was found by Cooper and Asrar (1989) to represent the best sea

145

**Table 5.1: Summary of the split-window coefficients evaluated.**

| | Assumed Surface Emissivity Conditions [a] | | | | | |
|---|---|---|---|---|---|---|
| $\Delta\varepsilon$: | -0.017 | 0.00 | 0.017 | -0.017 | 0.00 | 0.017 |
| $\varepsilon_a$: | 0.96 | 0.96 | 0.96 | 0.98 | 0.98 | 0.98 |

| | Becker and Li (1990b) Parameters | | | | | |
|---|---|---|---|---|---|---|
| A [b] | 1.274 | 1.274 | 1.274 | 1.274 | 1.274 | 1.274 |
| B | 3.367 | 3.716 | 4.065 | 3.337 | 3.672 | 4.007 |
| C | -2.352 | -2.710 | -3.068 | -2.326 | -2.669 | -3.013 |

| | Price (1984) Parameters | | | | | |
|---|---|---|---|---|---|---|
| A | 0.0 | 0.0 | 0.0 | 0.0 | 0.0 | 0.0 |
| B | 4.294 | 4.300 | 4.307 | 4.309 | 4.315 | 4.321 |
| C | -3.307 | -3.300 | -3.294 | -3.322 | -3.315 | -3.309 |

| | Empirical Parameters [c] | | | | |
|---|---|---|---|---|---|
| | Kerr1 | Kerr2 | McClain | Morning Regression | Evening Regression |
| A | 3.1 | -2.4 | -10.784 | -8.988 | -8.990 |
| B | 3.1 | 3.6 | 4.081 | 1.781 | 3.155 |
| C | -2.1 | -2.6 | -3.046 | -0.738 | -2.375 |

[a] $\Delta\varepsilon$ is the assumed difference between the thermal emissivity in the spectral range of AVHRR channels 4 and 5. $\varepsilon_a$ is the assumed average thermal emissivity of channels 4 and 5.

[b] A, B, and C are the parameters for the equation $Ts = A + B\ T_{b4} + C\ T_{b5}$, where $T_s$ is the predicted surface temperature (K), and $T_{b4}$ and $T_{b5}$ are the brightness temperatures (K) derived from AVHRR channels 4 and 5 respectively. For the Becker and Li (1990b) and Price (1984) parameters, the parameters correspond to the assumed emissivity conditions.

[c] Parameters derived empirically using observed surface temperatures. The Morning and Evening Regression are the parameters determined using 1.5 m air temperatures of this study as the dependent variable.

surface equation for estimation of land surface temperature. Cooper and Asrar (1989) adjusted the brightness temperatures for different emissivity values; however, in this analysis no adjustment is made.

Once the emissivity values are applied to Equations 5.1 and 5.4, all of the SWT equations were expressed in the form of Equation 5.5. Table 5.1 presents a summary of the parameters in Equation 5.5 for the SWT methods evaluated. The coefficients of Equation 5.5 were also determined using least squares linear regression, with air temperature as the dependent variable. The resulting regression coefficients are also included in Table 5.1.

The earth location information made it possible to automatically extract AVHRR data near Mesonet station locations. The navigation procedure for the HRPT files was adapted to extract AVHRR data for each of the 111 Mesonet sites using the latitude and longitude coordinates of the sites. While there is error in the navigation procedure, the AVHRR data still corresponds to an area within 7 km of the stations. This was considered sufficient to analyze spatial temperature trends.

The split-window surface temperature equations were evaluated by comparing the satellite derived surface temperatures to air temperatures at 1.5 m using morning (descending) overpasses of the satellite. As noted in Chapter 3, this time period results in the best agreement with IRT measured surface temperatures. Five images were used in the comparison from descending NOAA 11 passes. Additionally, surface temperatures derived from ten afternoon (ascending) images of NOAA 11 were compared to air temperatures to determine if the same relationships between SWT methods persisted. A

summary of the air temperature ranges and number of observations from each image used in the comparison of the SWT equations is provided in Table 5.2. The number of observations varies between images due to cloud contamination and the fact that the extracted portion of the image did not always cover the entire state. In most cases, the images did not cover the South East and North West corner of the state (see Figure 4.4). The conditions studied cover a wide range of temperatures and include both spring and summer data (Table 5.2).

The same statistical methods were used in the comparison as described in Chapter 3 in the comparison between IRT data and Mesonet temperatures. In this case the particular regression equation becomes:

$$T_s = A_r + B_r(T_a) \tag{5.6}$$

where $T_s$ is a surface temperature derived from one of the previously discussed SWT methods (converted from K to $^{o}$C), $T_a$ is the 1.5 m air temperature from a Mesonet station ($^{o}$C), and $A_r$ and $B_r$ are the least squares regression coefficients.

Comparison Results

*Descending (Morning) Pass Data*

The results of the regression analysis between surface and air temperature for the morning images is shown in Table 5.3. All of the methods provided estimates of surface temperature that were highly correlated with the morning air temperatures as indicated by the $r^2$ values. The methods also had $B_r$ values near 1, indicating the predicted surface temperatures varied in the same proportion as the air temperatures. The major difference

148

**Table 5.2: Summary of the images used to compare the split-window temperature equations and 1.5 m air temperature ranges corresponding to each image.**

| Date in 1994 | Time [a] (GMT) | n [b] | Air Temperature ($^{\circ}$C) Maximum | Minimum | Average | STD [c] |
|---|---|---|---|---|---|---|
| **Morning (Descending) Overpass** | | | | | | |
| March 15 | 11:40 | 22 | 12.6 | 6.1 | 9.1 | 1.7 |
| March 16 | 11:28 | 39 | 6.4 | -0.1 | 3.3 | 1.4 |
| March 31 | 11:45 | 80 | 6.4 | -3.9 | 1.2 | 2.1 |
| April 1 | 11:33 | 50 | 11.9 | 0.6 | 6.7 | 2.5 |
| June 29 | 11:47 | 17 | 26.1 | 17.4 | 21.1 | 2.7 |
| July 17 | 11:26 | 18 | 24.3 | 19.0 | 22.6 | 1.6 |
| All [d] | | 226 | 26.1 | -3.9 | 6.7 | 7.3 |
| **Afternoon (Ascending) Overpass** | | | | | | |
| March 16 | 22:45 | 23 | 23.7 | 20.0 | 21.8 | 1.0 |
| April 12 | 22:21 | 55 | 22.5 | 14.7 | 19.2 | 1.8 |
| May 20 | 22:58 | 59 | 28.7 | 23.6 | 26.4 | 1.1 |
| May 30 | 22:36 | 39 | 36.0 | 28.4 | 32.0 | 1.9 |
| June 5 | 22:51 | 26 | 34.6 | 29.9 | 32.2 | 1.3 |
| June 13 | 23:06 | 53 | 37.5 | 30.1 | 32.9 | 2.0 |
| June 30 | 22:58 | 70 | 40.8 | 28.4 | 35.7 | 2.0 |
| July 18 | 22:38 | 40 | 38.7 | 32.9 | 35.5 | 1.4 |
| July 19 | 22:25 | 72 | 39.6 | 32.2 | 35.3 | 2.0 |
| August 27 | 22:49 | 99 | 41.6 | 30.5 | 35.4 | 2.8 |
| All | | 537 | 41.6 | 14.7 | 31.5 | 5.9 |

[a] Approximate time of the satellite overpass.
[b] Number of points in the image corresponding to cloud free conditions near a Mesonet site.
[c] Standard deviation.
[d] Summary for all of the dates considered.

**Table 5.3: Regression results [a] from the comparison of surface temperatures from split-window parameters of Table 5.1 to air temperatures during morning (descending) passes.**

| | Assumed Surface Thermal Emissivity Conditions [b] | | | | | |
|---|---|---|---|---|---|---|
| $\Delta\varepsilon$: | -0.017 | 0.00 | 0.017 | -0.017 | 0.00 | 0.017 |
| $\varepsilon_a$: | 0.96 | 0.96 | 0.96 | 0.98 | 0.98 | 0.98 |

| | Becker and Li (1990) | | | | | |
|---|---|---|---|---|---|---|
| $r^2$ | 0.952 | 0.949 | 0.945 | 0.952 | 0.949 | 0.946 |
| $STD_{err}$ | 1.72 | 1.80 | 1.89 | 1.71 | 1.79 | 1.87 |
| $A_r$ | 2.18 | -0.43 | -3.03 | 1.19 | -1.31 | -3.81 |
| $B_r$ | 1.04 | 1.05 | 1.07 | 1.03 | 1.05 | 1.06 |

| | Price (1984) | | | | | |
|---|---|---|---|---|---|---|
| $r^2$ | 0.943 | 0.943 | 0.944 | 0.943 | 0.943 | 0.943 |
| $STD_{err}$ | 1.95 | 1.96 | 1.97 | 1.95 | 1.96 | 1.97 |
| $A_r$ | -7.25 | -3.79 | -0.327 | -7.26 | -3.80 | -0.335 |
| $B_r$ | 1.08 | 1.09 | 1.10 | 1.08 | 1.09 | 1.10 |

| | Empirical Methods | | | |
|---|---|---|---|---|
| | Kerr1 | Kerr2 | McClain | Regression [c] |
| $r^2$ | 0.953 | 0.949 | 0.946 | 0.958 |
| $STD_{err}$ | 1.642 | 1.764 | 1.922 | 1.468 |
| $A_r$ | -0.035 | -5.807 | -4.943 | 0.281 |
| $B_r$ | 1.009 | 1.041 | 1.101 | 0.958 |

[a] The least squares regression equation used in the comparison was $T_s = A_r + B_r T_a$, where $T_s$ is the estimated surface temperature for the particular parameter set of Table 5.1 converted to °C and $T_a$ is air temperature (°C). $r^2$ is the coefficient of determination between surface and air temperature and $STD_{err}$ is the standard error of the regression equation (°C).

[b] $\Delta\varepsilon$ is the assumed difference between the thermal emissivity in the spectral range of AVHRR channels 4 and 5. $\varepsilon_a$ is the assumed average thermal emissivity of channels 4 and 5.

[c] SWT parameters determined by fitting channel 4 and 5 brightness temperatures to the morning air temperatures.

in the relationship of the predicted surface temperatures and the morning air temperature was that of an offset as indicated by the $A_r$ statistic. The statistics are illustrated for predictions from both Becker and Li's method and Price's methods in Figure 5.1 for two sets of assumed emissivity values. The first set corresponds to an average emissivity of 0.96 with a difference between the emissivity of channel 4 and channel 5 of -0.017, while the second set is for an average emissivity of 0.98 and difference of 0.017. The assumption of a higher emissivity in channel 4 than channel 5 resulted in an overall decrease in predicted surface temperature for Becker and Li's method; however, for Price's method the primary effect was to increase the predicted surface temperature. The difference in the predicted effects of emissivity on surface temperature may be related to the fact that Becker and Li integrate emissivity into the radiative transfer equations, while Price accounts for emissivity after considering atmospheric effects.

Considering the Becker and Li equations, more variation in air temperature was accounted for using a $\Delta\varepsilon$ of -0.017 as indicated by the $r^2$ values. However, the $A_r$ statistic closest to zero corresponds to a $\Delta\varepsilon$ of 0 and average emissivity of 0.96. For Price's method, all of the values of emissivity provide similar $r^2$ and standard errors. The assumed difference in emissivity of 0.017 provided $A_r$ values closest to 0. The values assumed for the average emissivity had less impact on the predictions than did the assumed differences of emissivity between channels 4 and 5. Both the parameters of McClain for sea surface temperature and Kerr2 parameters provided estimates of surface temperature that were typically lower than the air temperature.
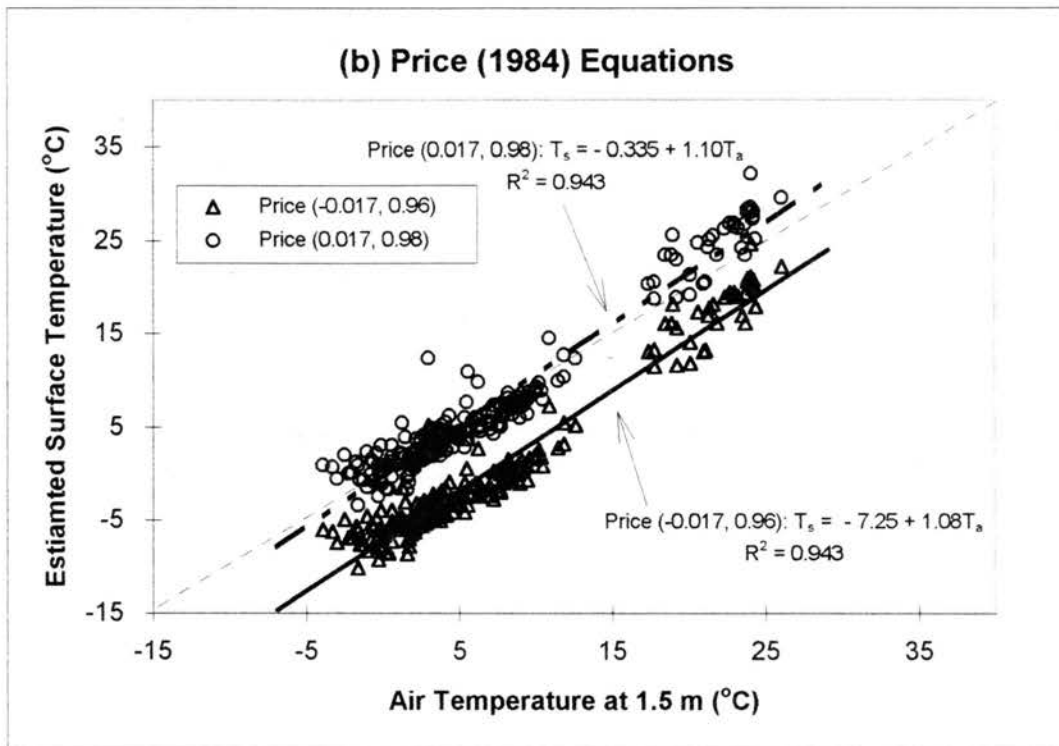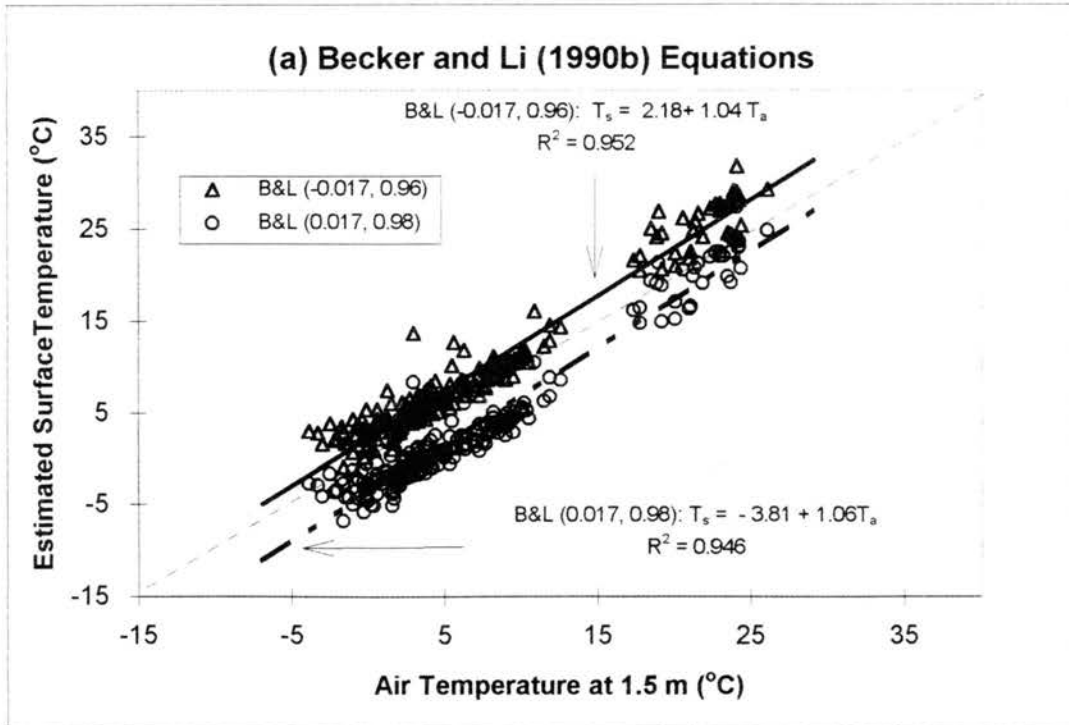
Figure 5.1: Comparison of split-window derived surface temperatures from the equations of (a) Becker and Li (1990b) and (b) Price (1984) to morning air temperature assuming two different thermal emissivity conditions.

The Kerr1 parameters provided the best overall fit of the data. The $A_r$ value is close to 0 and $B_r$ is close to 1. Additionally, this method has the lowest standard error of methods evaluated. Figure 5.2 shows plots of the SWT surface temperature based on the Kerr1 parameters. Also included in Figure 5.2 is a plot of a least squares regression fit of air temperature and channel 4 and 5 brightness temperatures. Some of the scatter for lower temperatures may be due to improper cloud screening, as only gray-scale thresholding was used to cloud screen these images. For cold morning surface temperatures, it is more difficult to distinguish between land and scattered clouds. For the most part the surface temperatures from the Kerr1 parameters are evenly distributed about the 1 to 1 line. Additionally, there is little difference in the scatter about the 1 to 1 line between the Kerr1 estimates and regression results.

*Ascending (Afternoon) Data*

Table 5.4 contains the evaluation regression statistics using the afternoon (ascending) images. The statistics for the afternoon passes indicate that for each method, the relationship between the surface and air temperature is not as strong as indicated by the lower $r^2$ values and increase in the standard error compared to that seen with the morning images. Some of the reduction in correlation can be attributed to the fact that in the afternoon surfaces with sparse or dry vegetation are expected to have a surface temperature higher than that of the air, as was shown by the comparison of air temperature with the IRT measured surface temperature.

The relationship between methods remains much the same as with the morning temperatures; however, in most cases the $B_r$ value is increased. To illustrate the
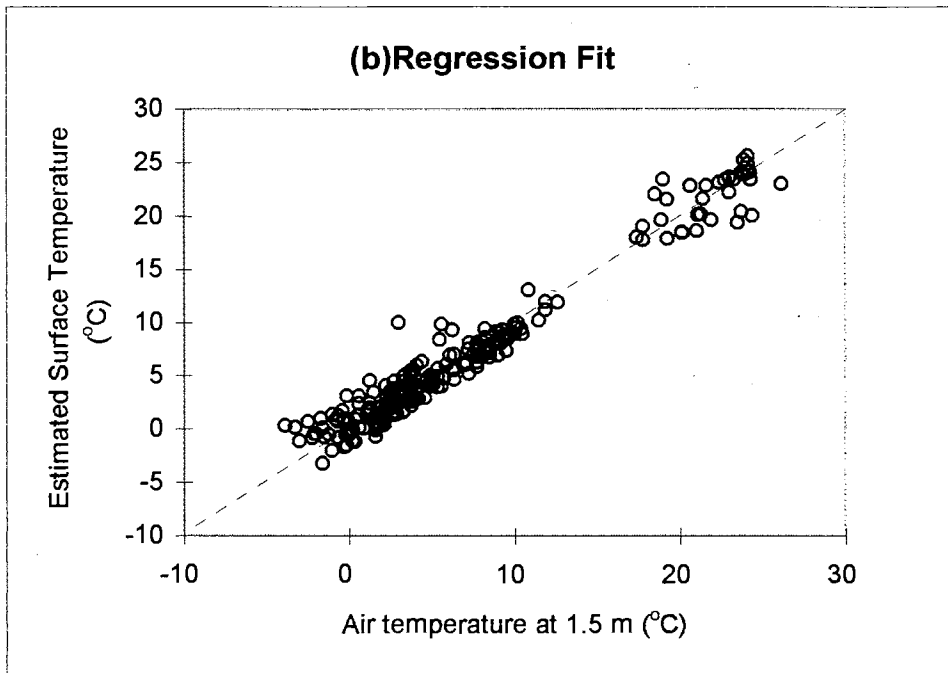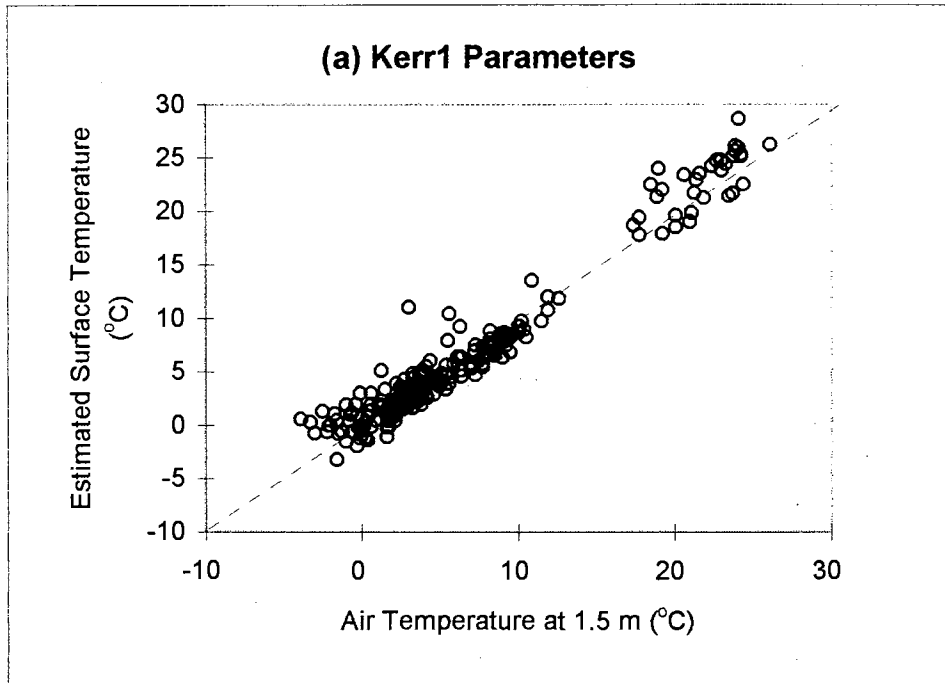
Figure 5.2: Satellite derived surface temperatures using (a) the Kerr1 parameters and (b) a regression fit of channel 4 and 5 brightness temperatures versus air temperature for morning (descending) passes.

**Table 5.4: Regression results [a] from the comparison of surface temperatures from the split-window parameters of Table 5.1 to air temperatures during afternoon (ascending) passes.**

| | Assumed Surface Thermal Emissivity Conditions [b] | | | | | |
|---|---|---|---|---|---|---|
| $\Delta\varepsilon$ | -0.017 | 0.00 | 0.017 | -0.017 | 0.00 | 0.017 |
| $\varepsilon_a$ | 0.96 | 0.96 | 0.96 | 0.98 | 0.98 | 0.98 |

| | Becker and Li (1990) | | | | | |
|---|---|---|---|---|---|---|
| $r^2$ | 0.908 | 0.909 | 0.909 | 0.907 | 0.909 | 0.909 |
| $STD_{err}$ | 2.06 | 2.13 | 2.20 | 2.05 | 2.11 | 2.18 |
| $A_r$ | 3.72 | 0.55 | -2.62 | 2.75 | -0.29 | -3.32 |
| $B_r$ | 1.09 | 1.13 | 1.17 | 1.08 | 1.12 | 1.16 |

| | Price (1984) | | | | | |
|---|---|---|---|---|---|---|
| $r^2$ | 0.909 | 0.909 | 0.909 | 0.909 | 0.909 | 0.909 |
| $STD_{err}$ | 2.24 | 2.26 | 2.28 | 2.25 | 2.26 | 2.28 |
| $A_r$ | -7.23 | -3.69 | -0.16 | -7.25 | -3.72 | -0.19 |
| $B_r$ | 1.19 | 1.20 | 1.21 | 1.19 | 1.20 | 1.21 |

| | Empirical Parameters | | | |
|---|---|---|---|---|
| | Kerr1 | Kerr2 | McClain | Regression [c] |
| $r^2$ | 0.906 | 0.909 | 0.909 | 0.909 |
| $STD_{err}$ | 1.99 | 2.09 | 2.25 | 1.79 |
| $A_r$ | 1.79 | -4.70 | -4.31 | 2.91 |
| $B_r$ | 1.04 | 1.11 | 1.19 | 0.91 |

[a] The least squares regression equation used in the comparison was $T_s = A_r + B_r T_a$, where $T_s$ is the estimated surface temperature for the particular parameter set of Table 5.1 converted to °C and $T_a$ is air temperature (°C). $r^2$ is the coefficient of determination between surface and air temperature and $STD_{err}$ is the standard error of the regression equation (°C).

[b] $\Delta\varepsilon$ is the assumed difference between the thermal emissivity in the spectral range of AVHRR channels 4 and 5. $\varepsilon_a$ is the assumed average thermal emissivity of channels 4 and 5.

[c] SWT parameters determined by fitting channel 4 and 5 brightness temperatures to the afternoon air temperatures.

evaluation statistic for the afternoon images, Figure 5.3(a) is a plot of SWT from the

equations of Becker and Li and Figure 5.3(b) presents Price's method for the ascending

images. As was the case in the morning images, the scatter in the data about the

regression line is similar despite the assumed emissivity conditions. The primary

difference resulting from the assumed emissivity values is that of a constant offset in the

predicted surface temperatures compared to air temperature.

The Kerr1 parameters still provide the lowest standard error with air temperature

of all of the SWT methods considered. Figure 5.4 (a) shows the Kerr1 parameters versus

air temperature, and Figure 5.4(b) illustrates the results of using regression to determine

the coefficients of Equation 5.5. There is greater scatter in the Kerr1 plot compared to the

regression results; however, greater variations in surface temperature are expected for the

evening surface temperatures compared to morning time periods as previously

mentioned. Additionally, the Kerr1 parameters resulted in surface temperatures that were

typically higher than air temperature; however, this is reasonable for the afternoon time

period.

The minimum standard error of 1.7 $^{\circ}$C between satellite derived surface

temperature and morning air temperature is typical of results obtained from other

investigators as noted in the literature review (Price, 1984; Kerr et al., 1992; Prata, 1994).

One factor that probably contributes to the appropriateness of the Kerr1 parameters is that

the parameters were derived for a grass covered surface and much of Oklahoma is

covered by pastures and rangeland. Therefore, the satellite derived surface temperatures

for the remainder of the study are based on Kerr1 parameters.

**(a) Becker and Li (1990b) Equations**

B&L(-0.017,0.96) $T_s = 1.09T_a + 3.72$
$r^2 = 0.908$

B&L (0.017, 0.98) $T_s = 1.16T_a - 3.32$
$r^2 = 0.909$

| | |
|---|---|
| △ | B&L(-0.017, 0.96) |
| ○ | B&L(0.017, 0.98) |

**(b) Price (1984) Equations**

Price (0.017, 0.98) $T_s = -0.191 + 1.21T_a$
$r^2 = 0.909$

Price (-0.017, 0.96) $T_s = -7.23 + 1.19T_a$
$r^2 = 0.909$

| | |
|---|---|
| △ | Price(-0.017, 0.96) |
| ○ | Price (0.017, 0.98) |
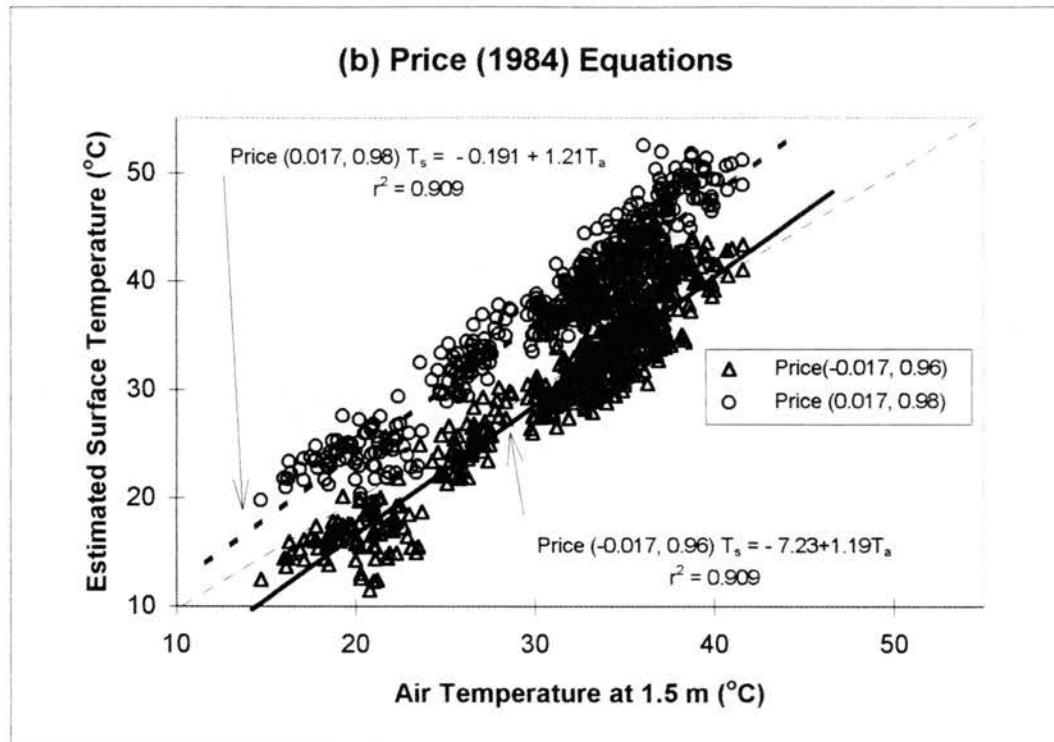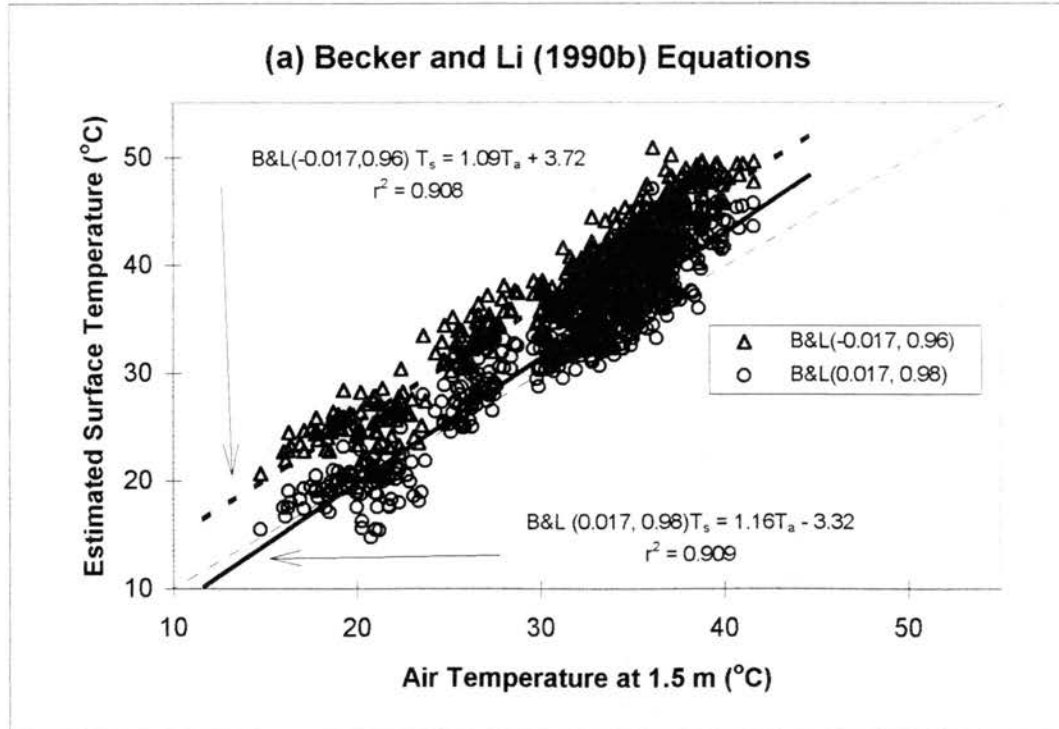
Figure 5.3: Comparison of split-window derived surface temperatures from both the equations of (a) Becker and Li (1990b) and (b) Price (1984) to afternoon air temperatures assuming two different thermal emissivity conditions.
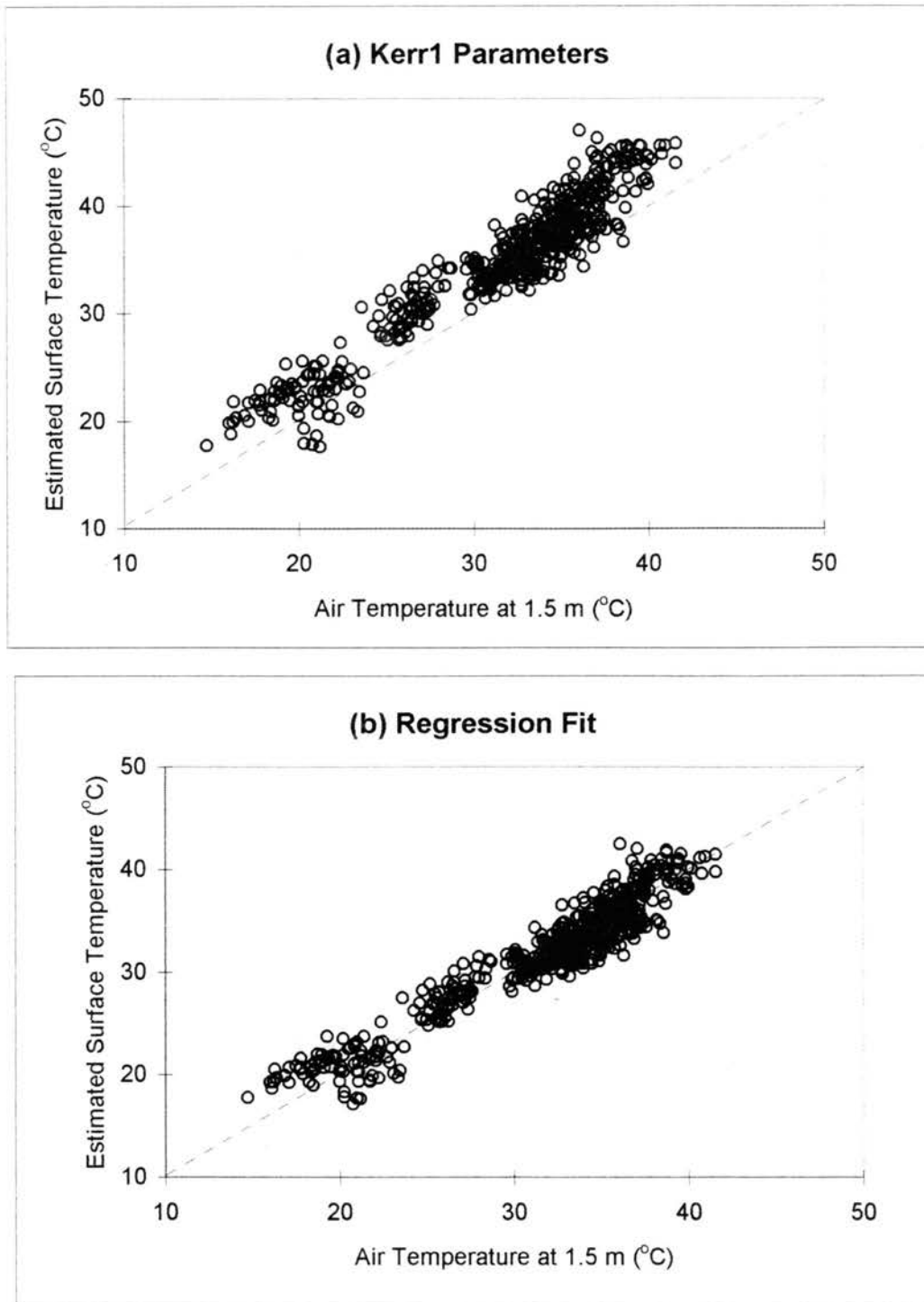
Figure 5.4: Comparison of AVHRR derived temperatures from (a) the Kerr1 parameters and (b) regression fit to air temperature at 1.5 m for afternoon (ascending) passes.

# Comparison of AVHRR Data and Weather Observations

This section begins by examining the correlation between AVHRR data and weather observations that have been related to ET. Particular attention is given to vapor pressure derived from the Mesonet observations.

## Correlation Between AVHRR and Weather Data

*Methods*

In an effort to identify potential relationships between the satellite data and meteorological variables that can impact the rate of evapotranspiration, the correlation coefficients between satellite and Mesonet observations were determined. The weather data selected for comparison (Table 5.5) have been shown to be useful in the estimation of ET. Both daily summary observations (maximum / minimum temperature and relative humidity, and average wind speed) and observations corresponding to the approximate time of over pass (relative humidity, air temperature, and vapor pressure) were considered. Correlation coefficients were determined between the weather data and AVHRR derived information shown in Table 5.5.

The AVHRR typically takes less than a minute to acquire an image that covers the entire state; therefore, all observations compared at the time of over pass represent five minute average data for the closest time period. Note that the same afternoon images listed in Table 5.2 were used for the following evaluation.

**Table 5.5: Ground-based and satellite derived data used for correlation analysis.**

<table>
<tr><td>5 Minute Averages</td><td>Daily Averages or Totals</td></tr>
<tr><td>

• Relative Humidity (RH)
• 1.5 m Air Temperature ($T_a$)
• Vapor Pressure

</td><td>

• Maximum and Minimum RH
• Maximum and Minimum $T_a$
• Average Daily 2 m Wind Speed

</td></tr>
</table>

AVHRR Derived Data:

• Channel 1 and 2 exoatmospheric reflectance
• NDVI and SAVI from exoatmospheric reflectance
• Difference in channel 4 and 5 brightness temperatures
• Satellite derived surface temperature

*Correlation Results*

Table 5.6 is a summary of the correlation coefficients between the image data and Mesonet observations. Also included in the table are the correlation coefficients between the satellite derived data and potential ET calculated from the daily weather data and vapor pressure at the time of satellite overpass, which will be further described in later sections. Appendix J includes a summary of the ground-based observations for each image. The appendix also includes the same correlation coefficients as shown in Table 5.6 calculated on a per image basis.

From Table 5.6, remotely sensed information derived from the reflective channels shows no strong correlation with temperature. The highest correlation between information derived from the reflective channels (NDVI, SAVI, $R_1$, $R_2$) is the correlation of NDVI with relative humidity and wind speed. The correlation can partially be

160

**Table 5.6: Correlation coefficients between AVHRR derived information and meteorological data.** [a]

| Remotely Sensed Information [b] | Based on 24 Hour Observations | | | | | Potential ET [c] | | At Time of Over Pass | | |
| | Air Temperature | | Relative Humidity | | Average Wind | | | Relative | Air | Vapor |
| | Max | Min | Max | Min | Speed | PMon | Harg | Humidity | Temperature | Pressure |
|---|---|---|---|---|---|---|---|---|---|---|
| NDVI | 0.025 | 0.185 | 0.490 | 0.610 | -0.533 | -0.286 | 0.048 | 0.594 | 0.035 | 0.421 |
| SAVI | -0.038 | 0.103 | 0.469 | 0.569 | -0.459 | -0.282 | 0.035 | 0.541 | -0.026 | 0.329 |
| $R_1$ | -0.122 | -0.272 | -0.305 | -0.444 | 0.450 | 0.171 | -0.050 | -0.463 | -0.124 | -0.417 |
| $R_2$ | -0.155 | -0.121 | 0.257 | 0.255 | -0.128 | -0.172 | -0.013 | 0.210 | -0.144 | 0.005 |
| $T_{b4}$-$T_{b5}$ | 0.870 | 0.818 | -0.310 | -0.043 | 0.148 | 0.780 | 0.740 | -0.046 | 0.867 | 0.549 |
| $T_s$ | 0.949 | 0.857 | -0.177 | 0.012 | 0.061 | 0.801 | 0.873 | -0.027 | 0.952 | 0.605 |

[a] The data used is for the same dates and images listed in Table 5.2 for afternoon overpasses of NOAA 11 (number of observations = 537).

[b] $R_1$ and $R_2$ are exoatmospheric reflectance from channels 1 and 2, respectively, $T_{b4}$ and $T_{b5}$ are the brightness temperatures from channel 4 and 5 data, and $T_s$ is satellite derived surface temperature (Kerr1 parameters, Equation 5.5).

[c] PMon is potential ET calculated from the Penman-Monteith equation (Equation 3.2) and Harg is ET calculated based on the Hargreaves equation (Equation 5.21).

attributed to the spatial distribution of the variables. In general, the NDVI decreases from east to west across the state of Oklahoma. There are generally higher wind speed speeds in the western part of the state and relative humidites are typically lower. While there is not a cause and effect relationship implied here, the correlation does have some physical meaning. Hot, dry, windy conditions do not favor the formation of dense, vegetative covers. Additionally, the greater the vigor and density of vegetation, the higher the rate of transpiration and thus an increase in atmospheric water vapor. When plants have developed a complete canopy, the surface roughness is increased, so some decrease in the wind speed near the surface is expected. The many factors that influence plant growth and vigor such as fertility, climate and moisture availability provide some explanation as to why the NDVI has been found to have correlation with so many different variables. The fact that the correlation with SAVI is not as high can be attributed to the impact of bi-directional reflectance. This could also partially explain why the correlation coefficients between NDVI and relativity humidity, and NDVI and wind speed are higher than the individual reflectance values from channels 1 and 2.

There is a high correlation between surface temperature and both the Penman-Monteith and Hargreaves estimate of potential ET. The correlation with the Hargreaves is definitely related to the correlation of surface temperature with air temperature, as temperature is the primary input to the model. The correlation with Penman-Monteith can be related not only to the correlation between surface temperature, but also the fact that higher air temperatures are an indication of more energy input for the evaporation of water. These relationships are further investigated later.

Data derived from the thermal channels all show strong correlation with air temperature. Note that the air temperature corresponding to the time of satellite overpass is highly correlated with the maximum daily temperature. There is a correlation between the difference in channel 4 and 5 brightness temperatures and vapor pressure; however, the correlation is stronger with surface temperature and vapor pressure. These correlations are most likely due to the fact that the atmosphere is capable of holding more moisture at higher temperatures and not exclusively due to the attenuation between channels 4 and 5. Efforts to develop a relationship between the satellite data and vapor pressure are the topic of the next section.

<u>Comparison of AVHRR Data and Vapor Pressure</u>

Based on several of the studies reviewed in the literature, there is evidence for a relationship between atmospheric vapor content and the difference between channel 4 and 5 brightness temperatures. As vapor pressure can be used in ET estimation, the following describes the steps taken to examine the relationships between AVHRR data and vapor pressure.

*Theoretical Development*

The difference between brightness temperatures in channels 4 and 5 has been related to the amount of water vapor in the atmosphere (for example, Eck and Holben, 1994). However, from Table 5.6, the correlation between the difference in channels 4 and 5 is stronger with air temperature than vapor pressure. Furthermore, the correlation between $T_{b4} - T_{b5}$ actually displayed a negative correlation with vapor pressure within

some images (see Appendix J).

An explanation for this effect can be shown by considering the radiative transfer

equation between the surface and satellite, expressed as:

$$L = \tau \, \varepsilon \, L_s + \tau(1 - \varepsilon)L_{atm}\downarrow + L_{atm}\uparrow \qquad (5.7)$$

where L is the radiance received by the satellite, $\tau$ is atmospheric transmittance, $\varepsilon$ is

thermal emissivity, $L_s$ is the radiance of the surface, $L_{atm}\downarrow$ is atmospheric downwelling

radiance, and $L_{atm}\uparrow$ is the upwelling atmospheric radiance. The first term in Equation 5.7

represents the radiance emitted from the surface, the second represents the radiance from

the atmosphere reaching the surface and then transmitted to the satellite, and the third

term is the radiance emitted directly from the atmosphere to the satellite (Kleespies and

McMillin, 1990).

If the emissivity is assumed near 1, the contribution of the second term in

Equation 5.7 can be neglected (Perry and Moran, 1994). If the upwelling atmospheric

radiance is assumed equal for channels 4 and 5 of the AVHRR, the difference in radiance

received at the satellite between the two channels can be expressed from Equation 5.7 as:

$$L_4 - L_5 = L_{s4}\,\tau_4\,\varepsilon_4 - L_{s5}\,\tau_5\,\varepsilon_5 \qquad (5.8)$$

where $L_4$ and $L_5$ are the radiances received at the satellite in channels 4 and 5 and $L_{si}$ is

the radiance emitted by the surface in the spectral range of channel i. The relationship

between atmospheric moisture and the difference in channel 4 and 5 brightness

temperatures is based on the fact that channel 5 experiences more attenuation than

channel 4. However, from Equation 5.8, it can be seen that the difference will also vary

with both changes in emissivity and with changes in radiance at the surface. An increase

in surface temperature will result in a net increase in the difference in radiance between

the two channels for the same atmospheric conditions.

In an effort to minimize the influence of changes in surface radiance on satellite

based estimates of vapor pressure, an alternative to the difference in channel 4 and 5

brightness temperatures is considered. If the downwelling atmospheric radiance of

Equation 5.7 is neglected, the transmittance in a particular channel can be expressed as:

$$\tau_i = \frac{L_i - L_{atm_i}}{\varepsilon_i L_{si}} \qquad (5.9)$$

Becker and Li (1990b) note that the relationship between transmittance and precipitable

water is fairly linear; however, the relationship is not independent of path length.

McMillin (1975) notes that for the spectral region of the AVHRR channels, Bouger's Law

can be applied to account for path length:

$$\tau_i = \exp(-k_i m_r) \qquad (5.10)$$

where $k_i$ is the extinction coefficient for channel i and $m_r$ is the relative path length

(approximated as $\cos(\theta_{sat})^{-1}$). If Equation 5.10 is solved for the extinction coefficient and

transmittance is expressed as in Equation 5.9, the following relationship is obtained:

$$k_i = \frac{-\ln(\frac{L_i - L_{atmi}}{\varepsilon_i L_{si}})}{m_r} \qquad (5.11)$$

Assuming most of the variation in $k_i$ is due to changes in atmospheric moisture, Equation

5.11 should be correlated with vapor pressure.

One limitation in the application of Equation 5.11 to AVHRR data is that an independent estimate of the atmospheric radiance is required. Rather than estimate this term from radiative transfer data, it is neglected, with hopes that a sufficient relationship between transmittance and vapor pressure can be derived without it. Channel 5 was selected for use with Equation 5.11 as it is more sensitive to atmospheric moisture than channel 4. A further assumption implicit in this attempt to correlate vapor pressure at the surface with the AVHRR data is that the atmosphere is well mixed. This will not always be the case; however, a majority of the atmospheric moisture is located within 2 km of the earth's surface.

Estimates of emissivity for use in Equation 5.11 were determined from NDVI values derived from exoatmospheric reflectance based on a procedure from Kerr et al. (1992). Emissivity is linearly weighted to the exoatmospheric NDVI by:

$$\varepsilon = \frac{NDVI - NDVI_{min}}{NDVI_{max} - NDVI_{min}}(\varepsilon_{max} - \varepsilon_{min}) + \varepsilon_{min} \qquad (5.12)$$

where $NDVI_{max}$ and $NDVI_{min}$ were the maximum and minimum NDVI values observed in the images under cloud free conditions over land surfaces (0.61 and 0.1 respectively), and $\varepsilon_{max}$ and $\varepsilon_{min}$ are the corresponding maximum and minimum thermal emissivity values. The maximum emissivity was assumed equal to the maximum possible value of 1. The minimum value of emissivity was selected to minimize the sum of squared errors in estimates of vapor pressure, with the added constraint that the extinction coefficient must remain greater than 0.

The radiance at the surface for channel 5 was approximated using the AVHRR

166

derived surface temperature. The radiance in the spectral range corresponding to the surface temperature was calculated by an inversion of Equation 4.11. It is assumed that the effects of the atmosphere and variable emissivity have been minimized by the appropriate selection of the split-window parameters.

In summary, the following equation was used in an attempt to estimate atmospheric attenuation in channel 5:

$$k_5 \approx \frac{-\ln(\frac{L_5}{\varepsilon_5 L_{s5}})}{m_r} \qquad (5.13)$$

where the subscript 5 indicates the values correspond to the spectral region of AVHRR channel 5, $k_5$ is the atmospheric extinction coefficient (to be empirically related to vapor pressure), $L_5$ is the radiance received at the satellite, $\varepsilon_5$ is thermal emissivity (estimated from NDVI as described in Equation 5.12), $L_{s5}$ is the radiance at the surface (based on the radiance corresponding to the satellite derived surface temperature) and $m_r$ is the relative optical mass $(\cos(\theta_{sat})^{-1})$.

*Evaluation Methods*

The ground-based values of vapor pressure were calculated from the 1.5 m temperature and relative humidity measurements. Saturated vapor pressure ($e^\circ$, kPa) was calculated based on a relationship from Jensen et al. (1990) as:

$$e^\circ = \exp(\frac{16.78 T_a - 116.9}{T_a + 237.3}) \qquad (5.14)$$

where $T_a$ is the 1.5 m air temperature ($^\circ$C). Vapor pressure (e, kPa) was then calculated

from the 1.5 m relative humidity (RH, %) measurements as:

$$e = \frac{e^\circ RH}{100}$$ (5.15)

The vapor pressures were calculated using the 5 minute average data corresponding to the time of satellite overpass.

Linear regression was used to relate $k_5$ in Equation 5.13 to vapor pressure. The difference in channel 4 and 5 brightness temperatures was evaluated for comparison purposes. Also considered were the methods of Jedlovec (1990), where the slope of channel 5 versus channel 4 vapor pressure in a 9x9 pixel array is used. That is, the parameter of interest is the least squares regression slope of the regression equation:

$$T_{b5} = constant + Slope_{5,4}\, T_{b4}$$ (5.16)

where $T_{bi}$ is the brightness temperature of channel i in a 9x9 pixel array centered on the area of interest, and constant and $Slope_{5,4}$ are the regression coefficients. Goward et al. (1994) found $Slope_{5,4}$ to be inversely proportional to absolute humidity at the surface. The same afternoon image data set described in the analysis of weather data was used to evaluate the vapor pressures.

Each of the procedures was evaluated using the regression relationship:

$$VP_{AVHRR} = A_r + B_r\, VP_{ground}$$ (5.17)

where $VP_{AVHRR}$ is the vapor pressure derived from the AVHRR data, $VP_{ground}$ is the vapor pressure derived from ground-based measurements and $A_r$ and $B_r$ regression coefficients. Additionally, the following evaluation statistics were also calculated:

$$MAD = \frac{\left| VP_{AVHRR} - VP_{ground} \right|}{n} \qquad (5.18)$$

$$RMSE = \sqrt{\frac{(VP_{AVHRR} - VP_{ground})^2}{n}} \qquad (5.19)$$

where n is the number of observations, MAD is the Mean Absolute Difference and

RMSE is the Root Mean Square Error. MAD represents the mean absolute error, while

RMSE is similar to standard error; however, the predicted data is not modified by the

regression relationship of Equation 5.17.

Once the vapor pressure relationships were evaluated with the afternoon data of

Table 5.2, the most promising relationship was evaluated with data from images extracted

over the lysimeter sites. The number of days on a per month basis on which quality

images were available for the lysimeter sites are summarized in Table 5.7. While this is

not a totally independent data set (it is from the same region and for the same year), it

does represent 45 separate AVHRR passes over Oklahoma. A summary of the lysimeter

image data used is included in Appendix I.

*Evaluation of Relationships Between Vapor Pressure and AVHRR Data*

Figure 5.5 (a) shows the relationship between vapor pressure and the difference in

the brightness temperatures of channels 4 and 5. The relationship between vapor pressure

and the ratio of the radiance received in channel 5 to the radiance at the surface as

estimated from the SWT equation ($E_5/E_{Ts}$) is shown in Figure 5.5 (b). In both cases there

is a considerable amount of scatter in the relationships. Also there is some clustering of

the data at the lower vapor pressures. The clusters correspond to data taken from the

same images. Under "dry" atmospheric conditions, Coll et al. (1994) note that the other

**Table 5.7: Summary of the time periods for which data was used from the lysimeter sites to evaluate AVHRR vapor pressure and potential ET relationships.**

| Month (1994) | Apache | Goodwell | Marena | Wister | Total per Month |
|---|---|---|---|---|---|
| Feb | 1 | | | 1 | **2** |
| March | 3 | | 2 | 1 | **6** |
| April | 2 | | 1 | 1 | **4** |
| May | 6 | 2 | 2 | 4 | **14** |
| June | 3 | 8 | 5 | 4 | **20** |
| July | 4 | 1 | 5 | 4 | **14** |
| August | 4 | 2 | 5 | 2 | **13** |
| Sept | | 2 | | 1 | **3** |
| **Total/site** | **23** | **15** | **20** | **18** | **76** |

Total number of independent image dates: 45

(a) Vapor pressure versus the difference in channel 4 and 5 brightness temperatures ($T_{b4}$-$T_{b5}$)

Vapor Pressure = 1.14 + 0.44 ($T_{b4}$-$T_{b5}$)

$r^2$ = 0.30

Vapor Pressure (kPa)

- Observed
Regression

($T_{b4}$-$T_{b5}$) (K)

(b) Vapor pressure versus the ratio of radiance received in AVHRR channel 5 to surface radiance ($L_5$/$L_{Ts5}$).

- Observed
Regression

Vapor Pressure (kPa)

Vapor Pressure = 14.0 -13.6($L_5$/$L_{Ts}$)

$r^2$ = 0.315

$L_5$/$L_{Ts5}$
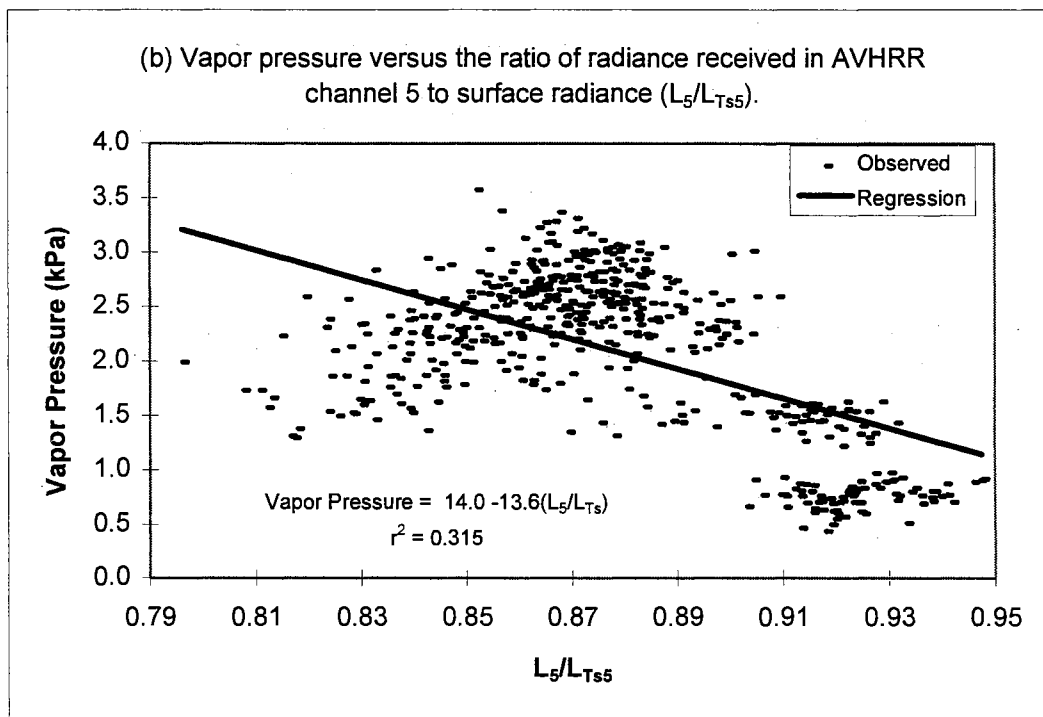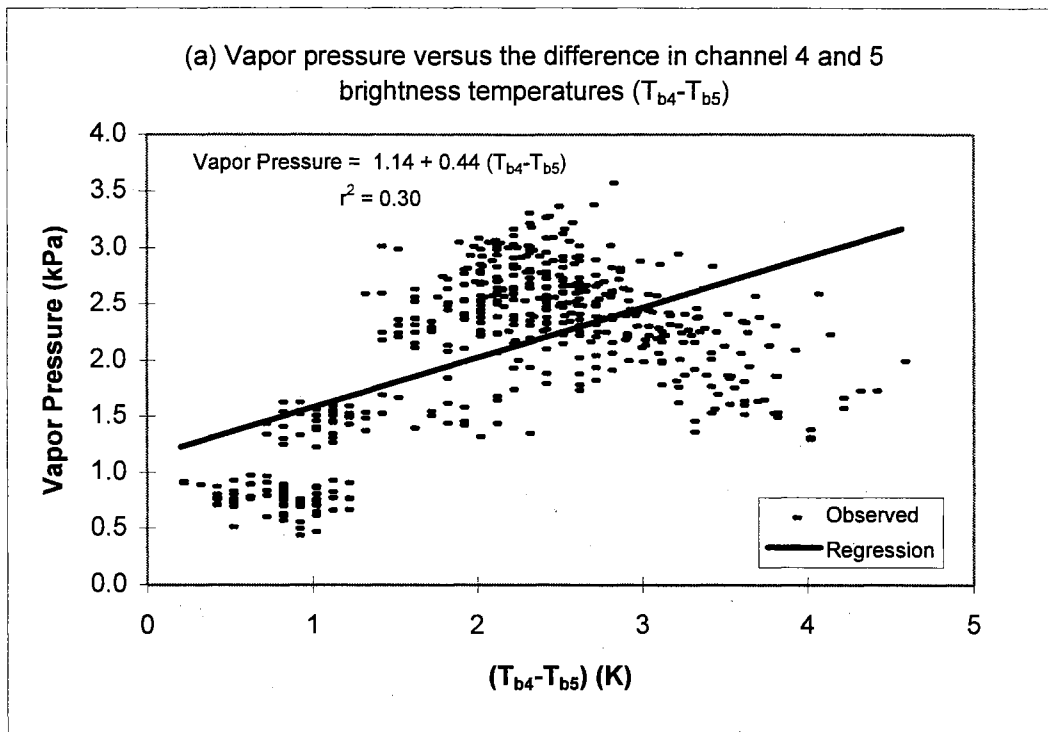
Figure 5.5: Vapor pressure versus (a) the difference in channel 4 and 5 brightness temperatures and (b) the ratio of radiance received in channel 5 to the radiance at the surface.

171

atmospheric gases begin to have a greater impact on the thermal transmittance.

The results of correlating vapor pressure with the extinction coefficient ($k_5$) from Equation 5.13 are presented in Figure 5.6. Note the much stronger correlation with vapor pressure than in Figure 5.5. All of the improvement cannot be necessarily attributed to the effect of emissivity. An emissivity range of 0.94 to 1 was found to minimize the error in the relationship between $k_5$ and vapor pressure. This range is broader than that typically reported in the literature for land surfaces. The fact that NDVI shows a positive correlation with vapor pressure (Table 5.6) is also contributing to the improvement. In addition to errors due to assumptions used to derive the relationships between vapor pressure and the thermal data, the assumption that the attenuation due to water vapor through the entire atmosphere can be related to vapor pressure at the surface also must be remembered.

To further investigate the impact of NDVI on the AVHRR estimate of vapor pressure, NDVI is plotted against both $T_{b4}$-$T_{b5}$ and $L_5/L_{s5}$ in Figure 5.7. The maximum difference in channel 4 and 5 corresponds to low values of NDVI. Low values of NDVI also correspond to low values of $L_5/L_{s5}$. For the same atmospheric conditions, an unaccounted for decrease in surface emissivity would result in an over prediction of surface radiance and thus decrease the ratio. Additionally, the difference in emissivity of channels 4 and 5 tends to increase for sparsely vegetative surfaces (Choudhury et al., 1995). A lower emissivity in channel 4 than in channel 5 would also account for the increase in the difference in brightness temperatures. Beyond emissivity effects, the fact that high surface temperatures and low NDVIs are also associated with dry, bare surfaces is probably contributing to the correlation with vapor pressure.
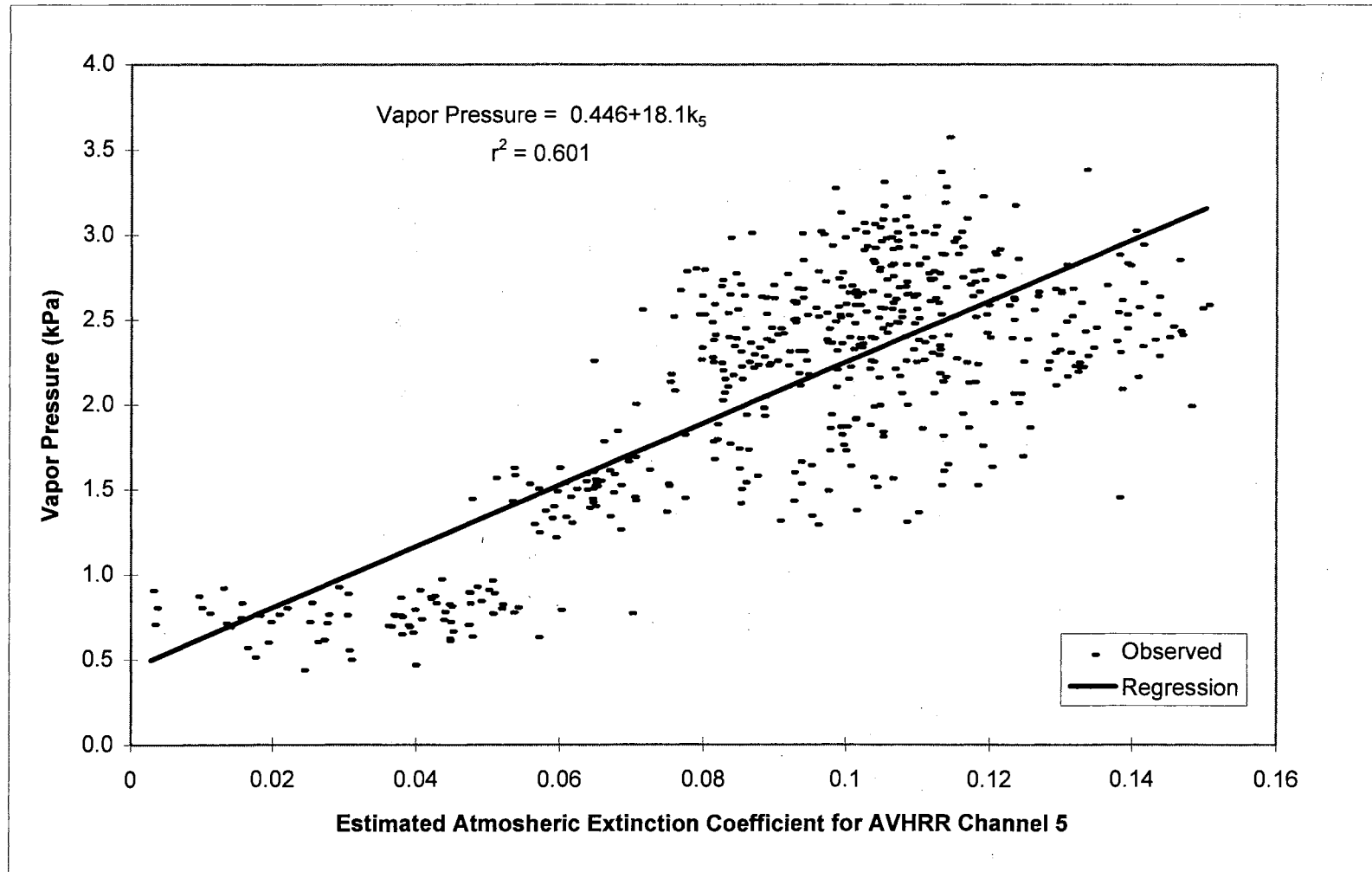
Figure 5.6: Vapor pressure derived from data at various Mesonet sites versus the atmospheric extinction coefficient estimated from Equation 5.13 ($k_5$).
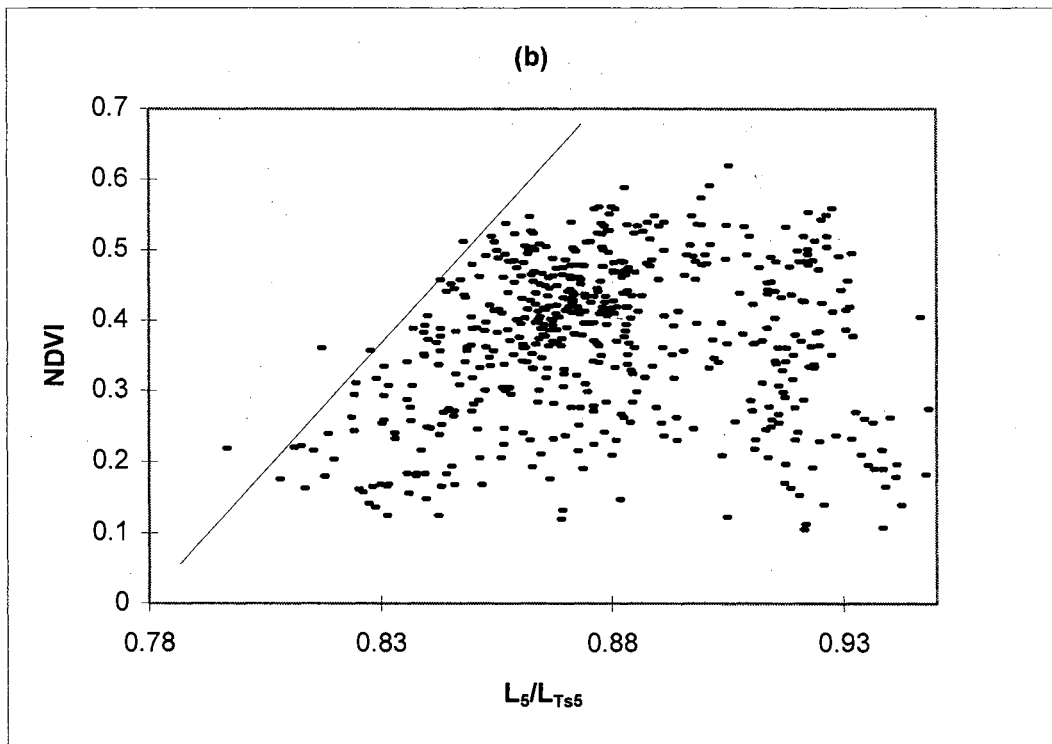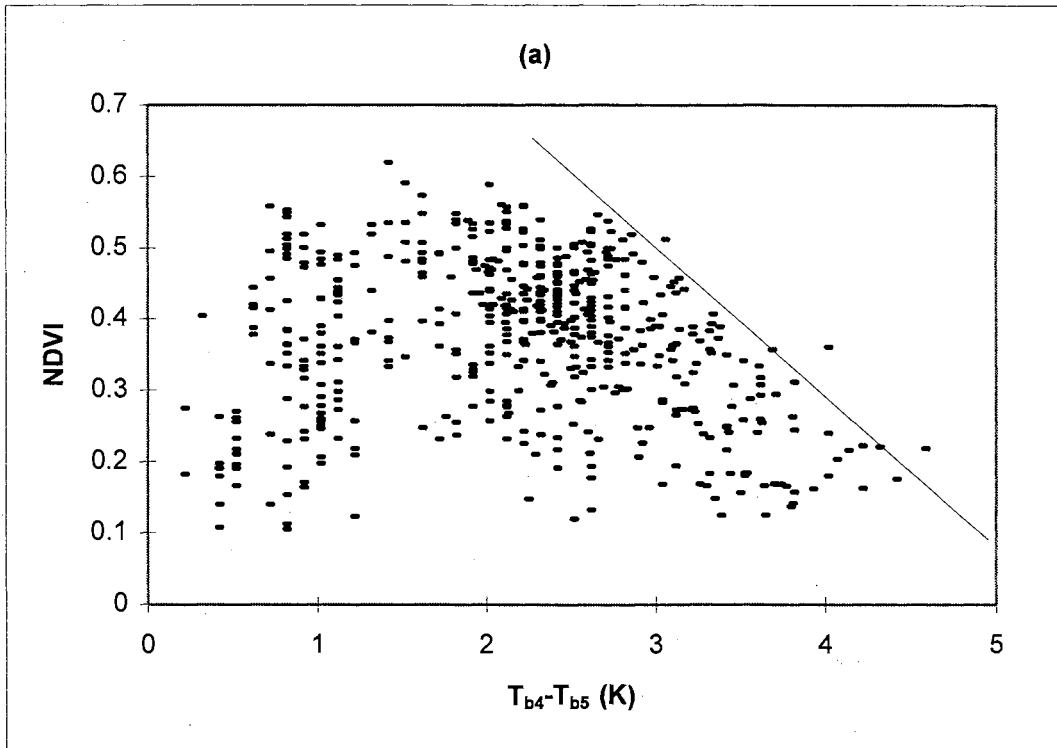
Figure 5.7: NDVI versus (a) the difference in channel 4 and 5 brightness temperature and (b) the ratio of radiance received at the satellite to the estimated surface radiance using descending AVHRR data.

174

Another relationship which has been used to relate the thermal channel data of the AVHRR to atmospheric moisture is the slope of channel 5 versus channel 4 in a 9x9 pixel array (Goward et al., 1994; Jedlovec, 1990). Vapor pressures versus the least squares linear regression slopes are shown in Figure 5.8. The correlation is much lower for this relationship than for either of the previously discussed relationships. Adding the NDVI as an independent variable did increase the $r^2$ to 0.29, but this is still considerably lower than the methods previously considered. One factor that may be contributing to the error is that the slope of the brightness temperatures is sensitive to cloud contamination. If only one or two pixels in the array are partially contaminated, the value can be significantly altered. For this comparison, only the pixels predicted to be centered on the Mesonet sites were cloud screened and not the other pixels in the 9x9 array.

A summary of the evaluation statistics for each of the relationships previously discussed is included in Table 5.8. Also included are the least squares regression parameters used to relate the AVHRR derived information to physical units of vapor pressure. Note that the atmospheric extinction coefficient for channel 5 estimated by Equation 5.13 explains almost twice the variation in vapor pressure than the other relationships considered. Additionally, the RMSE is reduced by about 0.15 kPa compared to the other relationships.

The relationship derived using the data shown in Figure 5.6 is:

$$VP_{AVHRR} = 0.445 + 18.1\, k_5 \qquad\qquad (5.20)$$

where $VP_{AVHRR}$ is the estimated vapor pressure (kPa) and $k_5$ is the extinction coefficient for AVHRR channel 5. Vapor pressure was estimated for the AVHRR data
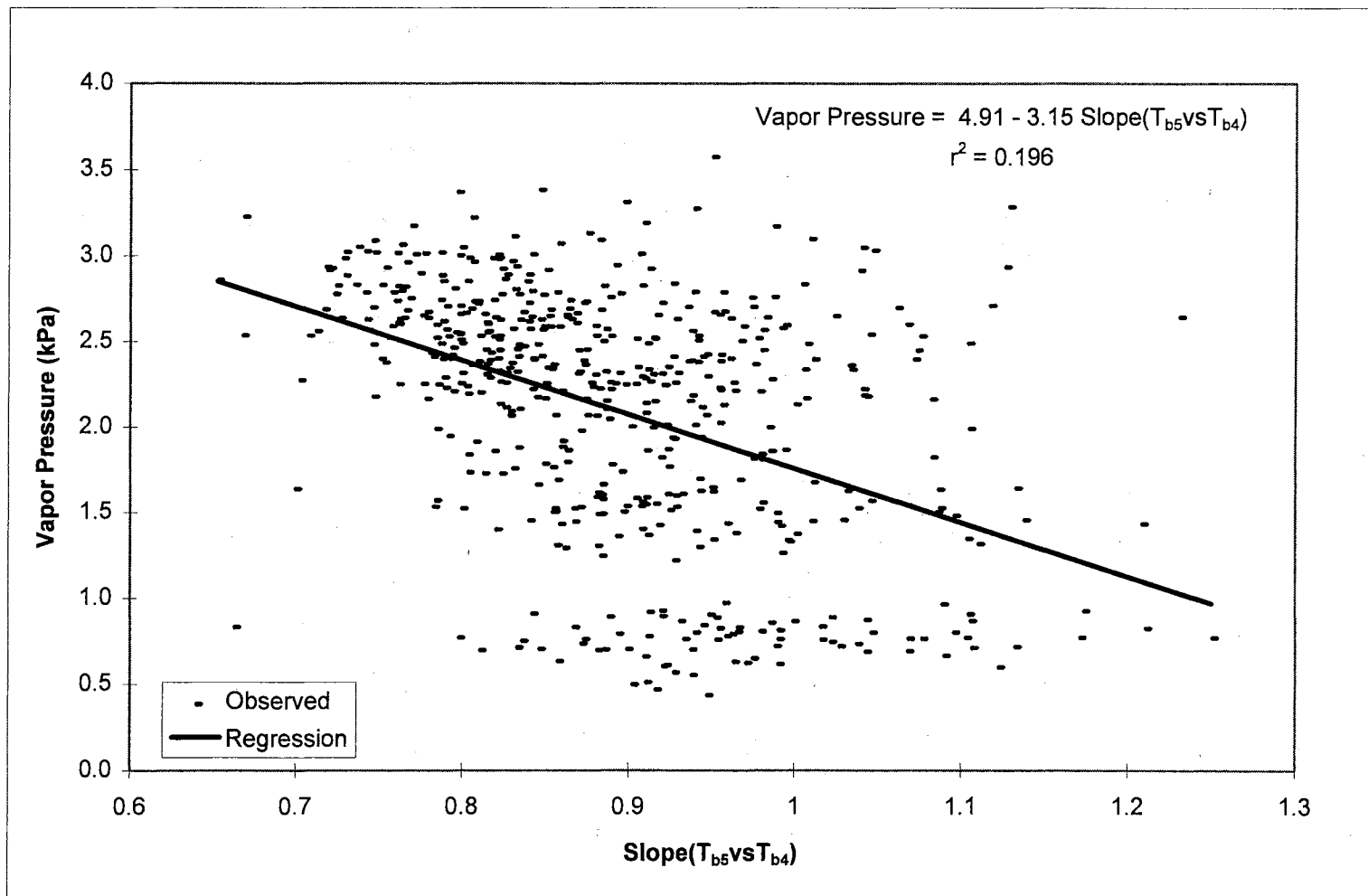
Figure 5.8: Vapor pressure versus the slope of channel 5 versus channel 4 brightness temperatures in a 9x9 pixel array ($SlopeT_{b5}vsT_{b4}$) using data from the afternoon images listed in Table 5.2.

**Table 5.8: Summary of evaluation statistics for the relationships considered in the development of estimates of potential ET from AVHRR data.**

| Relationship [a] | n [b] | Regression Between AVHRR value and Ground-Based Value [c] | | | | MAD [d] | RMSE | Units [e] |
|---|---|---|---|---|---|---|---|---|
| | | $r^2$ | $STD_{err}$ | $A_r$ | $B_r$ | | | |
| $VP_{AVHRR} = 1.14 + .44\ (T_{b4}-T_{b5})$ | 537 | 0.30 | 0.33 | 1.47 | 0.30 | 0.51 | 0.61 | kPa |
| $VP_{AVHRR} = 4.91-3.15\ Slope(T_{b5}vsT_{b4})$ | 537 | 0.20 | 0.29 | 1.69 | 0.20 | 0.51 | 0.65 | kPa |
| $VP_{AVHRR} = 15.0 - 13.6(L_5/L_{Ts})$ | 537 | 0.32 | 0.34 | 1.40 | 0.32 | 0.50 | 0.60 | kPa |
| $VP_{AVHRR*} = .445 + 18.1\ k_5$ | 537 | 0.60 | 0.36 | 0.60 | 0.84 | 0.38 | 0.46 | kPa |
| | 76 | 0.74 | 0.34 | 0.54 | 0.77 | 0.33 | 0.39 | kPa |
| $VP_{oAVHRR} = f(T_s)$ (Equation 5.22) | 537 | 0.87 | 0.67 | -0.15 | 1.23 | 0.99 | 1.22 | kPa |
| | 76 | 0.90 | 0.62 | -0.19 | 1.28 | 1.12 | 1.35 | kPa |
| $VPD_{AVHRR} = VP_{oAVHRR} - VP_{AVHRR*}$ | 537 | 0.80 | 0.68 | 1.25 | 1.22 | 1.86 | 1.99 | kPa |
| | 76 | 0.86 | 0.56 | 0.27 | 1.24 | 1.00 | 1.23 | kPa |
| $ET_{opm} = 2.10 + 0.912\ VPD_{AVHRR}$ | 537 | 0.72 | 0.73 | 0.72 | 1.76 | 0.61 | 0.86 | mm d$^{-1}$ |
| | 76 | 0.77 | 0.79 | 1.06 | 0.76 | 0.82 | 0.99 | mm d$^{-1}$ |
| $ET_{oharg} = 0.439 + .155\ T_s$ | 537 | 0.76 | 0.49 | 1.38 | 0.76 | 0.45 | 0.55 | mm d$^{-1}$ |
| | 76 | 0.88 | 0.41 | 1.20 | 0.77 | 0.45 | 0.55 | mm d$^{-1}$ |

**Table 5.8 Continued.**

[a] Notation used in relationships: $VP_{AVHRR}$ is vapor pressure estimated from AVHRR data; $VP_{AVHRR*}$ indicates the vapor pressure relationship used to calculate VPD; $T_{b4}$ - $T_{b5}$ are the difference in brightness temperatures (K) of channels 4 and 5; $Slope(T_{b5}vsT_{b4})$ is the slope of AVHRR channel 5 versus channel 4 brightness temperatures in a 9x9 pixel array centered on the point of interest; $L_5/L_{Ts}$ is the ratio of radiance received at the satellite to estimated surface radiation in channel 5; $k_5$ is the estimated atmospheric extinction coefficient for channel 5; $VP_{oAVHRR}$ is estimated saturated vapor pressure; $T_s$ is AVHRR estimated surface temperature (°C); $VPD_{AVHRR}$ is the estimated vapor pressure deficit; $ET_{opm}$ is AVHRR estimated Penman-Monteith potential ET; and $ET_{oharg}$ is AVHRR estimated Hargreaves potential ET.

[b] Number of observations used. Lines with 537 indicate data for various Mesonet sites are used, while 76 indicates data is limited to the four lysimeter sites.

[c] Regression results for the equation (AVHRR Estimate) = $A_r$ + $B_r$ (Ground-based Estimate), where $r^2$ is the coefficient of determination for the relationship and $STD_{err}$ is the standard error.

[d] MAD is the Mean Absolute Difference between the ground-based and AVHRR estimate, and RMSE is the Root-Mean Squared Error.

[e] Units apply to $A_r$, $STD_{err}$, MAD and RMSE. All other values are dimensionless.

corresponding to the lysimeter locations using Equation 5.20. Figure 5.9 is a plot of the resulting AVHRR estimated vapor pressure and vapor pressure derived from ground-based measurements. Note that no additional calibration of the emissivity range was conducted or of the relationship between vapor pressure and $k_5$. From Figure 5.9 and the evaluation statistics in Table 5.8, it appears the relationship between $k_5$ and vapor pressure is maintained with this data set. These results are used to further examine relationships between AVHRR data and potential ET in the next section.

**Use of AVHRR Data in the Estimation of Potential Evapotranspiration**

In Chapters 2 and 3, it was noted that several inputs can be required to obtain an estimate of potential ET. In the following section, the relationships between potential ET and AVHRR data are considered.

Methods

Potential ET was calculated for each of the Mesonet sites from the Penman-Monteith equation using the REF-ET program as previously discussed in Chapter 3. Note that the term "potential" is used here rather than "reference". The equations used are for reference ET; however, the Mesonet sites are not maintained at reference conditions. As the sites are non-irrigated, the ET calculated with data from these sites will tend to over estimate reference ET in dry conditions.

In addition to the Penman-Monteith potential ET, the temperature based potential ET method of Hargreaves and Samani (1985) was considered. The Hargreaves and Samani (1985) equation can be expressed as:

179
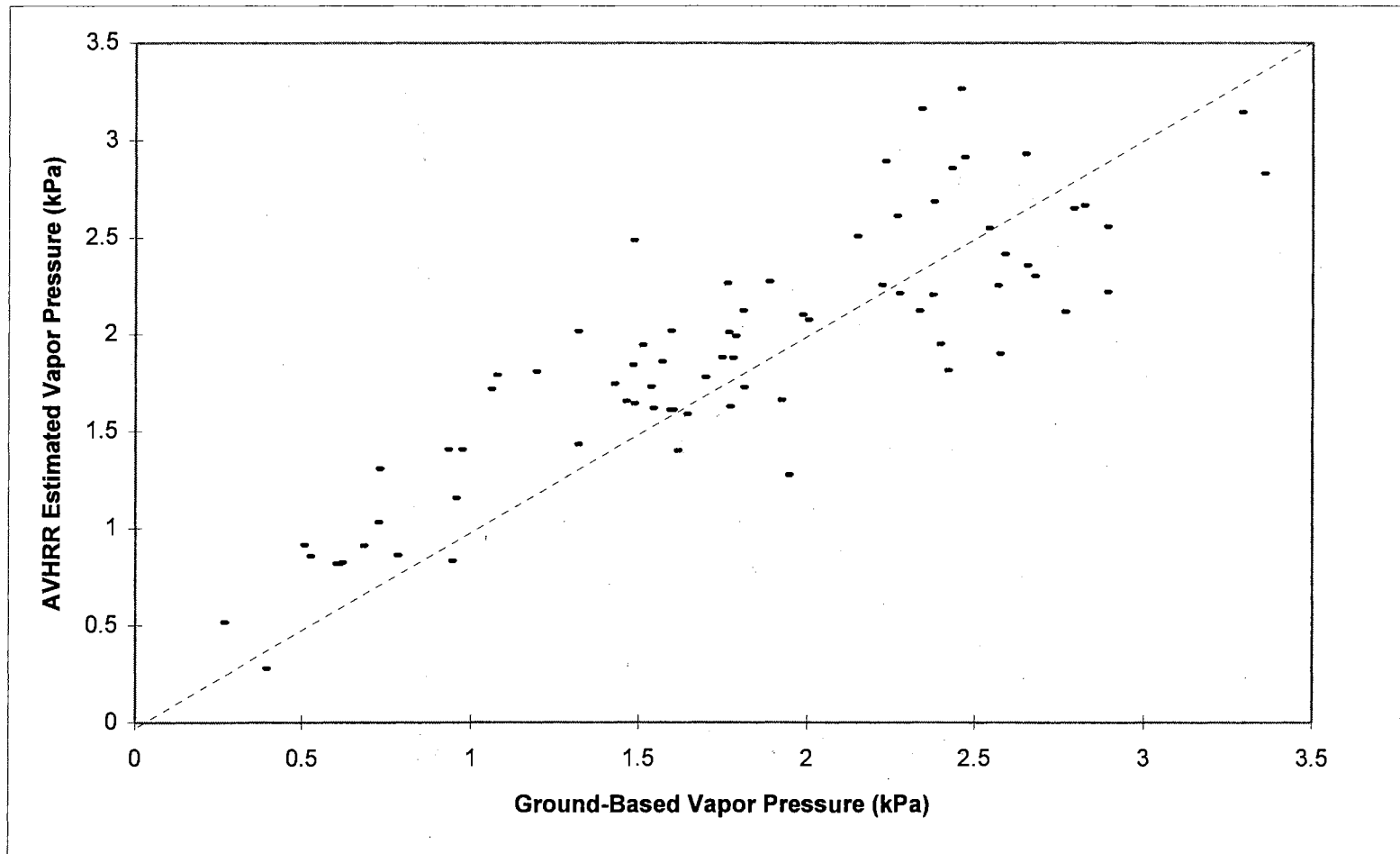
Figure 5.9: Comparison of the vapor pressure estimated from AVHRR data (Equation 5.20) and vapor pressure calculated from air temperature and relative humidity at the four lysimeter sites. The dashed line indicates a 1 to 1 relationship.

$$ET_{ref} = 0.0023 Ra\,TD^{0.5}(T_a + 17.8) \qquad (5.21)$$

where Ra is extraterrestrial radiation (evaporation units), TD is the difference between mean monthly maximum and mean monthly minimum air temperature ($^{o}$C) and $T_a$ is the air temperature ($^{o}$C). The only variable for a given time period and location is air temperature.

Vapor pressure alone is a not a good indicator of potential ET. Instead, the vapor pressure deficit is typically used as a partial indicator of the atmosphere's ability to transfer moisture from the surface. A vapor pressure deficit of 0 would indicate that the atmosphere can hold no more moisture for the given temperature. In order to derive an estimate of the vapor pressure deficit (VPD) using only the satellite data, the saturated vapor pressure was calculated from the satellite estimated surface temperature as:

$$VP_{oAVHRR} = \exp(\frac{16.78\,T_s - 116.9}{T_s + 237.3}) \qquad (5.22)$$

where $VP_{oAVHRR}$ is the satellite estimated saturated vapor pressure and $T_s$ is the satellite derived surface temperature. The AVHRR derived vapor pressure difference was then calculated as the difference between the results from Equation 5.22 and Equation 5.20.

The sufficiency of the AVHRR derived vapor pressure deficit for determining estimates of potential ET was evaluated by comparison with the Penman-Monteith calculated potential ET. Likewise, the use of the AVHRR derived surface temperature was compared to potential ET from the Hargreaves equation to evaluate its promise for use in temperature based estimates of potential ET. The relationships were first

181

calibrated using the AVHRR data for the afternoon time periods listed in Table 5.2. The calibrated relationships were then evaluated using the AVHRR data set corresponding to the individual lysimeter sites (Table 5.7). Evaluation statistics of the same form used in the investigation of the vapor pressure estimates were used for the comparison of the AVHRR data and potential ET.

<u>Results</u>

Figure 5.10 is a comparison of VPD calculated from the satellite data versus the VPD calculated from the ground-based data. Comparisons are shown using both the 10 images with automated location of the Mesonet sites (a) and the data extracted for each of the lysimeter sites from a collection of 45 independent images (b). Note in both cases, the satellite data typically over predicted the VPD. Most of the over prediction is directly related to the fact that SWT derived surface temperatures were higher than air temperatures, thus increasing the satellite estimated saturated vapor pressure. The over prediction of saturated vapor pressure is reflected in the $B_r$ statistic of Table 5.8. However, in both data sets, the over prediction is fairly consistent as vapor pressure increases.

Figure 5.11 (a) is a comparison between the same satellite derived VPD shown in Figure 5.10 and potential ET estimated by the Penman-Monteith equation. The residuals of the relationship were correlated with wind speed (r = 0.55). The increase in deviation from the regression line for a higher VPD can especially be attributed to wind speed. Under these conditions, the potential ET rate is not limited by the ability of the atmosphere to hold moisture, but is limited by the rate moisture can be transferred from
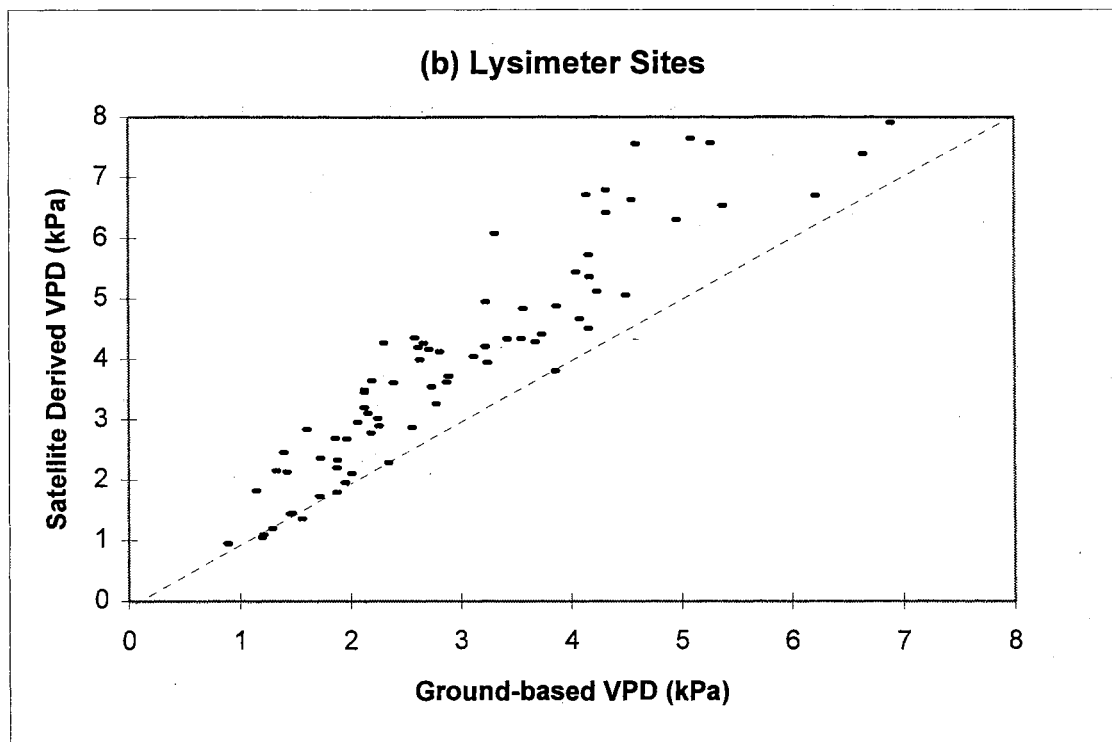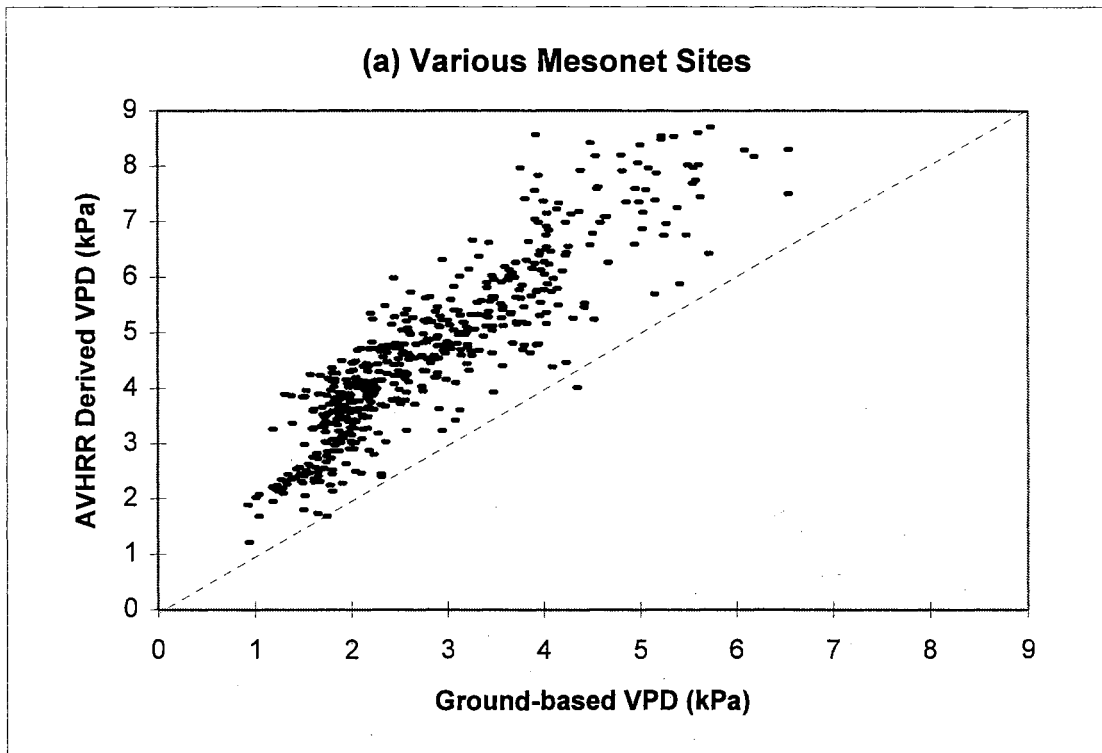
Figure 5.10: AVHRR derived vapor pressure deficit (VPD) versus ground-based VPD for (a) data at various Mesonet sites for the dates in Table 5.2 and (b) data at the four lysimeter sites.
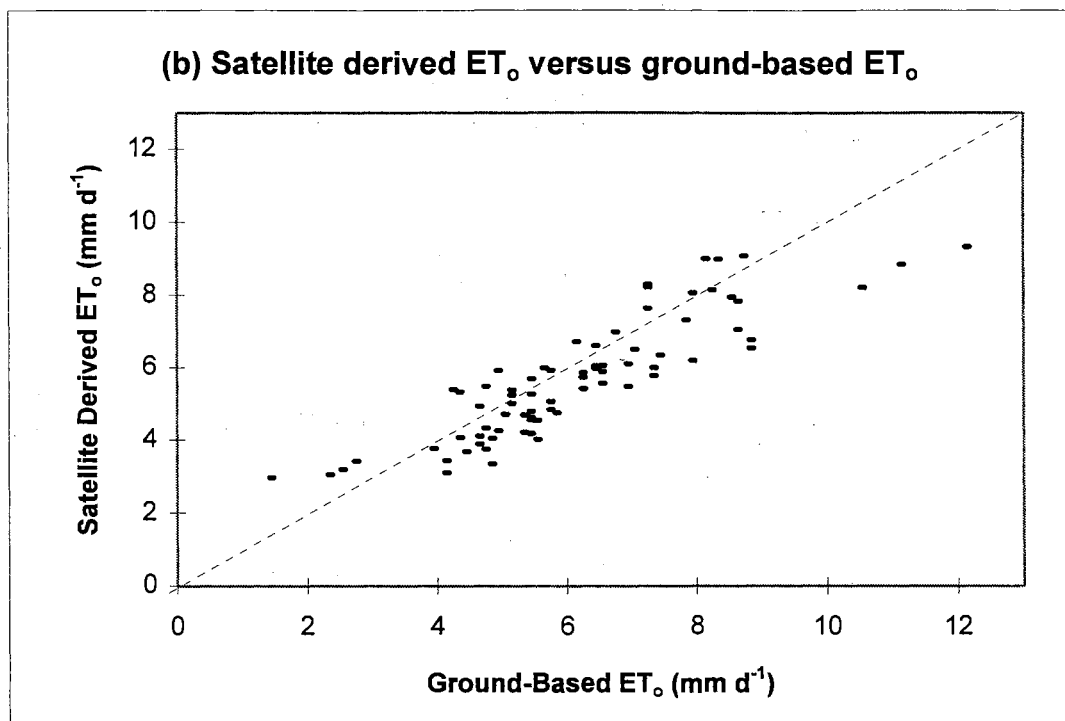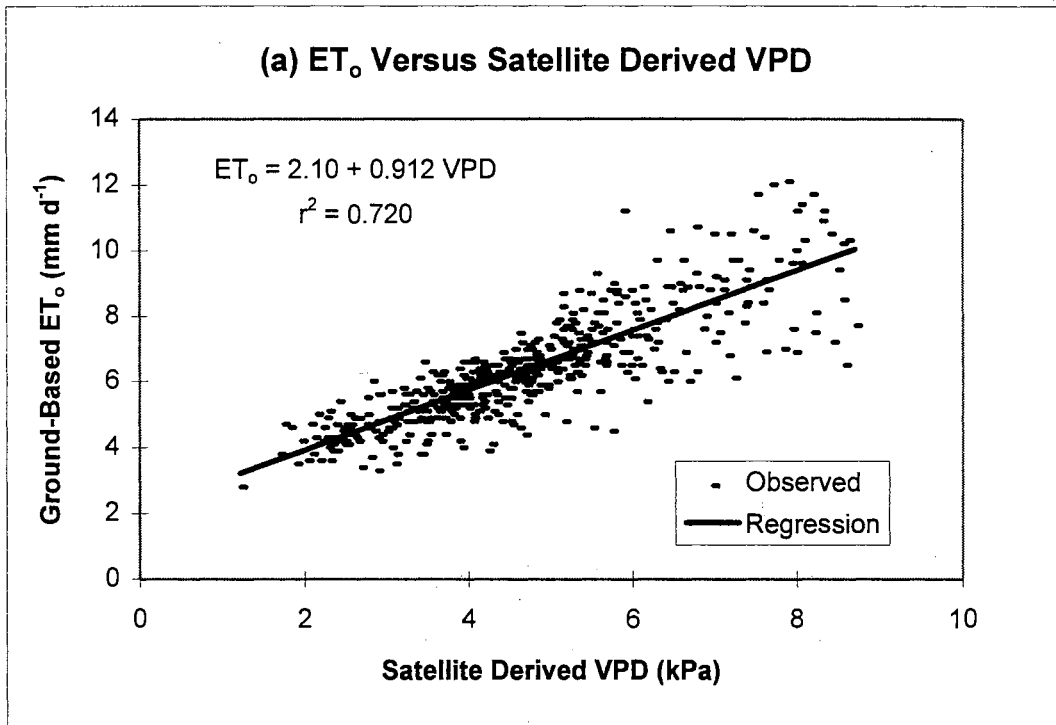
Figure 5.11: (a) Penman-Monteith calculated potential ET (ET$_o$) from ground-based observations versus the AVHRR derived vapor pressure deficit (VPD) for dates listed in Table 5.2 at various Mesonet sites and (b) AVHRR derived ET$_o$ using the relationship shown in (a) versus ground-based ET$_o$ for data at the lysimeter sites.

the surface. The data depicted in Figure 5.11 was used to derive the expression:

$$ET_{opmAVHRR} = 2.10 + 0.912 \ VPD_{AVHRR} \qquad (5.23)$$

where $ET_{opmAVHRR}$ is the estimate of potential ET (mm day$^{-1}$) from the VPD (kPa) derived from AVHRR data.

Equation 5.23 was applied to the image data for the lysimeter sites, with the results shown versus the Penman-Monteith potential ET calculated from ground-based measurements in Figure 5.11 (b). With the exception of the higher potential ET rates (> 10 mm day$^{-1}$), Equation 5.23 provides reasonable results for this data set. The three points correspond to the Goodwell site for days in June when the average daily wind speed at 2 m ranged from 6 to 7 m s$^{-1}$.

The relationship between satellite derived surface temperature and the Hargreaves calculated potential ET is shown in Figure 5.12 (a). The correlation is directly related to the fact that the Hargreaves equation is essentially a temperature based method and the surface temperatures are highly correlated with air temperature. Another factor contributing to the high correlation is that the time of satellite over pass corresponds to times of maximum air temperature. The Hargreaves potential ET is related to AVHRR surface temperature by:

$$ET_{ohargAVHRR} = 0.439 + 0.155 \ T_s \qquad (5.24)$$

where $ET_{ohargAVHRR}$ is the AVHRR estimate of the Hargreaves potential ET (mm d$^{-1}$) and $T_s$ is the AVHRR derived surface temperature ($^{o}$C). The potential ET from Equation 5.24 is plotted against the Hargreaves potential ET from ground-based estimates in Figure 5.12 (b). There is a consistent trend about the 1 to 1 line for this data set, indicating that the

**(a) Hargreaves ET$_o$ versus satellite derived surface temperature**

$ET_o = 0.439 + 0.155\ T_s$

$r^2 = 0.762$

- Ground-based
- Regression

ET$_o$ (mm d$^{-1}$)

Satellite Derived Surface Temperature ($^\circ$C)

**(b) Satellite derived ET$_o$ versus ground-based ET$_o$**

Satellite Derived ET$_o$ (mm d$^{-1}$)

Ground-Based ET$_o$ (mm d$^{-1}$)
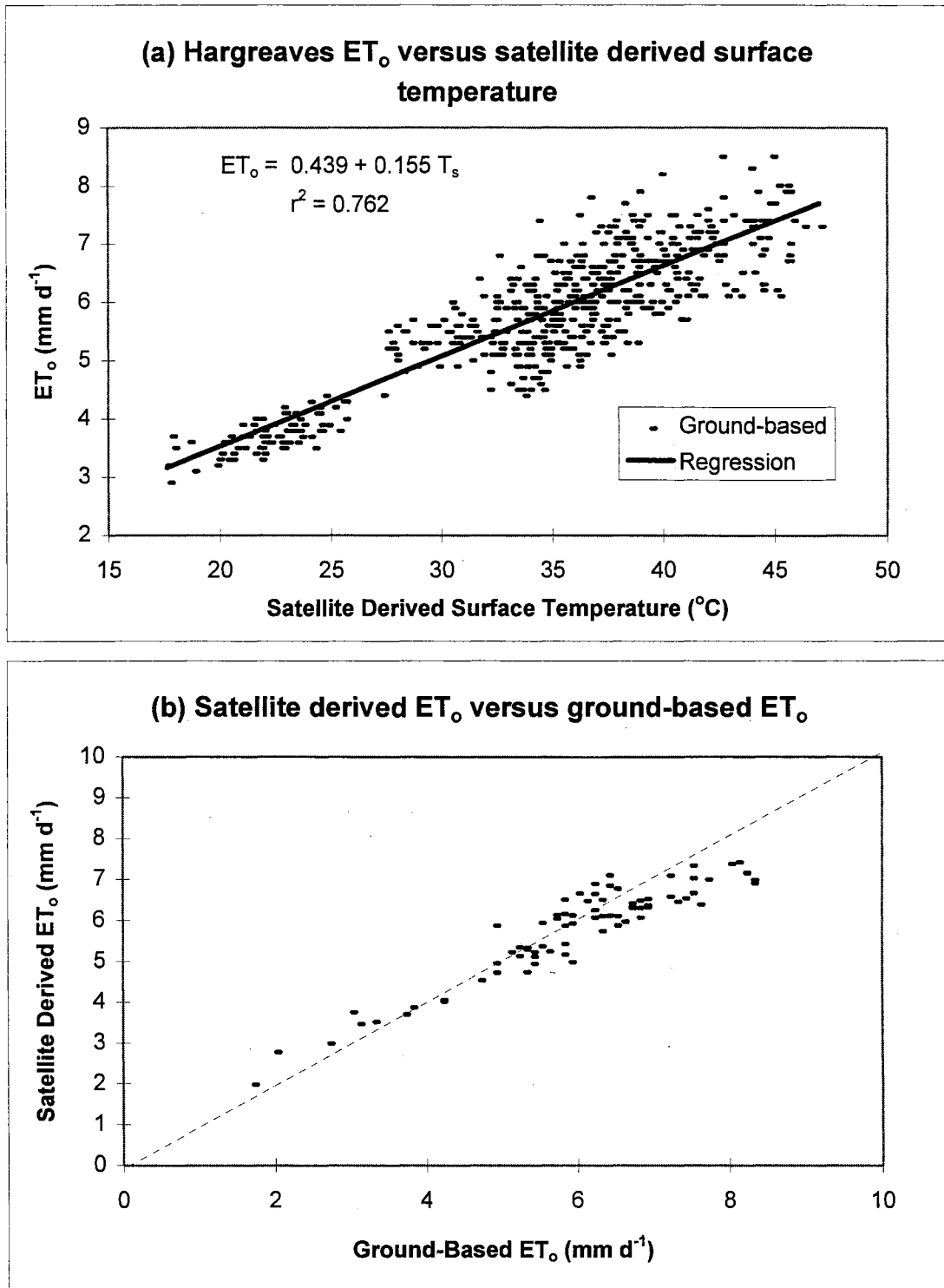
Figure 5.12: (a) Hargreaves calculated potential ET (ET$_o$) from ground-based observations versus AVHRR derived vapor pressure deficit (VPD) for dates listed in Table 5.2 at various Mesonet sites and (b) AVHRR derived ET$_o$ using the relationship shown in (a) versus ground-based ET$_o$ for data at the lysimeter sites.

calibration remains valid for this data set.

Evaluation statistics for the relationships depicted in Figures 5.10 to 5.12 are provided in Table 5.8. As noted, the fact that AVHRR derived surface temperatures were higher than air temperatures leads to an over prediction of saturated vapor pressure from the AVHRR data. This is reflected by the $B_r$ statistic greater than 1 and the larger MAD and RMSE values for saturated vapor pressure ($VP_o$). This leads to the same effect in the VPD; however, the trend is consistent enough, that much of the error is removed in the calibration to potential ET.

It does appear that fairly accurate estimates ($\pm$ 1 mm) of potential ET can be derived from the AVHRR data. The factors contributing to the relationships between the AVHRR data and potential ET are probably more inclusive than the independent variables considered. For example, seasonal variations in the weather observations exhibit correlation. In the winter time, air temperatures, potential solar radiation, and vapor pressure will be typically lower than in the summer months.

The value of estimates of potential ET is somewhat limited, as the actual ET rate is very dependent on soil moisture conditions. However, integration of AVHRR data with Geographic Information Systems containing data on land and crop type as has been done by Wade et al. (1994) would increase the value of these estimates. Additionally, work by those such as Bausch (1995) to relate spectral measurements to crop coefficients would allow for an estimate of actual ET. These estimates could also be integrated with other large scale models of the environment.

# Comparison of the AVHRR Data and Actual ET

Two methods were used to evaluate the relationships between AVHRR data and actual ET. The first was to follow an energy balance approach, primarily using relationships reported in the literature, with AVHRR data used to estimate as many of the inputs as possible. Based on the results of this investigation, the form of the energy balance equation was used as a starting point to examine empirical relationships that minimize ground-based data.

## Energy Balance Approach

The surface energy balance introduced in Equation 2.1 has been used to obtain estimates of actual evapotranspiration (Feddes et al. (1993), Kustas et al. (1994) and Moran et al. (1989)). First the development of the energy balance equations used is presented, followed by an evaluation of the relationships.

### Theoretical Development

The surface energy balance from Equation 2.1 (flux towards the surface is negative) can be solved so that ET is the residual such that:

$$\lambda ET = -R_n - H - G \tag{5.25}$$

where $\lambda$ is the latent heat of vaporization ($\sim 2.45$ MJ (kg water)$^{-1}$). Net radiation flux ($R_n$) is partitioned in the following manner:

$$R_n = -(1-\alpha) R_{sw} - \varepsilon_{at} \sigma T_a^4 + \varepsilon_s \sigma T_s^4 \tag{5.26}$$

where the short-wave components are described by $\alpha$, the short-wave surface albedo, and $R_{sw}$, the short-wave solar radiation incident at the surface (W m$^{-2}$). Long-wave sky emittance (W m$^{-2}$) is represented by the terms $\varepsilon_a \sigma T^4_a$, where $\varepsilon_{at}$ is the apparent emissivity of the atmosphere (dimensionless), $\sigma$ is the Stefan-Boltzman constant (W m$^{-2}$ K$^{-4}$), and $T_a$ is air temperature (K). The long-wave surface emittance (W m$^{-2}$) is given by $\varepsilon_s \sigma T^4_s$ where $T_s$ is the surface temperature (K), and $\varepsilon_s$ is land surface emissivity.

In order to apply Equation 5.26 with the available data, the net short wave component was determined by using the measured daily total solar radiation from the pyranometer measurements at each site and satellite estimated surface albedo. Albedo estimates from the AVHRR were calculated based on a relationship by weighting the reflectance in the reflective channels according to the incoming solar irradiance as given by Di and Rundquist (1994):

$$\alpha = 0.322 R_{b1} + 0.678 R_{b2} \qquad (5.27)$$

where $R_{bn}$ is the reflectance in channel n adjusted for bi-directional effects. The bi-directional adjustment was accomplished by the equation:

$$R_{bn} = C_{bn} + (R_{iqn} - R_{fitn}) \qquad (5.28)$$

where $C_{bn}$ is the constant of Equation 4.19 from Table 4.7, $R_{iqn}$ is the apparent reflectance in the spectral range of channel n corrected for the atmosphere effects using Iqbal's methods, and $R_{fitn}$ is the reflectance predicted from Equation 4.19 with the appropriate coefficients from Table 4.7. The constant of Equation 4.19 represents the average reflectance for a nadir viewing angle. Equation 5.28 assumes that deviations from the reflectance predicted by

Equation 4.19 represent true changes in surface conditions, not from viewing angle effects. While this correction is only approximate, it does remove much of the variation in apparent reflectance introduced by the viewing conditions.

Estimates of the long wave component of Equation 5.26 were determined using the measured air temperature at 1.5 m at the time of satellite over pass and the satellite derived surface temperature. An estimate of the long-wave sky emittance was taken from Jensen et al. (1990) as:

$$\varepsilon_{at} = 0.7 + \frac{59.5}{10^5} e \exp(\frac{1500}{T_a})$$ (5.29)

where e is the vapor pressure (kPa) and $T_a$ is the air temperature (K). Values of surface emissivity were estimated from the NDVI as described by Equation 5.12.

In order to obtain daily estimates of the net long wave radiation, the components are assumed to follow a solar trend. From Jackson et al. (1983), for cloud free conditions, a daily measurement ($M_d$) can be related to an instantaneous measurement (Mi) by:

$$M_d = M_i \frac{2N}{\pi \sin(\pi t / N)}$$ (5.30)

where N is day length which can be calculated as a function of latitude and day of the year (Iqbal, 1983) and t is the time past sunrise the measurement was taken.

An approximation of soil heat flux is related to the NDVI and net radiation using a relationship from Jackson et al. (1987) which can be expressed as:

$$G = -R_n 0.538 \exp(-2.31 NDVI_{iq})$$ (5.31)

where $R_n$ is the daily estimate of net radiation obtained from the previous relationships, and

190

$NDVI_{iq}$ is the NDVI derived from reflectance atmospherically corrected by the methods of Iqbal (1983).

Sensible heat flux is given by:

$$H = \frac{\rho_a c_p}{r_{ah}}(T_s - T_a) \qquad (5.32)$$

where, $\rho_a$ is air density (assumed a constant 1.23 kg m$^{-3}$), $c_p$ is the specific heat of air at constant pressure (assumed constant at 1.0046 J kg$^{-1}$ K$^{-1}$), and $r_{ah}$ is the mean turbulent resistance to heat transfer (s m$^{-1}$). Several expressions have been used for the mean turbulent resistance (Rosenberg et al. 1983; Feddes et al.,1993). The resistance term is analogous to resistance in Ohm's law in that heat flux will increase as the resistance term decreases. An approximation of the resistance term was calculated as:

$$r_{ah} = \frac{1}{k^2 u}[\ln(\frac{z - 0.667NDVI_{iq}d}{0.11NDVI_{iq}d})]^2 \qquad (5.33)$$

where k is von Karman's constant (0.41), z is the height of the wind speed measurements (2 m), $NDVI_{iq}$ is the NDVI based on atmospherically corrected reflectance of Iqbal (1983), d is an effective displacement height and u is wind velocity (m s$^{-1}$). The use of the NDVI to provide an estimate of the resistance term is based on the assumption that as the NDVI increases, the roughness of the surface will also increase (Tarpley, 1994).

As noted in Chapter 4, there was a total of 46 site-days on which both quality images were available and the lysimeters were providing reliable data. Because the sample size for a particular site is relatively small, the value of d was determined iteratively by minimizing the error sum of squares between the ET predicted by the

energy balance and area weighted ET at all sites. The units used in the energy balance analysis were MJ m$^{-2}$ d$^{-1}$; however, the results of the ET estimates were converted to mm d$^{-1}$ assuming a constant latent heat of evaporation of 2.45 MJ per kg of water.

*Results of the Energy Balance Method*

The value of d found to minimize the error sum of squares was 0.6 cm, much smaller than expected (discussed later). The predicted ET from the energy balance approach, and the estimated area ET are shown plotted for each day by site in Figure 5.13. The predicted ET is also plotted versus area-weighted ET in Figure 5.14. The estimated area ET is also shown for comparison purposes. In general, the predicted ET follows the same trends as the area weighted ET. The coefficient of determination between the area weighted ET and the energy balance ET was 0.66 with a RMSE of 0.98 mm d$^{-1}$. Many of the days on which the predicted ET and ET$_{area}$ show the greatest departures correspond to solar zenith angles greater than 60° at the time of satellite overpass (Apache: days 69, 74, 187, 221, 237; Wister days 102, 180). One factor previously discussed is the potential error in the reflectance estimates due to viewing geometry. Any error in reflectance will impact the estimates of albedo and NDVI. Additionally, for higher solar zenith angles, the relationship between surface and air temperature at these times may not accurately be represented by the solar cycle.

There was no apparent explanation for the deviations between the area weighted and energy balance ET for the Goodwell site. Some of the variation may be attributed to error in precisely locating the site, and the heterogeneous nature of the surface due to irrigated agriculture in the area. For example on day 175 the NDVI was 0.348 and it was
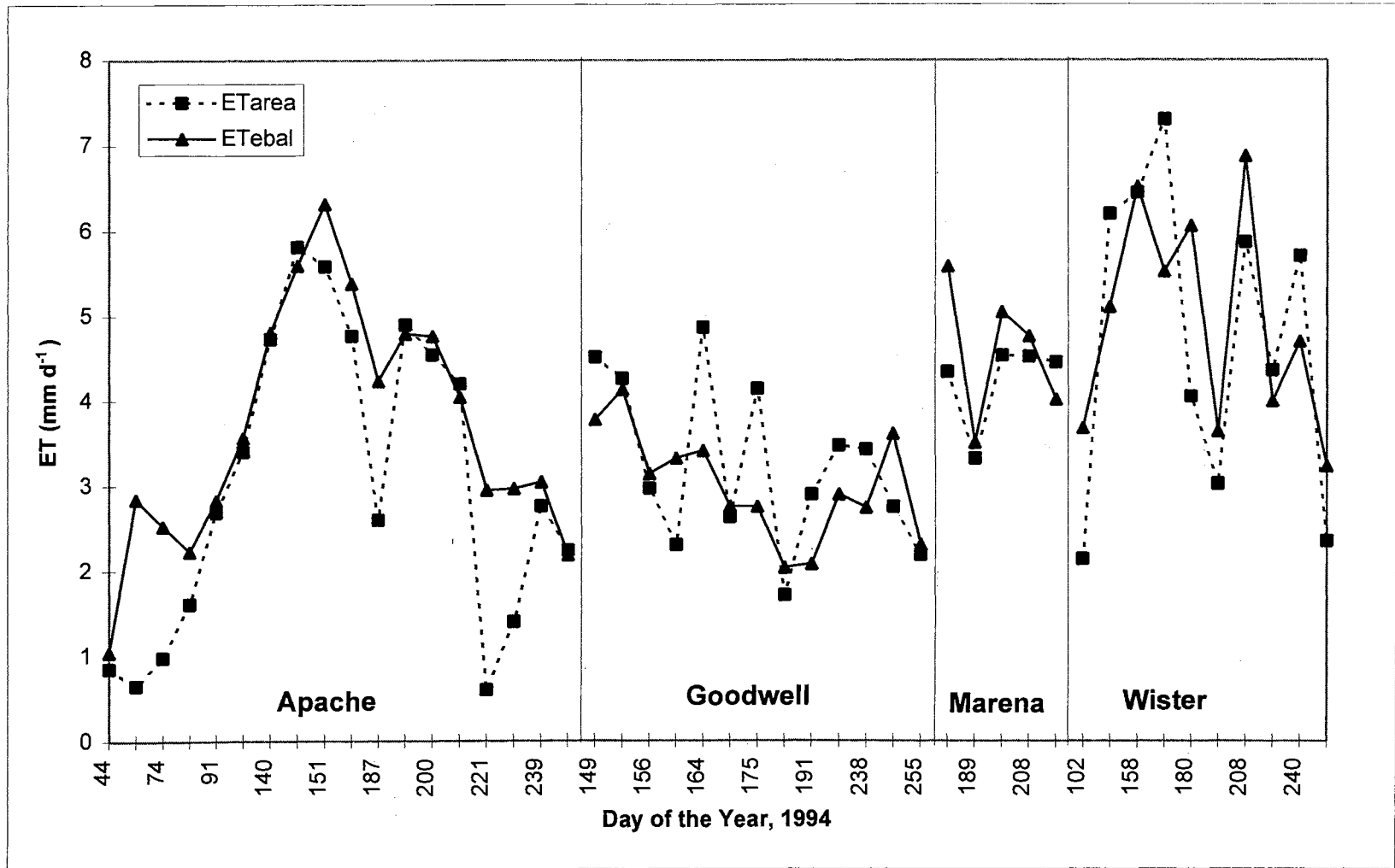
Figure 5.13: Comparison of ET predicted by the full-input energy balance ($ET_{ebal}$) and area weighted ET ($ET_{area}$) at the four lysimeter sites for dates on which quality data was available during 1994.
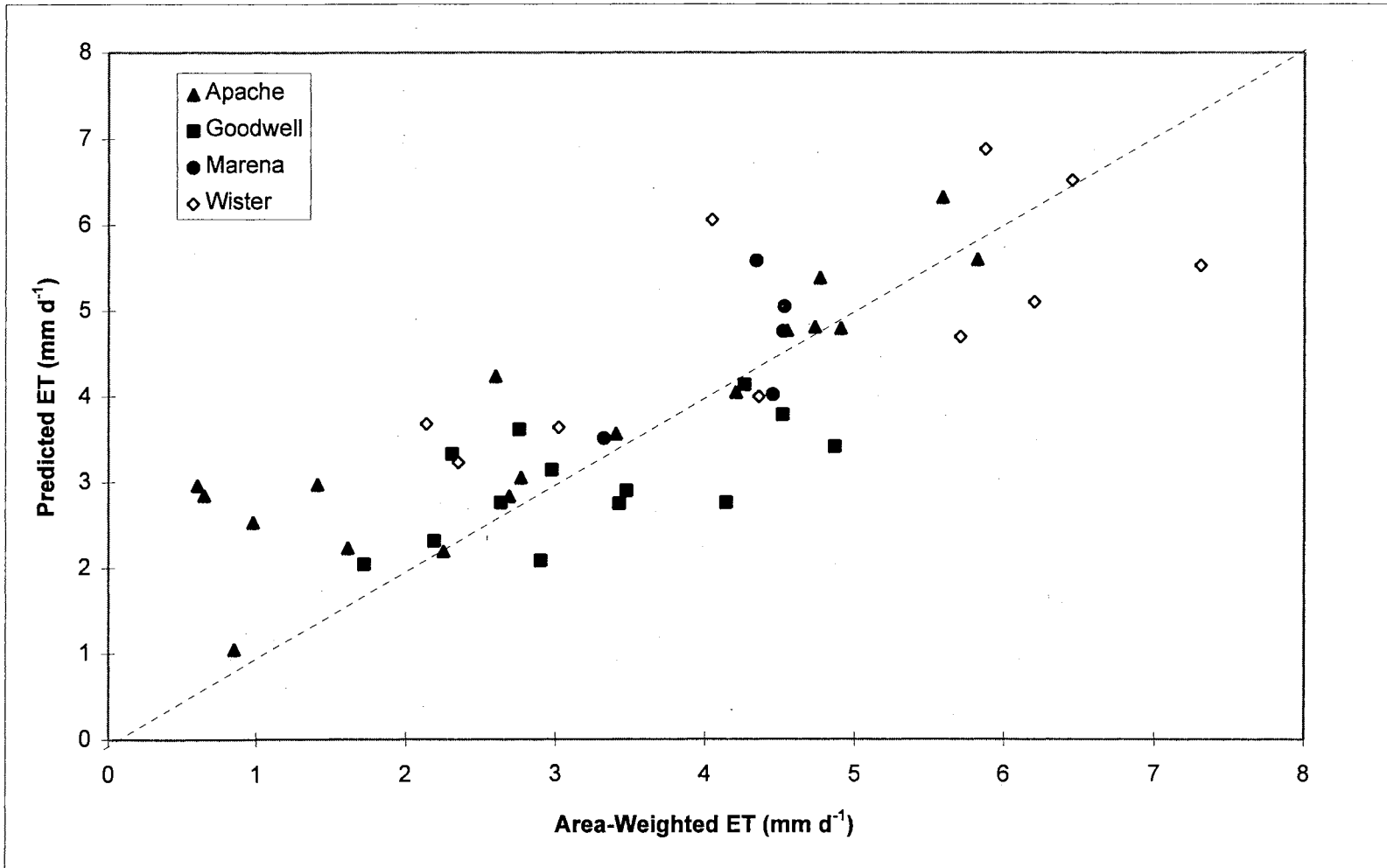
Figure 5.14: ET predicted by the full-input energy balance method versus area weighted ET. The dashed line represents a 1 to 1 relationship.

0.275 on day 179. Such a rapid change in the NDVI is not expected.

Figure 5.15 shows the remaining terms of the energy balance estimates. The estimates of soil heat flux (G) are generally greater than the estimates of sensible heat. As the relationship used to estimate G from NDVI is empirical, it is likely that G is over estimated. This would partly explain the low value found for the effective displacement height. Because the displacement term was not estimated based on an independent measure of H, any errors in estimates of net radiation and G impact this value. Additional error is added by the uncertainty in the estimates of surface temperature. On many days, the apparent difference between air and surface temperature was less than $3^{\circ}$ C, which is approaching the accuracy of the surface temperature estimates.

Table 5.9 is a summary of the correlation between the individual terms of the energy balance and area weighted ET. The correlation coefficients are shown by site and for the data set as a whole. The estimate of net radiation alone shows a strong correlation with area weighted ET. The correlation coefficients at the Goodwell site are consistently lower than the other sites; however, the area weighted ET varies over a smaller range than at the other sites. The range of ET rates is actually limited for the entire data set, as only 7 of the 46 site-days have area weighted ET values that exceed 5 mm.

Empirical Relationships

Empirical relationships based on the energy balance were evaluated to investigate how ground-based data may be reduced. In following sections, the correlation between AVHRR derived data and area weighted ET is first examined. Then empirical

195
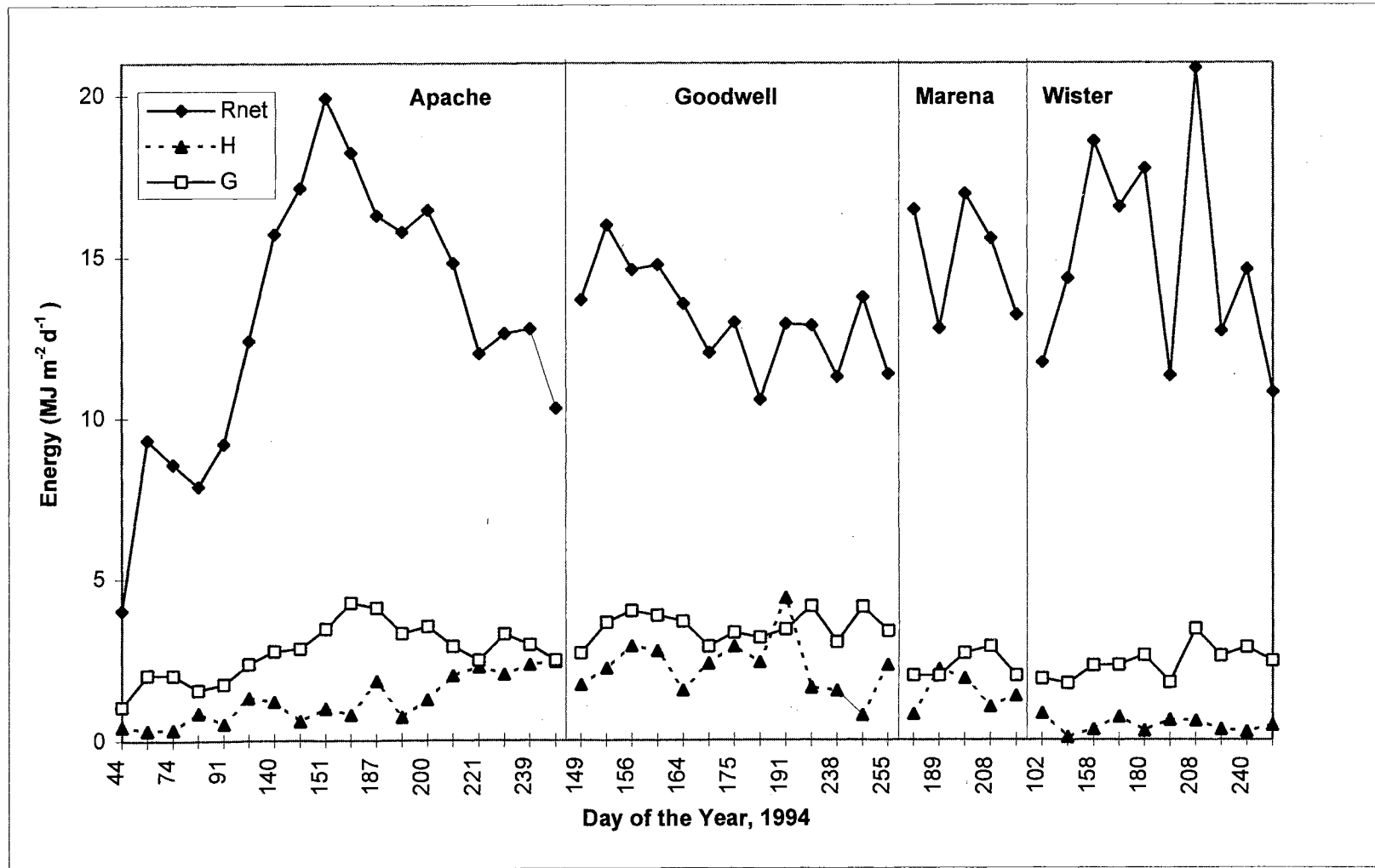
Figure 5.15: Energy balance terms estimated at each lysimeter site for days in 1994 in which there was quality data available.

**Table 5.9: Correlation coefficients and standard errors [a] between the individual energy balance components and area weighted ET ($ET_{area}$).**

| Site | Energy Balance Terms (MJ $m^{-2}$ $d^{-1}$) [b] | | | | | |
|---|---|---|---|---|---|---|
| | NetSW | $R_n$ | H | G | $R_n$ - G | $ET_{ebal}$ |
| | Correlation Between Column Data and $ET_{area}$ | | | | | |
| All | 0.506 | 0.766 | -0.285 | 0.156 | 0.806 | 0.812 |
| Apache | 0.770 | 0.832 | -0.089 | 0.586 | 0.865 | 0.890 |
| Goodwell | 0.464 | 0.450 | -0.251 | -0.080 | 0.532 | 0.605 |
| Marena/Wister | 0.383 | 0.677 | -0.284 | 0.289 | 0.689 | 0.721 |
| | Standard Error Between Column Data and $ET_{area}$ (mm $day^{-1}$) | | | | | |
| All | 1.42 | 1.06 | 1.58 | 1.62 | 0.97 | 0.96 |
| Apache | 1.17 | 1.02 | 1.83 | 1.49 | 0.92 | 0.84 |
| Goodwell | 0.90 | 0.91 | 0.98 | 1.01 | 0.86 | 0.81 |
| Marena/Wister | 1.45 | 1.15 | 1.50 | 1.50 | 1.14 | 1.09 |

[a] Standard error resulting from a simple linear regression model with $ET_{area}$ as the dependent variable.

[b] NetSW is the estimated net short-wave radiation, $R_n$ is net radiation (both short-wave and thermal), H is sensible heat, G is soil heat flux, and $ET_{ebal}$ is the estimated ET from the energy balance equations.

relationships are used to determine the minimum ground-based inputs needed to maintain reasonable estimates.

*Methods*

In order to evaluate potential methods to reduce the amount of ground-based data needed to obtain estimates of ET, several empirical relationships between the AVHRR data and area weighted ET were evaluated. As a starting point, the correlation coefficients between the AVHRR derived data and area weighted ET were determined. The standard error resulting from a simple linear regression relationship between the AVHRR data (independent variable) and the area weighted ET (dependent variable) was also calculated. Because only 5 observations were available for Marena, this data was combined with Wister are both surround by pasture and woodlands.

After examination of the direct correlation, regression analysis was performed on the data to determine what combination provided the best estimate of ET with minimal ground-based inputs. To begin the investigation, the following model was evaluated:

$$ET = A + B \ Net_{sw} + C \ (T_s\text{-}T_{11}) + D \ NDVI \qquad (5.34)$$

where A, B, C, and D are regression parameters, $Net_{sw}$ is an estimate of net short-wave radiation (evaporation units, mm of water) assuming 75% of potential solar irradiance reaches the earth's surface and a constant short-wave albedo of 0.20, $T_s$ is the AVHRR derived surface temperature ($^{\circ}$C) and $T_{11}$ is the air temperature at 11:00 GMT ($^{\circ}$C). While the 11:00 GMT temperature is obtained from ground-based measurements, it could be closely approximated by the morning overpass of the satellite. The NDVI is included as an empirical representation of factors such as roughness and soil heat flux. The

198

potential solar irradiance was determined by the procedures of Iqbal (1983). The assumption of 75% of the potential irradiance is based on a comparison of pyranometer data for the lysimeter sites with potential irradiance. A constant albedo of 0.20 is based on the average albedo values estimated from the AVHRR data for the lysimeter sites. The terms are included in an effort to adjust the seasonal variation of solar irradiance to the appropriate magnitude.

The coefficients of Equation 5.34 were determined using least-squares linear regression. The calculations were performed using the Microsoft Excel 5.0 spread sheet. As part of the regression output, t statistics relating the significance of each parameter are provided. The statistic is used to test the hypothesis that the given coefficient is 0, assuming all other coefficients remain part of the model. Using the results from this analysis other regression models are investigated following the same procedures.

*Correlation Between AVHRR Data and Actual ET*

The correlation coefficients and linear regression standard errors between the area weighted ET and the AVHRR derived data are presented in Table 5.10. The statistics are presented for the entire data set and sorted by lysimeter sites. The table is organized with data derived solely from the reflective channels first, followed by data derived from the thermal channels. Included with the thermal data are the estimates of vapor pressure, and the vapor pressure deficit derived from the AVHRR data (using Equations 5.20 and 5.22). Additionally, ground-based air temperature and vapor pressure is included for comparison purposes.

**Table 5.10: Evaluation of possible simple linear relationships between AVHRR derived data and area weighted ET estimates ($ET_{area}$).**

| Site | NDVI$_{iq}$ | SAVI$_{iq}$ | NDVI$_{ex}$ | SAVI$_{ex}$ | R1$_{iq}$ | R2$_{iq}$ | R1$_{ex}$ | R2$_{ex}$ |
|------|-------------|-------------|-------------|-------------|-----------|-----------|-----------|-----------|
| | | | AVHRR Derived Data (Reflective Channels) [a] | | | | | |
| | | | Correlation Coefficient Between Column Data and $ET_{area}$ | | | | | |
| All | 0.56 | 0.47 | 0.54 | 0.43 | -0.54 | 0.00 | -0.55 | -0.11 |
| Apache | 0.61 | 0.30 | 0.49 | 0.17 | -0.44 | -0.20 | -0.46 | -0.30 |
| Goodwell | 0.52 | 0.46 | 0.51 | 0.45 | -0.54 | -0.08 | -0.62 | -0.13 |
| Marena/Wiste | 0.43 | 0.42 | 0.42 | 0.40 | -0.30 | 0.24 | -0.26 | 0.20 |
| | | | Standard Error Between AVHRR Data and $ET_{area}$ (mm d$^{-1}$) | | | | | |
| All | 1.4 | 1.5 | 1.4 | 1.5 | 1.4 | 1.6 | 1.4 | 1.6 |
| Apache | 1.5 | 1.7 | 1.6 | 1.8 | 1.6 | 1.8 | 1.6 | 1.8 |
| Goodwell | 0.9 | 0.9 | 0.9 | 0.9 | 0.9 | 1.0 | 0.8 | 1.0 |
| Marena/Wiste | 1.4 | 1.4 | 1.4 | 1.4 | 1.5 | 1.5 | 1.5 | 1.5 |

| Site | $T_a$ | $T_s$ | $T_s$-$T_a$ | $T_{b4}$-$T_{b5}$ | VP$_{avhrr}$ | PD$_{avhrr}$ | VP$_{ground}$ |
|------|-------|-------|-------------|-------------------|--------------|--------------|---------------|
| | | AVHRR Derived Data (Thermal Channels) or Ground-Based Data [b] | | | | | |
| | | Correlation Coefficient Between Column Data and $ET_{area}$ | | | | | |
| All | 0.33 | 0.26 | -0.09 | 0.23 | 0.45 | 0.02 | 0.54 |
| Apache | 0.47 | 0.45 | 0.16 | 0.29 | 0.38 | 0.34 | 0.56 |
| Goodwell | 0.08 | -0.03 | -0.16 | -0.18 | 0.06 | -0.09 | -0.30 |
| Marena/Wiste | 0.23 | 0.18 | -0.24 | 0.10 | 0.25 | 0.04 | 0.50 |
| | | Standard Error Between Column Data and $ET_{area}$ (mm d$^{-1}$) | | | | | |
| All | 1.6 | 1.6 | 1.6 | 1.6 | 1.5 | 1.6 | 1.4 |
| Apache | 1.6 | 1.6 | 1.8 | 1.8 | 1.7 | 1.7 | 1.5 |
| Goodwell | 1.0 | 1.0 | 1.0 | 1.0 | 1.0 | 1.0 | 1.0 |
| Marena/Wiste | 1.5 | 1.5 | 1.5 | 1.6 | 1.5 | 1.6 | 1.4 |

[a] NDVI is Normalized Difference Vegetation Index, SAVI is Soil Adjusted Vegetation Index, R1 and R2 are reflectance values for AVHRR channels 1 and 2 respectively. The subscript ex indicates the values are based on exoatmospheric reflectance and iq indicates the values are based on atmospherically corrected reflectance by the methods of Iqbal (1983).

[b] $T_a$ is ground-based air temperature ($^\circ$C), $T_s$ is AVHRR derived surface temperature ($^\circ$C), $T_{b4}$-$T_{b5}$ is the difference in channel 4 and 5 brightness temperatures (K), VP is vapor pressure (kPa) from either AVHRR or ground-based estimates, and VPD$_{avhrr}$ is AVHRR estimated Vapor Pressure Deficit (kPa)

The positive correlation between ET and the vegetative indices can be partially attributed to seasonal variation, as most vegetation begins to actively grow in the summer when the incoming solar energy is the highest. Additionally, with actively growing vegetation, moisture can be extracted from deeper in the soil as compared to bare soil or partially vegetated conditions. When there is insufficient moisture, the plants' rate of chlorophyll production is reduced and the greenness decreases, decreasing the NDVI. The correlation coefficients are often lower at the Goodwell site compared to the other sites. The ET rates on the days considered were consistently low due to dry conditions. This is reflected in a consistently lower standard error. The higher correlation of NDVI with ET at Apache may be related to changes in the wheat fields surrounding the site. Early in the year the wheat is actively growing; however, later in the year the fields are fallow. The fallow fields typical have a lower ET rate and will reduce the NDVI compared to the times they are in production. Note that in most cases, atmospheric correction of the reflective channels did not greatly improve the correlation of this data with ET.

Figures 5.16 and 5.17 show NDVI and SAVI plotted with estimates of soil moisture at the lysimeter sites. The increase in NDVI early in the season at Apache corresponds to the development of wheat in the area with the corresponding decrease near the time of harvest. The general trends of the NDVI do follow that of ET and soil moisture, however, the NDVI appears to approach a lower limit that ceases to correspond to changes in soil moisture. Part of this limit can be related to the fact that the NDVI is also affected by plant density as well as greenness. This is apparent at the Wister and
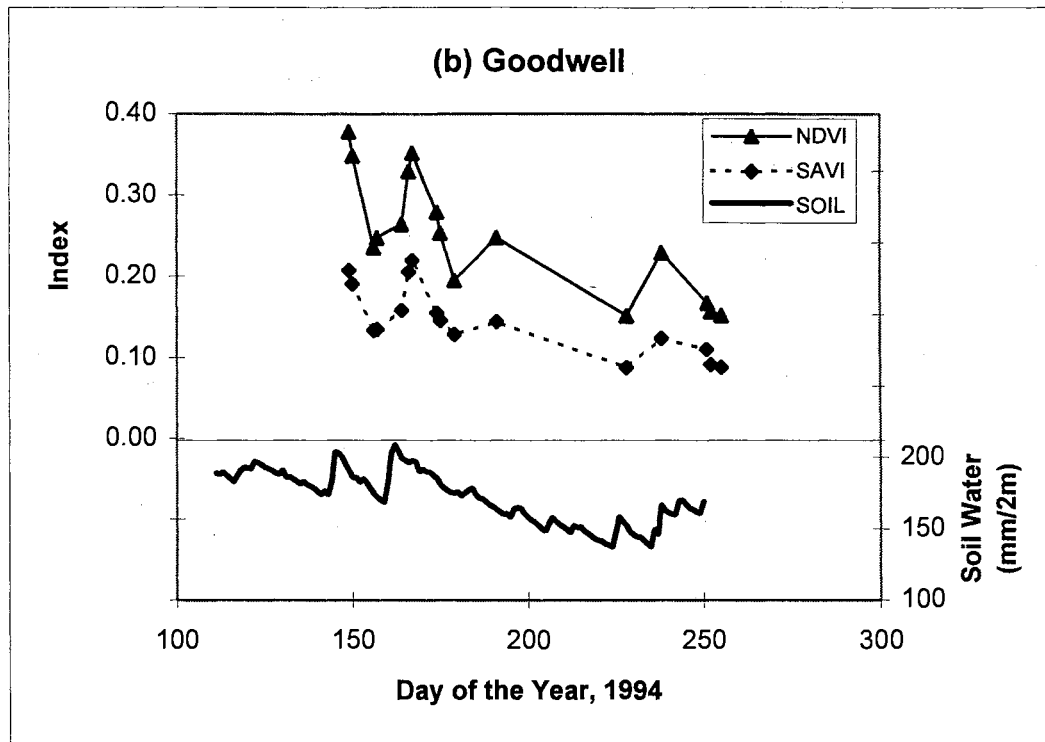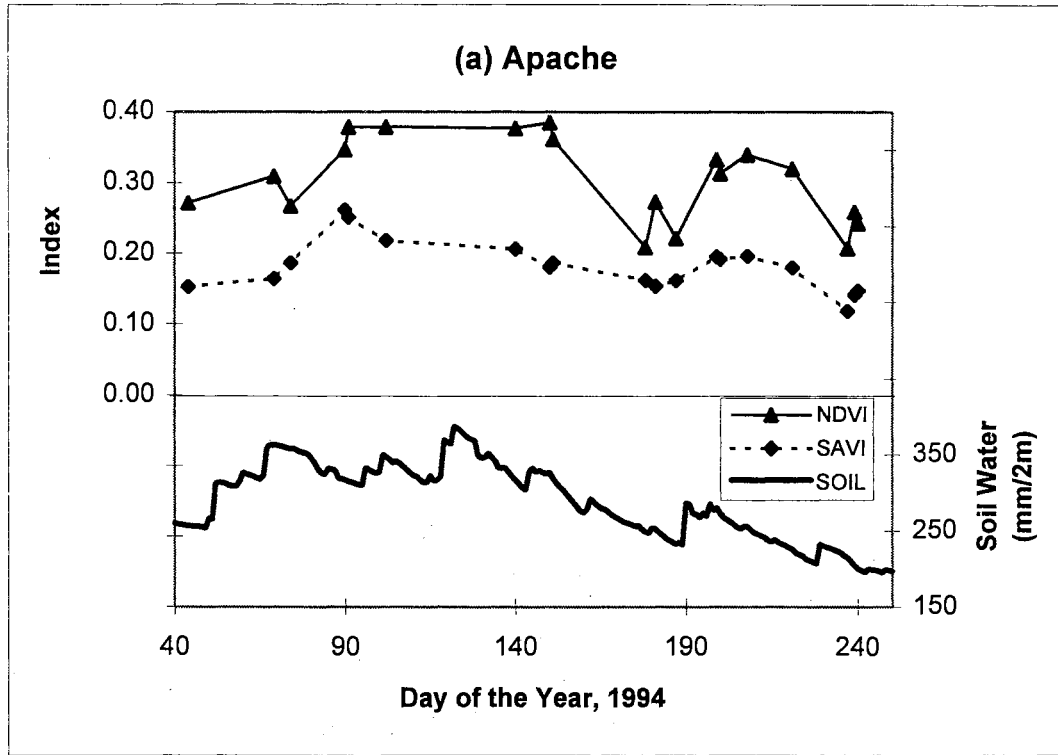
Figure 5.16: NDVI, SAVI and simulated soil water at the (a) Apache and
(b) Goodwell lysimeter sites during 1994.
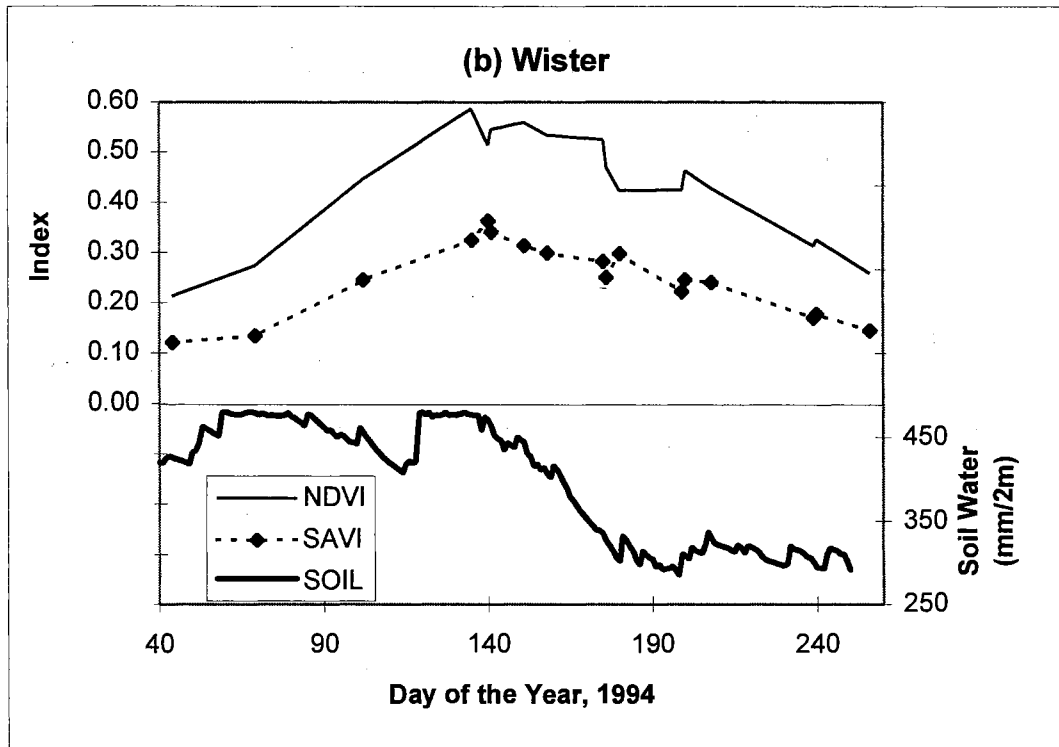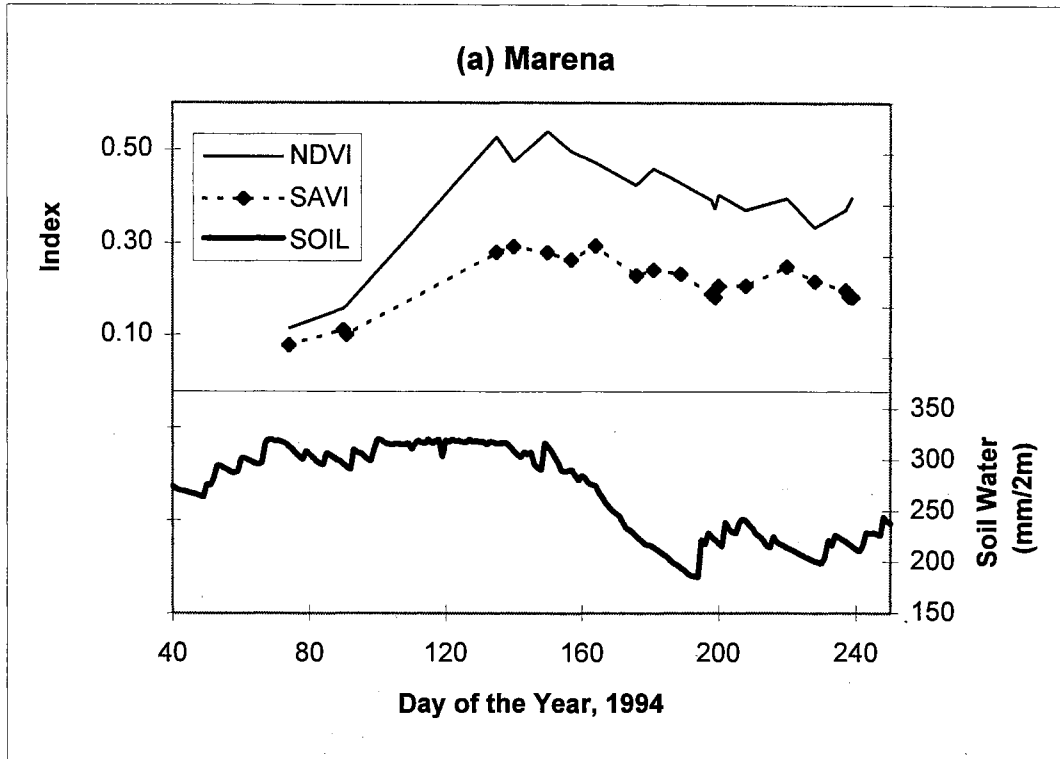
Figure 5.17: NDVI, SAVI and soil water at the (a) Marena and (b) Wister
lysimeter sites during 1994.

203

Marena sites. Both sites contain woodlands and pasture that are not cultivated and thus there is a more consistent plant density than at Goodwell and Apache.

The higher correlation of NDVI with ET than that of the SAVI (Table 5.10) can be attributed to the impact of viewing geometry as previously noted. An additional factor that may reduce the correlation of the SAVI with ET is its reduced sensitivity to red reflectance. As the denominator of the SAVI is multiplied by 1.5, this tends to weight the changes in the index more heavily with the NIR reflectance. While this does reduce the variation with soil color, it also lessons the sensitivity to changes in greenness.

The positive correlation of surface temperature with area weighted ET can be attributed to seasonal variations in incident radiation. The limited correlation of vapor pressure deficit derived from the AVHRR data is primarily a result of the dry conditions for most of the data set. The ET rates considered rarely approached potential conditions and were limited by available moisture; therefore, a measure of the ability of the atmosphere to hold moisture is not strongly related to ET.

From Table 5.11, the cross product of surface temperature and vegetation resulted in a slight increase in correlation of ET over that of either of the parameters alone. This is particularly the case at the Apache site. The positive correlation between ET and surface temperature can partially be attributed to seasonal variations. For example, in the winter months there is less incoming radiation and therefore less energy incident on the surface. In general, this will decrease surface temperature and limit the energy available for evaporation. The NDVI provides an estimate of the relative condition of the vegetation and thus some representation of the transpiration potential.

# Table 5.11: Evaluation of possible cross-product relationships between AVHRR derived data and area weighted ET estimates ($ET_{area}$).

| Site | $\dfrac{T_s^*}{NDVI_{iq}}$ [a] | $\dfrac{T_s^*}{NDVI_{ex}}$ | $\dfrac{T_s^*}{SAVI_{iq}}$ [b] | $\dfrac{T_s^*}{SAVI_{ex}}$ | $ET_{opmon}$ [c] | $\dfrac{NDVI_{ex}^*}{ET_{opmon}}$ |
|---|---|---|---|---|---|---|
| | Correlation Coefficient Between Column Data and $ET_{area}$ | | | | | |
| All | 0.67 | 0.68 | 0.61 | 0.61 | 0.10 | 0.54 |
| Apache | 0.71 | 0.76 | 0.61 | 0.64 | 0.35 | 0.63 |
| Goodwell | 0.42 | 0.43 | 0.36 | 0.36 | 0.15 | 0.39 |
| Marena/Wister | 0.43 | 0.49 | 0.44 | 0.48 | 0.13 | 0.30 |
| | Standard Error Between Column Data and $ET_{area}$ | | | | | |
| All | 1.2 | 1.2 | 1.3 | 1.3 | 1.6 | 1.4 |
| Apache | 1.3 | 1.2 | 1.4 | 1.4 | 1.7 | 1.4 |
| Goodwell | 0.9 | 0.9 | 0.9 | 0.9 | 1.0 | 0.9 |
| Marena/Wister | 1.4 | 1.4 | -1.4 | 1.4 | 1.6 | 1.5 |

[a] $T_s$ is the AVHRR derived surface temperature (°C), NDVI is the Normalized Difference Vegetation Index. The subscript ex indicates the index is derived from exoatmospheric reflectance and iq indicates the reflectance values have been corrected for the atmosphere using the methods of Iqbal (1983).

[b] SAVI is the Soil Adjusted Vegetation Index.

[c] $ET_{opmon}$ is potential ET calculated from the Penman-Monteith equation (mm d$^{-1}$). The values were calculated from ground-based measurements and included for comparison purposes.

*Regression Results*

The regression results from Equation 5.34 are shown in Table 5.12. Included in the table is the coefficient of determination ($r^2$) and standard error of the regression. Also included is the t statistic for each parameter in the model and the probability that the coefficient is 0 given that all other coefficients remain in the model. Equation 5.34 is only able to explain 50% of the variation in area weighted ET as indicated by the $r^2$ value. The difference in surface temperature and air temperature at 11:00 GMT does not significantly contribute to the relationship as indicated by the low t statistic and p-value of 0.72. It was hoped that the temperature difference would be sensitive to changing moisture conditions; however, it is possible that there are too many other factors involved in the intervening time periods. This could include morning dew, and passage of weather fronts.

Instead of using the air temperature at 11:00 GMT, air temperature at the time of satellite overpass is used for the next model:

$$ET = A + B\ Net_{sw} + C\ (T_s\text{-}T_a) + D\ NDVI \qquad\qquad (5.35)$$

where the $T_s$-$T_a$ term can be viewed as an estimate of sensible heat flux. The term also should reflect some of the variation in thermal net radiation. The inclusion of air temperature as a ground-based measurement is not considered as an extreme limitation, as measurements are readily available at many locations across the world. From Table 5.12, it can be seen that all the coefficients in Equation 5.35 are significant at least at the 0.05 level of probability. The significance of the NDVI term is reduced compared to the previous model, however, it is still significant at the 5% level. The negative coefficient

**Table 5.12: Results of the regression analysis between area weighted ET and AVHRR data**

| Equation Number | $r^2$ | Standard Error $(mm\ d^{-1})$ | Input Data | Regression Coefficients | t Statistic | P Value [i] |
|---|---|---|---|---|---|---|
| 5.34 | 0.501 | 1.19 | Constant [a] | -5.381 | -3.17 | 0.00 |
| | | | NetSW [b] | 0.774 | 3.96 | 0.00 |
| | | | $T_s$-$T_{11}$ [c] | -0.019 | -0.37 | 0.72 |
| | | | $NDVI_{ex}$ [d] | 6.456 | 3.20 | 0.00 |
| 5.35 | 0.567 | 1.11 | Constant | -6.627 | -4.23 | 0.00 |
| | | | NetSW | 1.054 | 5.11 | 0.00 |
| | | | $T_s$-$T_a$ [e] | -0.276 | -2.56 | 0.01 |
| | | | $NDVI_{ex}$ | 4.356 | 2.20 | 0.03 |
| 5.35 [f] | 0.581 | 1.09 | Constant | -6.906 | -4.49 | 0.00 |
| | | | NetSW | 1.036 | 5.16 | 0.00 |
| | | | $T_s$-$T_a$ | -0.262 | -2.47 | 0.02 |
| | | | $NDVI_{iq}$ | 4.010 | 2.53 | 0.02 |
| 5.36 | 0.517 | 1.16 | Constant | -6.813 | -4.18 | 0.00 |
| | | | NetSW | 1.271 | 6.73 | 0.00 |
| | | | $T_s$-$T_a$ | -0.387 | -3.89 | 0.00 |
| 5.37 | 0.500 | 1.18 | Constant | -5.568 | -3.47 | 0.00 |
| | | | NetSW | 0.746 | 4.19 | 0.00 |
| | | | $NDVI_{ex}$ | 6.728 | 3.62 | 0.00 |
| 5.38 | 0.665 | 0.99 | Constant | -9.091 | -5.81 | 0.00 |
| | | | NetSW | 1.195 | 6.36 | 0.00 |
| | | | $T_s$-$T_a$ | -0.372 | -3.72 | 0.00 |
| | | | $NDVI_{ex}$ | 3.636 | 2.05 | 0.05 |
| | | | THETA [g] | 0.024 | 3.47 | 0.00 |

**Table 5.12 (Continued)**

| Equation Number | $r^2$ | Standard Error (mm d$^{-1}$) | Input Data | Regression Coefficients | t Statistic | P Value [i] |
|---|---|---|---|---|---|---|
| 5.39 | 0.721 | 0.90 | Constant | -8.907 | -6.42 | 0.00 |
| | | | NetSW | 1.230 | 7.47 | 0.00 |
| | | | WS $(T_s-T_a)$ [h] | -0.106 | -4.98 | 0.00 |
| | | | NDVI$_{ex}$ | 0.677 | 0.36 | 0.72 |
| | | | THETA | 0.030 | 4.46 | 0.00 |
| | | | | | | |
| 5.40 | 0.720 | 0.89 | Constant | -8.965 | -6.57 | 0.00 |
| | | | NetSW | 1.262 | 9.25 | 0.00 |
| | | | WS $(T_s-T_a)$ | -0.111 | -6.97 | 0.00 |
| | | | THETA | 0.030 | 4.72 | 0.00 |

[a] Constant determined in the regression analysis.

[b] NetSW is the estimate of net short wave radiation assuming 75% atmospheric attenuation attenuation and a constant albedo of 0.20, mm of water per day.

[c] Difference in satellite derived surface temperature and the air temperature at 11:00 GMT, °C.

[d] Normalized Difference Vegetation Index derived from exoatmospheric reflectance. NDVI$_{iq}$ is the NDVI based on reflectance corrected for the atmosphere using Iqbal's (1983) methods.

[e] Difference in satellite derived surface temperature and air temperature at the time of satellite overpass, °C.

[f] NDVI is based on reflectance corrected for atmospheric effects by the methods of Iqbal (1983).

[g] Relative angle between the sun and satellite from the point of observation, degrees.

[h] WS is the daily average wind speed, m s$^{-1}$.

[i] Probability the regression value is 0 assuming all other coefficients remain in the model.

for C in Equation 5.35 is physically reasonable, as increasing surface temperature relative to air temperature is an indication more energy is partitioned to sensible heat rather than to ET. A surface temperature greater than air temperature also reduces the thermal net radiation. The positive coefficient for NDVI is also reasonable, as an increase in NDVI is an indication of a higher transpiration potential from vegetation. Equation 5.35 was also considered with NDVI derived from the atmospherically corrected reflectance values, with the results also in Table 5.12. This results in a slight improvement of the predictions of the model, however the small decrease in the standard error is not considered significant enough to justify the extra processing required to correct the data.

In order to examine the NDVI and (Ts - Ta) terms individually, the following models were used:

$$ET = A + B \, Net_{sw} + C \, (T_s - T_a) \tag{5.36}$$

$$ET = A + B \, Net_{sw} + C \, NDVI \tag{5.37}$$

The regression results for both of the above relationships are also shown in Table 5.12. From the $r^2$ values in the table, note that Equation 5.36 and 5.37 explain roughly the same amount of variation in the area weighted ET rates. As the use of NDVI only requires satellite derived information, Equation 5.37 would be the preferred relationship. However, the relationship only explains about 50% of the variation in ET.

The correlation coefficients between the residuals of Equation 5.37 (predicted ET - area weighted ET) and several variables including solar/viewing angles, and daily weather data were calculated. The parameter with the highest correlation with the residuals of the relationship was the relative angle between the sun and satellite. The

209

correlation is most likely a result of the shading effects and the directional pattern of radiation reflected from the surface. This could also include the effect of the variation of the difference in surface and air temperature based on the time of the satellite overpass. Adding this term as an independent variable to Equation 5.35 results in:

$$ET = A + B \: Net_{sw} + C \: (T_s - T_a) + D \: NDVI + E \: THETA \qquad \textbf{(5.38)}$$

where THETA is the relative angle between the sun and satellite in degrees. From Table 5.12, note that the resulting coefficient of THETA is positive, indicating that as the angle between the satellite and sun increases, Equation 5.37 under predicts ET. Shading cannot explain this effect, as the result of surface shading would result in a lower surface temperature and thus an over prediction of ET according to Equation 5.37. However, for larger relative angles, the NDVI uncorrected for the atmosphere would be decreased. The effect of the THETA term will be considered in more detail later. The residuals of Equation 5.38 were most highly correlated with average daily wind speed, based on the variables considered.

Wind speed does affect the aerodynamic resistance to heat transfer; therefore, the following relationship is considered:

$$ET = A + B \: Net_{sw} + C \: WS \: (T_s - T_a) + D \: NDVI + E \: THETA \qquad \textbf{(5.39)}$$

where WS is the average daily wind speed at 2 m (m s$^{-1}$). From Table 5.12, note that with the addition of wind speed into the relationship, the regression coefficient for NDVI is no longer significantly different than 0. There is a correlation between NDVI and wind speed as discussed previously. Additionally, the NDVI shows a positive correlation with potential solar irradiance and negative correlation with $T_s - T_a$. The positive correlation of

NDVI with potential solar irradiance can be attributed to the seasonal variation of annual plants. Surfaces with less vegetation tend to have a higher $T_s$-$T_a$ than non vegetative surfaces, thus the negative correlation with NDVI.

Removing NDVI from Equation 5.39 results in:

$$ET = A + B\ Net_{sw} + C\ WS\ (T_s\text{-}T_a) + D\ THETA \qquad (5.40)$$

with the regression results for this equation also given in Table 5.12. Note that the removal of NDVI from Equation 5.39 had little impact on $r^2$ or the standard error. The THETA term is still significant, indicating that there is a probable view angle effect in the data. Equation 5.40 does explain a greater amount of the variation than the energy balance method previously considered (Equations 5.25 to 5.33), however, Equation 5.40 includes 4 regression parameters, where only 1 fitting parameter was used for the energy balance method.

Line plots of the predicted ET from Equation 5.35 are shown in Figure 5.18, and the predicted ET from Equation 5.40 is shown in Figure 5.19. Also included in the figures are the corresponding values of area weighted ET. Predicted ET from Equation 5.35 and Equation 5.40 versus area weighted ET is shown in Figures 5.20 (a) and (b), respectively. The greatest improvement of Equation 5.40 over Equation 5.35 is for the Apache site. While there is a definite increase in the amount of variation explained by Equation 5.35 as compared to Equation 5.40, the standard error is not greatly different. The lack of variation present in the area weighted ET is a limitation. No significant correlation of the difference between the ET predicted from Equation 5.40 and area weighted ET existed with other ground-based measurements. It is possible that the error
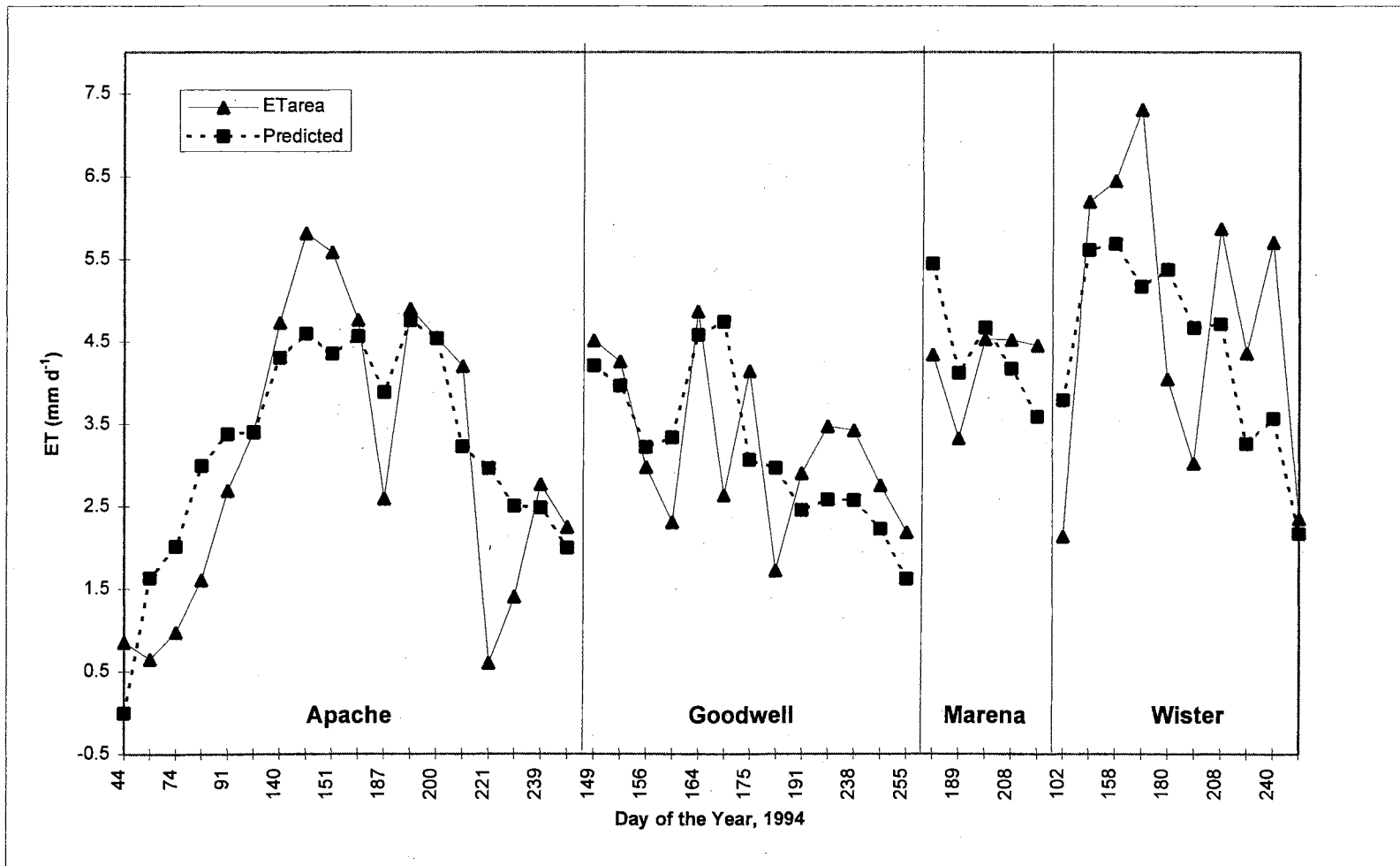
Figure 5.18 : Area weighted ET and ET predicted by the regression model of Equation 5.35 at each lysimeter site during 1994.
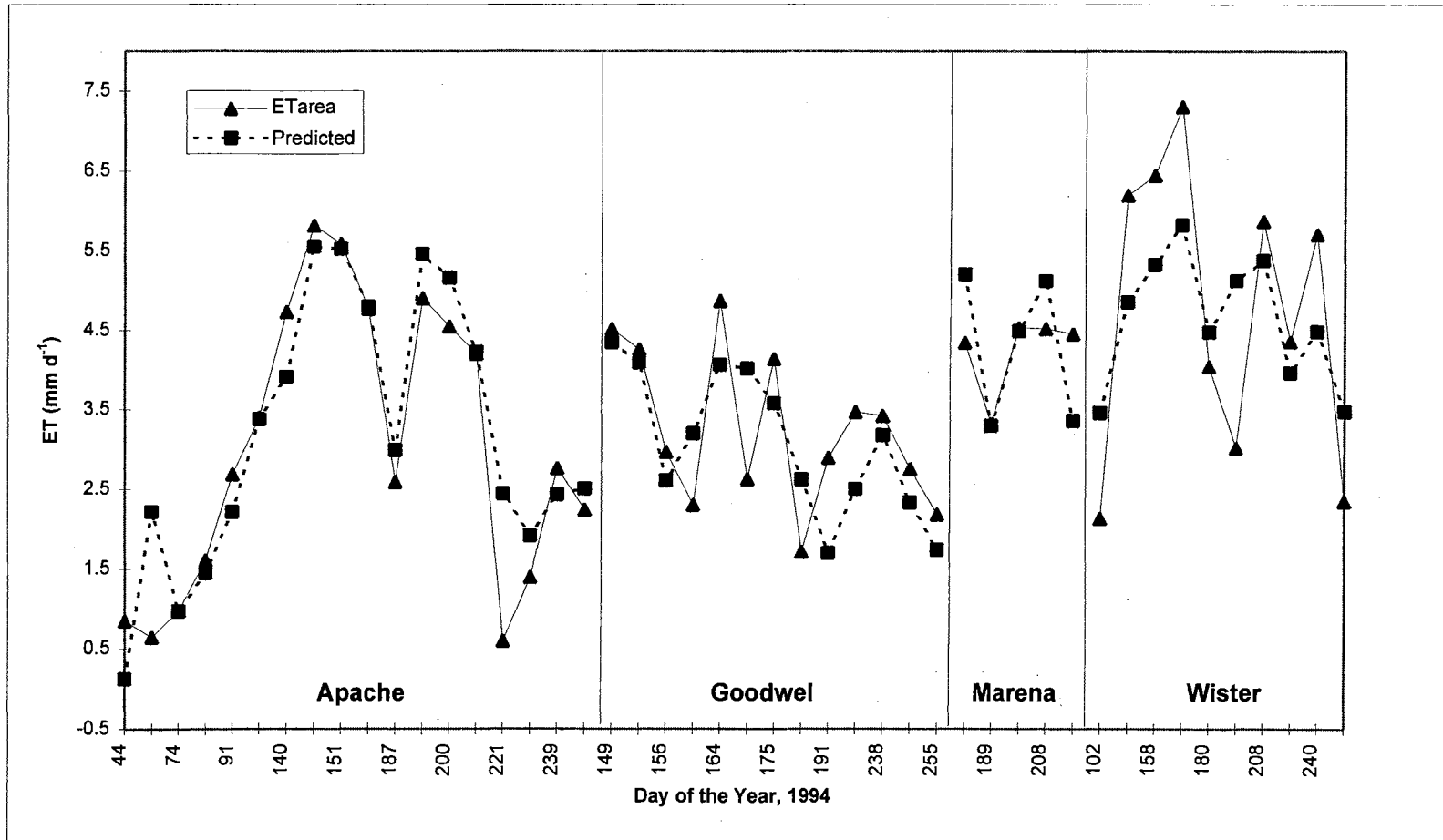
Figure 5. 19:  Area weighted ET and ET predicted by the regression Equation 5.40 at each lysimeter site during 1994.

## (a) Predicted from Equation 5.35



## (b) Predicted from Equation 5.40
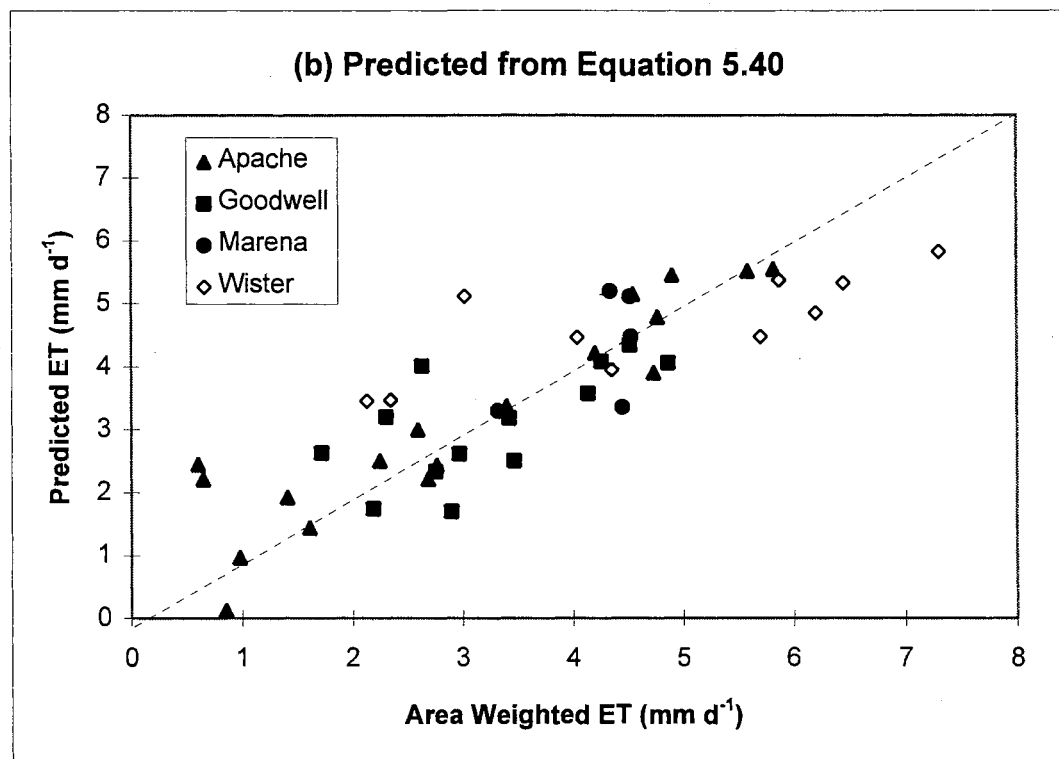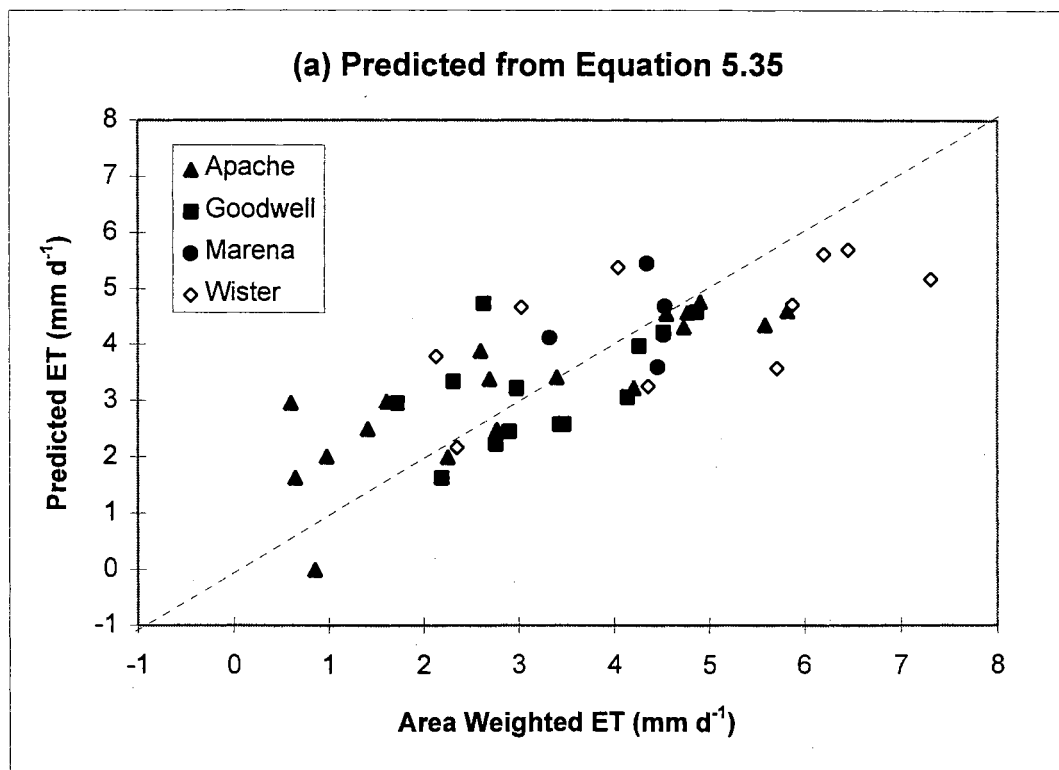


Figure 5.20: Predicted ET from equations (a) 5.35 and (b) 5.40 versus area weighted ET.

in the remotely sensed data is too large to account for the smaller variations in ET.

Summary

Table 5.13 presents summary statistics for the relationships evaluated between AVHRR data and area weighted ET. The last relationship shown is included to represent the amount of variation that can be attributed to seasonal variation, represented by the estimate of net short wave radiation. The error estimates (standard error, MAD, RMSE) are relatively low for each of the methods; however, the amount of variation explained by the relationships ($r^2$) must also be considered. The average area weighted ET was 3.6 mm $d^{-1}$ with a standard deviation of 1.6 mm $d^{-1}$. Therefore, the error for most of the methods is approximately 25% of the average area weighted ET for the dates considered.

## Chapter Summary

In this chapter, it was determined that the split-window parameters determined by Kerr et al. (1992) provided reasonable surface temperature estimates for the conditions in Oklahoma. The parameters also appeared to provide a better estimate than could be obtained by assuming specific emmissivity conditions with other methods.

The NDVI showed some correlation with wind speed and vapor pressure for the conditions in Oklahoma during 1994. Combining NDVI with data from the AVHRR thermal channels provided a better insight to vapor pressure than the use of the thermal channels alone. The estimate of vapor pressure obtained from the AVHRR data appeared sufficient to provide estimates of potential ET.

**Table 5.13: Summary statistics for the predictions of selected ET models compared to area weighted ET.**

| Model [a] | Model STD$_{err}$ [b] | Evaluation Regression [c] $r^2$ | STD$_{err}$ | A$_r$ | B$_r$ | MAD[d] | RMSE |
|---|---|---|---|---|---|---|---|
| Full-Input (Equations 5.25 to 5.33) | 0.95 | 0.660 | 0.79 | 1.46 | 0.67 | 0.75 | 0.98 |
| ET = -6.63 + 1.05 NetSW - 0.28(T$_s$-T$_a$) + 4.4 NDVI$_{ex}$ | 1.11 | 0.567 | 0.81 | 1.55 | 0.57 | 0.88 | 1.06 |
| ET = -9.0 + 1.3 NetSW - 0.11 WS (T$_s$-T$_a$) + 0.03 THETA | 0.89 | 0.720 | 0.74 | 1.00 | 0.72 | 0.67 | 0.85 |
| ET = -5.09 + 0.930 NetSW | 1.33 | 0.347 | 0.78 | 2.34 | 0.35 | 1.00 | 1.30 |

[a] Full-Input is the ET predicted using equations 5.25 to 5.33. NetSW is estimated net short-wave radiation in mm of equivalent water evaporated, T$_s$-T$_a$ is the difference in surface and air temperatures (°C), NDVI$_{ex}$ is the Normalized Difference Vegetation Index based on exoatmospheric reflectance and THETA is the relative angle between the sun and satellite (degrees).

[b] Standard error estimate with area weighted ET as the dependent variable (mm d$^{-1}$).

[c] Results from the regression equation: (Predicted ET) = A$_r$ + B$_r$ (Area weighted ET), where $r^2$ is the coefficient of determination and STD$_{err}$ is the standard error of the relationship. A$_r$ and STD$_{err}$ have units of mm d$^{-1}$.

[d] MAD is the Mean Absolute Difference and RMSE is the Root Mean Squared Error for the difference in predicted and area weighted ET, both with units of mm d$^{-1}$.

Attempts to estimate actual ET based on satellite observations alone had limited success. Use of AVHRR data alone was able to predict only 50% of the variation in actual ET. A theoretical energy balance approach using more ground-based inputs did provide a better fit to the data. It appears that viewing geometry effects on the AVHRR are significant in terms of the accuracy of actual ET estimates that can be obtained. The best results were obtained when ground-based estimates of wind speed and air temperature were included in the model.

CHAPTER 6

**CONCLUSIONS AND RECOMMENDATIONS**

**Image Analysis**

In order to develop quantitative application of AVHRR data, the following

processes must be considered:

- Geometric Registration

  A rough geometric registration of AVHRR images can be accomplished from

  automated procedures; however, to precisely locate an area to within a pixel,

  ground control points should be used.

- Cloud Screening

  Cloud screening of the AVHRR data is difficult, especially over heterogeneous

  surface conditions. Under such conditions, a simple gray-level thermal

  threshold is not sufficient to detect pixels which are partially cloud

  contaminated. Even uniformity tests of either the reflective or thermal

  channels will not provide consistent results. Temporal analysis of the trends in

  the values at a particular location can be useful; however, it becomes difficult

  to separate changes induced by viewing geometry from changes due to clouds.

Cloud cover is also a significant limitation to the frequency at which images can be obtained.

- Radiometric Calibration

For AVHRR channels 1 and 2, the degradation of the gain for these channels with time must be considered as no on-board calibration is available. For short-term, empirical applications, this is less of a concern if the data is only to be applied with the specific satellite and sensor; however, if a precise estimate of albedo is needed or atmospheric correction is to be performed, the degradation should be taken into account. Precise radiometric calibration is also needed if the relationships developed are going to be applied to another sensor. Based on the reasonable results that were obtained in the evaluation of the split-window methods, the on-board calibration procedures for the thermal channels appear to be sufficient to account for the changes in the sensitivity of the thermal sensors.

- Atmospheric Correction

Atmospheric correction of the reflective channels is needed if short-wave albedo is to be estimated from the AVHRR data. Atmospheric correction of the data is also necessary if empirical relationships have been derived from ground-based reflectance measurements and are to be applied to the satellite data without modification. Global, quantitative applications of the data would also benefit from atmospheric correction, as atmospheric profiles can vary significantly at this scale. However, the results of this analysis with the NDVI

imply that for regional applications, the noise introduced by changing atmospheric conditions does not mask the NDVI response to changes in vegetative cover.

The split-window methods do provide a means to account for atmospheric interference so that estimates of surface temperature can be obtained directly from the AVHRR data. However, careful selection of the split-window parameters is necessary to insure that they represent the surface and climatic conditions of interest.

- Viewing geometry correction

Viewing geometry did impact the AVHRR data used in this study. Due to the drift in the satellite's orbit, low solar zenith angles increased the sensitivity of the data to shadows and sensor orientation. The NDVI is less sensitive to viewing angle effects than are the individual reflectance values of channels 1 and 2. Any application using the reflectance values alone will probably require some correction for viewing geometry. Regardless of the solar geometry, data corresponding to satellite zenith angles of greater than $40^\circ$ do not show promise for quantitative applications. The large pixel size and viewing and atmospheric effects introduce too much variation into the data.

In summary, the major limitations of the use of the AVHRR data encountered in this study were the frequency at which clouds prevented a clear view of the surface and the late overpass of the satellite due to its orbital drift. Cloud contamination, combined with the constraint of satellite zenith angles less than $40^\circ$, seems to restrict the number of

images per month to no more than 10 for conditions in Oklahoma. Efforts should be made to minimize the drift of the NOAA series satellites, if the AVHRR data sets are to be used for long-term global monitoring. Correction of the viewing angle effect is difficult for AVHRR data, as a single pixel can cover an area containing different cover conditions and topography. Empirical correction methods using several images acquired in a short time period may provide a means to reduce the view angle effect; however, this would have to be conducted on an area by area basis.

## Application of AVHRR Data to ET Estimates

Despite the limitations noted in the AVHRR data, it was possible to determine methods to apply the data in a manner that could be useful for large-area ET monitoring. The NDVI showed several relationships with the ground-based data that indicates it is a useful measure of surface conditions. The correlation of NDVI with wind speed and relative humidity for this data set may be limited to Oklahoma; however, there are some physical relationships that imply this relationship may apply to other areas, particularly with respect to vapor pressure. NDVI also does respond to general trends in soil moisture; however, the annual variation of vegetation must be considered.

The inclusion of NDVI with the thermal data did provide a better estimation of vapor pressure than did the application of the thermal data alone. The relationship was strong enough to infer potential ET conditions from the AVHRR data after calibration to the region. While the relationship used to derive estimates of vapor pressure had some physical basis, the number of assumptions applied and the fact that the low emissivity

value was chosen to best fit the data implies that the relationship developed in this study may not apply to another location. This is a general limitation of relationships developed using the NDVI, as it is an index and its physical meaning is difficult to quantify unless applied to a specific cover type.

The results obtained for estimates of actual ET in this study have limited value, as the study was biased towards relatively dry conditions and thus lower ET rates. However, the following may be concluded:

- Any attempt to relate the AVHRR data to actual ET rates should take into consideration seasonal variation in incident radiation. If this is not accounted for, the seasonal signal can mask out changes due to moisture conditions at the surface.

- If only satellite data are available, the use of the NDVI combined with estimates of potential short-wave irradiance should provide the best estimate, versus use of the reflective data alone or some use of the thermal data.

- The most useful ground-based information to supplement the AVHRR data for estimates of actual ET is the air temperature corresponding to the time of satellite overpass. The next measurement of importance is wind speed.

- Integration of the NDVI into the ET estimates is difficult due to the fact that it is partially correlated with many variables. Application of the NDVI for ET estimates requires an empirical relationship and local calibration; therefore, the use of the NDVI to infer ET rates at a global scale may not provide very precise estimates.

- Use of the surface temperature derived from the split-window equations does show promise for ET estimates when used in conjunction with ground-based

measurements of air temperature. However, selection or adjustment of the split-window equation parameters must take into consideration the surface emissivity.

Overall, it is likely that any use of AVHRR data for actual ET estimates will require either calibration for a particular region or the data will need to be supplemented with other ground-based measurements. If corrected for the atmosphere and viewing geometry, the data should provide reasonable estimates of short-wave albedo. And as mentioned, estimates of surface temperature can be obtained. Beyond this data, it is not likely that any physical parameters can be inferred directly from the data. Estimates of vapor pressure may be possible; however, the number of assumptions needed to obtain this estimate suggest that some site-specific calibration will be required.

## Recommendations

This study was limited to measurements taken over a period of eight months, with many of the measurements limited to a five month period. Further investigation of the relationships between NDVI and meteorological parameters over longer time periods is needed to verify any relationships that may exist   The Oklahoma Mesonet provides a unique opportunity to analyze these relationships for AVHRR data, as well as data from other earth observing satellites such as Landsat and SPOT. NOAA 14 became operational in February of 1995. Because of its recent launch date its orbit will provide overpass times earlier in the day; therefore, the viewing angle effects should be lessened and there may be a stronger relationship between surface temperature and estimates of actual ET.

The methods used to estimate area weighted ET are considered valid; however, short-term placement of flux stations at areas surrounding the lysimeter sites would be helpful to further quantify the cover coefficients at each site. This would be particularly useful at the Goodwell site, where there are several irrigated fields in the area. With periodic measurements of the ET rates surrounding the lysimeter sites, these sites provide the continuous monitoring needed to further develop remotely sensed ET estimates. It should be possible to derive relationships that are at least valid for the area surrounding Oklahoma. Validation of any relationships would be required before they are applied to another region.

# REFERENCES

Abel, P., B. Guenther, R.N. Galimore, and J.W. Cooper. 1993. Calibration results for NOAA-11 AVHRR channels 1 and 2 from congruent path aircraft observations. Journal of Atmospheric and Oceanic Technology 10(4):493-508.

Allen, R.G. 1990. REF-ET, Reference Evapotranspiration Calculator. Version 1.1. Utah State University Foundation, Logan.

Allen, R.G. 1995. Assessing integrity of weather data for use in the reference evapotranspiration estimation. Journal of Irrigation and Drainage Engineering 30: (Submitted).

Allen, R.G., T.A. Howell, W.O. Pruitt, I. Walter, and M.E. Jensen (editors). 1991. Lysimeters for Evapotranspiration and and Environmental Measurements. Proceedings of the International Symposium on Lysimetry, ASCE, New York.

Alley, W.M. 1984. The Palmer drought severity index: Limitations and Assumptions. Journal of Climate and Applied Meteorology 23:1100-1109.

Anderson, E. 1993. A Continuous, Incremental Antecedent Precipitation Index (API) Mode for use with the National Weather Service River Forecasting System. Proceedings of the 1993 ASCE International Symposium of Engineering Hydrology, July, 1993, San Francisco, CA.

Bausch, W.C. 1995. Remote sensing of crop coefficients for improving the irrigation scheduling of corn. Agricultural Water Management 27:55-68.

Bausch, W.C. and C.M. Neale. 1987. Crop coefficients derived from reflected canopy radiation: a concept. Transactions of the ASAE 30:701-709.

Bausch, W.C., H.R. Duke, and L.K. Porter. 1994. Remote sensing of plant nitrogen status in corn. ASAE Paper No. 942117. ASAE, 2950 Niles Rd., St. Joseph, MI.

Becker, F, and Z-L. Li. 1990a. Temperature-independent spectral indices in thermal infrared bands. Remote Sensing of Environment 32:17-33.

Becker, F. and Z-L. Li. 1990b. Toward a local split window method over land surfaces. International Journal of Remote Sensing 3:369-393.

225

Ben-Asher, J., C.J. Phene and A. Kinarti. 1992. Canopy temperature to assess daily evapotranspiration and management of high frequency drip irrigation systems. Agricultural Water Management 22:379-390.

Blad, B.L. 1983. Atmospheric demand for water. In Crop-Water Relations, I.D. Teare and M.M. Peet, editors. John Wiley & Sons, New York. pp.1-44.

Blad, B.L. and N.J. Rosenberg. 1976. Evaluation of resistance and mass transport evapotranspiration models requiring canopy temperature data. Agronomy Journal 68:764-769.

Bouttier, F., J.-F. Mahfouf, and J. Noilhan. 1993. Sequential assimilation of soil moisture from atmospheric low-level parameters. Part I: Sensitivity and calibration studies. Journal of Applied Meteorology 32:1335-1351.

Bowen, I.S. 1926. The ratio of heat losses by conduction and by evaporation from any water surface. Physical Review 27:779-787.

Brock, F.V., K.C. Crawford, R.L. Elliott, G.W. Cuperus and S.J. Stadler. 1995. The Oklahoma Mesonet: a technical overview. Journal of Atmospheric and Oceanic Technology 12(1):1-19.

Brown, S.R. 1995. Amendments to NOAA Technical Memorandum 107 Appendix-B for NOAA-J/14. USDC, NOAA, NESDIS, Washington, DC.

Brutsaert, W. 1982. Evaporation into the Atmosphere: Theory, History and Applications. D. Reidel Publishing Company, Boston, MA.

Burgan, R.E. and R.A. Hartford. 1993. Monitoring Vegetation Greenness with Satellite Data. General Technical Report INT-297, U.S. Forest Service.

Calder, I.R. 1993. Hydrologic effects of land-use change. Chapter 13 in Handbook of Hydrology (D.R. Maidment editor). McGraw-Hill Inc., New York. pp. 13.1-13.50

Caselles, V. and Delegido, J. 1987. A simple model to estimate the daily value of the maximum evapotranspiration from satellite temperature and albedo images. International Journal of Remote Sensing 8:1151-62.

Che, N., and J.C. Price. 1992. Survey of radiometric calibration results and methods for visible and near infrared channels of NOAA-7,-9, and -11 AVHRRs. Remote Sensing of Environment, 41:19-27.

Chehbouni, A., Y.H. Kerr, J. Qi, A. R. Huete and S. Sorooshian. 1994. Toward the development of a multidirectional vegetation index. Water Resources Research 30(5):1281-1286.

Chong, D.L.S, E.Mourin, and J.P. Gastellu-Etchegorry. 1993. Relating the Global Vegetation Index to net primary productivity and actual evapotranspiration over Africa. International Journal of Remote Sensing 14(8):1517-1546.

Choudhury, B.J. 1994. Synergism of multispectral satellite observations for estimating regional land surface evaporation. Remote Sensing of Environment 49(3):264-274.

Choudhury, B. J., T.J. Dorman and A.Y. Hsu. 1995. Modeled and observed relations between the AVHRR split window temperature difference and atmospheric precipitable water over land surfaces. Remote Sensing of Environment 51:281-290.

Christensen, S. and J. Goudriaan. 1993. Deriving light interception and biomass from spectral reflectance ratio. Remote Sensing of Environment 43:87-95.

Cicone, R.C. and M.D. Metzler. 1984. Comparison of Landsat Mss, Nimbus-7 CZCS, and NOAA-7 AVHRR features for land-use analysis. Remote Sensing of Environment 14:257-265.

Cierniewski, J. 1989. The influence of the viewing geometry of bare rough soil surfaces on their spectral response in the visible and near-infrared range. Remote Sensing of Environment 27:135-142.

Cihlar, J and J. Howarth. 1994. Detection and removal of cloud contamination from AVHRR images. IEEE Transactions on Geoscience and Remote Sensing 32(3):583-589.

Cihlar, J., D. Manak, and N. Voisin. 1994. AVHRR bidirectional reflectance effects and compositing. Remote Sensing of Environment 48(1):77-88.

Clevers, J.G. 1988. The derivation of a simplified reflectance model for the estimation leaf area index. Remote Sensing of Environment 25:53-70.

Coll, C., V. Caselles, J.A. Sobrino, and E. Valor. 1994. On the atmospheric dependence of the split-window equation for land surface temperature. International Journal of Remote Sensing, 15(1):105-122.

Cooper, D.I. and G. Asrar. 1989. Evaluating atmospheric correction models for retrieving surface temperatures from the AVHRR over a tall grass prairie. Remote Sensing of Environment 27:93-192.

Crist, E.P. and R.C. Cicone. 1984. Application of the Tasseled Cap concept to simulated Thematic Mapper data. Photogrammetric Engineering and Remote Sensing 50(3):343-352.

Crist, E.P. and R.J. Kauth. 1986. The Tasseled Cap de-mystified. Photogrammetric Engineering and Remote Sensing 52:1:81-86.

Crosson, W.L. and C.A. Laymon. 1995. A remote-sensing based technique to account for sub-grid scale variability of land surface properties. American Meteorological Society Conference on Hydrology Preprints, January 15-20, Dallas, Texas. pp. 165-170.

Curran, P.J. and G.M. Foody. 1994. Environmental issues at regional to global scales. In Environmental Remote Sensing from Regional to Global Scales (G. Foody and P. Curran, editors). John Wiley & Sons, New York. pp. 1-7.

Dalu, G. 1986. Satellite remote sensing of atmospheric water vapor. International Journal of Remote Sensing 7(9):1089-1097.

Davidoff, B. and H.M. Selim. 1988. Correlation between spatially variable soil moisture content and soil temperature. Soil Science 145 (1):1-10.

Davies-Colley, R.J., W.N. Vant and D.G. Smith. 1993. Color and Clarity of Natural Waters - Science and Management of Optical Water Quality. Ellis Horword, New York. 310 pp.

Dedieu, G. 1990. Land surface spectral reflectances and vegetation index derived from NOAA/AVHRR. Proceedings of the Workshop on the Use of Satellite-Derived Vegetation Indices in Weather and Climate Prediction Models, Camp Springs, MD, Feb. 26-27, 1990. USDC, NOAA. pg. 62-70.

DeFries, R.S. and J.R.G. Townshend. 1994. Global land cover: comparison of ground-based data sets to classifications with AVHRR data. In Environmental Remote Sensing from Regional to Global Scales (G. Foody and P. Curran, editors). John Wiley & Sons, New York. pp. 84-110.

de Haan, J.F., J.W. Hovenier, J.M. Kokke and H.T van Stokkom. 1991. Removal of atmospheric influences on satellite-borne imagery: a radiative transfer approach. Remote Sensing of Environment 37(1):1-2.

Deirmendjian, D. 1969. Electromagnetic scattering on spherical polydispersions. American Elsevier Publishing Company, New York. 290 pp.

Dergileva, I. 1995. On the derivation of surface temperature from AVHRR. American Meteorological Society Conference on Hydrology Preprints, January 15-20, Dallas, Texas. pp. 133-136.

Dettinger, M.D. and J.L. Wilson. 1981. First order analysis of uncertainty in numerical models of groundwater flow. Part 1. Mathematical development. Water Resources Research 17(1): 149-161.

Di, L., and D.C. Rundquist. 1994. A one-step algorithm for correction and calibration of AVHRR level 1b data. Photogrammetric Engineering and Remote Sensing 60 (2): 165-171.

Diak, G.R., R. M. Rabin, K.P. Gallo and C.M. Neale. 1995. Regional-scale comparisons of NDVI, soil moisture indices from surface and microwave data and surface energy budgets evaluated from satellite and in-situ data. American Meteorological Society Conference on Hydrology Preprints, January 15-20, Dallas, Texas. pp. 161-164.

Diaz, R.A., A.D. Matthias, and R.J. Hanks. 1983. Evapotranspiration and yield estimation of spring wheat from canopy temperature. Agronomy Journal 75:805-810.

D'Iorio, M.A. 1990. Calibration and compositing of NOAA data. Proceedings of the Workshop on the Use of Satellite-Derived Vegetation Indices in Weather and Climate Prediction Models, Camp Springs, MD, Feb. 26-27, 1990. USDC, NOAA. pp. 45-55.

Doorenbos, J. and W.O. Pruitt. 1977. Guidelines for predicting crop water requirements. FAO Irrigation and Drainage Paper 24. Food and Agriculture Organization of the United Nations, Rome.

Doran, J.C. 1993. The sensitivity of flux parameterizations to surface characteristics. Proceedings of the Thir Atmospheric Radiation Measurement (ARM) Science Team Meeting, March 1-4, Norman, Oklahoma. U.S. Department of Energy, Washington, DC. pp. 73-76.

Dugas, W.A., W.L. Bland, and G.F. Arkin. 1985. Evapotranspiration measurements from different-sized lysimeters. In Advance in Evapotranspiration. ASAE Publication 14-85, ASAE, St. Joseph, Michigan. pp. 208-215.

Duncan, J., D. Stow, J. Franklin and A. Hope. 1993. Assessing the relationship between spectral vegetation indices and shrub cover in the Jornada Basin, New Mexico. International Journal of Remote Sensing 14(8):3395-3416.

Eck, T.F., and B.N. Holben. 1994. AVHRR split window temperature differences and total precipitable water over land surfaces. International Journal of Remote Sensing 15(3):567-582.

229

Engman, E.T., and R.J. Gurney. 1991. Remote Sensing in Hydrology. Chapman and Hall, New York.

Engman, E.T. 1993. Chapter 24: Remote Sensing. In Handbook of Hydrology, D.R. Maidment, editor. McGraw-Hill, Inc., New York.

Everdale, F. 1985. Satellite Oceanography - Volume 1: NOAA-N Advanced Very High Resolution Radiometer Digital Data. Assessment and Information Services Center, 3300 Whitehaven St, NW, Washington, DC 20235.

Feddes, R.A., M. Menenti, P. Kabat, and W.G.M Bastiaanssen. 1993. Is large-scale inverse modelling of unsaturated flow with aerial average evaporation and surface soil moisture as estimated from remote sensing feasible? Journal of Hydrology 143:125-152.

Ferencz, C., G. Tarcsai, and J. Lichtenberger. 1993. Correction of atmospheric effects of satellite remote sensing data (Landsat MSS-NOAA AVHRR) for surface canopy investigations. International Journal of Remote Sensing 14(18):3417-3431.

Fisher, D.K. 1995. Evapotranspiration measurements and resistance parameter estimation under range/pasture conditions in Oklahoma. PhD. Dissertation, Oklahoma State University, Stillwater.

Fisher, D.K. and R.L. Elliott. 1994. Experience with remote, low-cost, weighing lysimeters. Presented at the June 19-22 International Summer Meeting, Paper No. 94-2077. ASAE 2950 Niles Rd., St. Joseph, MI 49085-9659 USA.

Fogiel, M. 1992. Handbook of Mathematical, Scientific, and Engineering Formulas, Tables, Functions, Graphs, Transforms. Staff of Research and Education Association, 61 Ethel Road West, Piscataway, NJ. pg. 689.

Foster, B.C. 1984. Derivation of atmospheric correction procedures for LANDSAT MSS with particular reference to urban data. International Journal of Remote Sensing 5(5): 799-817.

Gillies, R.R., J.Cui, T.N. Carlson, W.P. Kustas and K.S. Humes. 1995. Implications of the NDVI and surface radiant temperature relationship. American Meteorological Society Conference on Hydrology Preprints, January 15-20, Dallas, Texas. pp. 157-160.

Goward, S.N., D.G. Dye, S. Turner and J. Yang. 1993. Objective assessment of the NOAA global vegetation index data product. International Journal of Remote Sensing 14(18): 3365-3394.

Goward, S.N., R.H. Waring, D.G. Dye and J. Yang. 1994. Ecological remote sensing at OTTER: Satellite macroscale observations. Ecological Applications 4(2): 322-343.

GRASS, 1991. Geographic Resources Analysis Support System (GRASS). U.S. Army Construction Engineering Research Laboratory.

Gupta, R.K. 1993. Comparative study of AVHRR ratio vegetation index and normalized difference vegetation index in district level agricultural monitoring. International Journal of Remote Sensing 14:1:53-73.

Gutman, G., D. Tarpley, A. Ignatov and S. Olson. 1995. Derivation of land characteristics from AVHRR for application to global hydrology. American Meteorological Society Conference on Hydrology Preprints, January 15-20, Dallas, Texas. pp. 125-128.

Guttman, N.B. 1991. A sensitivity analysis of the Palmer hydrologic drought index. Water Resource Bulletin 27(5):797-807.

Hanan, N.P., S.D. Prince, and B.H. Holben. 1995. Atmospheric correction of AVHRR data for biophysical remote sensing of the Sahel. Remote Sensing of Environment 51:306-316.

Hargreaves, G.H. 1994. Defining and using reference evapotranspiration. Journal of Irrigation and Drainage Engineering 120(6):1132-1139.

Hargreaves, G.H., and Z.A. Samani. 1985. Reference crop evapotranspiration from temperature. Applied Engineering in Agriculture 1(2):96-99.

Hatfield, J.L. 1983. Evapotranspiration from remote sensing methods. In Advances in Irrigation, D. Hillel, Ed. Academic Press, NY.

Houghton, J.T. 1986. The Physics of Atmospheres, Second Edition. Cambridge University Press, New York.

Huete, A.R. 1988. A soil-adjusted vegetation index (SAVI). Remote Sensing of the Environment 25:89-105.

Huete, A.R., G. Hua, J. Qi, A. Chehbouni and W.J.D. van Leeuwen. 1992. Normalization of multidirectional red and NIR reflectances with the SAVI. Remote Sensing of Environment 41: 143-154.

Humes, K.S., W.P. Kustas, M.S. Moran, W.D. Nichols, and M.A. Weltz. 1994. Variability of emissivity and surface temperature over a sparsely vegetated surface. Water Resources Research 30(5):1229-1310.

Humes, K.S., W.P. Kustas and T.J. Schmugge. 1995. Effects of soil moisture and spatial resolution on the surface temperature/vegetation index relationships for a semiarid watershed. American Meteorological Society Conference on Hydrology Preprints, January 15-20, Dallas, Texas. pp. 147-151.

Hurtado, E., M.M Artigao, and V. Caselles. 1994. Estimating maize (Zea mays) evapotranspiration from NOAA-AVHRR thermal data in the Albacete area, Spain. International Journal of Remote Sensing 15(10):2023-2037.

Iqbal, M. 1983. An Introduction to Solar Radiation. Academic Press, New York. 390 pp.

Jackson, R.D. 1985. Estimating aerial evapotranspiration by combining remote and ground-based data. In Remote Sensing Applications for Consumptive Use (Evapotranspiration), AWRA Monograph Series No. 6, Johnson, A.I. and A. Rango, editors.

Jackson, R.D., R.J. Reginato and S.B. Idso. 1977. Wheat canopy temperature: A practical tool for evaluation of water requirements. Water Resources Research 13:651-656.

Jackson, R.D., S.B. Idso, R.J. Reginato and P.J. Pinter Jr. 1981. Canopy temperature as a crop water stress indicator. Water Resources Research 17:1133-1138.

Jackson, R.D. J.L. Hatfield, R.J. Reginato, S.B. Idso, and P.J. Pinter, Jr. 1983. Estimation of daily evapotranspiration from one time-of-day measurements. Agricultural Water Management 7:351-362.

Jackson, R.D., M.S. Moran, L.W. Gay, and L.H. Raymond. 1987. Evaluating evaporation from field crops using airborne radiometry and ground-based meteorological data. Irrigation Science 8:81-90.

Jedlovec, G.J. 1990. Precipitable water estimation from high-resolution split window radiance measurements. Journal of Applied Meteorology 29:863-877.

Jensen, M.E. 1968. Water consumption by agricultural plants. In Water Deficits and Plant Growth, Vol. II, Academic Press, NY. pp. 1-22.

Jensen, M.E., R.D. Burman, and R.G. Allen. 1990. Evapotranspiration and Irrigation Water Requirements. ASCE Manuals and Reports on Engineering Practice No. 70.

Justice, C.O., T.F. Eck, D. Tanre, and D.B. Holben. 1991. The effect of water vapor on the normalized difference vegetation index derived for the Sahelian region from NOAA AVHRR data. International Journal of Remote Sensing 12(6):1165-1187.

Kasten, F. and E. Raschke. 1974. Reflection and transmission terminology by analogy with scattering. Applied Optics 13(3):460-464.

Kaufman, Y.J. and B.N. Holben. 1993. Calibration of the AVHRR visible and near-IR bands by atmospheric scattering, ocean glint and desert reflection. International Journal of Remote Sensing 14:1:21-52.

Kauth, R.J., and G.S. Thomas. 1976. The Tasseled Cap -- A graphical description of the spectral-temporal development of agricultural crops as seen by Landsat. Proceedings of the Symposium on Machine Processing of Remotely Sensed Data, Purdue University, West Lafayette, Indiana, pp. 4B41-4B51.

Kelso, T.S. 1992. TrakStar/SGP4 Version 2.15. 2340 Raider Drive, Fairborn, Ohio.

Kerr, Y.H., J.P. Lagouarde, and J. Imbernon. 1992. Accurate land surface temperature retrieval from AVHRR data with use of an improved split window algorithm. Remote Sensing of Environment 41:197-209.

Kidwell, K.B., Editor. 1991. NOAA Polar Orbiter Data Users Guide (TIROS-N, NOAA-6, NOAA-7, NOAA-8, NOAA-9, NOAA-10, NOAA-11, and NOAA-12). NOAA, NESDIS, National Climatic Data Center, Satellite Data Service Division, Princeton Executive Square, Room 100, Washington, DC, 20233.

Kirkham, M.B. and E.T. Kanemasu. 1983. Chapter 15: Wheat. In Crop-Water Relations, John Wiley and Sons. pp. 481-520.

Kleespies, T.J. and L.M. McMillin. 1990. Retrieval of precipitable water from observations in the split window over varying surface temperatures. Journal of Applied Meteorology 29(9):851-862.

Kneizys, F.X, E.P. Shettle, W.O. Gallery, J.H. Chetwynd, Jr., L.W. Abreu, J.E.A. Shelby, S.A. Clough, and R.W. Fenn. 1983. Atmospheric transmittance/radiance computer code LOWTRAN 6. AFGL-TR-83-0187, Environmental Research Paper No. 846, Optical Physics Division, Air Force Geophysics Laboratory, Hanscom, Mass.

Kneizys, F.X, E.P. Shettle, L.W. Abreu, J.H. Chetwynd, G.P. Anderson, W.O. Gallery, J.E.A. Shelby, and S.A. Clough. 1988. Atmospheric transmittance/radiance computer code LOWTRAN 7. AFGL-TR-88-0177. Optical Physics Division, Air Force Geophysics Laboratory, Hanscom, Mass.

Korobov, R.M. and V.Y. Railyan. 1993. Canonical correlation relationships among spectral and phytometeric variables for twenty winter wheat fields. Remote Sensing of Environment 43:1-10.

Kustas, W.P., E.M. Perry, P.C. Doraiswamy, and M.S. Moran. 1994. Using satellite remote sensing to extrapolate evapotranspiration estimates in time and space over a semiarid range land basin. Remote Sensing of Environment 49:275-286.

Lagouarde, J.P. and Y. Brunet. 1993. A simple model for estimating the daily upward longwave surface flux from NOAA-AVHRR data. International Journal of Remote Sensing 14(5):907-925.

Lenoble, J. 1993. Atmospheric Radiative Transfer. A. Deepack Publishing, Hampton, VA.

Leonard, R.A., W.G. Knisel, and D.A. Still. 1987. GLEAMS: Groundwater Loading Effects of Agricultural Management Systems. Transactions of the ASAE 30:1403-1418.

✓ Li, Z-L, and F. Becker. 1993. Feasibility of Land Surface Temperature and Emissivity Determination from AVHRR Data. Remote Sensing of Environment 43:67-85.

Lillesand, T.M., and R.W. Kiefer. 1994. Remote Sensing and Image Interpretation, Third Edition. John Wiley & Sons, New York. pp. 12-14.

Lindsey, S.D., R.W. Gunderson, and J.P. Riley. 1993. Spatial distribution of point soil moisture estimates using LANDSAT TM data and fuzzy-c classification. Water Resources Bulletin 28:865-875.

Los, S.O. 1993. Calibration adjustment of the NOAA AVHRR Normalized Difference Vegetation Index without recourse to component channel 1 and 2 data. International Journal of Remote Sensing 14(10):1907-1917.

Loveland, T.R. and D.O. Ohlen. 1993. Experimental AVHRR land data sets for environmental monitoring and modeling. In Environmental Modeling with GIS (M.F. Goodchild, B.O. Parks, L.T. Steyaert editors). Oxford University Press, New York. pp. 379-385.

Martin, D.L., N.L. Klocke and D.L. DeHaan. 1985. Measuring evaporation using mini-lysimeters. In Advances in Evapotranspiration. ASAE Publication 14-85, ASAE, St. Joseph, Michigan. pp. 231-240.

Mather, P.M. 1994. Earth observation data - or information? In Environmental Remote Sensing from Regional to Global Scales, G. Foody and P. Curran, editors. John Wiley & Sons, New York. pp. 202-213.

McCartney, E.J. 1976. Optics of the Atmosphere: Scattering by Molecules and Particles. John Wiley & Sons, New York. 408 pp.

McClain, E.P., W.G. Pichel, C.C. Walton, Z. Ahmad, and J. Sutton. 1983. Multichannel improvements to satellite-derived global sea surface temperatures. Advance Space Research 2:43-47.

234

McClatchey, R.A., R.W. Fenn, J.E. Selby, F.E. Volz, and J.S. Garing. 1972. Optical Properties of the atmosphere, 3rd ed, Environmental Research Paper No. 411, Air Force Cambridge Research Laboratories.

McGregor, J., and A.J. Gorman. 1994. Some Considerations for using AVHRR data in climatological studies: I. Orbital characteristics of NOAA satellites. International Journal of Remote Sensing 15(3):537-548.

McMillin, L.M. 1975. Estimation of sea surface temperatures from two infrared window measurements with different absorption. Journal of Geophysical Research 80(36):5113-5117.

Mekler, Y. and Y.J. Kaufman. 1995. Possible causes of calibration degradation of the Advanced Very High Resolution Radiometer visible and near-infrared channels. Applied Optics 34(6):1059-1062.

Millington, A.C., J. Wellens, J.J. Settle and R.J. Saull. 1994. Explaining and monitoring land cover dynamics in drylands using multi-temporal analysis of NOAA AVHRR imagery. In Environmental Remote Sensing from Regional to Global Scales (G.Foody and P. Curran, editors). John Wiley & Sons, New York. pp. 16-43.

Mintz, Y., and G.K. Walker. 1993. Global fields of soil moisture and land surface evapotranspiration derived from observed precipitation and surface air temperature. Journal of Applied Meteorology 32:1305-1334.

Mitchell, K. 1993. Use of Satellite-Derived Surface Fields for NWP. NOAA Colloquium on Operation Environmental Prediction. July, 1993, Silver Spring, Maryland.

Mitchell, R.M. and D.M. O'Brien. 1993. Correction of AVHRR short-wave channels for the effects of atmospheric scattering and absorption. Remote Sensing of Environment 46:129-145.

Monteith, J.L. 1981. Evaporation and surface temperature. Quarterly Journal of the Royal Meteorological Society 107:1-27.

Moran, M.S., R.D. Jackson, L.H. Raymond, L.W. Gay and P.N. Slater. 1989. Mapping surface energy balance components by combining Landsat Thematic Mapper and ground-based meteorological data. Remote Sensing of Environment 30:77-87.

Moran, M.S., R.D. Jackson, G.F. Hart, P.N. Slater, R.J. Bartel, S.F. Biggar, D.I. Gellman and R.P. Santer. 1990. Obtaining surface reflectance factors from atmospheric and view angle corrected Spot-1 HVR Data. Remote Sensing of Environment 32:203-214.

Moran, M.S. and R.D. Jackson. 1991. Assessing the spatial distribution of evaporation using remotely sensed inputs. Journal of Environmental Quality 20(4):725-737.

Moran, M.S., W.P. Kustas, A. Vidal, D.I. Stannard, J.H. Blanford and W.D. Nichols. 1994a. Use of ground-based remotely sensed data for surface energy balance evaluation of a semiarid rangeland. Water Resources Research 30(5):1339-1349.

Moran, M.S., T.R. Clarke, W.P. Kustas, M.Weltz, and S.A. Amer. 1994b. Evaluation of hydrologic parameters in a semiarid rangeland using remotely sensed spectral data. Water Resources Research 30(5):1287-1297.

Moran, M.S., T.R. Clarke, Y. Inoue and A. Vidal. 1994c. Estimating crop water deficit using the relation between surface-air temperature and spectral vegetation index. Remote Sensing of Environment 46(3): 246-263.

Moreno, J.F. and J. Melia. 1993. A method for accurate geometric correction of NOAA AVHRR HRPT data. IEEE Transaction on Geoscience and Remote Sensing 13:1:204-226.

Morton, F.I. 1983. Operation Estimates of Aerial Evapotranspiration and Their Significance to the Science and Practice of Hydrology. Journal of Hydrology 66:1-76.

Nemani, R.R., and S.W. Running. 1989a. Testing a theoretical climate-soil-leaf area hydrologic equilibrium of forests using satellite data and ecosystem simulation. Agricultural and Forest Meteorology 44:245-260.

Nemani, R.R. and S.W. Running. 1989b. Estimation of regional surface resistance to evapotranspiration from NDVI and thermal-IR AVHRR data. Journal of Applied Meteorology 28:276-284.

NESDIS, 1985. NESDIS Programs: NOAA Satellite Operations. NOAA National Environmental Satellite, Data, and Information Service, Washington, D.C.

Nicholson, S.E. and P. Santos. 1995. A simple model of vegetation atmospheric interactions. Conference on Hydrology Preprints, January 15-20, Dallas, Texas. American Meteorological Society.

Outcalt, S.I. 1972. The development and application of a simple digital surface-climate simulator. Journal of Applied Meteorology 11:629-636.

Or, D. and R.J. Hanks. 1992. Spatial and temporal soil water estimation considering soil variability and evapotranspiration uncertainty. Water Resources Research 28(3):803-814.

Palmer, W.C. 1965. Meteorological Drought. Research Paper No. 45, USDC, Weather Bureau, Washington, DC.

Paltridge, G.W. and C.M.R. Platt. 1976. Radiative Processes in Meteorology and Climatology. Elsevier Scientific Publishing Company, New York. 318 pp.

Paltridge, G.W. and R.M. Mitchell. 1990. Atmospheric and viewing angle correction of vegetation indices and grassland fuel moisture content derived from NOAA/AVHRR. Remote Sensing of Environment 31:121-135.

Pelton, W.L. 1961. The use of lysimetric methods to measure evapotranspiration. Proceedings of the 2nd Hydrology Symposium, Toronto. Queen's Printer, Ottawa, Canada. pp. 106-134.

Penman, H.L. 1948. Natural evaporation from open water, bare soil and grass. Proceedings from the Royal Society of London, Series A:120-144.

Perry, C.R. and L.F. Lautenschlage. 1984. Functional equivalence of spectral vegetation indices. Remote Sensing of Environment 14:169-182.

Perry, E.M., and M.S. Moran. 1994. An evaluation of atmospheric corrections of radiometric surface temperatures for a semiarid rangeland watershed. Water Resources Research 30(5): 1261-1269.

Pinter, P.J., R.D. Jackson and S.M. Moran. 1990. Bidirectional reflectance factors of agricultural targets: a comparison of ground-, aircraft-, and satellite-based observations. Remote Sensing of Environment 32:215-228.

Planet, W.G. (Editor). 1988. Data extraction and calibration of TIROS-N/NOAA Radiometers. NOAA Technical Memorandum NESDIS 107 - Rev. 1. USDC, NOAA, NESDIS, Washington, DC.

Potdar, M.B. 1993. Sorghum yield modelling based on crop growth parameters determined from visible and near-IR channel NOAA AVHRR data. International Journal of Remote Sensing 14(5):895-905.

Prata, A.J. 1994. Land surface temperatures derived from the advanced very high resolution radiometer and the along-track scanning radiometer 2. Experimental results and validation of AVHRR algorithms. Journal of Geophysical Research 96(D6):13025-13058.

Price, J.C. 1984. Land surface temperature measurements from the split window channels of the NOAA 7 Advanced Very High Resolution Radiometer. Journal of Geophysical Research 89:7231-7237.

Price, J.C. 1990. Using spatial context in satellite data to infer regional scale evapotranspiration. IEEE Transactions on Geoscience and Remote Sensing 28(2):940-948.

Priestley, C.H.B. and R.J. Taylor. 1972. One the assessment of surface heat flux and evaporation using large-scale parameters. Monthly Weather Review 100:81-92.

Prueger, J. 1994. Personal correspondence with. USDA, ARS National Soil Tilth Laboratory, Ames, Iowa.

Pruitt, W.O. and F.J. Lourence. 1985. Experiences in lysimetry for evapotranspiration and surface drag measurements. In Advance in Evapotranspiration. ASAE Publication 14-85, ASAE, St. Joseph, Michigan. pp. 51-69.

Qi, J., A. Chehbouni, A.R. Huete, Y.H. Kerr and S. Sorooshian. 1994. A modified soil adjusted vegetation index. Remote Sensing of Environment 48:119-126.

Rao, P.K., S.J. Holmes, R.K. Anderson, J.S. Winston and P.E. Lehr, editors. 1990a. Chapter IV-2: ATN and GOES sensors. In Weather Satellites: Systems, Data, and Environmental Applications. American Meteorological Society, Boston. pp. 118-132.

Rao, P.K., S.J. Holmes, R.K. Anderson, J.S. Winston and P.E. Lehr, editors. 1990b. Chapter VIII-4: Sea Surface Temperature. In Weather Satellites: Systems, Data, and Environmental Applications. American Meteorological Society, Boston. pp. 378-390.

Rao, P.K., S.J. Holmes, R.K. Anderson, J.S. Winston and P.E. Lehr, editors. 1990c. Chapter X-2: Solar radiation, max/min temperature, and daily precipitation. In Weather Satellites: Systems, Data, and Environmental Applications. American Meteorological Society, Boston. pp. 460-465.

Reginato, R.J., Jackson, R.D. and Pinter, Jr, P.J. 1985. Evapotranspiration calculated from remote multispectral and ground station meteorological data. Remote Sensing of Environment 18:75-89.

√ Reutter, H., F.S. Olesen, and H. Fischer. 1994. Distribution of the brightness temperature of land surfaces determined from AVHRR data. International Journal of Remote Sensing 15(1): 95-104.

Richards, J.A. 1986. Remote Sensing Digital Image Analysis, An Introduction. Springer-Verlag, New York. pp. 50-56.

Ritchie, J.T. 1972. Model for prediction of evaporation from a row crop with incomplete cover. Water Resources Research 8(5):1204-1213.

Rosborough, G.W., D.G. Baldwin, and W.J. Emery. 1994. Precise AVHRR image navigation. IEEE Transactions on Geoscience and Remote Sensing 32(3):644-657.

Rosema, A. 1993. Using METEOSAT for Operational Evapotranspiration and Biomass Monitoring in the Sahel region. Remote Sensing of Environment 46:27-44.

Rosenberg, N.J., and W. Powers. 1970. Potential for evapotranspiration and its manipulation in the Plains region. Proceedings of the Symposium on Evapotranspiration in the Great Plains. Great Plains Agricultural Council Publication No. 50. pp. 275-300.

Rosenberg, N.J., B.L. Blad, S. B. Verma. 1983. Microclimate, Second Edition. John Wiley & Sons, NY.

Running, S.W. 1991. Computer simulation of regional evapotranspiration by integrating landscape biophysical attributes with satellite data. In Land Surface Evaporation: Measurement and Parameterization (T.J. Schmugge and J. Andre, editors). Springer-Verlag, New York. pp. 337-358.

Sandholt, I and H.S. Anderson. 1993. Derivation of actual evapotranspiration in the Senegalese Sahel, using NOAA-AVHRR data during the 1987 growing season. Remote Sensing of Environment 48:164-172.

Saunders, R.W. and K.T. Kriebel. 1988. An improved method for detecting clear sky and cloudy radiances from AVHRR data. International Journal of Remote Sensing 9(1):123-150.

Schiebe, F. R., J.A. Harrington, Jr., and J.C. Ritchie. 1992. Remote sensing of suspended sediments: the Lake Chicot, Arkansas project. International Journal of Remote Sensing 13:1487-1509.

Schmuggee, T.J. and F.Becker. 1991. Remote sensing observations for the monitoring of land-surface fluxes and water budgets. In Land Surface Evaporation: Measurement and Parameterization (T.J. Schmugge and J. Andre, editors). Springer-Verlag, New York. pp. 337-358.

Seevers, P.M. and Ottman. 1994. Evapotranspiration estimation using a normalized difference vegetation index transform of satellite data. Hydrological Sciences 39(4):333-345.

Seguin, B., Assad, E., Freteaud, J.P, Imbernon, J. Kerr, Y. and Lagouarde, J.P. 1989. Use of meteorological satellites for water balance monitoring in Sahelian regions. International Journal of Remote Sensing 10:1101-17.

Seguin, B., D. Courault, and M. Guerif. 1994. Surface temperature and evapotranspiration: application of local scale methods to regional scales using satellite data. Remote Sensing of Environment 49:287-295.

Shih, S.F. and J.D. Jordan. 1993. Use of Landsat thermal-IR data and GIS in soil moisture assessment. Journal of Irrigation and Drainage Engineering 119(5):868-879.

Shuttleworth, W.J. 1993. Evaporation. Chapter 4 in Handbook of Hydrology (D.R. Maidment editor). McGraw-Hill Inc., New York. pp. 4.1-4.53

Shuttleworth, W.J. and J.S. Wallace. 1985. Evaporation from sparse crops-an energy combination theory. Quarterly Journal of the Royal Meteorological Society 111:839-855.

Shuttleworth, W.J. and R.J. Gurney. 1990. The theoretical relationship between foliage temperature and canopy resistance in sparse crops. Quarterly Journal of the Royal Meteorological Society 116:497-519.

Singh, S.M. 1989. Lowest-order correction to GVI data for solar zenith angle effect. International Journal of Remote Sensing 10(4,5):819-825.

Smith, R.C.G., and B.J. Choudhury. 1990. Relationship of multispectral satellite data to land surface evaporation from the Australian continent. International Journal of Remote Sensing 11:2069-2088.

Song, Z. and L.D. James. 1992. An objective test for hydrologic scale. Water Resources Bulletin 28(5):833-843.

Stannard, D.I., J.H. Blanford, W.P. Kustas, W.D. Nichols, S.A. Amer, T.J. Schmugge, and M.A. Weltz. 1994. Interpretation of surface flux measurements in heterogeneous terrain during the Monsoon '90 experiment. Water Resources Research 30(5):1227-1239.

Stone, J.F. 1977. Evapotranspiration Control on Agricultural Lands. Soil and Crop Science Society of Florida Proceeding, 37, Nov-Dec.

Stone, L.R. and M.L. Horton. 1974. Estimating evapotranspiration using canopy temperatures: field evaluation. Agronomy Journal 66:450-454.

Sullivan, J.T. 1995. A simple, accurate method to compute brightness temperature and/or radiance for the thermal infrared channels of the Advanced Very High Resolution Radiometer (AVHRR). International Journal of Remote Sensing 16(4):773-777.

Swinbank, W.C. 1951. The measurement of vertical transfers of heat and water vapor by eddies in the lower atmosphere. Journal of Meteorology 8:135-145.

Taconet, O., R. Bernard and D. Vidal-Madjar. 1986. Evapotranspiration over an agricultural region using a surface flux/temperature model based on NOAA-AVHRR data. Journal of Climate and Applied Meteorology 25:284-307.

Taiz, L and E. Zeiger. 1991. Plant Physiology. Benjamin/ Cummings Publishing Company, Inc., New York.

Takashi, H., S. Uchida, and K. Kotoda. 1989. Development of a system to estimate evapotranspiration over complex terrain using Landsat MSS, elevation and meteorological data. Hydrological Sciences Journal 34:635-645.

Tanner B.D., M.S. Tanner, W.A. Dugas, E.C. Campbell, and B.L. Bland. 1985. Evaluation of an operational eddy correlation system for evapotranspiration measurements. In Advances in Evapotranspiration. ASAE Publication 14-85, ASAE, St. Joseph, Michigan. pp. 87-99.

Tanre, D., C. Deroo, P. Duhaut, M. Herman, J.J. Morcrette, J.Perbos, and P.Y. Deschamps. 1990. Description of a computer code to simulate signal in the solar spectrum: the 5S code. International Journal of Remote Sensing 11(4):659-668.

Tanre, D., B.N. Holben, and Y.J. Kaufman. 1992. Atmospheric correction algorithm for NOAA-AVHRR products: theory and application. IEEE Transactions on Geoscience and Remote Sensing 30(2):231-248.

Tarpley, J.D. 1988. Some climatological aspects of satellite-observed surface heating in Kansas. Journal of Applied Meteorology 27:20-29.

Tarpley, J.D. 1990. NOAA's global vegetation index (GVI) product: review and future prospects. Proceedings of the Workshop on the Use of Satellite-Derived Vegetation Indices in Weather and Climate Prediction Models, Camp Springs, MD, Feb. 26-27, 1990. USDC, NOAA. pg. 45-55.

Tarpley, J.D. 1994. Monthly Evapotranspiration from Satellite and Conventional Meteorological Observations. Journal of Climate 7:704-713.

Teare, I.D. and M.M. Peat. 1983. Crop Water Relations. Wiley Press, New York.

Teillet, P.M. 1992. An algorithm for the radiometric and atmospheric correction of AVHRR data in the solar reflective channels. Remote sensing of Environment 41:185-195.

Thunnissen, H.A.M., and G.J.A. Nieuwenhuis. 1990. A simplified method to estimate regional 24-h evapotranspiration from thermal infrared data. Remote Sensing of Environment 31:211-225.

Turner, R.E., and M.M. Spencer. 1972. Atmospheric model for correction of spacecraft data. Proceedings of the Eighth International Symposium on Remote Sensing of Environment 2:895-934.

Turner, R.E., W.A. Malila, and R.F. Nalepka. 1971. Importance of atmospheric scattering in remote sensing, or everything you've always wanted to know about atmospheric scattering but were afraid to ask. Proceedings of the Seventh International Symposium on Remote Sensing of Environment 3:1651-1695.

USDA. 1993. Chapter 2: Irrigation water requirements. Part 623 of the National Engineering Handbook, USDA, Soil Conservation Service, Washington, DC.

van Bavel, C.H.M. 1966. Potential evaporation: The combination concept and its experimental verification. Water Resources Research 2:455-467.

Verma, S.B., N.J. Rosenberg, and B.L. Blad. 1978. Turbulent exchange coefficients for sensible heat and water vapor under advective conditions. Journal of Applied Meteorology 17:330-338.

Verseghy, D.L., N.A. McFarland, and M. Lazare. 1993. CLASS - A Canadian land surface scheme for GCMS, II. Vegetation model and coupled runs. International Journal of Climatology 13:347-370.

Verstraete, M.M, and B. Pinty. 1990. Surface anisotropy and its implication for NDVI. Proceedings of the Workshop on the Use of Satellite-Derived Vegetation Indices in Weather and Climate Prediction Models, Camp Springs, MD, Feb. 26-27, 1990. USDC, NOAA. pg. 50-55.

Vidal, A. and A. Perrier. 1990. Irrigation monitoring by following the water balance from NOAA-AVHRR thermal infrared data. IEEE Transactions of Geoscience and Remote Sensing 28:949-954.

Wade, G., R. Mueller, P. Cook, and P. Doraiswarmy. 1994. AVHRR Map products for crop condition assessment: a geographic information system approach. Photogrammetric Engineering and Remote Sensing 60(9):1145-1150.

Walthall, C.L., J.M. Norman, J.M. Welles, G. Campbell, and B.L. Blad. 1985. Simple equation to approximate bidirectional reflectance from vegetative canopies and bare soil surfaces. Applied Optics 24(3):383-385.

Wetzel, P.J., D. Atlas, and R. H. Woodward. 1984. Determining soil moisture from geosynchronous satellite infrared data: a feasibility study. Journal of Climate and Applied Meteorology 23:375-391.

Wilson, S.B., and J.M. Anderson. 1986. The applicability of LOWTRAN 5 computer code to aerial thermographic data correction. International Journal of Remote Sensing 7(3):379-388.

Wright, J.L. 1981. Crop coefficients for estimates of daily crop evapotranspiration. Irrigation scheduling for water and energy conservation in the 80's. ASAE, Dec. 18-26.

Woebbecke, D.M., G.E. Meyer, K. Von Bargen, and D.A. Mortensen. 1994. Color indices for weed identification under various soil, residue, and lighting conditions. ASAE Paper No. 943046. ASAE 2950 Niles Rd., St Joseph, MI.

Wooster, M.J., T.S. Richards, and K. Kidwell. 1995. NOAA-11 AVHRR/2 -- Thermal channel calibration update. International Journal of Remote Sensing 16(2):359-363.

Wu, A., and Q. Zhong. 1994. A method for determining the sensor degradation rates of NOAA AVHRR Channels 1 and 2. Journal of Applied Meteorology 33: 118-122.

Xinmei, H, T.J. Lyons, R.G. Smith, J. Hacker and P. Schwerdtfeger. 1993. Estimation of surface energy balance from radiant surface temperature and NOAA AVHRR sensor reflectances over agricultural and native vegetation. Journal of Applied Meteorology 32:1441-1449.

Yhann, S.R. and J.J. Simpson. 1995. Application of neural networks to AVHRR cloud segmentation. IEEE Transactions on Geoscience and Remote Sensing 33(3):590-604.

# APPENDICES

# APPENDIX A

## Area Weighted ET Estimates

## Appendix A.1: Daily estimates of evapotranspiration (ET) and weather conditions at the Apache lysimeter site.

| DOY [a] | PMon [b] | ETlys [c] | ETcool [d] | ETnative [e] | Kcwheat [f] | ETwheat [g] | ETarea [h] | Days Since Rain [i] | Days Since RF > 10 mm [j] | Tavg [k] $^{\circ}$C | RHmax [l] % | RHmin [m] % | WSavg [n] m s$^{-1}$ | Rad [o] MJ m$^{-2}$ d$^{-1}$ |
|---|---|---|---|---|---|---|---|---|---|---|---|---|---|---|
| | mm d$^{-1}$ | | | | | mm d$^{-1}$ | | | | | | | | |
| 44 | 2.5 | 0.9 | 0.6 | 0.7 | 1.00 | 0.9 | 0.9 | 3 | 44 | 2.3 | 76 | 17 | 2.68 | 18.2 |
| 69 | 2.7 | 0.7 | 0.4 | 0.5 | 1.10 | 0.7 | 0.6 | 1 | 2 | 7.3 | 95 | 23 | 2.01 | 21.9 |
| 74 | 4.1 | 1.0 | 0.6 | 0.7 | 1.15 | 1.1 | 1.0 | 2 | 7 | 14.3 | 92 | 29 | 4.34 | 22.1 |
| 90 | 4.7 | 1.5 | 0.9 | 1.0 | 1.33 | 2.0 | 1.6 | 5 | 23 | 12.3 | 80 | 24 | 4.34 | 25.1 |
| 91 | 5.4 | 2.5 | 1.5 | 1.7 | 1.34 | 3.3 | 2.7 | 6 | 24 | 17.3 | 79 | 25 | 5.01 | 24.9 |
| 102 | 4.8 | 2.9 | 1.8 | 2.1 | 1.46 | 4.3 | 3.4 | 1 | 1 | 11.7 | 86 | 28 | 4.65 | 26.6 |
| 140 | 5.4 | 5.2 | 4.1 | 6.2 | 0.84 | 4.3 | 4.7 | 6 | 18 | 20.3 | 94 | 46 | 2.32 | 28.6 |
| 150 | 4.9 | 7.4 | 5.4 | 8.8 | 0.61 | 4.5 | 5.8 | 0 | 6 | 25.0 | 100 | 45 | 1.34 | 27.3 |
| 151 | 5.6 | 7.3 | 4.4 | 8.8 | 0.59 | 4.3 | 5.6 | 1 | 7 | 26.0 | 100 | 46 | 2.01 | 29.5 |
| 178 | 9.1 | 3.6 | 2.1 | 4.3 | 0.36 | 1.3 | 2.3 | 2 | 16 | 33.3 | 83 | 22 | 3.98 | 28.6 |
| 181 | 7 | 4.8 | 2.9 | 5.8 | 0.57 | 2.7 | 3.6 | 0 | 1 | 28.3 | 87 | 37 | 2.68 | 28.0 |
| 187 | 6.5 | 4.5 | 2.7 | 5.4 | 0.20 | 0.9 | 2.5 | 0 | 7 | 27.0 | 91 | 49 | 3.67 | 25.7 |
| 199 | 7.4 | 6.5 | 3.9 | 7.8 | 0.57 | 3.7 | 4.9 | 2 | 2 | 30.0 | 83 | 31 | 3.35 | 28.0 |
| 200 | 8.8 | 7.1 | 4.2 | 8.5 | 0.36 | 2.6 | 4.5 | 3 | 3 | 29.7 | 81 | 27 | 5.01 | 28.5 |
| 208 | 6.4 | 5.6 | 3.4 | 6.7 | 0.57 | 3.2 | 4.2 | 1 | 11 | 22.7 | 93 | 32 | 2.68 | 29.1 |
| 221 | 6.4 | 1.1 | 0.7 | 1.3 | 0.20 | 0.2 | 0.6 | 5 | 24 | 26.3 | 96 | 33 | 3.00 | 27.5 |
| 237 | 7.3 | 2.8 | 1.7 | 3.3 | 0.20 | 0.6 | 1.6 | 5 | 8 | 30.0 | 83 | 33 | 4.34 | 23.4 |
| 239 | 8.6 | 5.5 | 3.3 | 6.5 | 0.20 | 1.1 | 3.1 | 7 | 10 | 30.7 | 78 | 31 | 4.65 | 24.9 |
| 240 | 8.2 | 4.4 | 2.7 | 5.3 | 0.20 | 0.9 | 2.5 | 8 | 11 | 29.7 | 79 | 27 | 3.98 | 24.6 |

[a] Day of the year, 1994.
[b] Penman-Monteith calculated reference ET.
[c] Measured daily ET from the lysimeter.
[d] Estimated cool season pastures daily ET.
[e] Estimated ET from Native pastures.
[f] Wheat crop coefficient used. Bare soil day 187 to 240.
[g] Estimated wheat ET.
[h] Area weighted ET.

[i] Days since any rainfall has occurred.
[j] Days since a total daily rainfall greater than 10 mm.
[k] Average daily temperature at 1.2 m.
[l] Maximum daily relative humidity
[m] Minimum daily relative humidity.
[n] Daily average wind speed at 2 m.
[o] Total daily solar radiation.

## Appendix A.2: Daily estimates of evapotranspiration (ET) and weather conditions at the Goodwell lysimeter site.

| | | | | | | | | | | Daily Weather Data | | | | |
|---|---|---|---|---|---|---|---|---|---|---|---|---|---|---|
| DOY [a] | PMon [b] mm d$^{-1}$ | ETlys [c] mm d$^{-1}$ | Kccorn [d] | ETcorn [e] mm d$^{-1}$ | Kcwheat [f] | ETwheat [g] mm d$^{-1}$ | ETarea [h] mm d$^{-1}$ | Days Since RF [i] | Days Since RF>10mm [j] | Tavg [k] °C | RHmax [l] % | RHmin [m] % | WSavg [n] m s$^{-1}$ | Rad [o] MJ m$^{-2}$ d$^{-1}$ |
| 149 | 7.1 | 5.1 | 0.44 | 2.8 | 0.76 | 4.6 | 4.5 | 4 | 4 | 22.7 | 98 | 20 | 3.00 | 30.9 |
| 150 | 9.1 | 4.5 | 0.36 | 2.9 | 0.71 | 4.8 | 4.3 | 5 | 5 | 25.7 | 82 | 22 | 4.34 | 30.7 |
| 156 | 7.8 | 3.7 | 0.20 | 1.4 | 0.47 | 2.7 | 3.0 | 3 | 11 | 28.0 | 78 | 19 | 3.98 | 30.9 |
| 157 | 8.3 | 2.4 | 0.24 | 1.8 | 0.45 | 2.4 | 2.3 | 4 | 12 | 26.7 | 98 | 30 | 3.98 | 29.1 |
| 164 | 9.1 | 4.8 | 0.71 | 5.8 | 0.62 | 4.3 | 4.9 | 2 | 3 | 30.0 | 74 | 13 | 5.68 | 31.0 |
| 166 | 10 | 1.6 | 0.63 | 5.6 | 0.43 | 2.5 | 2.6 | 4 | 5 | 29.0 | 85 | 7 | 7.64 | 31.2 |
| 175 | 8.6 | 4.4 | 0.97 | 7.5 | 0.20 | 0.9 | 4.1 | 2 | 14 | 28.3 | 82 | 17 | 3.67 | 28.8 |
| 179 | 7.6 | 0.5 | 1.05 | 7.2 | 0.20 | 0.1 | 1.7 | 6 | 18 | 28.0 | 74 | 18 | 3.00 | 28.5 |
| 191 | 8.3 | 2.0 | 1.15 | 8.6 | 0.20 | 0.4 | 2.9 | 7 | 30 | 27.0 | 91 | 16 | 4.65 | 30.3 |
| 224 | 8.7 | 1.4 | 1.15 | 9.0 | 0.20 | 0.3 | 2.6 | 1 | 63 | 28.7 | 74 | 22 | 5.99 | 27.8 |
| 228 | 8.3 | 3.1 | 1.12 | 8.4 | 0.70 | 2.1 | 3.9 | 2 | 2 | 24.3 | 84 | 24 | 3.67 | 26.9 |
| 238 | 6.8 | 3.1 | 1.00 | 6.1 | 0.70 | 2.1 | 3.4 | 2 | 2 | 29.0 | 66 | 17 | 3.67 | 26.3 |
| 240 | 6.3 | 1.8 | 0.98 | 5.5 | 0.48 | 0.9 | 2.3 | 4 | 4 | 27.3 | 76 | 35 | 4.34 | 24.9 |
| 252 | 6.1 | 3.2 | 0.75 | 4.1 | 0.20 | 0.6 | 2.8 | 1 | 16 | 22.0 | 97 | 38 | 3.67 | 23.8 |
| 255 | 7.2 | 2.2 | 0.69 | 4.5 | 0.20 | 0.4 | 2.2 | 4 | 19 | 25.0 | 87 | 33 | 7.02 | 23.0 |

[a] Day of the year, 1994.
[b] Penman-Monteith calculated reference ET.
[c] Measured daily ET from the lysimeter.
[d] Corn crop coefficient
[e] Estimated corn ET.
[f] Wheat crop coefficient.
[g] Estimated wheat ET.
[h] Area weighted ET.

[i] Days since any rainfall has occurred.
[j] Days since a total daily rainfall greater than 10 mm.
[k] Average daily temperature at 1.2 m.
[l] Maximum daily relative humidity
[m] Minimum daily relative humidity.
[n] Daily average wind speed at 2 m.
[o] Total daily solar radiation.

247

**Appendix A.3: Daily estimates of evapotranspiration (ET) and weather conditions at Marena and Wister.**

| DOY[a] | PMon[b] | ETlys[c] | ETtree[d] | ETarea[e] | Days Since RF[f] | Days Since RF>10mm[g] | Tavg[h] °C | RHmax[i] % | RHmin[j] % | WSavg[k] m s$^{-1}$ | Rad[l] MJ m$^{-2}$ d$^{-1}$ |
|---|---|---|---|---|---|---|---|---|---|---|---|
| | | --------- mm d$^{-1}$ --------- | | | | | | Daily Weather Data | | | |
| | | | | **Marena** | | | | | | | |
| 150 | 5.1 | 4.27 | 4.59 | 4.3436 | 1 | 1 | 25.7 | 100 | 49 | 0.00 | 28.6 |
| 189 | 6.9 | 2.46 | 6.21 | 3.3225 | 7 | 40 | 25.0 | 88 | 31 | 2.68 | 29.1 |
| 200 | 8.8 | 3.52 | 7.92 | 4.532 | 2 | 3 | 30.3 | 72 | 32 | 5.01 | 28.7 |
| 208 | 5.7 | 4.34 | 5.13 | 4.5217 | 1 | 2 | 22.0 | 92 | 37 | 2.32 | 28.6 |
| 239 | 7.9 | 3.66 | 7.11 | 4.4535 | 7 | 7 | 31.0 | 85 | 31 | 3.98 | 24.8 |
| | | | | **Wister** | | | | | | | |
| 102 | 4.1 | 2.43 | 2.187 | 2.13354 | 1 | 1 | 11.7 | 100 | 44 | 3.00 | 26.0 |
| 141 | 4.6 | 7.06 | 6.354 | 6.19868 | 5 | 8 | 18.0 | 100 | 47 | 0.31 | 29.7 |
| 158 | 5.3 | 7.94 | 4.77 | 6.4486 | 1 | 9 | 26.7 | 100 | 65 | 0.98 | 28.1 |
| 176 | 6.2 | 8.94 | 5.58 | 7.3068 | 2 | 16 | 27.7 | 100 | 49 | 1.65 | 29.3 |
| 180 | 6.1 | 4.17 | 5.49 | 4.0434 | 6 | 20 | 30.3 | 100 | 21 | 0.98 | 28.4 |
| 199 | 5.4 | 2.87 | 4.86 | 3.0208 | 3 | 12 | 28.0 | 100 | 47 | 1.34 | 25.5 |
| 208 | 5.3 | 7.09 | 4.77 | 5.8706 | 1 | 1 | 22.0 | 96 | 48 | 1.65 | 27.9 |
| 209 | 4.6 | 6.23 | 4.14 | 5.1472 | 2 | 2 | 21.3 | 98 | 42 | 1.34 | 24.9 |
| 239 | 4.7 | 5.04 | 4.23 | 4.3578 | 2 | 7 | 27.3 | 99 | 46 | 0.98 | 22.6 |
| 240 | 5.4 | 6.82 | 4.86 | 5.7068 | 3 | 8 | 27.0 | 99 | 40 | 1.34 | 24.9 |
| 256 | 4.3 | 2.2 | 3.87 | 2.3474 | 4 | 13 | 25.0 | 99 | 41 | 1.34 | 21.6 |

[a] Day of the year, 1994.
[b] Penman-Monteith calculated reference ET.
[c] Measured daily ET from the lysimeter.
[d] Estimated woodland ET.
[e] Area weighted ET.
[f] Days since any rainfall has occurred.
[g] Days since a total daily rainfall of 10 mm.
[h] Average daily temperature at 1.2 m.
[i] Maximum daily relative humidity
[j] Minimum daily relative humidity.
[k] Daily average wind speed at 2 m.
[l] Total daily solar radiation.

248

# APPENDIX B

## Listing of a Program to Automatically Extract Data from

## AVHRR or GAC Image Files Corresponding to

## Mesonet Locations

The following C code illustrates the routines used to process HRPT and GAC formatted image files retrieved from the SAA system. The program presented here is the one used to extract the digital numbers for a given set of latitude and longitude coordinates contained in the ASCII file MESLOC.DAT.

The program first determines the row and column of the image corresponding to the given coordinates and then extracts the digital numbers to an ASCII file. Additionally, the program calculates the radiance for channels 4 and 5 using the coefficients contained in the image file, as well as the base plate temperature.

At the time of this study, the first image line of the file was improperly extracted by the SAA system; therefore, this program does not process the first line.

```c
/* satvmes2.c */
/* ========== executable file name svm2 ============== */

/* Used to extract brightness temperatures for Mesonet locations */
/* emb 2/28/95 */
/* Updated 3/2/95 */
/* Updated 4-8-95 : Fix column offset of GCP */
/* Linearly interpolates between GCPs */
/* Converts latitude/longitude to xyz and then finds distance to the point of interest/

/* Puts output in two files : General information and thermal coefficient information */

/* For LAC/HRPT data - 14800 line width or
       GAC data - 3220 line width */

#include<stdio.h> /* standard input and output routines */
#include<math.h> /* math functions: sqrt, cos, sin */

/* Number of sites to find */
#define defNsites 111

/* on sun: cc satvmes2.c -lm -o svm2 */

void main()
{
static char infile[25],    /* input file name */
        header[122],    /* tera header */
        IBUF[40],       /* intermediate buffer to hold thermal coefficients */
        inline[14800]; /* input line */



/* -------------------------------------- GCP variables -------------------------------------- */
unsigned int d1, d2, d3;    /* used to translate lat/longs to floating point numbers */
int d4;

int Ngcp;                  /* number of GCPs in a scan line */
```

```c
static  float lat[51], lon[51];  /* lat/longs on one scan line */
float la, lo;                     /* interpolated lat and longs */

/* max and min points in image */
static float minlat = 999.0,
        minlong = 999.0,
        maxlat = -999.0,
        maxlong = -999.0;

float xg, yg, zg;  /* three dimensional Cartesian coordinates derived from file */

static float lyslat[defNsites],  /* latitude and longitudes of Mesonet stations */
        lyslon[defNsites];

static float x[defNsites], y[defNsites], z[defNsites];  /* Mesonet cart. coordinates. */

static float RE = 6367.5;    /* radius of earth, km */
                             /* average of polar and equatorial radius */

static float RC = 0.0174533;  /* PI over 180 */

static float mindist[defNsites];  /* min distance between GCP and site, km */
static char sites[defNsites][5];  /* name of site */
static int sID[defNsites];        /* site number */
int elv;                          /* site elevation - not stored */

float dist;  /* distance from GCP to site, km */

static int bestline[defNsites],  /* line number of image with best lat and long */
        bestcol[defNsites];  /* column of lat and long */


/* ---------------------------------------------- Counters and switches -------------------------------------- */
int fr,          /* counts sites */
    i,           /* line counter */
    j,           /* count bytes for GCPs */
    p=0,         /* counts GCPs */
    w,   /* second GCP counter */
    k,           /* switch for lat long */
    tp = 0,      /* counter for TPRT */
    allLines;    /* total number of lines in file */

static int minl = 999,     /* first line with site data */
        maxl =0; /* maximum line in image containing sites */

/* ------------- thermal coefficient variables --------------- */
static double ofactor,    /* 2^22 - offset */
        sfactor,          /* 2^30 - slope */
        inter[3],         /* thermal intercept */
        slope[3];         /* thermal slope */

unsigned long bytes[4], /* temporary variable */
                temp1;            /* holds slope or offset before converting
```

```c
                                           to signed long */
long temp2;

static unsigned int vch[2500][5];        /* channel video data */
static int pix = 0;                       /* pixel counter for video data */
static float ch4[defNsites];              /* channel radiance for Mesonet sites */
static float ch5[defNsites];
static unsigned int MesDN[defNsites][5];  /* DN values for each channel corresponding to a site */
 int ddd;                                  /* counter used to copy dn values */


/* ----------------- Base Plate variables ----------- */
int Block;                                 /* Used to find word with base plate temperature */
long ll;                                   /* Used to extract 10 bit word */
static float PRT = 0.0;                     /* Avg. of the 4 PRT temperatures */
static float Tprt[4];                       /* four individual PRT values */
static float A[3];                          /* coefficients needed to calculate base
                                              plate temperature. Same for nl1 or nl2 */


static int Ref = 0;       /* used to get PRT values */
static int BlLength;      /* block length of HRPT or GAC data */




/* ----------- File variables -------------------- */
static int linelen; /* length of input line */
static char OUTFILE1[25],        /* output file name with radiance values for ch 4 and 5 */
       OUTFILE2[25];   /* output file name for dn values at each site */

FILE *FIN;              /* Site data */
FILE *JUNK;            /* DN values, 1-5 */
FILE *IN;
FILE *OUT;               /* ch 4 and 5 radiance values */

if( (FIN = fopen("mesloc.dat", "r")) == NULL)
  {
   printf("\n\n File mesloc.dat not found");
   exit(-1);
  }

 /* Read in the location of the sites of interest */
for(i=0; i < (int) defNsites; i++)
  fscanf(FIN, "%s %d %f %f %d", sites[i], &sID[i], &lyslat[i], &lyslon[i], &elv);

fclose(FIN);



/* calculate factor to convert slopes and offsets */
 ofactor = pow( (double) 2.0, (double) 22.0);
 sfactor = pow( (double) 2.0, (double) 30.0);

for(fr = 0; fr < (int) defNsites; fr++)
 { mindist[fr] = 99999.9;
   /* compute Cartesian coordinates. of lysimeters */
```

252

```c
  lyslon[fr] *= (float) -1.0;
  x[fr] = RE * cos( (double) (RC * lyslat[fr])) * cos( (double) (RC * lyslon[fr]));
  y[fr] = RE * cos( (double) (RC * lyslat[fr])) * sin( (double) (RC * lyslon[fr]));
  z[fr] = RE * sin( (double) (RC * lyslat[fr]));
}


/* initialize base plate arrays */
A[0] = 276.597;
A[1] = 0.051275;
A[2] = 0.000001363;


/* initialize stats used to track position */
minlat = 999.0;
minlong = 999.0;
maxlat = -999.0;
maxlong = -999.0;

minl = 999;
maxl = 0;


/* ------------------------------------------------------------- */
/*        First pass to find lysimeter lines        */

printf("\n\n Enter the GAC or HRPT file to get Mesonet sites: ");
scanf("%s", infile);

printf("\n\n Enter the file to hold the radiance values of ch 4 and 5: ");
scanf("%s", OUTFILE1);

printf("\n\n Enter the file name for the DN values: ");
scanf("%s", OUTFILE2);

/* open input file */
if( (IN = fopen(infile, "rb")) == NULL)
  { printf("\n\n File %s not found! \n", infile);
    exit(-1);}

OUT = fopen(OUTFILE1, "w");
JUNK = fopen(OUTFILE2, "w");


/* read header - TBM, Terabit memory */
fr = fread( (void*) header, 122, 1, IN);

/* see if this is GAC or HRPT */

if (header[34] == 'G') {linelen = 3220;
                                BlLength = 794;}
else if (header[34] == 'H' || header[34] == 'L') {linelen = 14800;
                                                        BlLength = 3526;}
else {printf("\n\n Header 34 = %c \n", header[34]); exit(-1);}
```

253

```
/* read image header - 1 line */
fr = fread( (void*) inline, linelen, 1, IN);

/* NOTE: currently there is a bug in the SAA program and all
    first lines contain information. for another part of the globe. Ignore it */
fr = fread( (void*) inline, linelen, 1, IN);


/* read rest of image */
i = 0;
while ( fread((void*) inline, linelen, 1, IN) == 1)
  {
  /* try to get at earth location information */
  k = 0; /* start with lat */
  p =0;
  if( (i%5) == 0) printf("\r First Pass: On line: %d", i);

  /* find number of GCPs in line */
  Ngcp = (unsigned char) inline[52];

  j=104;
  while (j < 308)
    {
        /* assume high byte/low byte format */
    d1 = (unsigned char) inline[j];
    d2 = (unsigned char) inline[j+1];
    d3 = d1*256 + d2;
    d4 = d3;
        j += 2;

      if(k == 0)
        {
        lat[p] = (float) d4 / 128.0;
        if(lat[p] > maxlat) maxlat = lat[p];
        if(lat[p] < minlat) minlat = lat[p];
        k = 1;
        }
      else
        {
      /* NOTE: next line is only needed when run on the sun
        due to the difference in integer definitions */
      d4 = -1*(65536-d4);
        lon[p] = (float) d4  / 128.0;
        if(lon[p] > maxlong) maxlong = lon[p];
        if(lon[p] < minlong) minlong = lon[p];
        k = 0;

        ++p;
        }

        /* quit if all GCPs not meaningful */
        if( p >= Ngcp) break;
```

```
                                    } /* while j */




/* check line for point near lysimeter */
     for(w=0; w < (Ngcp-1); w++)
      {

      /* don't bother if not close */
      if( (lat[w] > 33.5 && lat[w] < 37.0) && (lon[w] < -94.0 && lon[w] > -103.0))
        {
        /* interpolate between each GCP - assuming not at edges */
      /* Note that the first GCP begins at pixel 25 and continues
        every 40 there after until 2025. Only consider 39 points
        per every 2 GCPS as the 40 is the start of a new GCP set */
        for(p=0; p < 39; p++)
          {
               la = (lat[w+1] - lat[w])*((float) p)/39.0 + lat[w];
               lo = (lon[w+1] - lon[w])*((float) p)/39.0 + lon[w];

               /* translate into Cartesian coordinates */
               xg = RE * cos( (double) (RC * la)) * cos( (double) (RC * lo));
               yg = RE * cos( (double) (RC * la)) * sin( (double) (RC * lo));
               zg = RE * sin( (double) (RC * la));


      for(fr = 0; fr < (int) defNsites; fr++)
            {
            /* find dist from GCP to site */
            dist =(float) sqrt( (double) ( (x[fr] - xg)*(x[fr] - xg) +
                        (y[fr] - yg) * (y[fr] - yg) +
                        (z[fr] - zg) * (z[fr] - zg) ) );

            /* don't continue to check if the point is no where
               close */
            if(dist > 1000.0) break;

             if( dist < mindist[fr])
                    {
                    mindist[fr] = dist;
                    bestline[fr] = i;
      /* Note that 25 is added to account for the fact that the first point is for pixel 25.
         This program will not find pixels < 25 or > 2025 along the swath width.
         Also, p starts at 0 and so does the image array, therefore 1 does not need to be
         subtracted from the total */
                    bestcol[fr] = w * 40 + p + 25;

      /* There is one GAC pixel for every 5 HRPT */
                    if(linelen == 3220) bestcol[fr] = bestcol[fr] / 5;
                    } /* if  mindist */

            } /* for site sites - fr */
        } /* for interpolate -  p */


                                    255
```

```c
        } /* if lat / long not close */
    } /* for w - GCP's in one line */


    /* ------------------ base plate temp ---------------- */
    /* use one reading for TPRT from one file */
    /* start the process 10 lines into the file */
    if(i >= 10 && PRT == 0.0)
      {
      Block = 82; /* word position for PRT */
      ll = ( (long) ( (unsigned char) inline[Block*4]) )*256L*256L*256L +
           ( (long) ((unsigned char) inline[Block*4+1]) )*256L*256L +
           ( (long) ( (unsigned char) inline[Block*4+2]) )*256L +
            (long) ( (unsigned char) inline[Block*4+3]);


    /* find reference value */
    /* 0x3FF = binary 1111111111 */
      if(Ref == 0)
              { Tprt[0] = (float) ( ll & 0x3FF);
                if(Tprt[0] < 10) Ref = 1;}
      else if(Ref < 5) /* now get actual counts */
              {
              Tprt[Ref-1] = (float) (ll & 0x3FF);


              /* Convert to temperature */
              Tprt[Ref-1] = (A[0] + Tprt[Ref-1] * A[1] +
                                 Tprt[Ref-1] * Tprt[Ref-1] * A[2]);


              Ref += 1;
              } /* Reference < 5 */


              /* compute average base plate temperature */
      if(Ref == 5)
              {
              for(tp=0; tp < 4; tp++)
                PRT += Tprt[tp];


                PRT = PRT / (float) (4.0) - (float) 273.15;


              } /* ref = 5 */
      } /* if don't have PRT */


  ++i;
} /* read line */

fclose(IN);

allLines = i;

/* find maximum/min line containing site information */
for(fr=0; fr < (int) defNsites; fr++)
  {
        if(bestline[fr] > maxl) maxl = bestline[fr];
        if(bestline[fr] < minl) minl = bestline[fr];
```

256

```c
  } /* find max/min lines */

        if(minl <= 0) minl = 1;
        if(maxl >= allLines) maxl = allLines-1;

/* --------------------------------------------------- */
/*          Second pass through file          */
/* open input file - 2nd pass */
if( (IN = fopen(infile, "rb")) == NULL)
  { printf("\n\n File %s not found! 2nd pass \n", infile);
    exit(-1);}

/* read header - TBM, Terabit memory */
fr = fread( (void*) header, 122, 1, IN);

/* extract some of the header information to use in output */
header[98] = '\0';

/* read image header - 1 line */
fr = fread( (void*) inline, linelen, 1, IN);

printf("\n\n Second pass... \n\n");

/* skip lines without site information */
for(i = 0; i < minl; i++)
  fread((void*) inline, linelen, 1, IN);

/* ------------------------ extraction loop ------------ */
for(i = minl; i <= maxl; i++)
{
   fread((void*) inline, linelen, 1, IN);
   if( (i%5) == 0) printf("\r Second Pass: On line: %d", i);

   /* check each site */
   for(fr=0; fr < defNsites; fr++)
       {
         /* get data for locations */
         if( i == bestline[fr] )
           {
              /* -------------- Thermal coefficients ----------------- */
              /* store thermal information in temp buffer */
              for(p=12; p < 52; p++)
                IBUF[p-12] = inline[p];

              k = 16; /* start on channel 3 */
              /* high to low byte */
              for (j=0; j < 3; j++) /* channel loop - skip ch1 and 2 */
                {
                  bytes[0] = (unsigned char) IBUF[k];
                  bytes[1] = (unsigned char) IBUF[k+1];
                  bytes[2] = (unsigned char) IBUF[k+2];
                  bytes[3] = (unsigned char) IBUF[k+3];

                  temp1 = bytes[0]* 16777216 + bytes[1]* 65536
```

257

```
                              + bytes[2] * 256 + bytes[3];

         temp2 = temp1; /* convert to signed long */


         /* convert to actual value */
         slope[j] = (double) temp2 / sfactor;


         k += 4;
         bytes[0] = (unsigned char) IBUF[k];
         bytes[1] = (unsigned char) IBUF[k+1];
         bytes[2] = (unsigned char) IBUF[k+2];
         bytes[3] = (unsigned char) IBUF[k+3];


         temp1 = bytes[0] * 16777216 + bytes[1] *  65536 +
                       bytes[2] * 256 + bytes[3];


         temp2 = temp1;


         inter[j] = (double) temp2 / ofactor;


         k += 4;

      } /* channel coefficients */


      /* ----------------- video data ---------------- */
      /* video data begins at byte 448 (first = 0) for
         both GAC and HRPT data */
      /* Data is packed in 10 bit words, 3 words/byte */
      /* Processed here in 4 byte blocks - 3 points/block */
      /* Go a head and extract the video data into separate
         arrays. */
      /* 112 = 1st block position for video data */
      /* last block = Bytes Video/4 + 112 */
      j = 0; /* channel counter */
      pix = 0; /* pixel counter */
      for(Block = 112; Block < BlLength; Block++)
        {
            ll = ( (long) ( (unsigned char) inline[Block*4]) )*256L*256L*256L +
                  ( (long) ( (unsigned char) inline[Block*4+1]) )*256L*256L +
                  ( (long) ( (unsigned char) inline[Block*4+2]) )*256L +
                  (long) ( (unsigned char) inline[Block*4+3]);

            /* get 10 bit data from the block */
            /* 0x3FF = binary 1111111111 */
            /* xxAAAAAAAAAABBBBBBBBBBCCCCCCCCCC */

            /*    0x3FF = 00000000000000000000001111111111 */
            /* (ll >> 20) = 00000000000000000000xxAAAAAAAAAA */
            /* this extracts the A's (above) */
            vch[pix][j] = (unsigned int) ( (ll >> 20) & 0x3FF );
            ++j;
            if(j > 4) {j = 0;  ++pix;}

            /* (ll >> 10) = 0000000000xxAAAAAAAAAABBBBBBBBBB */
```

```c
        /* this extracts the B's (above) */
          vch[pix][j] = (unsigned int) ( (ll >> 10) & 0x3FF );
        ++j;
        if(j > 4) {j = 0; ++pix;}

        /* this extracts the C's (above) */
        vch[pix][j] = (unsigned int) ( ll & 0x3FF );
        ++j;
        if(j > 4) {j = 0;++pix;}

    } /* extract video - for block */

    /* convert video data to radiance for point of interest */
    ch4[fr] = inter[1] + slope[1] * (float) vch[bestcol[fr]][3];
    ch5[fr] = inter[2] + slope[2] * (float) vch[bestcol[fr]][4];


        /* get DN values too */
        for(ddd = 0; ddd < 5; ddd++)
        MesDN[fr][ddd] = vch[bestcol[fr]][ddd];


        } /* lines with site */
    } /* chk sites */
} /* extraction loop */

fclose(IN);


/* ------------------- output ---------------------- */
/* output ASCII file for coefficients and GCP information */
fprintf(OUT, "%f\n", PRT);

for(fr=0; fr < defNsites; fr++)
  {
    fprintf(OUT,"%s %d %f %f %f %d %d \n",
                sites[fr], sID[fr], ch4[fr], ch5[fr],
                mindist[fr], bestline[fr], bestcol[fr]);

    fprintf(JUNK, "%s %d ", sites[fr], sID[fr]);
    for(ddd = 0; ddd < 5; ddd++)
        fprintf(JUNK, " %d", MesDN[fr][ddd]);
    fprintf(JUNK, "\n");
    } /* site write */

fclose(OUT);
fclose(JUNK);
printf("\n\n DONE! \n");
exit(0);
}
```

# APPENDIX C

**Procedures Used to View Images from GAC or HRPT Files**

The following program written in C, extracts a user specified channel of the HRPT or GAC image. To minimize file size, the image is linearly scaled from 10 bit to 8 bits. The program also allows the options of extracting the thermal coefficients of each line and the earth location information to ASCII files.

In performing the geometric correction of these images, this program was used to first extract channel 2 to a binary file. The binary file was then appended with a TIF (tagged image format) header and imported in to Paint Shop Pro, a share ware image processing program.

```c
/* exgach.c */

/* emb 3/2/95 */
/* update 4/4/94 */

/* Extracts a channel from GAC or HRPT data files */
/* Scales to 8 bit and puts in a binary file */
/* for LAC/HRPT data - 14800 line width or
     GAC data - 3220 line width */

/* optional output files not named by user:
    thermal.dat - thermal coefficients. for each line
    gcplong.dat - long. GCP
    gcplat.dat  - latitude GCPs */

#include<stdio.h>
#include<math.h> /* sqrt, cos, sin */

/* on sun: cc exgach.c -lm -o exgach */

void main()
{
static char infile[25],       /* input file name */
        outfile[25],          /* channel output file name */
        header[122],          /* tera header */
        IBUF[40],             /* intermediate buffer to hold thermal coefficients */
        inline[14800];        /* input line */

char chout;                   /* 8 bit value output */
static int Pixels;            /* number of output pixels / line */
static char outline[2500];    /* output line */

/* ------------- User defined switches --------------------- */
static int  channel,          /* channel user selects to extract */
        getTHC,               /* = 1 store thermal coefficients for each line */
        getLOC;               /* = 1 store earth location data in file */

/* ---------------------- GCP variables ---------------------- */
    unsigned int d1, d2, d3; /* used to translate lat/longs */
    int d4;

    int Ngcp; /* number of GCPs on line */
```

```c
static int DNmax = 0,    /* range of DN values scaled by dividing by 4 */
    DNmin = 256;

static  float lat[51], lon[51];  /* lat/longs on one scan line */

/* ----------------- Counters and switches ---------------- */
    int i,          /* line counter */
        j,          /* count bytes for GCPs */
        p=0,        /* counts GCPs */
        w,          /* second GCP counter */
        k,          /* switch for lat long */
        tp = 0,     /* counter for TPRT */
        allLines;   /* total number of lines in file */


/* -------------- thermal coefficients stuff --------------- */
    static double ofactor,    /* 2^22 - offset */
            sfactor,          /* 2^30 - slope */
            inter[3],         /* thermal intercept */
            slope[3];         /* thermal slope */

    unsigned long bytes[4],  /* temporary variable */
                temp1;          /* holds slope or offset before converting to signed long */
    long temp2;

    static int vch[2500];   /* channel video data */
    static int pix = 0;     /* pixel counter for video data */


/* ----------------- Base Plate variables ----------- */
    int Block;              /* Used to find word with base plate temperature */
    long ll;                /* Used to extract 10 bit word */
    static float PRT = 0.0;  /* Avg. of the 4 PRT temperatures */
    static float Tprt[4];    /* four individual PRT values */
    static float A[3];       /* coefficients needed to calculate base
                                plate temperature. Same for n11 or n12 */


    static int Ref = 0;     /* used to get PRT values */
    static int BlLength;    /* block length of HRPT or GAC data */


/* ----------- File variables -------------------- */
    static int linelen; /* length of input line */

    FILE *IN;  /* input file */
    FILE *OUT; /* output file for 1 channel */
    FILE *OP1; /* thermal coefficients. data */
    FILE *OP2; /* long GCPs */
    FILE *OP3; /* lat GCPs */

/* calculate factor to convert slopes and offsets */
    ofactor = pow( (double) 2.0, (double) 22.0);
    sfactor = pow( (double) 2.0, (double) 30.0);

/* initialize base plate arrays */
    A[0] = 276.597;
```

```c
A[1] = 0.051275;
A[2] = 0.000001363;

/* -------------------------------------------------- */

printf("\n\n Enter the GAC or HRPT file to extract from: ");
scanf("%s", infile);

/* open input file */
if( (IN = fopen(infile, "rb")) == NULL)
  { printf("\n\n File %s not found! \n", infile);
    exit(-1);}

printf("\n\n Enter the file name for the channel output: ");
scanf("%s", outfile);

OUT = fopen(outfile, "wb");

printf("\n\n Enter the channel number to extract [1-5]: ");
scanf("%d", &channel);

printf("\n\n Extract thermal coefficients to thermal.dat? [1 = yes] ");
scanf("%d", &getTHC);

if(getTHC == 1)
  OP1 = fopen("thermal.dat", "w");

printf(" \n\n Extract GCP information. to GCP???.DAT? [1=yes] ");
scanf("%d", &getLOC);

if(getLOC == 1)
  {OP2 = fopen("gcplong.dat", "w");
   OP3 = fopen("gcplat.dat", "w");}

/* read header - TBM, Terabit memory */
fread( (void*) header, 122, 1, IN);

/* see if this is GAC or HRPT */

if (header[34] == 'G') {linelen = 3220;
                        Pixels = 408;
                        BlLength = 794;}
else if (header[34] == 'H' || header[34] == 'L') {linelen = 14800;
                                                  Pixels = 2040;
                                                  BlLength = 3526;}
else {printf("\n\n Header 34 = %c \n", header[34]); exit(-1);}


/* read image header - 1 line */
fread( (void*) inline, linelen, 1, IN);

/* these images are messed up in that the first line is for some area on another part of the globe */
fread( (void*) inline, linelen, 1, IN);
```

263

```c
/* --------------------------- read rest of image --------------- */
i = 0;
while ( fread((void*) inline, linelen, 1, IN) == 1)
  {
  /* try to get at earth location information */
  k = 0; /* start with lat */
  p =0;
  if( (i%5) == 0) printf("\r First Pass: On line: %d", i);



  /* --------------- find number of GCPs in line --------------- */

  if(getLOC == 1 || i == 0)
    {
        Ngcp = (unsigned char) inline[52];

        j=104;
        while (j < 308)
          {
          /* assume high byte/low byte format */
          d1 = (unsigned char) inline[j];
          d2 = (unsigned char) inline[j+1];
          d3 = d1*256 + d2;
          d4 = d3;

          j += 2;

          if(k == 0)
            {
                lat[p] = (float) d4 / 128.0;
                k = 1;
            }
          else
            {
                /* sun conversion */
                d4 =  (d4 - 65536);
                lon[p] = (float) d4  / 128.0;
                k = 0;
                ++p;
            }

          /* quit if all GCPs not meaningful */
          if( p >= Ngcp) break;
        } /* while j */

        if( getLOC == 1)
          {
          for(p = 0; p < Ngcp; p++)
            {fprintf(OP2, " %6.1f", lon[p]);
             fprintf(OP3, " %6.1f", lat[p]);}

          fprintf(OP2, "\n"); fprintf(OP3, "\n");
        }
```

```
} /* if GCP */


        /* ------------------ base plate temp ---------------- */
        /* use one reading for TPRT from one file */
        /* start the process 10 lines into the file */

if(getTHC == 1)
    {
    if(i >= 10 && PRT == 0.0)
        {
        Block = 82; /* word position for PRT */
        ll = ( (long) ( (unsigned char) inline[Block*4]) )*256L*256L*256L + ( (long) ( (unsigned
            char) inline[Block*4+1]) )*256L*256L + ( (long) ( (unsigned char) inline[Block*4+2])
            )*256L + (long) ( (unsigned char) inline[Block*4+3]);

        /* find reference value */
        /* 0x3FF = binary 1111111111 */
          if(Ref == 0)
                { Tprt[0] = (float) ( ll & 0x3FF);
                  if(Tprt[0] < 10) Ref = 1;}
          else if(Ref < 5) /* now get actual counts */
                {
                Tprt[Ref-1] = (float) (ll & 0x3FF);

                /* Convert to temperature */
                Tprt[Ref-1] = (A[0] + Tprt[Ref-1] * A[1] +
                                    Tprt[Ref-1] * Tprt[Ref-1] * A[2]);

                Ref += 1;
                } /* ref < 5 */

                /* compute average base plate temperature */
          if(Ref == 5)
                {
                for(tp=0; tp < 4; tp++)
                  PRT += Tprt[tp];

                PRT = PRT / (float) (4.0) - (float) 273.15;

                } /* ref = 5 */
        } /* if don't have PRT */


        /* -------------- Thermal coefficients ---------------- */
        /* store thermal information in temp buffer */
        for(p=12; p < 52; p++)
          IBUF[p-12] = inline[p];

                k = 16; /* start on channel 3 */
                /* high to low byte */
                for (j=0; j < 3; j++) /* channel loop - skip ch1 and 2 */
                    {
                    bytes[0] = (unsigned char) IBUF[k];
```

265

```c
        bytes[1] = (unsigned char) IBUF[k+1];
        bytes[2] = (unsigned char) IBUF[k+2];
        bytes[3] = (unsigned char) IBUF[k+3];

        temp1 =  bytes[0]* 16777216 + bytes[1]* 65536
                        + bytes[2] * 256 + bytes[3];

        temp2 = temp1; /* convert to signed long */

        /* convert to actual value */
        slope[j] = (double) temp2 / sfactor;

        k += 4;
        bytes[0] = (unsigned char) IBUF[k];
        bytes[1] = (unsigned char) IBUF[k+1];
        bytes[2] = (unsigned char) IBUF[k+2];
        bytes[3] = (unsigned char) IBUF[k+3];

        temp1 = bytes[0] * 16777216 + bytes[1] *  65536 +
                        bytes[2] * 256 + bytes[3];

        temp2 = temp1;

        inter[j] = (double) temp2 / ofactor;

        k += 4;
    if(j == 0) fprintf(OP1, " %le %le ", inter[j], slope[j]);
        else fprintf(OP1, " %lf %lf ", inter[j], slope[j]);
        } /* channel coefficients */

        fprintf(OP1, "\n");

  } /* if extracting thermal information */

/* ------------------ video data ---------------- */
/* video data begins at byte 448 (first = 0) for
     both GAC and HRPT data */
/* Data is packed in 10 bit words, 3 words/byte */
/* Processed here in 4 byte blocks - 3 points/block */
    /* Go a head and extract the video data into separate
                arrays. */
/* 112 = 1st block position for video data */
/* last block = Bytes Video/4 + 112 */
j = 0; /* channel counter */
pix = 0; /* pixel counter */
for(Block = 112; Block < BlLength; Block++)
  {
   ll = ( (long) ( (unsigned char) inline[Block*4]) )*256L*256L*256L +
          ( (long) ( (unsigned char) inline[Block*4+1]) )*256L*256L +
           ( (long) ( (unsigned char) inline[Block*4+2]) )*256L +
           (long) ( (unsigned char) inline[Block*4+3]);

   /* get 10 bit data from the block */
   /* 0x3FF = binary 1111111111 */
```

266

```c
/* xxAAAAAAAAAABBBBBBBBBBCCCCCCCCCC */

/*    0x3FF = 00000000000000000000001111111111 */
/* (ll >> 20) = 00000000000000000000xxAAAAAAAAAA */
if(j == (channel - 1))
  vch[pix] = (unsigned int) ( (ll >> 20) & 0x3FF ); /* this extracts the A's (above) */
  ++j;
  if(j > 4) {j = 0;  ++pix;}


/* (ll >> 10) = 0000000000xxAAAAAAAAAABBBBBBBBBB */
if(j == (channel -1))
  vch[pix] = (unsigned int) ( (ll >> 10) & 0x3FF ); /* this extracts the B's (above) */
  ++j;
  if(j > 4) {j = 0; ++pix;}


if(j == (channel -1))
  vch[pix] = (unsigned int) ( ll & 0x3FF ); /* this extracts the C's (above) */
  ++j;
  if(j > 4) {j = 0;++pix;}


} /* extract video - for block */

++i;


/* write line to output file after converting from 10 bit to 8 bit */
for(pix = 0; pix < Pixels; pix++)
      {vch[pix] = vch[pix] / 4;
      if(vch[pix] < DNmin) DNmin = vch[pix];
      if(vch[pix] > DNmax) DNmax = vch[pix];
      outline[pix] = (unsigned char) vch[pix];}

fwrite( (void*) outline, Pixels, 1, OUT);
} /* read line */

printf("\n\n Summary on %s:", infile);
printf("\n\n %d lines in file. ", (i-1));
printf("\n Max DN: %d  Min DN: %d", DNmax, DNmin);
printf("\n Lat/long range on top line:");
printf("\n %f %f \t %f %f", lat[0], lon[0], lat[Ngcp - 1], lon[Ngcp - 1]);


fclose(IN);
fclose(OUT);

if(getTHC == 1)
  { fprintf(OP1, "\n\n %f", PRT);
        fclose(OP1);}

if(getLOC == 1)
  {fclose(OP2); fclose(OP3);}

printf("\n\n DONE! \n");
exit(0);
}
```

# APPENDIX D

## Extraction of Data from the NCAR Formatted Images

The following C program was used to convert the binary data at a given row and column position in the NCAR formatted images to ASCII values. The images received from NCAR had one file per channel in a high byte, low byte format. The program below is specifically designed for the 512x512 images from the NCAR system covering Oklahoma with the exception of the Panhandle.

The program will request the center x and y coordinates of the three lysimeter sites and then extract the DN values for each channel to a nxn array centered on the given site in an ASCII file.

```
/* lysext.c */
/* Extracts portions of 2 byte images */
/* This version allows for variable block size and extracts the
   values into an ASCII file, all channels in one file */
/* Assumes 512x512 original 2 byte image of Oklahoma */

/* For UNIX files:
   Nsn_94.mn.da_ti.c
   012345678901234 56 - array position
   sn = sat number
   mn = month
   da = day
   ti = time
   c = channel

   Extract to:
   Ssnmnda.tic
   01234567890 where S = site M,A,W [Marena, Apache, Wister] */


#include <stdio.h>

void main()
  {
  static int i,            /* x counter */
        j,                  /* y counter */
        k,                  /* channel counter */
        s,                  /* site counter */
        e[3] = {0,0,0},     /* element counter in output array for each site */
        range=6,            /* Number of pixels to be extracted on each side of the lysimeter pixel */
        Dsize,              /* Number of data points per row per channel */
        xL[4],              /* Lysimeter coordinates, 1=M, 2 = A, 3 = W */
        yL[4],
        x1[4]={0,0,0,0},    /* upper left corner to extract */
        x2[4]={0,0,0,0},    /* lower right corner to extract */
        y1[4]={0,0,0,0},    /* Array: 1 = M, 2 = A, 3 = W */
        y2[4]={0,0,0,0},
        ymin = 999,         /* Row range */
        ymax = 0,
        NCH,                /* number of channels to extract from  3 = thermal only 5 = all + SZA */
```

269

```c
        rowl=1024,      /* row length of image * 2 */
        chSta,          /* channel to start from */
        chEnd,          /* channel to end with */
        sw = 0,         /* switch used in calculating DN value */
        fr;             /* file read test */

unsigned char c1, c2;   /* 2 byte pixel - high, low */

static unsigned int Aout[3][6][121];    /* Output array.
                                        Element 1: 0=M, 1 = A, 2 = W = site
                                        Element 2: Channels + solar
                                        Element 3: Extracted DN values */

char line[1024],        /* one image row */
        infile[25],     /* core input file */
        outfile[12];    /* Output file */

float solarZA;  /* solar zenith angle */

FILE *IN;
FILE *OUT; /* output */

/* get user inputs */
printf("\n\n Core file name example:\n\t Nsnmnda.ti");
printf("\n\n CORE Name of file to extract FROM: ");
  scanf("%s", infile);

printf("\n\n Number of channels [3 or 5]: ");
  scanf("%d", &NCH);

printf("\n\n Enter x, y position of Marena: ");
  scanf("%d %d", &xL[1], &yL[1]);

printf("\n\n Enter x, y position of Apache: ");
  scanf("%d %d", &xL[2], &yL[2]);

printf("\n\n Enter x, y position of Wister: ");
  scanf("%d %d", &xL[3], &yL[3]);

/* limit range size */
while(range > 5)
  {
        printf("\n\n Enter range to extract [<=5]: ");
          scanf("%d", &range);
  }

/* calculate number of pixels per row this results in */
Dsize = range * 2 + 1;

/* Set x,y limits on extraction areas */
for(i=1; i <=3; i++)
  {
        x1[i] = xL[i] - range;
        x2[i] = xL[i] + range;
```

270

```c
        y1[i] = yL[i] - range;
           if(y1[i] < ymin) ymin = y1[i];
        y2[i] = yL[i] + range;
           if(y2[i] > ymax) ymax = y2[i];
   }

/* create CORE output file names */
outfile[0] = 'E';
outfile[1] = infile[1]; /* sat num */
outfile[2] = infile[2];
outfile[3] = infile[3]; /* Month */
outfile[4] = infile[4];
outfile[5] = infile[5]; /* day */
outfile[6] = infile[6];
outfile[7] = '.';
outfile[8] = infile[8]; /* time GMT */
outfile[9] = infile[9];
outfile[10] = 't';      /* Three sites */
outfile[11] = '\0';

/* Open Extraction file */
if( (OUT = fopen(outfile, "w")) == NULL)
        { printf("\n\n\a File not open: %s", outfile);
          exit(-1);}


/* Set channel limits */
 if (NCH == 3)
  {chSta = 3; chEnd = 5;} /* night time, thermal only */
 else
  {chSta = 1; chEnd = 6;} /* day, include SZA */

/* ----------- Channel loop --------------- */

for(k = chSta; k <= chEnd; k++)
  {
        e[0] = 0; e[1] = 0; e[2] = 0;
        /* Set appropriate input and output file */
        switch(k)
          {
            case 1: infile[10] = '1'; break;
            case 2: infile[10] = '2'; break;
            case 3: infile[10] = '3'; break;
            case 4: infile[10] = '4'; break;
            case 5: infile[10] = '5'; break;
            case 6: infile[10] = 'Z'; break;
            default: printf("\n\n\a Major Error making channel name");
                       exit(-1);
                       break;
          }
        infile[11] = '\0';

        /* Open input file */
        if( (IN = fopen(infile, "rb")) == NULL)
```

271

```c
        { printf("\n\n\a File not found: %s", infile);
          exit(-1);}


printf("\n\n Starting Channel %d ... \n\n ", k);

i = 0; j = 0;
/* ------ Read to row above extraction ---------- */
for(j=0; j < ymin; j++)
      {
        if( (j % 20) == 0) printf("\r Jumping row: %d", j);

        fr = fread( (void*) line, rowl, 1, IN);
        if( fr != 1)
          {printf("\n\n \a Error reading file at line: %d", j);
          exit(-1);
          }
      } /* for j 1 */



/* ---------------- Begin extraction ------------------- */
/* read all rows that contain a site - top of Marena 1 to bottom Apache 2 */
for(j = ymin; j <= ymax; j++)
      {
        if( (j % 20) == 0) printf("\r Extracting row: %d", j);

        /* read row */
        fr = fread( (void*) line, rowl, 1, IN);
        if( fr != 1)
          {printf("\n\n \a Error reading file at line: %d", j);
          exit(-1);
          }

        /* extract x portion of row if in a site block */
        /* Check all three sites */
        for(s = 1; s < 4; s++)
          {
          if(j <= y2[s] && j >= y1[s]) /* If site in row */
                {
                sw = 0; /* high byte */
                /* Write column of row containing site */
                for(i = (x1[s]*2); i <= ((x2[s]*2) + 1); i++)
                  {
                        /* high byte */
                        if(sw == 0)
                          {c1 = (unsigned char) line[i];
                          sw = 1;}
                        else
                          {
                          c2 = (unsigned char) line[i];
                          Aout[s-1][k-1][e[s-1]] = (unsigned int) c1 * 256 + (unsigned int) c2;
                          ++e[s-1];
                          sw = 0;
                          }
                  } /* extracting within row */
```

```c
                } /* if site in row */
            } /* site counter - s */
        } /* for j - row extract */
    /* --------------- End extraction loop ---------------- */

    fclose(IN);
} /* k - channel loop */
printf("\n\n Writing output to %s ...", outfile);


/* ---------------- OUTPUT ------------------ */
/* Write all three sites to one file */
for(s=0; s < 3; s++) /* site */
    {
        /* OLD fprintf(OUT, "\n\n Site %d \n", s); */

    for(k = (chSta-1); k <= (chEnd - 1); k++) /* channel */
        {
        /* OLD fprintf(OUT, "\n Site %d Channel %d \n", s, k+1); */

        /* don't write SZA info. for each pixel. convert to float */
        if(k == 5)
            {
            solarZA = (float) Aout[s][k][e[s]/2] / (float) 10.0;
            fprintf(OUT, "%f \n", solarZA);
            } /* k = 5 (ch-1) - solar zenith angle */
        else /* not 5 */
            {
            for(i=0; i < e[s]; i++) /* data */
                {
                    fprintf(OUT, "%d \t", Aout[s][k][i]);
                    if( ((i+1) % Dsize) == 0) fprintf(OUT, "\n"); /* break out in rows */
                } /* data */
            } /* not 6 */

        } /* channel */

    } /* site */

/* write original coordinates used */
fprintf(OUT, "\n\n\n Original image position: x,y");
for(i=1; i <=3; i++)
    fprintf(OUT, "\n  Site %d: %d  %d", i, xL[i], yL[i]);


    fclose(OUT);
    exit(0);
} /* end main */
```

273

# APPENDIX E

## Instantaneous Field of View Equations

The instantaneous field of view (IFOV) is the area contributing reflected radiance to the sensor at the time a reading is taken. This area varies with the altitude of the sensor above the target and the angle at which the sensor views the target. Geometrical relationships can be used to determine the area give the field of view of the instrument, expressed as a conical angle.

The derivation is based on the relationships depicted in Figure E.1. In order to adequately represent all of the angles, the figure is not to scale. The thick dashed line represents the earth's surface and all the lines below are equal to the Earth's radius. Angle A is, the satellite zenith angle. The dashed lines represent the field of view of the satellite sensor and the angle B represents half the field of view. The angles C, D and E can all be determined from the Law of Sines. For example angles (A-B), C and H form a triangle; therefore, from the Law of Sines:

$$\frac{\sin(C)}{(Re+ Alt)} = \frac{\sin(A - B)}{Re} \tag{E.1}$$

where Re is the radius of the earth and Alt is the altitude of the satellite.

Multiplying both sides of the equation by Re and (Re + Alt):

$$\sin(C)\,Re = \sin(A - B)(Re+ Alt) \tag{E.2}$$

Multiplying both sides of Equation E.2 by $Re^{-1}$ and taking the inverse sine of both sides:

$$C = \sin^{-1}[\sin(A - B)(\frac{Alt}{Re} + 1)] \tag{E.3}$$

The solution for C in Equation in E.3 is ambiguous, as the solution is based on the length of two sites and one angle. It can be shown that the only angle that results in a true triangle satisfying the conditions of E.3 is given by:

$$C = \pi - \sin^{-1}[\sin(A - B)(\frac{Alt}{Re} + 1)] \tag{E.4}$$

for the angle C expressed in radians.

The same procedures can be used to determine angles D and E, resulting in:

$$D = \pi - \sin^{-1}[\sin(A)(\frac{Alt}{Re} + 1)] \tag{E.5}$$

$$E = \pi - \sin^{-1}[\sin(A + B)(\frac{Alt}{Re} + 1)] \tag{E.6}$$
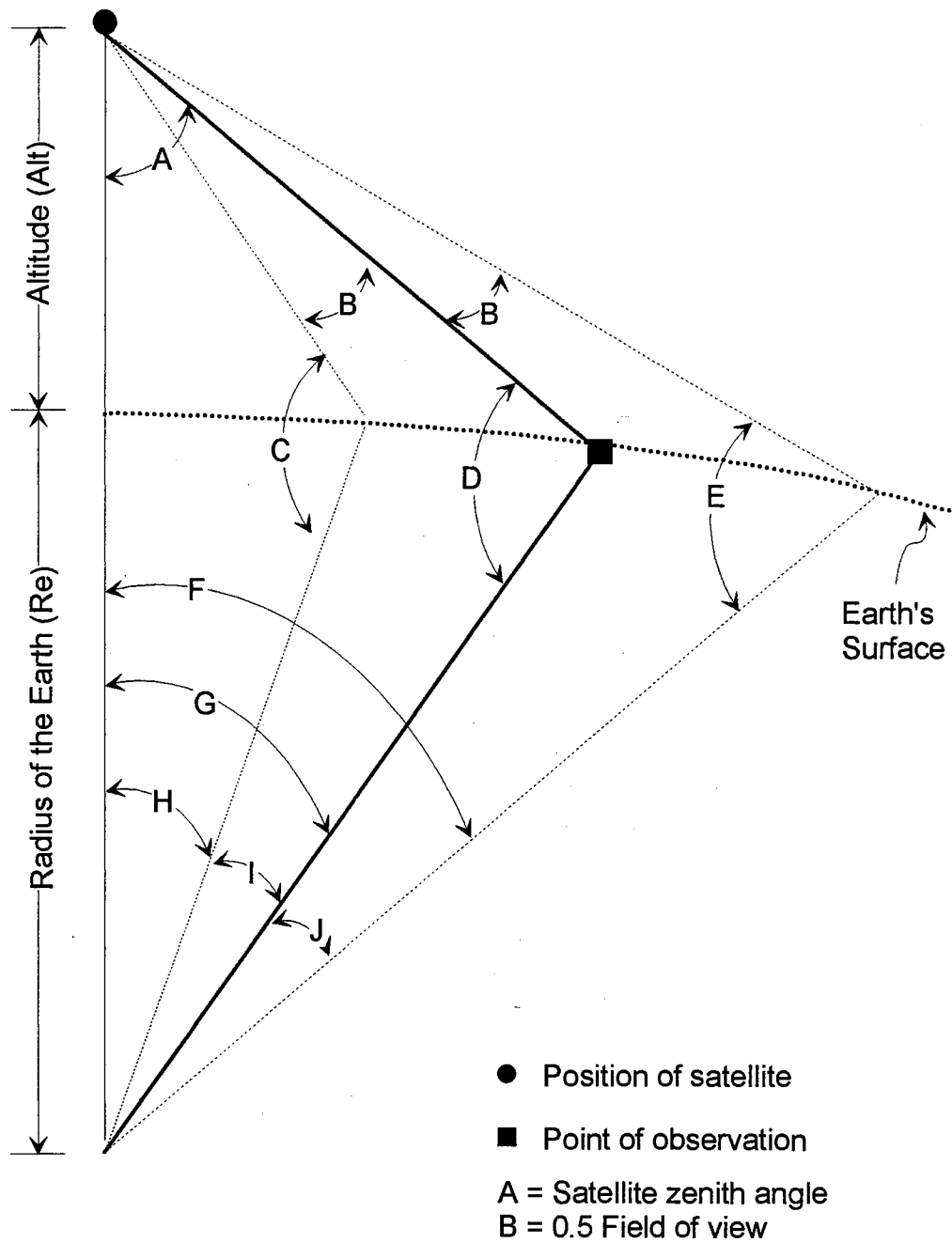
Figure E.1: Ilustration of the geometrical parameters used in the derivation of the instantaneous field of view for the AVHRR.

276

Noting that the sum of angles in a triangle must equal $\pi$ radians (180 degrees), angles F, G, and H can be expressed as:

$$F = \pi - E - (A + B) \tag{E.7}$$
$$G = \pi - D - A \tag{E.8}$$
$$H = \pi - C - (A\text{-}B) \tag{E.9}$$

Angle I corresponds to the arc length between the center of the field of view and the point closest to the satellite contributing radiance to the sensor. It can be found from angle G and H as:

$$I = G - H \tag{E.10}$$

Combining the results of Equations E.8, E.9 and E.10:

$$I = (\pi - D - A) - [\pi - C - (A\text{-}B)] \tag{E.11}$$

$$= \text{-}D + C - B \tag{E.12}$$

Expressing the angles D and C in the forms of equations E.4 and E.5 in Equation E.12:

$$I = -\{\pi - \sin^{-1}[\sin(A)(\frac{Alt}{Re} + 1)]\} + \pi - \{\sin^{-1}[\sin(A - B)(\frac{Alt}{Re} + 1)\} - B \tag{E.13}$$

Canceling like terms:

$$I = \sin^{-1}[\sin(A)(\frac{Alt}{Re} + 1)]\} - \sin^{-1}[\sin(A - B)(\frac{Alt}{Re} + 1) - B \tag{E.14}$$

The expression for angle I in Equation E.14 is a function of the altitude of the satellite (~850 km), the radius of the earth (6367 km) and the field of view of the sensor (~ 1.4 x $10^{-3}$ radians). Note that the angle B represents one half the field of view.

For angle J, corresponding to the arc formed between the center of the field of view and the far point contributing radiance to the sensor:

$$J = F - G \tag{E.15}$$

Substituting the expressions in E.7 and E.8 for F and G respectively:

$$J = \pi - E - (A + B) - (\pi - D - A) \tag{E.16}$$
$$= \text{-}E + D - B \tag{E.17}$$

Expression D and E in the forms of equations E.5 and E.6 respective:

$$J = -\{\pi - \sin^{-1}[\sin(A+B)(\frac{Alt}{Re}+1)]\} + \pi - \sin^{-1}[\sin(A)(\frac{Alt}{Re}+1)] - B \quad \textbf{(E.18)}$$

Canceling like terms and rearranging:

$$J = \sin^{-1}[\sin(A+B)(\frac{Alt}{Re}+1)] - \sin^{-1}[\sin(A)(\frac{Alt}{Re}+1)] - B \quad \textbf{(E.19)}$$

As in the expression for I in Equation E.14, this expression for J is in terms of the Earth's radius, altitude of the satellite and field of view of the sensor.

For angles I and J expressed as radians, the total arc length contributing radiance to the sensor is given by:

$$\text{IFOV} = \text{Re} \, (I + J) \quad \textbf{(E.20)}$$

where Re is the radius of the earth and IFOV is the instantaneous field of view, representing the distance along the scan line contributing radiance to the sensor. This equation was used to determine the IFOV pictured in Figure 4.5.

The differences between IFOV and resolution can be demonstrated by considering that a reading is recorded from the sensor 1024 times as the scanning mirror is rotated 55.4 degrees (0.967 radians). Therefore, the angle corresponding to each reading is $9.44 \times 10^{-4}$ radians. If half of this angle ($4.72 \times 10^{-4}$ radians) is substituted for the angle B in Equations E.14 and E.19, the length of equation E.20 now represents the distance between image pixels along the scan line. This procedure was used to represent the "resolution" picture in Figure 4.5.

278

# APPENDIX F

**Source Code Used in the Calculation of Brightness Temperature**

The following C program was used to calculate the brightness temperatures for the AVHRR thermal channels. The program assumes that response function information and the look up tables to correct for nonlinearities in the sensor are in the file N11PLANK.IN (included at the end of this appendix).

This program was designed to process an extracted 9x9 block of data for each of the lysimeter sites resulting from the output of the program presented in Appendix D. The same subroutines were used for calculating brightness temperature with the HRPT files.

```c
/* mdnbrt11.c */

/* This version averages DN values before conducting calculations */

/* emb 1/26/95 */

/* Calculate brightness temperature of AVHRR thermal channels */
/* Uses central wave number as a first guest and then
   iterates a numeric solution to the Planck function */

/* This version contains constants specific to NOAA 11 AVHRR */
/* Added multiple file input to this version */

/* emb 12/14/94 */

#include <stdio.h> /* input/output routines */
#include <math.h>  /* exp, log and pow functions */

#define KELV 273.15   /* convert Kelvin to C */

/* ------------- external (global) variables ----------------- */

/* Numeric Planck function variables */
static double nu1[3];       /* starting wave number (cm^-1) */
static double DELTnu[3];  /* Increment of wave numbers (cm^-1) */
static double PHI[3][60];   /* Normalized response function */

/* Non linearity correction factors */
static int ntemps;              /* number of correction brightness temperatures */
static double NLBT[28];         /* Brightness temperature range - ch 4&5 */
static double NLBASE[4];         /* Base plate temperature range */
static double NLcorr[4][28];     /* correction values */

/* ------------------- Function Definitions ------------------------------*/
/* Compute Planck function, weighted to a spectral response function */
double Nplanck(int ch, double TK);

/* iterates to get brightness temperature */
double Bright(double E, double TK1, int ch);

/* Correction for nonlinearities */
double Nline(double TK, double Tprt, int ch);
```

```c
void main()
{

/* Functions */
double Iplanck(); /* find T given E and satellite # */


/* Variable declarations */

    static int  i,      /* Row [Y] counter */
            j=0,                /* Column [X] counter */
            k = 0,              /* site counter */
            c = 0,              /* channel counter */
            ei = 0,  /* element counter */
            nsites,             /* number of sites in file */
            nch,                /* number of channels in the file per site */
            chstart,            /* starting channel number */
            chend = 5,          /* ending channel number */
            xd=9,               /* X dimension */
            yd=9;               /* Y dimension */

    static double Adn[3][5][3],     /* average DN vaules */
            T[3][3][3],             /* average brightness temperature:
                                        [site][channel][avg: 9x9, 3x3, center] initially in Kelvin */
            TK1,                    /* Brightness temperature from Inverse Planck */
            Tgain[3][3],            /* Gain for thermal channels - mW/(m^2 sr cm^-1) per count */
            Toff[3][3],             /* Offset for thermal channels - mW/(m^2 sr cm^-1) */
            TPRT[3],                /* Base plate temperature, C - 1/site */
            E,                      /* radiance in a thermal channel mW/(m^2 sr cm^-1) */


            /* inputs: */
            /* Angles input in degrees, converted to radians */
            SZA[3],     /* Solar zenith angle */
            LA[3];      /* Satellite look angle (converted to zenith) */


    unsigned int Cdn[3][5][121];    /* channel DN values */
                                    /* 3 sites, 5 channels, 121 values */

    char user[25],          /* File name for list of input files */
            chin[25],           /* Input file name */
            Tfile[25];          /* Output file name - Brightness temps */


    FILE *NIN;          /* file pointers - channels */
    FILE *THOUT;        /* file pointer to thermal channel output */
    FILE *RF;           /* Response function input file pointer */
    FILE *UIN;          /* pointer to list of input file names */

    /* -------------- Initial response function arrays ------------- */
    /* read response functions for each channel */
    if( (RF = fopen("n11plank.in", "r") ) == NULL)
```

```c
    { printf("\n\a n1 1plank.in not found. \n");
          exit(0);
    }

/* read starting wave numbers for each channel */
fscanf(RF, "%lf %lf %lf", &nu1[0], &nu1[1], &nu1[2]);

/* read wave number increment */
fscanf(RF, "%lf %lf %lf", &DELTnu[0], &DELTnu[1], &DELTnu[2]);

/* read number of increments */
for(i=0; i<3; i++) fscanf(RF, "%d", &j);

/* read weighting function */
for(i=0; i < 60; i++)
  fscanf(RF, "%lf %lf %lf", &PHI[0][i], &PHI[1][i], &PHI[2][i]);

/* Initial nonlinearity correction arrays */
/* Read number of brightness temperatures / channel */
fscanf(RF, "%d", &ntemps);

/* read base plate temps */
fscanf(RF, "%lf %lf %lf", &NLBASE[0], &NLBASE[1], &NLBASE[2]);

/* read brightness temperature range and corrections */
for(i=0; i < (2 * ntemps); i++)
  { fscanf(RF, "%lf", &NLBT[i]);
        for(j=0; j < 3; j++)
          fscanf(RF, "%lf", &NLcorr[j][i]);
  }

fclose(RF);

/* ------------ End response function initialization --------- */

/* Get name of file with input files from user */
printf("\n\n Enter file with input file names: ");
  scanf("%s", user);

if( (UIN = fopen(user, "r")) == NULL)
        { printf("\n\n\t File %s not found.", user);
          exit(0);}

printf("\n\n Enter the file to contain output values: ");
  scanf("%s", Tfile);

if( (THOUT = fopen(Tfile, "a")) == NULL)
        { printf("\n\n\t File %s not opened.", Tfile);
          exit(0);}


/* --------------------------------------------------------------------- */
/* --------------------------------------------------------------------- */
/* Start of input file loop */
```

282

```
while( fscanf(UIN, "%s", chin) != EOF)
  {
  /* ------------------ get file names ------------------------- */
  if( (NIN = fopen(chin, "r")) == NULL)
        { printf("\n\n\t File %s not found.", chin);
         exit(0);}


  /* -------------------- read input file --------------- */

  /* Read the number of sites and channels in the file */
  fscanf(NIN, "%d  %d", &nsites, &nch);
  if (nch == 3) chstart = 2;
  else chstart = 0;

  for(k=0; k < nsites; k++)
    {
        for(c=chstart; c < chend; c++)
          {
           ei = 0;
          for(i=0; i < yd; i++)
            {
                for(j=0; j < xd; j++)
                  {
                   fscanf(NIN, "%d", &Cdn[k][c][ei]);
                   ++ei;
                  } /* col of site */
            } /* row */
          } /* channel */
        if(nch == 5) fscanf(NIN, "%lf", &SZA[k]);
        if(nch == 5) fscanf(NIN, "%lf", &LA[k]);
    } /* site */

  /* read thermal coefficients appended to end of file */

  for(k=0; k < nsites; k++)
    {
        fscanf(NIN, "%lf", &TPRT[k]);

     for(c=0; c < 3; c++)
         fscanf(NIN, " %d %lf %lf", &i, &Tgain[k][c], &Toff[k][c]);

    } /* site coef */

  fclose(NIN);

  /* ----------------------------------------------------------- */
  /* Average DN values before converting to brightness temperatures */

  /* first initialize variables */
  for(k=0; k < nsites; k++)
    for(c=0; c < 5; c++)
        for(ei=0; ei < 3; ei++)
```

283

```
                Adn[k][c][ei] = 0.0;

/* 9x9 average */
for(k=0; k < nsites; k++)
 for(c=2; c < 5; c++)
        for(ei=0; ei < (xd*yd); ei++)
          Adn[k][c][0] += Cdn[k][c][ei];

/* 3x3 average + center */
for(k=0; k < nsites; k++)
 for(c=2; c < 5; c++)
        {
          Adn[k][c][1] = Cdn[k][c][30] + Cdn[k][c][31] + Cdn[k][c][32] +
                         Cdn[k][c][39] + Cdn[k][c][40] + Cdn[k][c][41] +
                         Cdn[k][c][48] + Cdn[k][c][49] + Cdn[k][c][50];

          Adn[k][c][1] = (double) Adn[k][c][1] / (double) 9.0;
          Adn[k][c][2] = (double) Cdn[k][c][40];
          Adn[k][c][0] = (double) Adn[k][c][0] / (double) 81.0;
        }



/* ----- Begin calculation of brightness temps ----------- */
printf("\n\n  On file: %s", chin);


for(k=0; k < nsites; k++)
 {
        for(c=2; c < 5; c++)
          {
          /* printf("\r On site: %d  Channel: %d", k, c+1); */
          ei = 0;
          for(ei=0; ei < 3; ei++)
           {
                  /* get radiance from calibration */
                  E = Tgain[k][c-2] * (double) Adn[k][c][ei] + Toff[k][c-2];
                  /* call plank function to get Tbright */
                  TK1 = Iplanck(E, c-2, 3);

                  /* Using the Inverse Planck as a first estimate,
                       use an iterative solution to get the precise
                       brightness temperature */
                  T[k][c-2][ei] = Bright(E, TK1, c-2);

                  /* Correct for nonlinearity - ch 4 & 5 only */
                  if(c == 3 || c == 4)
                          T[k][c-2][ei] = Nline(T[k][c-2][ei], TPRT[k], c-2);
           } /* elements */
          } /* channel */
 } /* site */

/* write results of this image */
/* Format:
```

284

```
              image, site ID, ch3, ch4, ch5 :9x9 average brightness temps
               "              " :3x3 average
               "              " : center */
    for(k=0; k < nsites; k++)
        for(ei=0; ei < 3; ei++)
            fprintf(THOUT, "%s %d %7.2lf %7.2lf %7.2lf \n",
                        chin, k, T[k][0][ei], T[k][1][ei], T[k][2][ei]);


   } /* end input file loop */


   fclose(THOUT);
   fclose(UIN);
   exit(0);
} /* end main */


/* -------------------------------------------------------------------------------- */
/*                          Inverse Plank function                      */
double Iplanck(E, chNum, wrange)
  double E;  /* radiance computed from DN values */
  int chNum; /* channel number */
  int wrange; /* range temperature is in */
{

/* NOTE: will have to add an additional array position to handle
         other satellites. Currently NOAA 11 */


        /* constants in Planck function */
   double  C1 = 1.1910659E-05,  /* mW/ (m^2 sr cm^-4) */
           C2 = 1.438833;      /* K/cm^-1 */


        /* temperature range over which central wave is valid, K */
   double TrangeLow[4] = {0.0, 225.0, 270.0, 285.0},
          TrangeHigh[4] = {225.0, 270.0, 285.0, 999.0},


        /* Central wave number (cm^-1) for given ranges - [range][ch] */
        Cwave[3][4] = {{2663.50, 2668.15, 2670.96, 2671.40},
                       {926.81, 927.36, 927.75, 927.83},
                       {841.40, 841.81, 842.14, 842.20}};


        double TK; /* temperature returned, K */
        double nu; /* central wave number used */


        int newrange=0,
           i;


        /* Initially use range given */
        nu = Cwave[chNum][wrange];


        /* calculate brightness temperature based on this range */
        TK = C2 * nu / log( (double) 1.0 + C1 * pow(nu, (double) 3.0) / E);


        /* see what range this temperature is in */
        for(i=0; i<4; i++)
          {
```

```
                    if(TK > TrangeLow[i] && TK <= TrangeHigh[i])
                            {
                              newrange = i;
                              break;
                            }
              } /* for i */


              /* Use recursion to find new temp if not in range */
              if (newrange != wrange)
                      TK = Iplanck(E, chNum, newrange);


    return(TK);
} /* end planck function */



/* ---------------------------------------------------------------------------------------- */
/* Numeric solution of planck function over a spectral
   response region */
/* --------------------------------------------------------- */


double Nplanck(int ch, double TK)
  {
    int i; /* wave increment counter */

    /* constants in Planck's function */
    static double c1 = 1.1910659E-05; /* mW cm^4 / m^2 sr */
    static double c2 = 1.438833;  /* K cm */

    static double nu; /* wave number */
    static double NUM = 0.0; /* numerator of numeric solution */
    static double DENOM = 0.0; /* denominator */
    static double B; /* Planck function */

    nu = nu1[ch];
    NUM = 0.0;
    DENOM = 0.0;

    for(i = 0; i < 60; i++)
      {
          /* compute the Planck function at this wave number */
          B = c1*pow(nu, (double) 3.0) / (exp( (c2*nu/TK) ) - (double) 1.0);

          NUM += (B * PHI[ch][i] * DELTnu[ch]);
          DENOM += (PHI[ch][i] * DELTnu[ch]);

          nu += DELTnu[ch];
      }

    return( (NUM/DENOM) );
  }
/* ----------------------- End Numeric Plank Function -------------- */
```

286

```
/* -------------------------------------------------------------------------- */
/* Iterative solution of the Plank function to get brightness temperature */
/* -------------------------------------------------------------------------- */
double Bright(double E1, double TK1, int ch)
  {
  /* allowable difference in radiance */
  static double tolerance[3] = {0.00001, 0.001, 0.001};
  static double E2, E3, /* radiance from Planck function */
              TK2, TK3, Etemp, /* Used in interpolation */
              slope, interc;

  /* Iterative solution based on interpolation:

        TK1     E2
        TK2     -------> Etemp
        TK3     E3    */


  /* find radiance based on temperature from Inverse Planck */
  E2 = Nplanck(ch, TK1);
  Etemp = E2;

  TK3 = TK1 + 0.1;
  E3 = Nplanck(ch, TK3);

  /* see if inverse planck close enough */
  do
    {
        slope = (TK3 - TK1) / (E3 - E2);
        interc = TK3 - slope * E3;

        TK2 = interc + E1 * slope;

        Etemp = Nplanck(ch, TK2);

        if(Etemp > E3)
          { TK1 = TK3; E2 = E3;
            E3 = Etemp;
            TK3 = TK2;
          }
        else if (Etemp < E2)
          { E3 = E2; TK3 = TK1;
            E2 = Etemp; TK1 = TK2;
          }
        else if ( fabs(E2 - Etemp) > fabs(E3 - Etemp)) /* upper closer */
          {
            E2 = Etemp;
            TK1 = TK2;
          }
        else /* lower closer */
          {
            E3 = Etemp;
            TK3 = TK2;
          }
```

```
    } /* tolerance chk 1 */
    while ( fabs( (E1 - Etemp) ) > tolerance[ch]);

    return(TK2);
}


/* ------------------------------------------------------------ */
/* Correct for instrument nonlinearities */
/* ------------------------------------------------------------ */
double Nline(double TK, double Tprt, int ch)
{

    int start; /* start of array for channel ch */
    int end;  /* end of array for channel ch */
    int i;
    int highT; /* high brightness temp array position */
    double slope;
    double intercept;
    int Pr;
    double ecor1;
    double ecor2;
    double ecor;

    if (ch == 1) /* channel 4 */
      { start = 0; end = ntemps - 1;}
    else
      { start = ntemps; end = ntemps*2 - 1;}

    /* find brightness temperature range */
    i = start;
    while(TK < NLBT[i] && i < end)
       ++i;

    highT = i - 1;

    /* determine base plate range */
    if(Tprt < NLBASE[1]) Pr = 0;
    else  Pr = 1;

    /* account for values on edge */
    if(i == start || i == end)
       {
       if(i == end) i -= 1;
       slope = (NLcorr[Pr + 1][i] - NLcorr[Pr][i]) / (NLBASE[Pr+1] - NLBASE[Pr]);
       intercept = NLcorr[Pr][i] - slope * NLBASE[Pr];
       ecor1 = slope * Tprt + intercept;
       TK += ecor1;
       return(TK);
       }

    /* interpolate across base plate temperature */
    /* low BT range */
    slope = (NLcorr[Pr + 1][i] - NLcorr[Pr][i]) / (NLBASE[Pr+1] - NLBASE[Pr]);
    intercept = NLcorr[Pr][i] - slope * NLBASE[Pr];
```

```
ecor1 = slope * Tprt + intercept;

/* high BT range */
slope = (NLcorr[Pr + 1][highT] - NLcorr[Pr][highT]) / (NLBASE[Pr+1] - NLBASE[Pr]);
intercept = NLcorr[Pr][highT] - slope * NLBASE[Pr];
ecor2 = slope * Tprt + intercept;

/* interpolate across brightness temperature */
slope = (ecor2 - ecor1) / (NLBT[highT] - NLBT[i]);
intercept = ecor2 - slope * NLBT[highT];
ecor = slope * TK + intercept;

TK += ecor;

return(TK);
}
```

## N11PLANK.IN

First part of this file is the weights for the Plank function while the second part is non-linear correction factors.

Line 1: Starting wave numbers for channels 3, 4 and 5.
Line 2: Wave number increment.
Line 3: Number of wave increments.
Lines 4 to 63: Response functions.
Line 64: PRT temperature ranges ($^o$C).
Lines 65 to 92: Apparent brightness temperature (K) followed by correction factors for channels 3, 4 and 5.

| | | |
|---|---|---|
| 2484.47217 | 854.70068 | 781.24976 |
| 7.13929 | 2.50516 | 2.06295 |
| 60 | 60 | 60 |
| 0.0000E+00 | 1.2838E-05 | 1.3817E-04 |
| 1.0945E-05 | 0.0000E+00 | 1.3106E-04 |
| 2.8150E-05 | 0.0000E+00 | 1.3327E-04 |
| 6.0983E-05 | 5.6581E-05 | 1.5412E-04 |
| 1.4006E-04 | 1.7545E-04 | 1.9677E-04 |
| 3.0581E-04 | 3.1639E-04 | 2.4099E-04 |
| 6.1175E-04 | 4.2930E-04 | 2.6101E-04 |
| 1.1183E-03 | 5.2284E-04 | 2.7834E-04 |
| 1.7813E-03 | 7.9863E-04 | 5.1016E-04 |
| 2.4182E-03 | 1.4977E-03 | 1.2242E-03 |
| 2.8923E-03 | 2.7592E-03 | 2.6155E-03 |
| 3.2167E-03 | 4.3408E-03 | 4.4979E-03 |
| 3.4267E-03 | 5.9102E-03 | 6.5607E-03 |
| 3.5421E-03 | 7.1887E-03 | 8.5105E-03 |
| 3.5775E-03 | 8.1658E-03 | 1.0182E-02 |
| 3.5651E-03 | 8.9152E-03 | 1.1472E-02 |
| 3.5534E-03 | 9.5077E-03 | 1.2285E-02 |
| 3.5689E-03 | 9.9887E-03 | 1.2691E-02 |
| 3.5852E-03 | 1.0391E-02 | 1.2880E-02 |
| 3.5727E-03 | 1.0748E-02 | 1.3042E-02 |
| 3.5346E-03 | 1.1065E-02 | 1.3290E-02 |
| 3.4888E-03 | 1.1329E-02 | 1.3626E-02 |
| 3.4493E-03 | 1.1527E-02 | 1.4043E-02 |
| 3.4248E-03 | 1.1658E-02 | 1.4516E-02 |
| 3.4216E-03 | 1.1748E-02 | 1.4965E-02 |
| 3.4349E-03 | 1.1821E-02 | 1.5298E-02 |
| 3.4568E-03 | 1.1901E-02 | 1.5437E-02 |
| 3.4775E-03 | 1.1991E-02 | 1.5392E-02 |
| 3.4852E-03 | 1.2088E-02 | 1.5223E-02 |

```
3.4733E-03        1.2191E-02        1.4989E-02
3.4581E-03        1.2297E-02        1.4741E-02
3.4613E-03        1.2406E-02        1.4516E-02
3.4858E-03        1.2517E-02        1.4351E-02
3.5114E-03        1.2627E-02        1.4271E-02
3.5197E-03        1.2724E-02        1.4252E-02
3.5126E-03        1.2794E-02        1.4254E-02
3.4999E-03        1.2827E-02        1.4235E-02
3.4871E-03        1.2830E-02        1.4171E-02
3.4715E-03        1.2826E-02        1.4062E-02
3.4493E-03        1.2838E-02        1.3910E-02
3.4129E-03        1.2845E-02        1.3708E-02
3.3519E-03        1.2645E-02        1.3402E-02
3.2592E-03        1.1996E-02        1.2918E-02
3.1470E-03        1.0657E-02        1.2181E-02
3.0333E-03        8.6431E-03        1.1144E-02
2.9110E-03        6.3424E-03        9.8207E-03
2.7154E-03        4.1718E-03        8.2362E-03
2.3767E-03        2.5247E-03        6.4174E-03
1.9012E-03        1.4741E-03        4.4925E-03
1.3852E-03        8.6297E-04        2.6917E-03
9.2617E-04        5.2935E-04        1.2499E-03
5.3593E-04        3.2464E-04        3.7444E-04
3.0800E-04        1.9180E-04        1.5195E-05
1.5192E-04        1.1184E-04        0.0000E+00
7.4249E-05        6.5860E-05        8.2010E-05
4.1157E-05        3.7159E-05        1.5007E-04
2.2843E-05        1.9221E-05        1.5868E-04
1.0043E-05        8.4591E-06        1.2764E-04
3.4684E-10        1.2845E-06        7.6770E-05
0.0000E+00        0.0000E+00        0.0000E+00
          14    10.0      15.0      20.0
       320.0     4.29      3.71      3.25
       315.0     3.50      2.98      2.55
       310.0     2.85      2.33      1.91
       305.0     2.23      1.73      1.32
       295.0     1.05      0.68      0.22
       285.0     0.24     -0.21     -0.67
       275.0    -0.45     -0.79     -1.15
       265.0    -1.06     -1.37     -1.66
       255.0    -1.41     -1.72     -2.03
       245.0    -1.70     -1.96     -2.22
       235.0    -1.87     -2.10     -2.28
       225.0    -1.90     -2.14     -2.36
       215.0    -1.82     -2.02     -2.20
```

| | | | |
|---|---|---|---|
| 205.0 | -1.54 | -1.76 | -1.98 |
| 320.0 | 1.43 | 1.26 | 1.12 |
| 315.0 | 1.23 | 1.03 | 0.89 |
| 310.0 | 1.05 | 0.84 | 0.70 |
| 305.0 | 0.85 | 0.64 | 0.47 |
| 295.0 | 0.43 | 0.28 | 0.09 |
| 285.0 | 0.07 | -0.07 | -0.23 |
| 275.0 | -0.19 | -0.34 | -0.47 |
| 265.0 | -0.37 | -0.51 | -0.60 |
| 255.0 | -0.60 | -0.77 | -0.78 |
| 245.0 | -0.72 | -0.90 | -0.92 |
| 235.0 | -0.84 | -1.02 | -1.00 |
| 225.0 | -0.94 | -1.06 | -1.16 |
| 215.0 | -1.12 | -1.24 | -1.16 |
| 205.0 | -1.15 | -1.27 | -1.23 |

# APPENDIX G

## Details of the Atmospheric Correction Procedures

# Nomenclature Used in Appendix G

| Symbol | Description | Defining Equation |
|---|---|---|
| $F_{Caer}$ | Fraction of aerosol scattered irradiance directed at the target of interest | |
| $F_{Cray}$ | Fraction of Rayleigh scattered irradiance directed at the target of interest | |
| $I_{aer}$ | Diffuse sky irradiance due to aerosol scattering | G.25 |
| $I_o$ | Exoatmospheric irradiance | |
| $I_g$ | Irradiance reaching the surface (both direct and diffuse) | G.26 |
| $I_{ray}$ | Diffuse sky irradiance due to Rayleigh scattering | G.24 |
| $k_\lambda$ | Extinction coefficient (dimensionless) | |
| $k_{O3}$ | Extinction coefficient for ozone ($cm^{-1}$) | |
| $k_w$ | Extinction coefficient for water vapor ($cm^{-1}$) | |
| $I_{sky}$ | Total diffuse sky irradiance | |
| $L_p$ | Path radiance | G.29 |
| $L_{Paer}$ | Path radiance due to aerosol scattering | G.28 |
| $L_{Pray}$ | Path radiance due to Rayleigh scattering | G.27 |
| $L_{sat}$ | Radiance received at the satellite | |
| $m_r$ | Relative optical mass | G.1 |
| $m_a$ | Actual air mass of the atmosphere | G.11 |
| $m_{all}$ | Relative optical mass from the sun to the target to the satellite | |
| $P$ | Local air pressure | |
| $P_{ray}(\Theta)$ | Rayleigh scattering phase function | G.23 |
| $P_{aer}(\Theta)$ | Aerosol scattering phase function | |
| $T_{aer}$ | Aerosol transmittance | G.13 |
| $T_{abH20}$ | Water vapor transmittance | G.19 |
| $T_{abO3}$ | Ozone transmittance | G.17 |
| $T_{abs}$ | Transmittance as a function of selective absorption | |
| $T_{abs1}$ | Transmittance as a function of selective absorption in AVHRR channel 1 | |
| $T_{abs2}$ | Transmittance as a function of selective absorption in AVHRR channel 2 | |
| $T_{ray}$ | Rayleigh transmittance | G.10 |
| $w$ | Precipitable water | G.18 |
| $\lambda$ | Wavelength | |
| $\Theta$ | Scattering angle | G.22 |
| $\theta_{sun}$ | Solar zenith angle | |
| $\theta_{sat}$ | Satellite zenith angle | |
| $\Psi$ | Azimuth angle | |

This appendix provides a more complete review of the atmospheric correction procedures evaluated in this study. First, a definition of terms is provided, followed by a description of the atmospheric transmittance relationships defined by Iqbal (1983) and the methods used to apply these to reduce atmospheric variation in the AVHRR's reflective channels (channels 1 and 2). Additional details are also provided on the methods developed by Paltridge and Mitchell (1990). The code used to execute the correction procedures is provided in Appendix H. The last section of the appendix compares predicted ground-level irradiance (Iqbal's methods) to pyranometer measurements.

## Definition of Terms

In order to present the methods, several terms are first defined. Unless otherwise indicated, the primary source for the following information is from Iqbal (1983).

### Relative Optical Mass

The distance a solar ray travels will increase due to collisions with particles in the atmosphere. The distance traveled by the ray is referred to as path length. The relative optical mass is defined as the ratio of the path length of an oblique radiation source to the zenith path length. Assuming a non-refractive and homogeneous atmosphere, the relative optical mass ($m_r$) was estimated by:

$$m_r = \sec(\theta_{sat}) \tag{G.1}$$

where $\theta_{sat}$ is the zenith angle. Iqbal notes that this approximation can cause errors for zenith angles greater than 80 degrees due to the vertical distribution of various molecules in the atmosphere, with ozone being some what more sensitive.

### Optical Depth and Transmittance

Bouger's Law describes the attenuation of light through a medium as:

$$I_{e\lambda} = I_{o\lambda} \exp(-k_\lambda \, m_r) \tag{G.2}$$

where $I_{e\lambda}$ is the radiant flux exiting the medium, $I_{o\lambda}$ the initial intensity of the flux, $k_\lambda$ is the extinction coefficient and m is the distance traveled. The subscript is included to indicate that attenuation is dependent on the wavelength considered. If m is expressed as the optical path length, the product of $k_\lambda$ and $m_r$ is referred to as optical depth. Transmittance is defined as the ratio of energy transmitted through a medium to the energy entering ($\exp(-k_\lambda m)$) in Equation G.2.

Often processes attenuating radiation in the atmosphere (such as molecular and aerosol scattering and selective absorption) are assumed to be independent. Under this

assumption, the combined attenuation due to the various processes can be obtained by adding the optical depths or multiplying the individual transmittance values.

## Total Integrated Transmittance

In order to account for the wave length dependence of the: solar spectral irradiance in the band width of the sensor, $F(\lambda)$, the relative spectral response of the sensor, $f(\lambda)$, and the wavelength dependence of transmittance for a process x, $T(\lambda,k,m)$ the total integrated transmittance $(TI(k,m))$ for a given channel was defined as:

$$TI(k,m) = \frac{\int_{\lambda 1}^{\lambda 2} T(\lambda,k,m)F(\lambda)f(\lambda)d\lambda}{\int_{\lambda 1}^{\lambda 2} F(\lambda)f(\lambda)d\lambda} \qquad (G.3)$$

where $\lambda 1$ and $\lambda 2$ indicate the sensor band width limits, and x indicates the process of interest. In reality, no continuous function are readily available for the above terms, so the expression was evaluated numerically, using values for the terms centered on a wavelength interval.

## Exoatmospheric Reflectance

Exoatmospheric reflection $(R_{ex})$ was based on the definition given by Schiebe et al. (1992) which is:

$$R_{ex} = \frac{\pi L_{sat}}{Ecc\, I_o \cos(\theta_{sun})} \qquad (G.4)$$

where $L_{sat}$ is the radiance received at the satellite, Ecc is the eccentricity correction factor of the earth's orbit, $I_o$ is the radiation received at the surface of the atmosphere weighted according to the sensor's response function and $\theta_{sun}$ is the solar zenith angle. The Ecc is the square of the ratio between the average distance of the earth from the sun and the sun and earth distance on the day of interest. Therefore, it normalizes the variations in of solar flux due to the eccentricity of the earth's orbit. The term $\cos(\theta_{sun})$ normalizes the solar flux from an area perpendicular to the incoming radiation to an area perpendicular to the surface. Multiplication of the radiance received at the satellite by $\pi$ is based on the assumption that the reflected radiance at the surface is perfectly diffuse.

The origination of the numerator of Equation G.4 can be found by reviewing the definition of intensity of radiation at a surface (i), expressed as:

$$i = \frac{dF}{dw\, dA \cos(\theta)} \qquad (G.5)$$

296

where dF is the amount of energy either received or emitted by the surface of area dA within a solid angle dw.

Noting that flux is the amount of energy per surface area, Equation G.5 becomes:

$$\frac{dF}{dA} = i\, dw\cos(\theta) \qquad\qquad \textbf{(G.6)}$$

Considering the flux passing though some surface area of a hemisphere, the solid angle in Equation G.6 can be expressed as:

$$dw = \sin(\theta)\, d\theta\, d\Psi \qquad\qquad \textbf{(G.7)}$$

where $\theta$ is the zenith angle $\Psi$ is the azimuth angle. Substituting equation G.7 into G.6 and integrating over the surface area of a hemisphere:

$$\frac{F}{dA} = \int\limits_{0}^{2\pi}\int\limits_{0}^{\pi/2} i\sin(\theta)\cos(\Psi)\, d\theta\, d\Psi \qquad\qquad \textbf{(G.8)}$$

If the surface is assumed complete diffuse, then i is independent of direction and can be factored out of the integral. Assuming diffuse reflection, integration of Equation G.8 yields:

$$F/dA = i\,\pi \qquad\qquad \textbf{(G.9)}$$

If the surface is not diffuse, then i is not independent of $\theta$ and $\Psi$ and must be considered in the integration.

**Iqbal (1983) Atmospheric Correction Methods**

The following section describes the methods used to estimate atmospheric transmittance in for AVHRR channels 1 and 2 using relationships and data presented by Iqbal (1983).

Rayleigh (Molecular) Scattering

The scattering of radiation by air particles can be described as an approximate function of $1/\lambda^4$. The following expression was used to describe Rayleigh transmittance ($T_{ray}$):

$$T_{ray} = \exp(-0.008735\, \lambda^{-4.08}\, m_a) \qquad\qquad \textbf{(G.10)}$$

The symbol $m_a$ is to indicate the actual mass of the atmosphere as the above relationship is based on dry air at standard conditions. An approximate correction for differences in station pressure was accomplished by:

$$m_a = m_r \, (P/1013.25) \tag{G.11}$$

where P is the local pressure in mbars and 1013.25 is the standard pressure at sea level. If P is only available as sea level pressure ($P_o$) it can be determined by:

$$P = P_o \, \exp(-0.0001184 \, z) \tag{G.12}$$

where z is the elevation above sea level in m. Variation of Rayleigh scattering is not sensitive to changes in the water vapor content of the atmosphere.

Aerosol (Mie) Scattering

In addition to Rayleigh scattering, radiation can also be scattered by water vapor and dust particles, ie aerosols. The scattering process due to aerosols is much harder to describe, as it varies with both the size and distribution of the particles.

Angstrom's turbidity formula for aerosol transmittance ($T_{aer}$) was used:

$$T_{aer} = \exp(-B \, \lambda^{-a} \, m_a) \tag{G.13}$$

where B is turbidity, a representation of the number of aerosols present, and a is a function of the size distribution of the aerosols. Iqbal suggest 1.3 as a good average value of the size parameter for most natural atmospheres and this value was used in the correction procedures.

B can be determined using a sun photometer to measure aerosol attenuation at wave lengths where molecular absorption is not significant. B can also be determined by measuring the concentration of dust particles in the atmosphere. In this study, B was approximated from meteorological range as:

$$B = (0.55)^a \, (3.912/Vis - 0.01162) \, [0.02472(Vis - 5) + 1.132] \tag{G.14}$$

where Vis is meteorological range in km. The factor 0.55 is due to the assumption that the sensitivity of human sight is centered on the 0.55 um wavelength. The relationship is only valid for ranges greater than 5 km. McCartney (1976) provides an extensive discussion of both visual and meteorological range. Visual range ($R_v$) is defined as:

$$R_v = \frac{1}{B_{sc}} \ln \frac{C}{\varepsilon} \tag{G.15}$$

where C is a measure of the contrast of the target being viewed against the background, $\varepsilon$ represents an observer dependent contrast, and $B_{sc}$ is a measure of horizontal optical depth.

If a large, black target is used, McLatchey (1976) indicates that C approaches 1 and $\varepsilon$ assumes a value of 0.02. Using these values, meteorological range is defined as:

$$\text{Vis} = 3.912/B_{sc} \qquad \qquad \textbf{(G.16)}$$

Kneizys, et al. (1983) recommend multiplying visual range by 1.3 to obtain an estimate of meteorological range. The National Weather Service (NWS) typically reports visual range and not meteorological range based on personal correspondence with the Tulsa NWS office. Therefore, all visual ranges were multiplied by 1.3 as an approximation of meteorological range.

Selective Absorption

In addition to scattering processes, selective absorption can also attenuate irradiance. Selective absorption refers the absorption of energy at discreet wavelengths by atmospheric gases and water vapor. The energy is absorbed and not scattered as is the case in Rayleigh and aerosol attenuation.

The two primary selective absorbers of the reflective channels of the AVHRR are ozone and water vapor in channels 1 and 2 respectively. Irradiance in channel 2 is also attenuated by carbon dioxide; however, it occurs over a very short wavelength interval and was not considered in this analysis.

From Iqbal, ozone transmittance ($T_{abO3}$) was calculated as:

$$T_{abO3} = \exp(-k_{O3} \, c \, m_a) \qquad \qquad \textbf{(G.17)}$$

where $k_{O3}$ is the extinction coefficient for ozone ($cm^{-1}$) and c is the ozone concentration (cm). Iqbal provides tables of both $k_{O3}$ for wavelength intervals of 0.005 um that correspond to the spectral region of AVHRR channel 1. Additionally, average ozone concentrations for various latitudes and time periods are given. For latitudes of approximately 35 North, concentrations range from 0.27 to 0.34 cm during the year. A constant value of 0.3 cm was used in this study.

Transmittance of water vapor can be related to the concentration of water vapor in the atmosphere. Precipitable water can be defined as the thickness of liquid water if all the water in a column of unit area were condensed at the surface normal to the column. Precipitable water (w, cm) was estimated by:

$$w = [0.439 \, (RH/100) \, \exp(26.23 - 5416/T_a)] / T_a \qquad \qquad \textbf{(G.18)}$$

where $T_a$ is air temperature (K) and RH is relative humidity (%), both at 1.5 m.

Transmittance as a function of selective water vapor absorption ($T_{abH20}$) was then calculated as:

$$T_{abH20} = \exp[-0.2385 \, k_w \, w \, m_r \, / \, (1 + 20.7 \, k_w \, w \, m_r)] \qquad \qquad \textbf{(G.19)}$$

where $k_w$ is the spectral absorption coefficient for water vapor ($cm^{-1}$). Iqbal presents a table of $k_w$ at intervals of 0.01 um in the spectral region corresponding to AVHRR

channel 2.

## Scattering Phase Functions

In addition to describing the magnitude of aerosol and Rayleigh scattering, the directional distribution of the scattered radiation must also be described. McCartney (1976) defines the scattering phase function as the ratio of energy per unit solid angle directed towards angle $\Theta$ to the average energy scattered in all directions per unit solid angle. Expressed mathematically:

$$\frac{1}{4\pi} \int_0^{4\pi} P(\Theta)dw = 1 \qquad \text{(G.20)}$$

where dw is the solid angle and $4\pi$ is the solid angle of a sphere. The angle $\Theta$ is called the scattering angle and is the angle between the plane of the incident light and the plane of the observation. For the special case when the satellite and sun are at opposite azimuth angles:

$$\Theta = 180 - (\theta_{sun} + \theta_{sat}) \qquad \text{(G.21)}$$

where $\theta_{sun}$ is the solar zenith angle and $\theta_{sat}$ is the satellite zenith angle (both in degrees).

When the relative azimuth angle between the sun and satellite is $\Delta\Psi$, Kasten and Raschke (1974) provide the relationship for the scattering angle as:

$$\Theta = 180 - \cos^{-1}[\cos(\theta_{sat})\cos(\theta_{sun}) + \sin(\theta_{sat})\sin(\theta_{sun})\cos(\Delta\Psi)] \qquad \text{(G.22)}$$

In this study, the scattering angle was calculated according to Equation G.22.

The phase function for Rayleigh scattering $P_{ray}(\Theta)$ used was:

$$P_{ray}(\Theta) = 0.75\,(1 + \cos^2(\Theta)) \qquad \text{(G.23)}$$

(McCartney, 1976; Paltridge and Mitchell, 1990). As this indicates, most of Rayleigh scattering occurs in the forward or backward directions, with little scattered normal to the direction of travel.

Aerosol scattering is primarily in the forward direction and is dependent on the vertical distribution of aerosols. A aerosol phase function for a continental type aerosol was used from McClatchey et al. (1972) as presented by Paltridge and Mitchell (1990).

## Path Radiance

Both the diffuse sky irradiance and path radiance are functions of the amount of scattered irradiance. The directional distribution of the components of the scattered irradiance is process dependent (either from Rayleigh or aerosol scattering); therefore, the components are expressed independently as:

$$I_{ray} = I_o \, T_{abs} \, (1 - T_{ray}) T_{aer} \qquad\qquad \textbf{(G.24)}$$

$$I_{aer} = I_o \, T_{abs} \, (1 - T_{aer}) T_{ray} \qquad\qquad \textbf{(G.25)}$$

where $I_{ray}$ is the amount of sky irradiance due to Rayleigh scattering, $T_{abs}$ is the transmittance as a function of absorbed irradiance, ozone in channel 1 (Equation G.17), water vapor in channel 2 (Equation G.19), $T_{ray}$ is transmittance as a function of Rayleigh scatter (Equation G.10), $T_{aer}$ is transmittance as a function of aerosol scatter(Equation G.13), and $I_{aer}$ is the total amount of sky irradiance due to aerosol scattering. Note that the transmittances for equations G.24 and G.25 are defined using the relative optical path length of the sun ($m_r = 1/\cos(\theta_{sun})$).

Ignoring background reflectance, the irradiance at the target ($I_g$) can be expressed as:

$$I_g = \cos(\theta_{sun}) \, [T_{abs} \, T_{ray} \, T_{aer} \, I_o + I_{ray} \, F_{Cray} + I_{aer} \, F_{Caer}] \qquad\qquad \textbf{(G.26)}$$

where $F_{Cray}$ and $F_{Caer}$ is the fraction of Rayleigh and aerosol scattered irradiance in the forward direction as a function of the solar zenith angle. Iqbal (1983) suggest a value of 0.5 for $F_{Cray}$ and presents $F_{Caer}$ in tabular form as a function of solar zenith angle. The table values were fit to a forth order polynomial for use in the computations.

As with the diffuse sky irradiance, path radiance ($L_p$) is divided between aerosol and Rayleigh processes. From Paltridge and Mitchell (1990):

$$L_{Pray} = P_{ray}(\Theta) \, T_{abs1} \, I_o \, (1 - T_{rayA}) / (4\,\pi) \qquad\qquad \textbf{(G.27)}$$

$$L_{Paer} = P_{aer}(\Theta) \, T_{abs2} \, I_o \, (1 - T_{aerA}) \, T_{rayA} / (4\,\pi) \qquad\qquad \textbf{(G.28)}$$

$$L_p = \sec(\theta_{sat}) \, (L_{Pray} + L_{Paer}) / m_{all} \qquad\qquad \textbf{(G.29)}$$

where $L_{Pray}$ is the path radiance due to Rayleigh scattering, $L_{Paer}$ is path radiance due to aerosol scattering, $m_{all}$ is the total relative air mass from the sun to the target to the satellite, $T_{rayA}$ and $T_{aerA}$ are the Rayleigh and aerosol transmittance through the path length defined by $m_{all}$, $P_{ray}(\Theta)$ is the Rayleigh scattering phase function (Equation G.23), and $P_{aer}(\Theta)$ is the aerosol scattering phase function . Note that transmittance values for these equations are for the total optical path from the sun to the target to the satellite. $T_{abs1}$ and $T_{abs2}$ are defined in the next paragraph.

In estimating path radiance, it is necessary to consider the vertical distribution of absorbers in the atmosphere. Following recommendations of Tanre et al. (1992), both the Rayleigh and aerosol scattered radiance is assumed to be attenuate by Ozone as it is concentrated above where these processes occur; however, water vapor and aerosols are concentrated in the lower 2 km of the atmosphere. Therefore, the following selective

absorption transmittances are defined as:

$$T_{abs1} = T_{abs2} = T_{abO3} \text{ for AVHRR channel 1,}$$
$$T_{abs2} = T_{abH20}(0.5w) \text{ for AVHRR channel 2,}$$

where $T_{abH20}$ is the transmittance of water vapor at 50 percent of the actual precipitable water content (using Equation G.19). This is based on the assumption that the aerosols and water vapor are well mixed in the lower portion of the atmosphere. Mitchell and O'Brien (1993) provide a more detailed explanation of the equations G.27 to G.29.

The path radiance expressed in Equation G.29 represents the fraction of scattered irradiation in the direction of the sensor. Limitations of the phase functions used in Equations G.27 and G.28 are discussed by Deirmendjian (1969). The assumptions include: the properties of the aerosol are constant through out the atmosphere, the atmosphere is modeled as a slab, and irradiance is scattered without change of wavelength.

The irradiance received at the satellite due to the reflected irradiance at the target is also attenuated by the atmosphere. Assuming a lambertian surface, the actual irradiance reflected from by target is:

$$L_g = \pi\,(L_{sat} - L_p)\,/\,(T_{aerS}\;T_{rayS}\;T_{absS}) = \pi\,I_g\,R \qquad\qquad \textbf{(G.30)}$$

where R is the reflectance of the target and the addition of the subscript "S" indicates the transmittances are calculated based on the relative optical path between the ground and satellite.

Irradiance or radiance due to multiple scattering is ignored. Paltridge and Mitchell (1990) note that multiple scattering due to aerosols is small relative to the other radiances reaching the satellite. It is further noted that Rayleigh multiple scattering is fairly constant in the AVHRR reflective channels for satellite and solar zenith angles less than 85 degrees (transmittance for channels 1 and 2 = 0.9 and 0.95 respectively). Additionally, background reflectance was assumed small in comparison to the other scattering processes.

Based on the previous discussion, the reflectance at the satellite corrected for single scattering ($R_{sc}$) can be expressed as:

$$R_{sc} = \frac{L_g}{I_g} = \frac{\dfrac{\pi}{T_{atm}^{sat}}(L_{sat} - L_p)}{\cos(\theta_{sun})(I_o T_{atm}^{sun} + I_{sky})} \qquad\qquad \textbf{(G.31)}$$

where $T^{sat}{}_{atm}$ is the total transmittance between the ground and satellite, $L_{sat}$ is the radiance received by the satellite, $L_p$ is path radiance, $T^{sun}{}_{atm}$ is the total atmospheric transmittance between the sun and the ground, $I_o$ is exoatmospheric irradiance and $I_{sky}$ is

diffuse sky irradiance (= $I_{ray} F_{Cray} + I_{aer} F_{Caer}$ of Equation G.26). The basic form of Equation G.31 was used in the correction of AVHRR channels 1 and 2.


Paltridge and Mitchell (1990) Correction Methods

Paltridge and Mitchell (1990) use LOWTRAN 6 (Kneizys et al., 1983) to define atmospheric transmittances using a U.S. Standard Atmosphere to define the atmospheric profiles. Using the nomenclature already defined, their correction procedure can be expressed as:

$$R_{pm} = \frac{A_{sat}(1 - M) - Lp}{4\cos(\theta_{sun})T_{ray}T_{aer}(1 + m\tau_{aer})} \qquad \text{(G.32)}$$

where, $A_{sat}$ is the apparent albedo measured by the satellite ($L_{sat} \pi / I_0$), M is the fraction of radiance at the satellite contributed by molecular multiple scattering ( 0.1 for channel 1 and 0.05 for channel 2), m is the total relative air mass from the ground to the satellite ($\sec(\theta_{sun}) + \sec(\phi_{sat})$), $\tau_{aer}$ is the relative aerosol optical depth and the transmittances are defined based on the path from the sun to the target to the satellite.

The parameterization presented by Paltridge and Mitchell was developed for NOAA 9; however, channels 1 and 2 of NOAA 11 have response curves very similar to those of NOAA 9.

Paltridge and Mitchell (1990) report that the values of M are very constant for a wide range of solar zenith angles and surface reflectance. Following their recommendations, M for channel 1 is assumed constant a 0.1 for channel 1 and 0.05 for channel 2. An overview of the derivation of Equation G.32 follows.

Irradiance reflected from the target at ground level (assuming diffuse reflectance) is calculated as:

$$L_{dir} = \pi \cos(\theta_{sun}) R I_0 T_{rayA} T_{aerA} \qquad \text{(G.33)}$$

where $L_{dir}$ represents the radiance received at the satellite after direct reflection from the target.

Discussion of the calculation of the path radiance is essentially the same as discussed with Iqbal's procedures. However, Paltridge and Mitchell use LOWTRAN to define the vertical profile of the atmosphere for Rayleigh attenuation.

To account for both reflected direct sky irradiance and back ground reflection, the diffuse sky irradiance is assumed mainly due to aerosols which are assumed to scatter irradiance

primarily in the forward direction. They further assume that the aerosol optical depth is small and arrive at:

$$I_{sky} = R \tau T_{aer} T_{ray} I_o / \pi \qquad \text{(G.34)}$$

Background radiance ($L_{rb}$) is expressed as:

$$L_{rb} = \cos(\theta_{sun}) \sec(\phi_{sat}) I_{sky} \qquad \text{(G.35)}$$

leading to the approximation:

$$I_{sky} + I_{rb} \approx m \tau I_{dir} \qquad \text{(G.36)}$$

The source of the derivations is expanded by Mitchell and O'Brien (1993).


## Comparison of Iqbal Predicted Irradiance to Pyranometer Measurements


### Methods

In addition to the comparison of solar radiation received at the earth's surface predicted using the methods of Iqbal (1983) to that measured by the pyranometer at the Mandill Mesonet site discussed in Chapter 4, a comparison was also made for the complete solar cycle on select days at the lysimeter sites. The dates used in the comparison are shown in Table G.1, with summary statistics of air temperature, precipitable water, and station pressure also included.

The predicted values were determined by Iqbal's methods previously discussed for the spectral region of the pyranometer (Equation G.26). The relative response function for the pyranometers used with the Mesonet stations is shown in Figure G.2a (from Brock et al., 1995). Exoatmospheric solar irradiance based on the World Radiation Center spectrum as presented by Iqbal (1983) is also shown in the figure. To represent the selective absorption due to atmospheric ozone and water vapor, the extinction coefficients corresponding to these process is also plotted versus wavelength. The pyranometer is sensitive to the complete spectral range of AVHRR channels 1 and 2, as indicated by Figure G.1 b.

The comparison is based on 15 minute data reported by the Mesonet stations. The time period considered is limited to times where the solar zenith angle is less than 90 degrees. Precipitable water was estimated according to Equation G.19 using the 15 minute values of temperature and relative humidity at 1.5 m. The relative optical mass was also corrected for station pressure according to Equation G.11.

304

## Results

Plots of pyranometer and predicted solar radiation are presented in Figure G.2 for the Marena, Goodwell, Apache and Wister Mesonet sites on the dates listed in Table G.1. Overall, predicted and measured radiation was in close agreement. Obvious departures occur due to scattered clouds on May 18 at Marena and on the two days at Apache. The Root Mean Square Error between measured and predicted solar radiation for each day is included in Table G.1. For the days without cloud interference, the RMSE is typical less than 20 W m$^{-2}$. On June 27 at Marena, solar radiation was under predicted for the time period around solar noon. From Table G.1, the standard deviation of pressure for the day was much higher than the other days considered. A time series plot of pressure on that day indicated a sharp drop in pressure at about the time the solar zenith angle was 60°. This may be an indication that a weather front was passing through the area. Under such conditions, the assumption that the atmospheric profile is uniformly mixed is not valid. This does indicate the limitations of approximating the atmospheric profile from surface measurements. However, with the acceptation of this date and days with cloud interference, Iqbal's method does provide very reasonable estimates of solar radiation.

**Table G.1: Average 1.5 m air temperature, precipitable water, station air pressure, and Root Mean Square Error (RMSE) between predicted and measured solar radiation.**

| Site | Date (1994) | Air Temperature (°C) Average [a] | STD [b] | Precipitable Water (cm) [c] Average | STD | Station Pressure (mbars) Average | STD | RMSE (W m$^{-2}$) |
|---|---|---|---|---|---|---|---|---|
| Marena | March 15 | 16.6 | 3.2 | 1.11 | 0.16 | 979.4 | 1.0 | 15.1 |
|  | May 18 | 24.2 | 3.8 | 3.15 | 0.11 | 980.7 | 1.2 | 51.8 |
|  | June 27 | 32.9 | 5.4 | 4.20 | 0.44 | 939.8 | 13.7 | 21.2 |
| Goodwell | May 29 | 25.9 | 5.6 | 2.22 | 0.32 | 877.2 | 0.4 | 13.9 |
|  | May 30 | 28.7 | 6.2 | 2.71 | 0.24 | 878.3 | 1.2 | 10.4 |
|  | June 13 | 33.4 | 6.0 | 2.40 | 0.46 | 871.6 | 1.1 | 9.6 |
| Apache | April 15 | 16.9 | 3.3 | 1.28 | 0.13 | 966.4 | 2.6 | 42.3 |
|  | July 20 | 31.4 | 4.1 | 3.72 | 0.14 | 962.9 | 0.9 | 76.9 |
| Wister | June 25 | 30.3 | 5.8 | 4.54 | 0.47 | 992.4 | 1.4 | 19.3 |
|  | Sept. 19 | 24.4 | 6.2 | 2.42 | 0.25 | 1003.2 | 1.5 | 12.7 |

[a] Average of 15 minute readings during the time period the solar zenith angle was less than 90 degrees.

[b] Standard deviation of the 15 minute readings during the time period the solar zenith angle was less than 90 degrees.

[c] Precipitable water estimated using 1.5 m relative humidity and temperature data (Equation G.18).
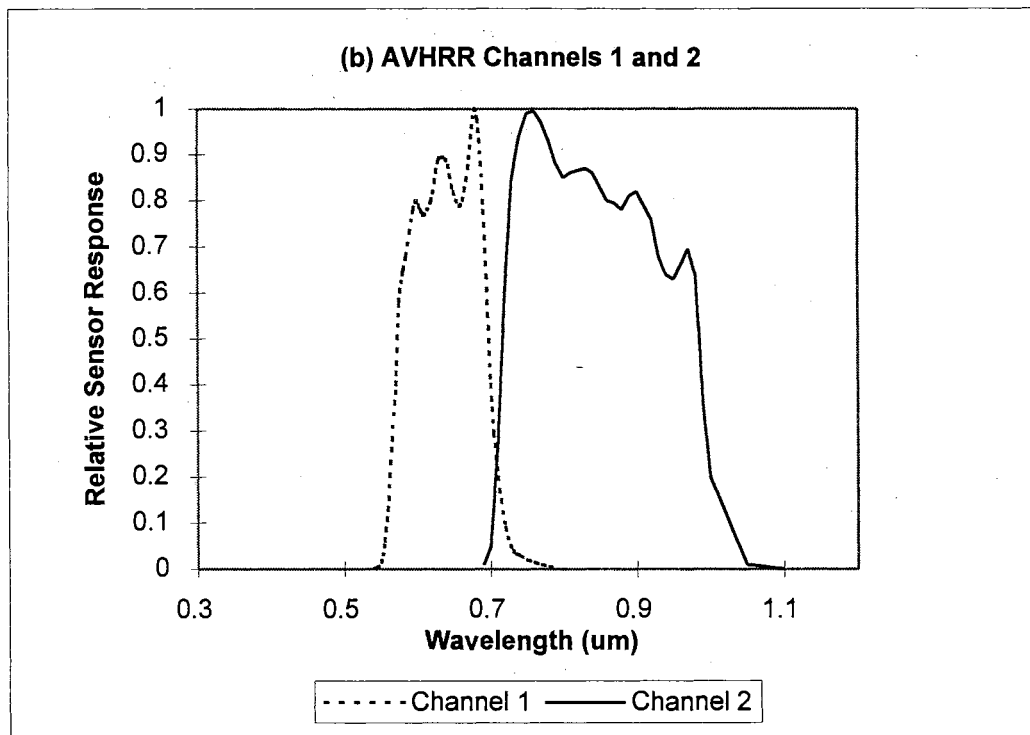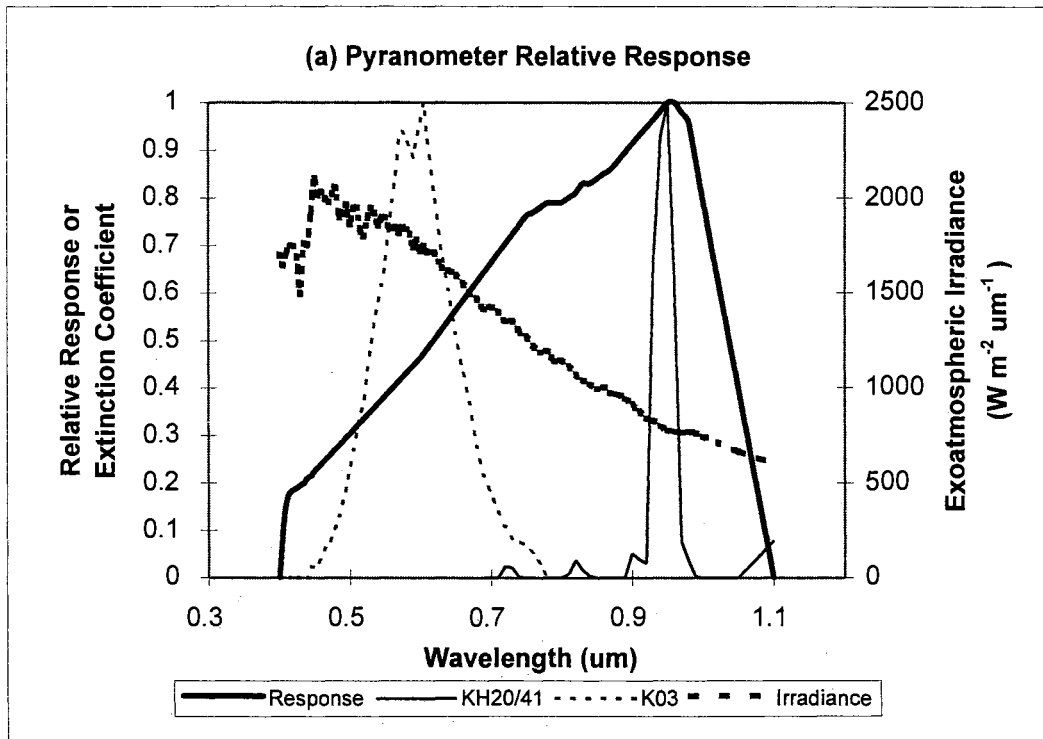
Figure G.1: Relative response functions for (a) the pyranometer and (b) AVHRR channels 1 and 2. Also shown in (a) is exoatmospheric irradiance and the extinction coefficients of ozone (K03, cm$^{-1}$) and water vapor (KH20, cm$^{-1}$ * 41$^{-1}$, divided by 41 for scaling purposes).
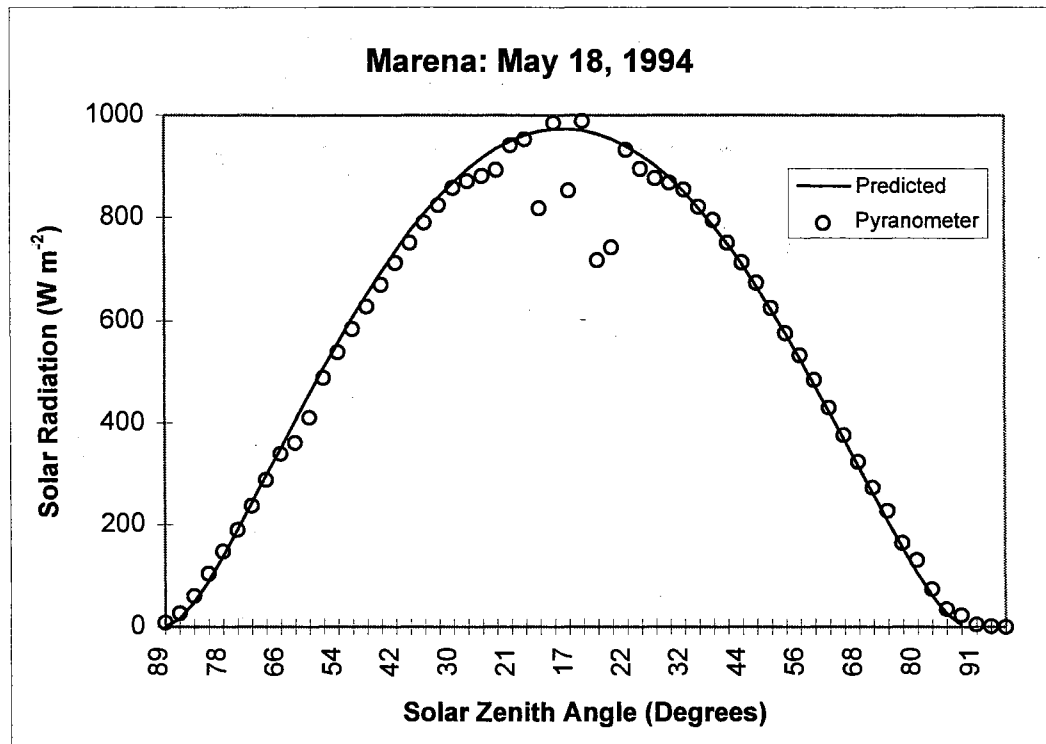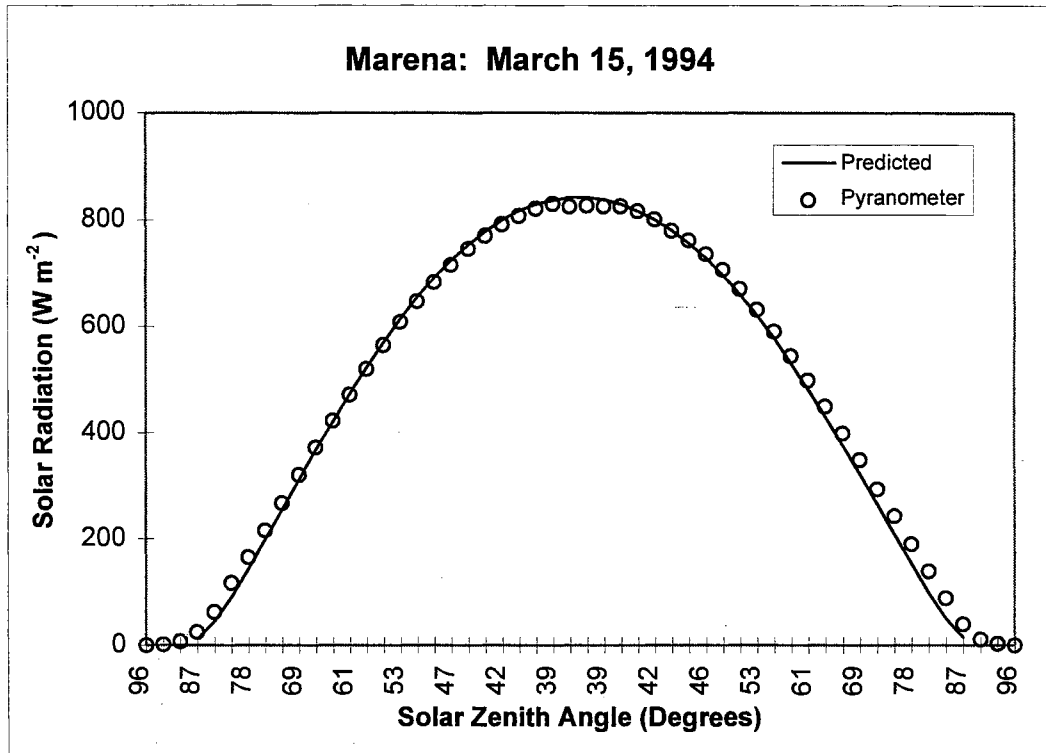
Figure G.2: Comparison of irradiance at the surface measured by the pyranometer at select Mesonet stations and irradiance predicted using the atmospheric transmission functions from Iqbal (1983).

**Marena: June 27, 1994**



**Goodwell: May 29, 1994**

Figure G.2 Continued.

Goodwell: May 30, 1994



Goodwell: June 13, 1994

Figure G.2 Continued.

**Apache: April 15, 1994**

**Apache: July 20, 1994**
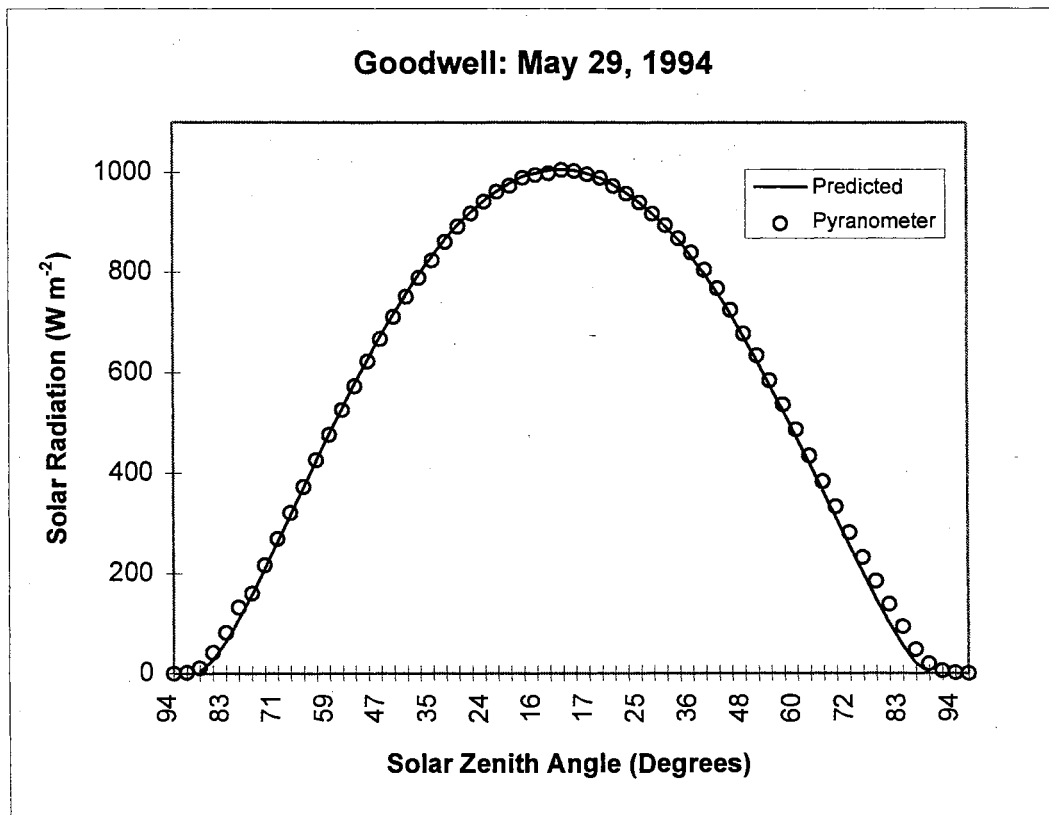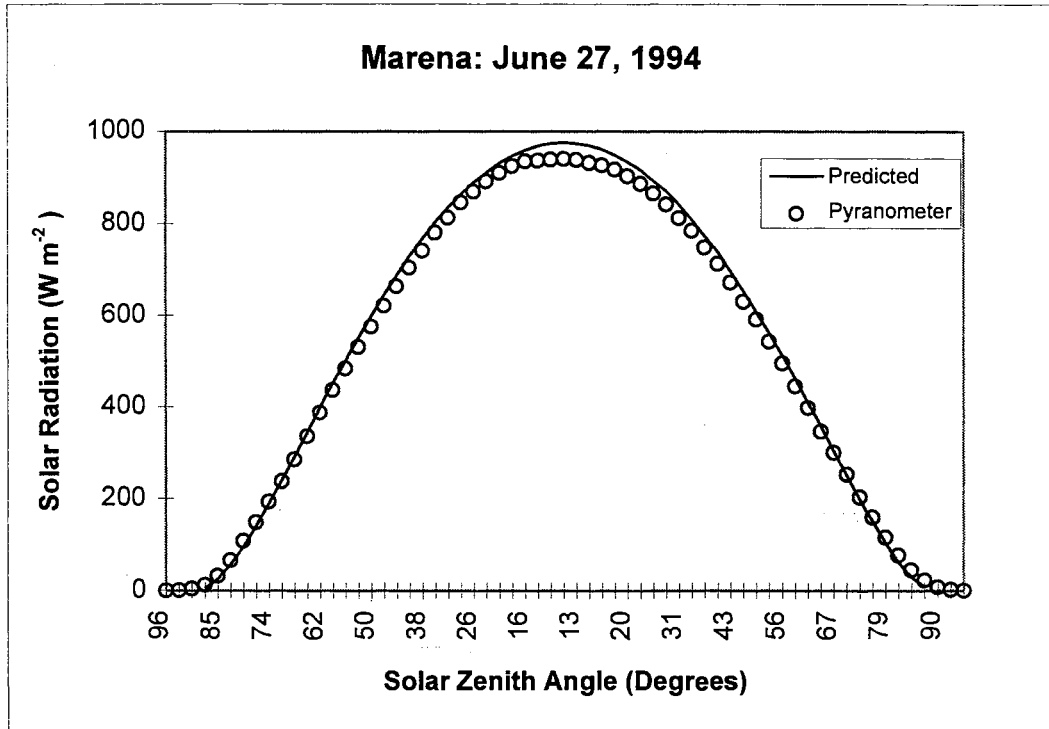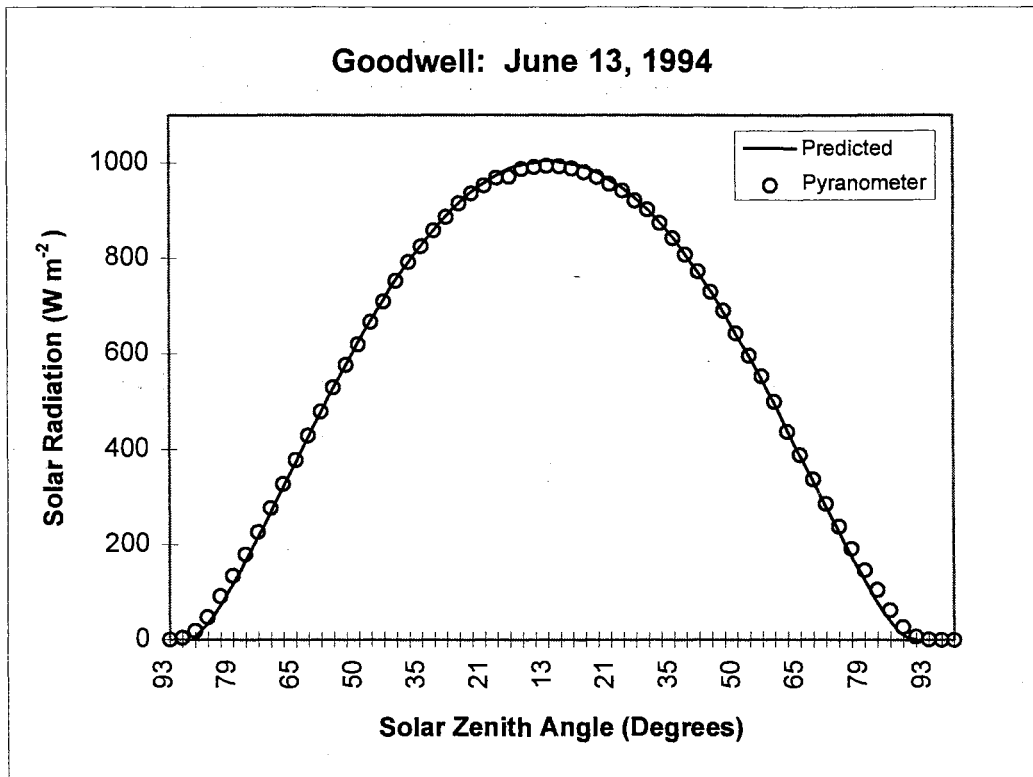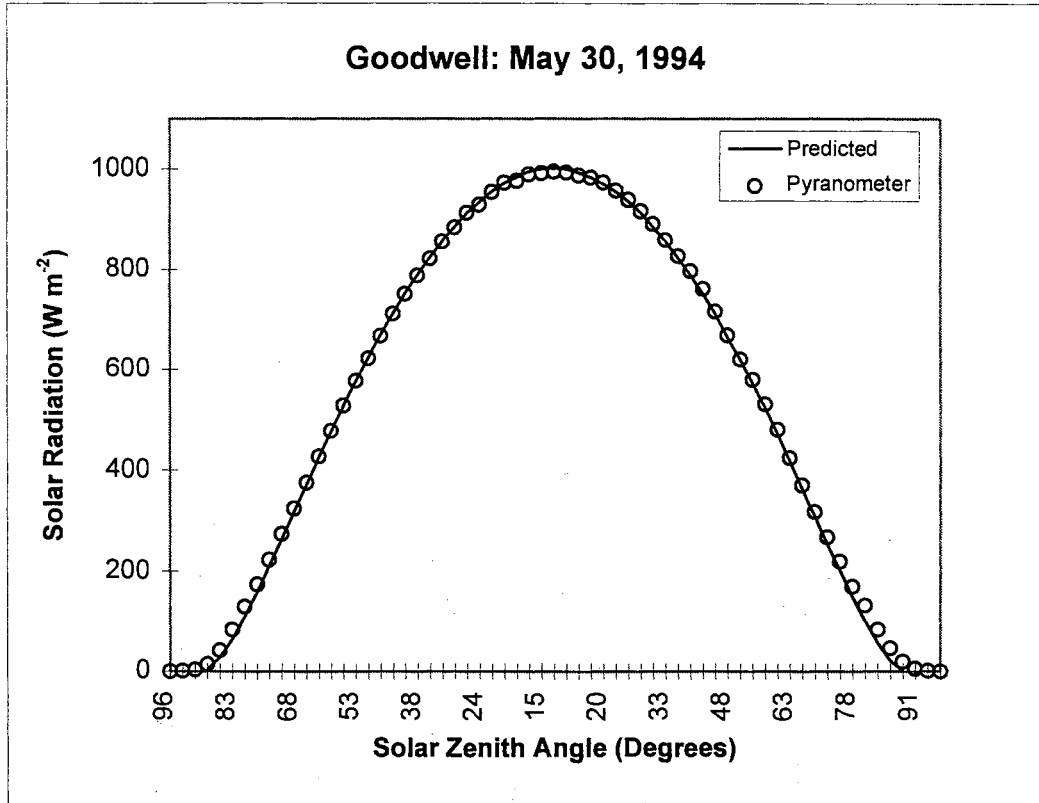
Figure G.2 Continued.

Figure G.2 Continued.

312
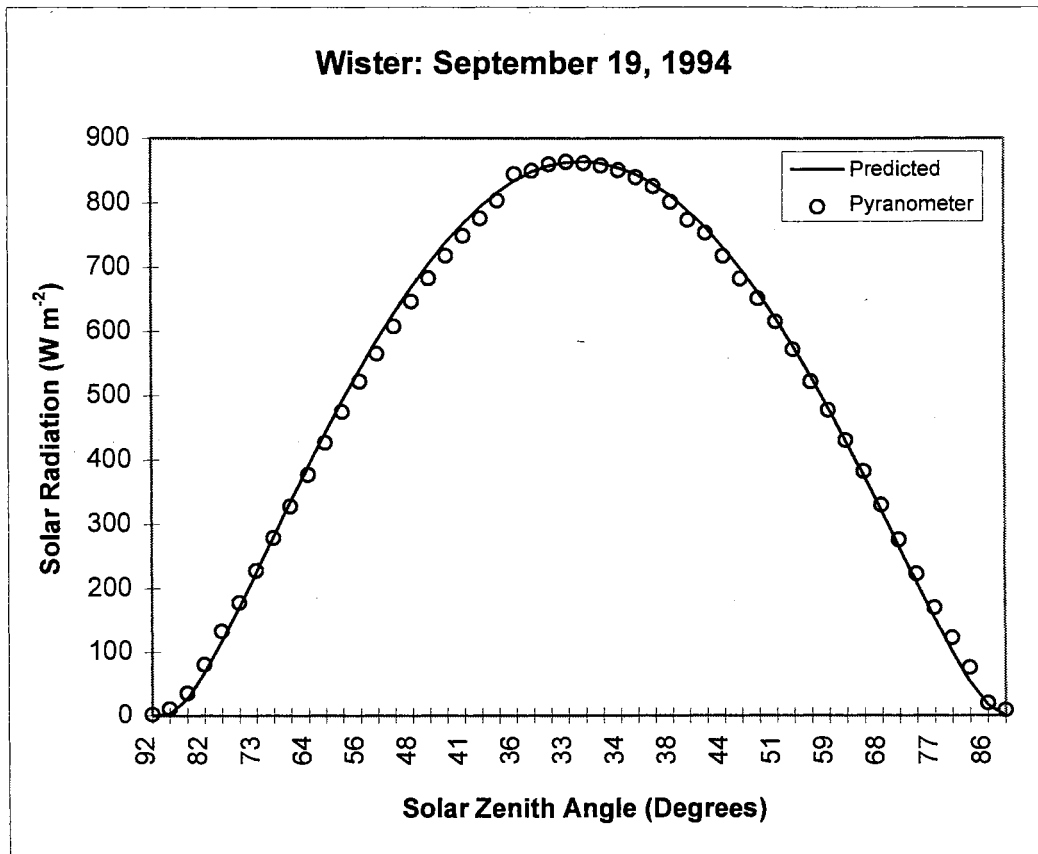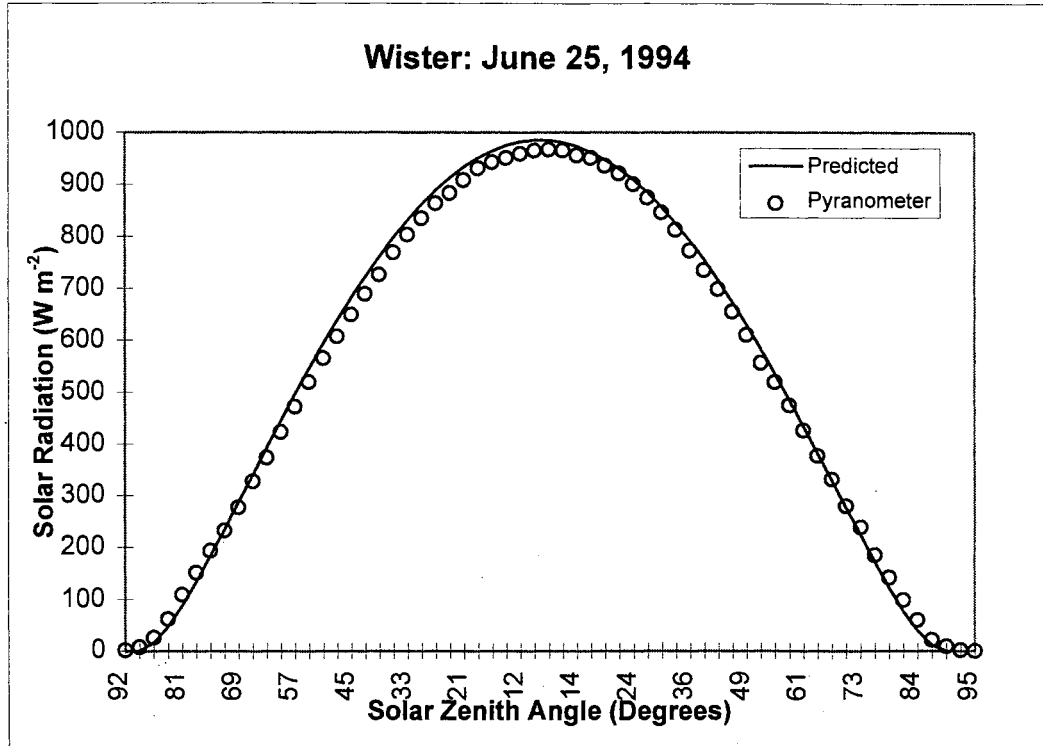
# Appendix H

## Atmospheric Correction Functions

The following is a listing of Visual Basic Code used with Microsoft Excel 5.0 to perform the atmospheric correction procedures. This includes the functions used to calculate solar position as a function of time and location. It also includes the functions used to calculate exoatmospheric reflectance.

Over view of the functions in the order presented in this appendix:

| Function | Purpose |
|----------|---------|
| zenith | Solar geometry calculations, including calculation of the eccentricity correction factor (Ecc) and calculation of total daily potential irradiance (Io) |
| Iqbal2 | Primary function for the correction procedures of Iqbal (1983) |
| TrayCh1 | Calculates Rayleigh and Aerosol transmittance for channel 1 |
| TrayCh2 | Caculates Rayleigh and Aerosol transmittance for channel 2 |
| tauO | Calculation of ozone transmittance in channel 1 |
| tauw | Calculation of water vapor transmittance for channel 2 |
| ThSS | Calculation of scattering angle |
| McPhase | Aerosol scattering phase function |
| Acor | Primary function to implement Paltridge and Mitchel (1990) methods |
| ExAtR | Exoatmospheric reflectance |

---

**Solar Geometry Calculations**

---

Function **zenith**(Jday2 As Double, CSThr As Double, CSTmin As Double, Lat2 As Double, Long2 As Double, What As Integer) As Double

```
' Calculates:
'   1 = Solar zenith angle
'   2 = Solar azimuth
'   3 = Eccentricity correction factor
'   4 = Day length
'   5 = Sunrise, HR GMT


Information Passed to the function:
' Jday2 = day of the year
' CSTHr = hour of the day - CST - NOTE: Pass as GMT then 6 is subtracted
' CSTmin = minute of the day - CST
' Lat = latitude in degrees
' Long2 = longitude in degrees
' What = switch to determine what is returned (1-5)


Variable Definitions:

Dim GAM As Double          ' Day Angle
Dim ECC As Double          ' ECCENTRICITY CORRECTION FACTOR
Dim DELT As Double         ' ANGLE OF DECLINATION
```

314

```
Dim IO As Double              ' Potential short-wave exoatmospheric irradiance
Dim PIE As Double
Dim WS As Double              ' sun rise angle
Dim W As Double               ' hour angle, 0 at noon, morning positive
Dim ND As Double              ' day length, hours
Dim Et As Double              ' time correction
Dim Dt As Double              ' difference between solar and local time, minutes
Dim LAT As Double             ' local apparent time = solar time, hours
Dim ELV As Double             ' solar elevation angle
Dim Azimuth As Double         ' solar azimuth angle
Dim Sunrise As Double         ' sunrise in local standard - hours


PIE = 3.141593
Lat2 = Lat2 * PIE / 180#

' Convert GMT to CST
CSThr = CSThr - 6

    ' DAY ANGLE (GAM)
    GAM = 2# * PIE * (Jday2 - 1#) / 365#

    ' ECCENTRICITY CORRECTION FACTOR (ECC)
    ECC = 1.00011 + 0.034221 * Cos(GAM) + 0.00128 * Sin(GAM) + 0.000719 * Cos(2 * GAM) +
0.000077 * Sin(2 * GAM)

    ' ESTIMATE OF THE ANGLE OF DECLINATION (DELT)
    DELT = 0.006918 - 0.399912 * Cos(GAM) + 0.070257 * Sin(GAM) - 0.006758 * Cos(2 * GAM) +
0.000907 * Sin(2 * GAM) - 0.002697 * Cos(3 * GAM) + 0.00148 * Sin(3 * GAM)


    ' SUNRISE HOUR ANGLE (WS)
    WS = (-Tan(Lat2) * Tan(DELT))
    ' Acos the fun way
    WS = ArCos(WS)

    ' ESTIMATION OF TOTAL DAILY SHORT-WAVE EXOAMTOSPHERIC IRRADIANCE (IO)
    IO = (24# / PIE) * 1367# * ECC * Cos(Lat2) * Cos(DELT) * (Sin(WS) - WS * Cos(WS))

    ' equation of time - used to find solar time
    ' note 229.18 is conversion from radians to minutes = 2*360 / PIE
    Et = (0.000075 + 0.001868 * Cos(GAM) - 0.032077 * Sin(GAM) - 0.014615 * Cos(2 * GAM) -
0.04089 * Sin(2 * GAM)) * 229.18

    ' FIND DAY LENGTH
    ND = (2# / 15#) * WS * (180# / PIE)


    ' Assume that this is in the central time zone
    ' Longitude correction - Standard meridian:
    '   standard: 60 W for Atlantic (4h)
    '    75 W for eastern standard (5h)
    '    90 W for central standard time (6h)
    '   105 W for mountain (7)
```

```
'  120 W for Pacific (8)
' 135 W for Alaska (9)
 '150 W for Hawaii (10)
' Longitude correction is positive if the local meridian is
    'east of the standard or negative if west
Dt = 4# * (90# - Long2) + Et
CSTmin = CSTmin + Dt
LAT = CSThr + CSTmin / 60#

' find hour angle based on this- noon = 0, morning positive
W = 12# - LAT

' convert to radians
' 360 degrees / 24 hr = 15
W = (W * 15#) * PIE / 180#

' find zenith angle
zenith = Sin(DELT) * Sin(Lat2) + Cos(DELT) * Cos(Lat2) * Cos(W)
zenith = ArCos(zenith)

' Elevation angle is just 90 - Zenith
ELV = 1.5707963 - zenith

' find solar azimuth
Azimuth = (Sin(ELV) * Sin(Lat2) - Sin(DELT)) / (Cos(ELV) * Cos(Lat2))
' note:  Az >= 0  0 to 90 degrees
 ' Az <= 0  90 to 180 degrees
' This is based on an azimuth relative to south

Azimuth = ArCos(Azimuth)

' Obtain the Azimuth relative to the North
' W > 0 is am and sun is to the east
If (W > 0#) Then
  Azimuth = PIE - Azimuth
Else
  Azimuth = PIE + Azimuth
End If

' find sunrise in terms of solar time
WS = 12# - WS * (180# / PIE) / 15# ' convert to degrees then hr

' convert to local standard
WS = WS - (Dt / 60#)

Select Case What

  Case 1
    zenith = zenith * 180# / 3.14159
 Case 2
    zenith = Azimuth * 180# / 3.14159
  Case 3
    zenith = ECC
 Case 4
```

316

```
    zenith = ND
Case 5
    zenith = WS + 6#
Case Else
    zenith = -999#
End Select



End Function

' Determine the inverse cosine
Function ArCos(X As Double) As Double
        ArCos = Atn(-X / Sqr(-X * X + 1)) + 1.5708
End Function
```

---

## Primary Function for Iqbal's Methods

---

' Atmospheric correction using transmission functions from Iqbal (1983).
' Total solar irradiance at the target is calculated from relationships of Iqbal (1983).
' Path radiance due to single scattering based on Paltridge and Mitchell (1990).


' Inputs
' THsat - satellite zenith angle (degrees)
' AZsat - satellite azimuth angle (degrees from the north)
' THsun - solar zenith angle (degrees)
' AZsun - solar azimuth angle (Degrees from North)
' Ecc - eccentricity correction
' RH - relative humidity (%)
' T - air temperature (C)
' Vis - Visibility (visual range, km)
' Pres - station pressure (mb)
' DN - satellite DN value
' CH - channel (1 or 2)
' SN - satellite number (11 or 12)

Function **Iqbal2**(THsat As Double, AZsat As Double, THsun As Double, AZsun As Double, Ecc As Double, RH As Double, T As Double, Vis As Double, Pres As Double, DN As Double, CH As Integer, SN As Integer) As Double

Variable Definitions

| | |
|---|---|
| Dim Lsat As Double | ' Total radiance received at the satellite |
| Dim Tray As Double | ' Rayleigh transmission - defined at times based on the |
| | ' optical path from ground to satellite, or sun to ground or total |
| Dim Tmie As Double | ' Mie (aerosol) transmission |
| Dim Tabs As Double | ' Ozone for channel 1 or water vapor for channel 2 |
| Dim Iray As Double | ' Irradiance or radiance due to Rayleigh scattering |

317

```
Dim Imie As Double         ' Irradiance or radiance due to Mie scattering
Dim Fc As Double           ' Fraction of mie irradiance hitting target
Dim THETA As Double        ' Scattering angle
Dim Pmie As Double         ' Mie phase function
Dim Pray As Double         ' Rayleigh phase function
Dim Idir As Double         ' Direct irradiance
Dim Lg As Double           ' Radiance from the target
Dim W As Double            ' Precipitable water
Dim Io As Double           ' Spectral in bound irradiance
Dim msun As Double         ' Relative optical depth from sun to target
Dim msat As Double         ' " " " satellite
Dim mtotal As Double       ' Sun to ground to satellite
Dim Ig As Double           ' Total irradiance on target


'First determine channel and satellite dependent parameters

    If (SN = 12) Then
    If (CH = 1) Then
      Lsat = 0.524 * (DN - 40#)
      Io = 1613.7 * Ecc
    Else
      Lsat = 0.344 * (DN - 40#)
      Io = 1049.8 * Ecc
    End If 'Ch N12
    Else  'NOAA 11
      If CH = 1 Then
        Lsat = 0.599 * (DN - 40#)
        Io = 1630# * Ecc
      Else
        Lsat = 0.408 * (DN - 40#)
        Io = 1053# * Ecc
      End If 'Ch n11
    End If 'Satellite #


' Determine viewing geometries

' Fraction of Mie scattering to the target pg 150
Fc = 0.00000001247 * THsun ^ 4 - 0.000002965 * THsun ^ 3 + 0.0001302 * THsun ^ 2 - 0.002121 *
THsun + 0.922


'Get Scattering angle
' Note that this function also coverts THsun and THsat to radians
  THETA = ThSS(AZsun, THsun, AZsat, THsat)


' Convert zenith angles to radians
'     THsat = THsat * 3.14159 / 180#
'     THsun = THsun * 3.14159 / 180#

    ' Pressure correction - page 100, Iqbal
    msun = (1 / Cos(THsun)) * Pres / 1013.25
    msat = (1 / Cos(THsat)) * Pres / 1013.25
    mtotal = msun + msat
```

318

```
' ----------------- Determine total irradiance at the target ----------------------------

' First determine transmissions based on relative optical
'     depth from the sun to the satellite
If CH = 1 Then
  Tray = TrayCh1(msun, 0, 0)
  Tmie = TrayCh1(msun, Vis * 1.3, 1)
  Tabs = tauO(0.3, msun)
Else
  Tray = TrayCh2(msun, 0, 0)
  Tmie = TrayCh2(msun, Vis * 1.3, 1)
  T = 273.15 + T ' Celsius to Kelvin
  W = 0.493 * (RH / 100#) * Exp(26.23 - 5416# / T) / T
  Tabs = tauw(W, msun)
End If ' transmission for channels

' Rayleigh irradiance assuming half reaches target
Iray = Io * Tabs * (1 - Tray) * Tmie * 0.5

' Mie
Imie = Io * Tabs * (1 - Tmie) * Tray * Fc * 0.9

'Direct
Idir = Io * Tabs * Tmie * Tray

Ig = (Iray + Imie + Idir) * Cos(THsun)


' ----------------- Determine Path Radiance ----------------------------

' First determine transmissions based on relative optical
'     depth from the sun to the ground to the satellite
If CH = 1 Then
  Tray = TrayCh1(mtotal, 0, 0)
  Tmie = TrayCh1(mtotal, Vis * 1.3, 1)
  Tabs = tauO(0.3, mtotal)
Else
  Tray = TrayCh2(mtotal, 0, 0)
  Tmie = TrayCh2(mtotal, Vis * 1.3, 1)
  Tabs = tauw(0.5 * W, mtotal) 'Account for vertical distribution of water vapor
                      ' with respect to Mie scattering
End If ' transmission for channels

' Rayleigh irradiance assuming half reaches target
Pray = 0.75 * (1# + Cos(THETA) ^ 2) / (4# * 3.14159)
Iray = Io * (1 - Tray) * Pray
If (CH = 1) Then
  Iray = Iray * Tabs 'Ozone attenuates Rayleigh
End If

' Mie
Pmie = McPhase(THETA) / (4# * 3.14159)
Imie = Io * Tabs * (1 - Tmie) * Tray * Pmie
```

319

' Subtract out the irradiance due to single scatting
Lsat = Lsat - msat * (Imie + Iray) / mtotal


' ----------- Account for attenuation from ground to satellite -------------


' Define transmission from ground to satellite
If CH = 1 Then
  Tray = TrayCh1(msat, 0, 0)
  Tmie = TrayCh1(msat, Vis * 1.3, 1)
  Tabs = tauO(0.3, msat)
Else
  Tray = TrayCh2(msat, 0, 0)
  Tmie = TrayCh2(msat, Vis * 1.3, 1)
  Tabs = tauw(W, msat)
End If ' transmission for channels


Lg = Lsat / (Tray * Tmie * Tabs)


' Now determine the corrected reflectance
Iqbal2 = Lg * 3.14159 / Ig


End Function

---

## Iqbal: Rayleigh and Mie Transmittance In AVHRR Channel 1

'Computes Rayleigh or Mie transmittance for channel 1

Inputs:
' m is relative air mass
' Vis is the visual range in km (0 if Rayleigh
' Mie = 0, calculate Rayleigh, otherwise Mie


Function **TrayCh1**(m As Double, Vis As Double, Mie As Integer) As Double


| | |
|---|---|
| Dim Kray As Double | 'Spectral absorption coefficient of ozone |
| Dim fch1(34) As Double | 'Spectral response function of channel 1 |
| Dim FrCh1(34) As Double | ' Spectral irradiance in channel 1 as a function of irradiance |
| Dim Rbase As Double | 'Numerator - used to get weighted mean response |
| Dim Lambda As Double | 'wavelength - um |
| Dim b As Double | 'used to find Taer as a function of visibility |
| Dim i As Integer | |


' Spectral interval from 0.54 um to .79 um
' Interval is 0.005 um to element 14 and then 0.01 um for the rest


' Spectral response function of AVHRR channel 1
fch1(0) = 0
fch1(1) = 0.005
fch1(2) = 0.015

fch1(3) = 0.06
fch1(4) = 0.15
fch1(5) = 0.28
fch1(6) = 0.4
fch1(7) = 0.58
fch1(8) = 0.64
fch1(9) = 0.68
fch1(10) = 0.73
fch1(11) = 0.78
fch1(12) = 0.8
fch1(13) = 0.78
fch1(14) = 0.77
fch1(15) = 0.8
fch1(16) = 0.89
fch1(17) = 0.89
fch1(18) = 0.82
fch1(19) = 0.79
fch1(20) = 0.87
fch1(21) = 1
fch1(22) = 0.8
fch1(23) = 0.4
fch1(24) = 0.2
fch1(25) = 0.09
fch1(26) = 0.04
fch1(27) = 0.03
fch1(28) = 0.02
fch1(29) = 0.015
fch1(30) = 0.01
fch1(31) = 0.005
fch1(32) = 0.005

' Exoatmospheric irradiance
FrCh1(0) = 1857.5
FrCh1(1) = 1895
FrCh1(2) = 1902.5
FrCh1(3) = 1855
FrCh1(4) = 1840
FrCh1(5) = 1850
FrCh1(6) = 1817.5
FrCh1(7) = 1848.8
FrCh1(8) = 1840
FrCh1(9) = 1817.5
FrCh1(10) = 1742.5
FrCh1(11) = 1785
FrCh1(12) = 1720
FrCh1(13) = 1751.3
FrCh1(14) = 1715
FrCh1(15) = 1715
FrCh1(16) = 1637.5
FrCh1(17) = 1622.5
FrCh1(18) = 1597.5
FrCh1(19) = 1555
FrCh1(20) = 1505
FrCh1(21) = 1472.5

```
FrCh1(22) = 1415        :   FrCh1(23) = 1427.5      :   FrCh1(24) = 1402.5
FrCh1(25) = 1355        :   FrCh1(26) = 1355        :   FrCh1(27) = 1300
FrCh1(28) = 1272.5      :   FrCh1(29) = 1222.5      :   FrCh1(30) = 1187.5
FrCh1(31) = 1195        :   FrCh1(32) = 1142.5

TrayCh1 = 0#
Rbase = 0#


 Lambda = 0.535
For i = 0 To 33


 ' Wave length increment 0.005 um
 If (i <= 14) Then
   Lambda = Lambda + 0.005
   If Mie = 0 Then
     Kray = 0.008735 * (Lambda ^ -4.08)
     TrayCh1 = TrayCh1 + Exp(-Kray * m) * fch1(i) * FrCh1(i) * 0.005
   Else
     b = (0.55 ^ 1.3) * (3.912 / Vis - 0.01162) * (0.02472 * (Vis - 5#) + 1.132)
     TrayCh1 = TrayCh1 + Exp(-b * (Lambda ^ -1.3) * m) * fch1(i) * FrCh1(i) * 0.005
   End If 'Mie
   Rbase = Rbase + fch1(i) * FrCh1(i) * 0.005
 Else  ' interval 0.01 um
   Lambda = Lambda + 0.01
   If Mie = 0 Then
     Kray = 0.008735 * (Lambda ^ -4.08)
     TrayCh1 = TrayCh1 + Exp(-Kray * m) * fch1(i) * FrCh1(i) * 0.01
   Else
     b = (0.55 ^ 1.3) * (3.912 / Vis - 0.01162) * (0.02472 * (Vis - 5#) + 1.132)
     TrayCh1 = TrayCh1 + Exp(-b * (Lambda ^ -1.3) * m) * fch1(i) * FrCh1(i) * 0.01
   End If ' mie
   Rbase = Rbase + fch1(i) * FrCh1(i) * 0.01
 End If

Next i


 ' Find the weighted mean
 TrayCh1 = TrayCh1 / Rbase
 End Function
```

---

**Iqbal: Rayleigh and Aerosol Transmittance in Channel 2**

---

```
'Computes Rayleigh or Mie transmittance for channel 2

Inputs:
' m is relative air mass
' Vis is the visual range in km (0 if Rayleigh
' Mie = 0, calculate Rayleigh, otherwise Mie


Function TrayCh2(m As Double, Vis As Double, Mie As Integer) As Double
```

```
Dim Kray As Double              'Spectral absorption coefficient
Dim fch2(34) As Double          'Spectral response function of channel 2
Dim FrCh2(34) As Double         'Solar irradiance in channel 2 as a function of wavelength - WRC
                                values
Dim Rbase As Double             'Numerator - used to get weighted mean response
Dim Lambda As Double            'wavelength - um
Dim b As Double                 'used to find Taer as a function of visibility
Dim i As Integer
Dim a As Double


' channel 2 response function initialization
' Response function from NESDIS Appendix B for NOAA 11 Channel 2
fch2(0) = 0.01
fch2(1) = 0.05
fch2(2) = 0.28
fch2(3) = 0.61
fch2(4) = 0.85
fch2(5) = 0.94
fch2(6) = 0.99
fch2(7) = 0.995
fch2(8) = 0.97
fch2(9) = 0.93
fch2(10) = 0.88
fch2(11) = 0.85
fch2(12) = 0.86
fch2(13) = 0.865
fch2(14) = 0.87
fch2(15) = 0.86
fch2(16) = 0.83
fch2(17) = 0.8
fch2(18) = 0.795
fch2(19) = 0.78
fch2(20) = 0.81
fch2(21) = 0.82
fch2(22) = 0.79
fch2(23) = 0.76
fch2(24) = 0.68
fch2(25) = 0.64
fch2(26) = 0.63
fch2(27) = 0.66
fch2(28) = 0.695
fch2(29) = 0.64
fch2(30) = 0.36
fch2(31) = 0.2
fch2(32) = 0.01
fch2(33) = 0


' Exoatmospheric Solar Irradiance
FrCh2(0) = 1415
FrCh2(1) = 1428
FrCh2(2) = 1403
FrCh2(3) = 1355
FrCh2(4) = 1355
FrCh2(5) = 1300
```

```
FrCh2(6) = 1273
FrCh2(7) = 1223
FrCh2(8) = 1188
FrCh2(9) = 1195
FrCh2(10) = 1143
FrCh2(11) = 1145
FrCh2(12) = 1113
FrCh2(13) = 1070
FrCh2(14) = 1041
FrCh2(15) = 1020
FrCh2(16) = 994
FrCh2(17) = 1002
FrCh2(18) = 972
FrCh2(19) = 966
FrCh2(20) = 945
FrCh2(21) = 913
FrCh2(22) = 876
FrCh2(23) = 841
FrCh2(24) = 830
FrCh2(25) = 801
FrCh2(26) = 778
FrCh2(27) = 771
FrCh2(28) = 764
FrCh2(29) = 769
FrCh2(30) = 762
FrCh2(31) = 744
FrCh2(32) = 666
FrCh2(33) = 606.4

TrayCh2 = 0#
Rbase = 0#
a = 1.3


 Lambda = 0.68
For i = 0 To 33

 ' Wave length increment 0.01 um
 If (i <= 31) Then
  Lambda = Lambda + 0.01

  'Calculation of Rayleigh scatter
  If Mie = 0 Then
     Kray = 0.008735 * (Lambda ^ -4.08)
     TrayCh2 = TrayCh2 + Exp(-Kray * m) * fch2(i) * FrCh2(i) * 0.01
  Else 'calculate mie transmittance
     ' Estimate aerosol optical depth from visibility - Iqbal (1983) pg 119
     b = (0.55 ^ a) * (3.912 / Vis - 0.01162) * (0.02472 * (Vis - 5#) + 1.132)
     TrayCh2 = TrayCh2 + Exp(-b * (Lambda ^ -a) * m) * fch2(i) * FrCh2(i) * 0.01
  End If 'Mie = 0
  Rbase = Rbase + fch2(i) * FrCh2(i) * 0.01
 Else ' interval 0.05 um
  Lambda = Lambda + 0.05
  If Mie = 0 Then
    Kray = 0.008735 * (Lambda ^ -4.08)
```

```
        TrayCh2 = TrayCh2 + Exp(-Kray * m) * fch2(i) * FrCh2(i) * 0.05
    Else
        b = (0.55 ^ a) * (3.912 / Vis - 0.01162) * (0.02472 * (Vis - 5#) + 1.132)
        TrayCh2 = TrayCh2 + Exp(-b * (Lambda ^ -a) * m) * fch2(i) * FrCh2(i) * 0.05
    End If 'mie
        Rbase = Rbase + fch2(i) * FrCh2(i) * 0.05
End If

Next i

' Find the weighted mean
TrayCh2 = TrayCh2 / Rbase
End Function
```

---

## Iqbal: Ozone Transmittance

Estimates ozone transmittance for AVHRR channel 1.

Inputs:

L - Ozone concentration (cm)
m - relative optical mass

```
Function tauO(L As Double, m As Double) As Double

Dim Ko3(34) As Double          'Spectral absorption coefficient of ozone
Dim fch1(34) As Double         'Spectral response function of channel 1 (defined in TrayCh1)
Dim FrCh1(34) As Double        ' Spectral irradiance in channel 1 as a function of irradiance
                               (defined in TrayCh1)
Dim Obase As Double 'Numerator - used to get weighted mean response
Dim i As Integer

' Spectral interval from 0.54 um to .79 um
' Interval is 0.005 um to element 14 and then 0.01 um for the rest

' Ko3 - spectral absorption of ozone
' Ozone absorption based on Iqbal (1983) page 127
Ko3(0) = 0.075
Ko3(1) = 0.08
Ko3(2) = 0.085
Ko3(3) = 0.095
Ko3(4) = 0.103
Ko3(5) = 0.11
Ko3(6) = 0.12
Ko3(7) = 0.122
Ko3(8) = 0.12
Ko3(9) = 0.118
Ko3(10) = 0.115
Ko3(11) = 0.12
Ko3(12) = 0.125
Ko3(13) = 0.13
```

Ko3(14) = 0.12      :     Ko3(15) = 0.105    :     Ko3(16) = 0.09
Ko3(17) = 0.079   :     Ko3(18) = 0.067    :     Ko3(19) = 0.057
Ko3(20) = 0.048   :     Ko3(21) = 0.036    :     Ko3(22) = 0.028
Ko3(23) = 0.023   :     Ko3(24) = 0.018    :     Ko3(25) = 0.014
Ko3(26) = 0.011   :     Ko3(27) = 0.01     :     Ko3(28) = 0.009
Ko3(29) = 0.007   :     Ko3(30) = 0.004    :     Ko3(31) = 0
Ko3(32) = 0

```
tauO = 0#
Obase = 0#


' Compute the transmittance due to water vapor - based on Iqbal (1983) pg 129
' Weight the transmittance according to the response function

For i = 0 To 33

  ' Wave length increment 0.005 um
  If (i <= 14) Then
    tauO = tauO + Exp(-Ko3(i) * L * m) * fch1(i) * FrCh1(i) * 0.005
    Obase = Obase + fch1(i) * FrCh1(i) * 0.005
  Else  ' interval 0.01 um
    tauO = tauO + Exp(-Ko3(i) * L * m) * fch1(i) * FrCh1(i) * 0.01
    Obase = Obase + fch1(i) * FrCh1(i) * 0.01
  End If

Next i

  ' Find the weighted mean
  tauO = tauO / Obase
End Function
```

---

## Iqbal: Water Vapor Transmittance

Inputs:

```
'w = precipitable water (cm)
' m = and relative air mass


Function tauw(W As Double, m As Double) As Double

Dim Kwal(34) As Double        'Spectral absorption coefficient of water vapor
Dim fch2(34) As Double        'Spectral response function of channel 2 (defined in TrayCh2)
Dim FrCh2(34) As Double        'Solar irradiance in channel 2 as a function of wavelength
                               WRC values (defined in TrayCh2)
Dim Wbase As Double            'Numerator - used to get weighted mean response
Dim i As Integer

' Spectral interval from 0.69 um to 1.1 um
' Interval is 0.01 um except for last two points which are 0.05 um


' Kwal - spectral absorption of water vapor
```

' Water vapor absorption based on Iqbal (1983) page 130
```
Kwal(0) = 0.016        : Kwal(1) = 0.024     :     Kwal(2) = 0.0125
Kwal(3) = 1            : Kwal(4) = 0.87      :     Kwal(5) = 0.061
Kwal(6) = 0.001        : Kwal(7) = 0.00001   :     Kwal(8) = 0.00001
Kwal(9) = 0.0006       : Kwal(10) = 0.0175   :     Kwal(11) = 0.036
Kwal(12) = 0.33        : Kwal(13) = 1.53     :     Kwal(14) = 0.66
Kwal(15) = 0.155       : Kwal(16) = 0.003    :     Kwal(17) = 0.00001
Kwal(18) = 0.00001     : Kwal(19) = 0.0026   :     Kwal(20) = 0.063
Kwal(21) = 2.1         : Kwal(22) = 1.6      :     Kwal(23) = 1.25
Kwal(24) = 27          : Kwal(25) = 38       :     Kwal(26) = 41
Kwal(27) = 26          : Kwal(28) = 3.1      :     Kwal(29) = 1.48
Kwal(30) = 0.125       : Kwal(31) = 0.0025   :     Kwal(32) = 0.00001
Kwal(33) = 3.2

tauw = 0#
Wbase = 0#


' Compute the transmittance due to water vapor - based on Iqbal (1983) pg 129
' Weight the transmittance according to the response function

For i = 0 To 33

  ' Wave length increment 0.01 um
  If (i <= 31) Then
    tauw = tauw + Exp(-0.2385 * Kwal(i) * W * m / (1 + 20.07 * Kwal(i) * W * m) ^ 0.45) * fch2(i) *
FrCh2(i) * 0.01
    Wbase = Wbase + fch2(i) * FrCh2(i) * 0.01
  Else ' interval 0.05 um
    tauw = tauw + Exp(-0.2385 * Kwal(i) * W * m / (1 + 20.07 * Kwal(i) * W * m) ^ 0.45) * fch2(i) *
FrCh2(i) * 0.05
    Wbase = Wbase + fch2(i) * FrCh2(i) * 0.05
  End If

Next i

  ' Find the weighted mean
  tauw = tauw / Wbase
End Function
```

---

## Scattering Angle

' Computes the scattering angle between the sun and satellite

Inputs:

```
' AzSat = solar azimuth angle from north in degrees (ALL)
' SZA = Solar zenith angle
'Az sun = satellite azimuth angle
'ZLA = satellite zenith angle

Function ThSS(AZsun As Double, SZA As Double, AZsat As Double, ZLA As Double) As Double
```

327

```
Dim dAZ As Double 'relative azimuth angle between satellite and sun
Dim temp As Double 'temporary variable
Dim Pi As Double

Pi = 3.141592654

    dAZ = Abs(AZsun - AZsat)
    If (dAZ > 180#) Then
      dAZ = 360# - dAZ
    End If

  SZA = SZA * Pi / 180#
  ZLA = ZLA * Pi / 180#
  dAZ = dAZ * Pi / 180#

  temp = (Sin(ZLA) * Cos(dAZ) - Sin(SZA)) ^ 2 + (Sin(ZLA) * Sin(dAZ)) ^ 2# + (Cos(ZLA) -
Cos(SZA)) ^ 2

  temp = 1# - temp / 2#
  ' compute the arc cosine the fun way
  temp = Atn(-temp / Sqr(-temp * temp + 1)) + (Pi / 2#)
  ThSS = Pi - temp
End Function
```

---

## Estimate of the Mclatchey Mie Phase Function

```
'log linear interpolation of Mclatchey Mie phase function

'Input: Scattering angle (degrees)

Function McPhase(ScatA As Double) As Double
'/* Based on table look up values; however, applies a
'   ln/ln interpolation to determine the values

'/* minimum value is set to 40

    Dim i As Integer ' counter

    Dim ftheta(4) As Double ' used to find range of scattering angle
    ftheta(0) = 40#: ftheta(1) = 120#: ftheta(2) = 140#: ftheta(3) = 180#
    Dim Pi As Double
    Pi = 3.1415927

'   /* interpolate to find value
    ScatA = ScatA * 180# / Pi

    i = 0
    While (ScatA > ftheta(i))
      i = i + 1
    Wend
```

328

```
'    /* don't allow values less than 20 degrees
     If (ScatA < 20) Then
       ScatA = 20
     End If


'    /* select the appropriate range for the interpolation
     Select Case i

        Case 0    '/* 20 to 40 range
        McPhase = 61.82 * ScatA ^ -1.61143

        Case 1   '/* 40 to 120 range
        McPhase = 2252# * ScatA ^ -2.58

        Case 2   '/* 120 to 140 range
        McPhase = 0.000034442 * ScatA ^ 1.1827

        Case 3  '/* 140 to 180 range
         McPhase = Exp(-26.612) * ScatA ^ 4.4962

        Case Else
'        Print " ERROR: Scattering angle out of range!"
     End Select

     McPhase = McPhase * 4# * Pi
End Function
```

---

## Primary Function for Paltridge and Mitchell Correction Methods

```
' Visual Basic function "Acor"
' Adapted from pmline.c

' Code to implement atmospheric correction scheme of Paltridge
'    and Mitchell (1990) - RS Env. 31:121-135
' Current version uses analytical functions versus table look up


'      inputs:
'      Angles input in degrees, converted to radians
'      SN = satellite number, 11 or 12
'      CH = channel number, 1 or 2
'      SZA,    ' Solar zenith angle
'      ZLA,     ' Satellite zenith angle
'      AZsun,  ' azimuth angle of sun
'      AZsat,  ' azimuth of satellite
'      Ecc,    ' eccentricity correction of earth's orbit
'      VIS,    ' visibility (km)
'      Tsat,   ' Correction for water absorption in channel 2 - air mass to sat
'      Tsun,   ' Correction for water absorption in channel 2 - air mass to sun
'      Pcor,   ' Pressure correction
```

Function **Acor**(SN As Integer, CH As Integer, Ecc As Double, AZsat As Double, ZLA As Double, AZsun As Double, SZA As Double, Vis As Double, DN As Double, Tsat As Double, Tsun As Double, Pcorr As Double) As Double


Static Pi As Double
Pi = 3.14159265

Static Kelv As Double
Kelv = 273.15     '          convert Kelvin to C


Dim SatNum As Integer '  satellite number
SatNum = SN
Dim gain1 As Double '     red gain - W/(m^2 um sr)
Dim off1 As Double '      red offset
  off1 = 40#
Dim gain2 As Double '     NIR gain
Dim off2 As Double '      NIR offset
  off2 = 40#
Dim F1 As Double '        exoatmospheric radiance in band 1
Dim F2 As Double '        W/(m^2 um)
Dim FG1 As Double '       gain over F1 times PI
Dim FG2 As Double
Dim R1 As Double '        radiometerically corrected reflectance - AVHRR channel 1
Dim R2 As Double '        " " channel 2
Dim b As Double '         Aerosol coefficient
Dim temp As Double '      used in finding tau
Dim t2 As Double '        used in varying azimuth angle

*'Atmospheric correction parameters*
Dim dAZ As Double '                relative azimuth angle

Dim tau1 As Double     '           Aerosol optical depth for channel 1
Dim tau2 As Double     '           Aerosol optical depth for channel 2
Dim M1 As Double '= 0.1, '    . Fraction of radiation from multiple scat in channel 1
  M1 = 0.1
Dim M2 As Double 'M2 = 0.05, '   " " in channel 2
  M2 = 0.05


*'Calculated:*
Dim Rg1 As Double '                corrected reflectance for channel 1
Dim Rg2 As Double          '       corrected reflectance for channel 2
Dim m As Double       "            Total air mass from sun to ground to sat
Dim msat As Double    '            Air mass relative to the satellite
Dim msun As Double    '            Air mass relative to the sun
Dim PHI0 As Double '               Scattering phase function for molecular scatter
Dim PHI1 As Double '               " " for aerosol scattering
Dim THETA As Double '              Scattering angle
Dim scc As Double '                used to pass THETA to the McPhase function
Dim gm1 As Double '                gm function for channel 1
Dim gm2 As Double '                gm function for channel 2
Dim Q01 As Double     '            Integrated molecular source function for channel 1

330

```
Dim Q02 As Double          '        " " for channel 2
 Dim Q1m1 As Double        '        Integrated aerosol scatter source function  for AVHRR channel 1
Dim Q1m2 As Double   '              " " for channel 2



    ' visibility to met range
    Vis = Vis * 1.3

    ' find relative azimuth angle
    dAZ = Abs(AZsun - AZsat)
    If (dAZ > 180#) Then
      dAZ = 360# - dAZ
    End If

    ' if NOAA 12, change calibration parameters
    If (SatNum = 12) Then
      gain1 = 0.524
      gain2 = 0.344
      F1 = 1613.7
      F2 = 1049.8
    Else
      gain1 = 0.599
      gain2 = 0.408
      F1 = 1630#
      F2 = 1053#
    End If

    FG1 = Pi * gain1 / F1 / Ecc
    FG2 = Pi * gain2 / F2 / Ecc

    SZA = SZA * Pi / 180#
    ZLA = ZLA * Pi / 180#
    dAZ = dAZ * Pi / 180#


   ' Estimate aerosol optical depth from visibility - Iqbal (1983) pg 119
   '    b = (0.55 ^ 1.3) * (3.912 / Vis - 0.01162) * (0.02472 * (Vis - 5#) + 1.132)

      ' find tau at central wave numbers of channels
      ' note - function is for transmittance - want depth
      tau1 = -Log(TrayCh1(1, Vis, 1))
      tau2 = -Log(TrayCh2(1, Vis, 1))


  ' estimate tau based on visual range

      ' ---------- atmospheric correction ----------
      ' Total air mass from sun to ground to sat
      m = 1# / Cos(SZA) + 1# / Cos(ZLA)
      m = m * Pcorr ' pressure correction

   temp = (Sin(ZLA) * Cos(dAZ) - Sin(SZA)) ^ 2 + (Sin(ZLA) * Sin(dAZ)) ^ 2# + (Cos(ZLA) -
        Cos(SZA)) ^ 2
```

331

```
temp = 1# - temp / 2#
' compute the arc cosine the fun way
temp = Atn(-temp / Sqr(-temp * temp + 1)) + (Pi / 2#)
THETA = Pi - temp
scc = THETA

  PHI0 = 0.75 * (1# + Cos(THETA) * Cos(THETA))
  PHI1 = McPhase(scc)

  ' Integrated source functions - Channel dependent
  gm1 = 0.25 * Exp(-0.0853 * m)
  Q01 = 0.0145 * Exp(-0.0441 * m)
  Q1m1 = (1# - Exp(-m * tau1)) * gm1 / m

  gm2 = 0.235 * Exp(-0.0724 * m)
  Q02 = 0.0049 * Exp(-0.0335 * m)
  Q1m2 = (1# - Exp(-m * tau2)) * gm2 / m


  ' ------ radiometric correction ----
  If (CH = 1) Then
   R1 = FG1 * (DN - off1)
  Else
   R2 = FG2 * (DN - off2)
  End If

' ------- Correct reflectance for each channel --------
  If (CH = 1) Then
   Rg1 = R1 * (1 - M1) - (1# / Cos(ZLA)) * (PHI0 * Q01 + PHI1 * Q1m1)

   If (Rg1 < 0#) Then
     Rg1 = 0#
   Else
     Rg1 = Rg1 / (4# * Cos(SZA) * gm1 * Exp(-m * tau1) * (1# + m * tau1))
   End If ' 0
   Acor = Rg1
  Else ' Channel 2
   Rg2 = (R2) * (1 - M2 * Tsat) - (1# / Cos(ZLA)) * (PHI0 * Q02 + PHI1 * Q1m2) * Tsat

   If (Rg2 < 0#) Then
     Rg2 = 0#
   Else
     Rg2 = Rg2 / ((4# * Cos(SZA) * gm2 * Exp(-m * tau2) * (1# + m * tau2)) * Tsun)
   End If
   Acor = Rg2
  End If ' channel

End Function
```

```
'Calculate exoatmospheric reflectance as defined by Schiebe et al.

'Input:
' SN - satellite number (11 or 12)
' CH - channel number (1 or 2)
' DN - DN value for channel
' SZA - solar zenith angle
' ecc - eccentricity correction factor

Option Explicit
Function ExAtR(SN As Integer, CH As Integer, DN As Double, SZA As Double, Ecc As Double)

Static Pi As Double
Pi = 3.14159265


Dim off As Double          offset
  off = 40#
Dim gain1 As Double '      red gain
Dim gain2 As Double '      NIR gain
Dim F1 As Double '         exoatmospheric integrated radiance in band 1
Dim F2 As Double '         W/(m^2 um)
Dim FG1 As Double '        gain over F1 times PI
Dim FG2 As Double
Dim G As Double '          Gain value divided by exoatmospheric irradiance for channel * PI

    If (SN = 12) Then
      gain1 = 0.524
      gain2 = 0.344
      F1 = 1613.7
      F2 = 1049.8
    Else
      gain1 = 0.599
      gain2 = 0.408
      F1 = 1630#
      F2 = 1053#
    End If

If (CH = 1) Then
  G = gain1 * Pi / F1
Else
  G = gain2 * Pi / F2
End If

ExAtR = G * (DN - off) / Ecc / Cos(Pi * SZA / 180)

End Function
```

# Appendix I

## Satellite Derived Data and Meteorological Data for

## Cloud-Free Conditions at the Lysimeter Sites

Below is a definition of column headings for the tables that follow:

| Column Heading | Definition |
|---|---|
| Mn | Month |
| Da | Day of the corresponding month |
| DOY | Day of the year (1994) |
| Lys | A "1" in this column indicates that both a quality image was available and the lysimeter was functioning properly (this data was used to investigate estimation of actual ET). |
| Img | A "1" in this column indicates that the image data was of sufficient quality, but the lysimeter was not functioning properly. Dates without a 1 in either the Lys or Img column appeared cloud-free, but were at large zenith angles. |
| Time of Over-Pass | Hour of the satellite over pass (GMT) |

Angles (Degrees):

| | |
|---|---|
| Satellite Zenith | Angle from the perspective of the point of observation |
| Satellite Azimuth | Degrees from North |
| Relative | Relative angle between the satellite, sun and point of observation ($180°$ - scattering angle) |
| Solar Azimuth | Degrees from North |
| Solar Zenith | Solar zenith angle at the time of satellite overpass. |

Correction Methods:

| | |
|---|---|
| Iqbal | Methods of Iqbal (1983) |
| P&M | Methods of Paltridge and Mitchell (1990) |
| ExoAtmo | Exoatmospheric reflectance |
| DOS | Dark object subtraction used to estimate path radiance with the remain correction terms from Iqbal's (1983). |
| No-Path | Correction for atmospheric attenuation from the method's of Iqbal, without account for path radiance ($L_p = 0$) |
| R1 | Reflectance in channel 1 based on the specified correction method. |
| R2 | Reflectance in channel 2 based on the specified correction method. |
| NDVI | NDVI calculated from the reflectance values to the left |
| $T_{b4}$ | Brightness temperature from channel 4 (K) |
| $T_{b5}$ | Brightness temperature from channel 5 (K) |

| Column Heading | Definition |
| --- | --- |
| $T_s$ | Satellite derived surface temperature using the Kerr1 split-window coefficients ($^{o}$C) |

**Based on Daily Observations:**

*Air Temperature ($^{o}$C):*

| | |
| --- | --- |
| Max | Maximum daily air temperature |
| Min | Minimum daily air temperature |

*Relative Humidity (%):*

| | |
| --- | --- |
| Max | Maximum daily relative humidity |
| Min | Minimum daily relative humidity |

| | |
| --- | --- |
| Average Wind Spd. | Average daily wind speed (m/s) |
| Total Solar Rad. | Total solar radiation for the day (MJ m$^{-2}$ d$^{-1}$ ) |

**Potential ET estimated from:**

| | |
| --- | --- |
| PMon | Penman-Monteith equation (mm d$^{-1}$) |
| Harg | Hargreaves equation (mm d$^{-1}$ ) |

| | |
| --- | --- |
| Days Since Rain | Number of days since rainfall occurred. |
| Days Since Rain > 10 mm | Number of days since a total daily rainfall of 10 mm. |

**At Time of Over-Pass:**

| | |
| --- | --- |
| AirTemp. | 1.5 m air temperature at the time of satellite overpass ($^{o}$C) |
| Relative Humidity | Relative humidity at the time of satellite overpass (%) |
| Vapor Pressure | Calculated vapor pressure at the time of satellite overpass (kPa) |

| Mn | Da | DOY | Lys | Img | Time of Over-Pass (Hr GMT) | Satellite Azimuth | Satellite Zenith | Relative | Solar Azimuth | Solar Zenith | Iqbal R1 | R2 | NDVI |
|---|---|---|---|---|---|---|---|---|---|---|---|---|---|

**Apache**

| Mn | Da | DOY | Lys | Img | Time | Sat Azimuth | Sat Zenith | Relative | Solar Azimuth | Solar Zenith | R1 | R2 | NDVI |
|---|---|---|---|---|---|---|---|---|---|---|---|---|---|
| 2 | 13 | 44 | 1 | 1 | 22.47 | 76 | 13 | 84 | 237 | 71 | 0.114 | 0.233 | 0.342 |
| 3 | 10 | 69 | 1 | 1 | 22.40 | 73 | 26 | 90 | 244 | 65 | 0.092 | 0.228 | 0.425 |
| 3 | 15 | 74 | 1 | 1 | 23.05 | 259 | 35 | 37 | 253 | 71 | 0.169 | 0.382 | 0.386 |
| 3 | 21 | 80 | | | 21.83 | 68 | 60 | 116 | 242 | 56 | 0.091 | 0.377 | 0.612 |
| 3 | 31 | 90 | 1 | 1 | 23.14 | 260 | 38 | 31 | 260 | 69 | 0.171 | 0.473 | 0.468 |
| 4 | 1 | 91 | 1 | 1 | 22.93 | 257 | 21 | 46 | 258 | 67 | 0.129 | 0.377 | 0.491 |
| 4 | 12 | 102 | 1 | 1 | 22.36 | 72 | 35 | 93 | 257 | 58 | 0.095 | 0.278 | 0.489 |
| 5 | 15 | 135 | | 1 | 22.32 | 71 | 43 | 95 | 268 | 53 | 0.072 | 0.311 | 0.625 |
| 5 | 18 | 138 | | 1 | 23.38 | 260 | 46 | 25 | 277 | 66 | 0.157 | 0.486 | 0.511 |
| 5 | 20 | 140 | 1 | 1 | 22.97 | 261 | 13 | 48 | 275 | 61 | 0.085 | 0.275 | 0.527 |
| 5 | 21 | 141 | | 1 | 22.77 | 69 | 8 | 65 | 273 | 58 | 0.075 | 0.231 | 0.508 |
| 5 | 30 | 150 | 1 | 1 | 22.60 | 73 | 26 | 79 | 273 | 55 | 0.065 | 0.228 | 0.555 |
| 5 | 31 | 151 | 1 | 1 | 22.40 | 71 | 41 | 92 | 272 | 52 | 0.079 | 0.259 | 0.533 |
| 6 | 5 | 156 | | 1 | 23.05 | 259 | 16 | 45 | 278 | 60 | 0.101 | 0.266 | 0.450 |
| 6 | 8 | 159 | | 1 | 22.44 | 71 | 40 | 90 | 273 | 52 | 0.111 | 0.285 | 0.439 |
| 6 | 26 | 177 | | | 22.11 | 68 | 59 | 103 | 271 | 47 | 0.127 | 0.286 | 0.384 |
| 6 | 27 | 178 | | | 23.58 | 261 | 51 | 22 | 282 | 65 | 0.233 | 0.504 | 0.368 |
| 6 | 30 | 181 | 1 | 1 | 22.97 | 277 | 1 | 56 | 277 | 57 | 0.121 | 0.279 | 0.393 |
| 7 | 6 | 187 | 1 | 1 | 23.41 | 260 | 40 | 27 | 280 | 63 | 0.205 | 0.433 | 0.358 |
| 7 | 18 | 199 | 1 | 1 | 22.63 | 73 | 34 | 86 | 272 | 54 | 0.118 | 0.304 | 0.442 |
| 7 | 19 | 200 | 1 | 1 | 22.42 | 70 | 48 | 97 | 270 | 51 | 0.127 | 0.319 | 0.432 |
| 7 | 20 | 201 | | | 22.96 | 68 | 57 | 104 | 268 | 49 | 0.148 | 0.351 | 0.407 |
| 7 | 27 | 208 | 1 | 1 | 22.46 | 71 | 47 | 98 | 268 | 52 | 0.102 | 0.286 | 0.473 |
| 8 | 9 | 221 | 1 | 1 | 23.15 | 259 | 9 | 54 | 271 | 63 | 0.106 | 0.280 | 0.450 |
| 8 | 13 | 225 | | | 22.33 | 69 | 55 | 107 | 263 | 53 | 0.298 | 0.417 | 0.167 |

| Mn | Da | DOY | Lys | Img | Time of Over-Pass (Hr GMT) | Satellite Azimuth | Satellite Zenith | Relative | Solar Azimuth | Solar Zenith | Iqbal R1 | Iqbal R2 | Iqbal NDVI |
|---|---|---|---|---|---|---|---|---|---|---|---|---|---|
| 8 | 21 | 233 | | | 22.37 | 69 | 55 | 109 | 261 | 55 | 0.197 | 0.336 | 0.261 |
| 8 | 25 | 237 | 1 | 1 | 23.22 | 259 | 12 | 55 | 267 | 67 | 0.130 | 0.265 | 0.340 |
| 8 | 27 | 239 | 1 | 1 | 22.81 | 72 | 28 | 90 | 263 | 62 | 0.109 | 0.253 | 0.396 |
| 8 | 28 | 240 | 1 | 1 | 22.61 | 71 | 43 | 102 | 261 | 60 | 0.131 | 0.290 | 0.376 |

**Goodwell**

| Mn | Da | DOY | Lys | Img | Time of Over-Pass (Hr GMT) | Satellite Azimuth | Satellite Zenith | Relative | Solar Azimuth | Solar Zenith | Iqbal R1 | Iqbal R2 | Iqbal NDVI |
|---|---|---|---|---|---|---|---|---|---|---|---|---|---|
| 5 | 29 | 149 | 1 | 1 | 22.82 | 71 | 23 | 77 | 272 | 55 | 0.098 | 0.274 | 0.472 |
| 5 | 30 | 150 | 1 | 1 | 22.61 | 70 | 39 | 89 | 270 | 52 | 0.098 | 0.277 | 0.475 |
| 6 | 5 | 156 | 1 | 1 | 23.06 | 64 | 2 | 59 | 275 | 57 | 0.137 | 0.263 | 0.317 |
| 6 | 6 | 157 | 1 | 1 | 22.86 | 73 | 22 | 75 | 273 | 55 | 0.118 | 0.240 | 0.340 |
| 6 | 13 | 164 | 1 | 1 | 23.10 | 153 | 1 | 57 | 276 | 57 | 0.145 | 0.283 | 0.323 |
| 6 | 15 | 166 | 1 | 1 | 22.69 | 71 | 37 | 86 | 272 | 52 | 0.140 | 0.310 | 0.378 |
| 6 | 16 | 167 | | 1 | 22.49 | 69 | 49 | 96 | 271 | 49 | 0.126 | 0.318 | 0.431 |
| 6 | 23 | 174 | | 1 | 22.73 | 71 | 35 | 85 | 273 | 52 | 0.116 | 0.254 | 0.373 |
| 6 | 24 | 175 | 1 | 1 | 22.53 | 69 | 48 | 95 | 271 | 49 | 0.124 | 0.256 | 0.348 |
| 6 | 26 | 177 | | | 22.12 | 66 | 65 | 106 | 267 | 44 | 0.140 | 0.324 | 0.397 |
| 6 | 28 | 179 | 1 | 1 | 23.38 | 259 | 23 | 38 | 278 | 60 | 0.181 | 0.317 | 0.275 |
| 7 | 10 | 191 | 1 | 1 | 22.60 | 70 | 46 | 95 | 270 | 50 | 0.130 | 0.259 | 0.333 |
| 8 | 12 | 224 | | | 22.55 | 68 | 53 | 106 | 262 | 53 | 0.126 | 0.218 | 0.266 |
| 8 | 16 | 228 | 1 | 1 | 23.40 | 260 | 13 | 51 | 269 | 64 | 0.149 | 0.244 | 0.241 |
| 8 | 26 | 238 | 1 | 1 | 23.03 | 72 | 25 | 87 | 263 | 62 | 0.114 | 0.224 | 0.326 |
| 8 | 28 | 240 | | | 22.62 | 69 | 52 | 109 | 258 | 58 | 0.155 | 0.271 | 0.274 |
| 9 | 9 | 252 | 1 | 1 | 23.51 | 258 | 17 | 55 | 263 | 72 | 0.155 | 0.273 | 0.274 |
| 9 | 12 | 255 | 1 | 1 | 22.89 | 71 | 38 | 104 | 257 | 66 | 0.134 | 0.238 | 0.279 |

| Mn | Da | DOY | Lys | Img | Time of Over-Pass (Hr GMT) | Satellite Azimuth | Satellite Zenith | Relative | Solar Azimuth | Solar Zenith | Iqbal R1 | Iqbal R2 | Iqbal NDVI |
|---|---|---|---|---|---|---|---|---|---|---|---|---|---|
| **Marena** | | | | | | | | | | | | | |
| 3 | 15 | 74 | | 1 | 23.06 | 260 | 41 | 32 | 253 | 73 | 0.205 | 0.310 | 0.205 |
| 3 | 31 | 90 | | 1 | 23.14 | 260 | 44 | 27 | 260 | 71 | 0.197 | 0.342 | 0.270 |
| 4 | 1 | 91 | | 1 | 22.94 | 258 | 29 | 39 | 259 | 68 | 0.152 | 0.266 | 0.272 |
| 4 | 7 | 97 | | | 23.39 | 262 | 56 | 17 | 265 | 72 | 0.248 | 0.455 | 0.295 |
| 5 | 15 | 135 | | 1 | 22.32 | 72 | 37 | 90 | 268 | 54 | 0.051 | 0.290 | 0.699 |
| 5 | 18 | 138 | | | 23.39 | 261 | 50 | 21 | 278 | 67 | 0.134 | 0.591 | 0.631 |
| 5 | 20 | 140 | | 1 | 22.98 | 258 | 21 | 41 | 275 | 61 | 0.082 | 0.363 | 0.630 |
| 5 | 30 | 150 | 1 | 1 | 22.61 | 74 | 17 | 72 | 273 | 56 | 0.054 | 0.305 | 0.700 |
| 6 | 6 | 157 | | 1 | 22.85 | 260 | 5 | 53 | 276 | 58 | 0.060 | 0.301 | 0.668 |
| 6 | 13 | 164 | | 1 | 23.09 | 257 | 26 | 37 | 278 | 60 | 0.081 | 0.391 | 0.655 |
| 6 | 25 | 176 | | 1 | 22.32 | 70 | 44 | 93 | 272 | 50 | 0.075 | 0.280 | 0.577 |
| 6 | 26 | 177 | | | 22.11 | 68 | 55 | 100 | 270 | 48 | 0.069 | 0.292 | 0.617 |
| 6 | 27 | 178 | | | 23.58 | 262 | 55 | 20 | 282 | 65 | 0.176 | 0.524 | 0.496 |
| 6 | 30 | 181 | | 1 | 22.97 | 261 | 11 | 48 | 277 | 58 | 0.063 | 0.283 | 0.635 |
| 7 | 8 | 189 | 1 | 1 | 23.00 | 259 | 12 | 47 | 276 | 59 | 0.072 | 0.275 | 0.583 |
| 7 | 17 | 198 | | 1 | 22.84 | 67 | 7 | 63 | 274 | 57 | 0.069 | 0.235 | 0.547 |
| 7 | 18 | 199 | | 1 | 22.63 | 73 | 26 | 80 | 272 | 54 | 0.074 | 0.236 | 0.523 |
| 7 | 19 | 200 | 1 | 1 | 22.43 | 71 | 42 | 92 | 270 | 52 | 0.069 | 0.254 | 0.573 |
| 7 | 27 | 208 | 1 | 1 | 22.46 | 71 | 41 | 93 | 268 | 53 | 0.093 | 0.280 | 0.500 |
| 7 | 28 | 209 | | | 22.26 | 69 | 52 | 101 | 266 | 51 | 0.120 | 0.307 | 0.438 |
| 8 | 8 | 220 | | 1 | 23.36 | 259 | 36 | 32 | 273 | 66 | 0.086 | 0.374 | 0.625 |
| 8 | 16 | 228 | | 1 | 23.39 | 260 | 37 | 32 | 271 | 68 | 0.113 | 0.362 | 0.526 |
| 8 | 21 | 233 | | | 22.37 | 69 | 50 | 105 | 261 | 57 | 0.115 | 0.302 | 0.450 |
| 8 | 22 | 234 | | | 22.17 | 68 | 59 | 112 | 258 | 54 | 0.169 | 0.344 | 0.342 |
| 8 | 25 | 237 | | 1 | 23.22 | 257 | 21 | 47 | 268 | 68 | 0.070 | 0.271 | 0.591 |

| Mn | Da | DOY | Lys | Img | Time of Over-Pass (Hr GMT) | Satellite Azimuth | Satellite Zenith | Relative | Solar Azimuth | Solar Zenith | Iqbal R1 | R2 | NDVI |
|---|---|---|---|---|---|---|---|---|---|---|---|---|---|
| 8 | 26 | 238 |  | 1 | 23.02 | 254 | 1 | 65 | 266 | 66 | 0.062 | 0.228 | 0.571 |
| 8 | 27 | 239 | 1 | 1 | 22.81 | 72 | 19 | 82 | 263 | 63 | 0.054 | 0.213 | 0.598 |

**Wister**

| Mn | Da | DOY | Lys | Img | Time of Over-Pass (Hr GMT) | Satellite Azimuth | Satellite Zenith | Relative | Solar Azimuth | Solar Zenith | Iqbal R1 | R2 | NDVI |
|---|---|---|---|---|---|---|---|---|---|---|---|---|---|
| 2 | 13 | 44 |  | 1 | 22.47 | 258 | 11 | 63 | 240 | 74 | 0.132 | 0.240 | 0.289 |
| 3 | 10 | 69 |  | 1 | 22.40 | 74 | 3 | 70 | 247 | 67 | 0.088 | 0.200 | 0.389 |
| 3 | 15 | 74 |  |  | 23.05 | 261 | 50 | 24 | 255 | 74 | 0.198 | 0.415 | 0.355 |
| 3 | 21 | 80 |  |  | 21.83 | 70 | 50 | 109 | 245 | 59 | 0.105 | 0.268 | 0.439 |
| 3 | 31 | 90 |  |  | 23.14 | 261 | 52 | 20 | 262 | 72 | 0.195 | 0.506 | 0.444 |
| 4 | 12 | 102 | 1 | 1 | 22.36 | 72 | 15 | 76 | 259 | 61 | 0.078 | 0.281 | 0.566 |
| 5 | 15 | 135 |  | 1 | 22.32 | 73 | 26 | 81 | 270 | 56 | 0.049 | 0.338 | 0.746 |
| 5 | 20 | 140 |  | 1 | 22.97 | 260 | 34 | 32 | 276 | 63 | 0.089 | 0.490 | 0.692 |
| 5 | 21 | 141 | 1 | 1 | 22.76 | 258 | 16 | 46 | 275 | 61 | 0.071 | 0.398 | 0.699 |
| 5 | 31 | 151 |  | 1 | 22.40 | 74 | 23 | 77 | 274 | 55 | 0.059 | 0.348 | 0.710 |
| 6 | 7 | 158 | 1 | 1 | 22.64 | 50 | 1 | 58 | 276 | 58 | 0.063 | 0.344 | 0.693 |
| 6 | 24 | 175 |  | 1 | 22.51 | 71 | 18 | 72 | 276 | 55 | 0.061 | 0.304 | 0.668 |
| 6 | 25 | 176 | 1 | 1 | 22.31 | 72 | 36 | 86 | 274 | 52 | 0.067 | 0.300 | 0.633 |
| 6 | 29 | 180 | 1 | 1 | 23.16 | 259 | 41 | 27 | 280 | 63 | 0.113 | 0.464 | 0.609 |
| 7 | 18 | 199 | 1 | 1 | 22.62 | 73 | 14 | 69 | 274 | 56 | 0.076 | 0.287 | 0.580 |
| 7 | 19 | 200 |  | 1 | 22.42 | 72 | 32 | 85 | 272 | 54 | 0.068 | 0.296 | 0.625 |
| 7 | 27 | 208 | 1 | 1 | 22.46 | 73 | 31 | 85 | 270 | 55 | 0.086 | 0.303 | 0.558 |
| 7 | 28 | 209 |  | 1 | 22.25 | 70 | 45 | 96 | 268 | 53 | 0.163 | 0.375 | 0.396 |
| 8 | 27 | 239 | 1 | 1 | 22.81 | 67 | 6 | 71 | 265 | 65 | 0.104 | 0.278 | 0.456 |
| 8 | 28 | 240 | 1 | 1 | 22.60 | 73 | 25 | 88 | 263 | 63 | 0.098 | 0.276 | 0.475 |
| 9 | 13 | 256 | 1 | 1 | 22.67 | 73 | 23 | 91 | 259 | 68 | 0.115 | 0.274 | 0.408 |

| | | P&M | | | ExoAtmo | | | DOS | | | No Path | | |
|---|---|---|---|---|---|---|---|---|---|---|---|---|---|
| Mn | Da | R1 | R2 | NDVI | R1 | R2 | NDVI | R1 | R2 | NDVI | R1 | R2 | NDVI |

**Apache**

| | | | | | | | | | | | | | |
|---|---|---|---|---|---|---|---|---|---|---|---|---|---|
| 2 | 13 | 0.088 | 0.243 | 0.467 | 0.108 | 0.189 | 0.272 | 0.103 | 0.238 | 0.396 | 0.179 | 0.264 | 0.193 |
| 3 | 10 | 0.069 | 0.218 | 0.519 | 0.095 | 0.180 | 0.310 | 0.082 | 0.230 | 0.474 | 0.150 | 0.258 | 0.266 |
| 3 | 15 | 0.124 | 0.365 | 0.492 | 0.159 | 0.276 | 0.268 | 0.137 | 0.368 | 0.459 | 0.282 | 0.433 | 0.212 |
| 3 | 21 | 0.055 | 0.358 | 0.735 | 0.130 | 0.303 | 0.400 | 0.125 | 0.343 | 0.467 | 0.224 | 0.453 | 0.338 |
| 3 | 31 | 0.125 | 0.449 | 0.564 | 0.165 | 0.341 | 0.347 | 0.126 | 0.440 | 0.554 | 0.285 | 0.525 | 0.296 |
| 4 | 1 | 0.098 | 0.350 | 0.563 | 0.123 | 0.273 | 0.379 | 0.112 | 0.357 | 0.523 | 0.196 | 0.408 | 0.350 |
| 4 | 12 | 0.071 | 0.258 | 0.566 | 0.097 | 0.215 | 0.379 | 0.080 | 0.250 | 0.512 | 0.148 | 0.306 | 0.349 |
| 5 | 15 | 0.051 | 0.268 | 0.680 | 0.082 | 0.224 | 0.465 | 0.072 | 0.282 | 0.595 | 0.126 | 0.342 | 0.461 |
| 5 | 18 | 0.108 | 0.407 | 0.582 | 0.160 | 0.318 | 0.330 | 0.122 | 0.462 | 0.582 | 0.287 | 0.552 | 0.316 |
| 5 | 20 | 0.064 | 0.240 | 0.579 | 0.090 | 0.198 | 0.377 | 0.055 | 0.253 | 0.642 | 0.134 | 0.298 | 0.380 |
| 5 | 21 | 0.058 | 0.201 | 0.554 | 0.077 | 0.168 | 0.371 | 0.044 | 0.208 | 0.648 | 0.113 | 0.250 | 0.378 |
| 5 | 30 | 0.047 | 0.186 | 0.597 | 0.070 | 0.157 | 0.386 | 0.063 | 0.213 | 0.542 | 0.108 | 0.251 | 0.398 |
| 5 | 31 | 0.057 | 0.210 | 0.574 | 0.084 | 0.179 | 0.362 | 0.082 | 0.246 | 0.499 | 0.131 | 0.289 | 0.378 |
| 6 | 5 | 0.077 | 0.219 | 0.481 | 0.102 | 0.184 | 0.287 | 0.060 | 0.236 | 0.595 | 0.151 | 0.291 | 0.316 |
| 6 | 8 | 0.084 | 0.236 | 0.473 | 0.104 | 0.199 | 0.312 | 0.108 | 0.248 | 0.394 | 0.158 | 0.312 | 0.329 |
| 6 | 26 | 0.088 | 0.226 | 0.439 | 0.124 | 0.195 | 0.222 | 0.139 | 0.240 | 0.269 | 0.210 | 0.336 | 0.231 |
| 6 | 27 | 0.168 | 0.405 | 0.414 | 0.211 | 0.322 | 0.209 | 0.225 | 0.458 | 0.342 | 0.366 | 0.574 | 0.222 |
| 6 | 30 | 0.095 | 0.231 | 0.416 | 0.109 | 0.191 | 0.273 | 0.103 | 0.259 | 0.432 | 0.162 | 0.299 | 0.298 |
| 7 | 6 | 0.154 | 0.355 | 0.396 | 0.183 | 0.287 | 0.222 | 0.213 | 0.403 | 0.308 | 0.298 | 0.481 | 0.235 |
| 7 | 18 | 0.091 | 0.257 | 0.479 | 0.107 | 0.214 | 0.333 | 0.113 | 0.283 | 0.430 | 0.161 | 0.328 | 0.342 |
| 7 | 19 | 0.094 | 0.270 | 0.482 | 0.118 | 0.226 | 0.314 | 0.137 | 0.274 | 0.334 | 0.184 | 0.352 | 0.313 |
| 7 | 20 | 0.105 | 0.285 | 0.461 | 0.137 | 0.240 | 0.271 | 0.154 | 0.250 | 0.238 | 0.229 | 0.400 | 0.271 |
| 7 | 27 | 0.075 | 0.248 | 0.537 | 0.103 | 0.210 | 0.340 | 0.104 | 0.248 | 0.411 | 0.161 | 0.320 | 0.330 |
| 8 | 9 | 0.082 | 0.243 | 0.497 | 0.102 | 0.198 | 0.320 | 0.097 | 0.258 | 0.455 | 0.156 | 0.304 | 0.323 |
| 8 | 13 | 0.219 | 0.345 | 0.224 | 0.229 | 0.286 | 0.109 | 0.335 | 0.439 | 0.134 | 0.397 | 0.477 | 0.092 |

| Mn | Da | P&M | | | ExoAtmo | | | DOS | | | No Path | | |
|---|---|---|---|---|---|---|---|---|---|---|---|---|---|
| | | R1 | R2 | NDVI | R1 | R2 | NDVI | R1 | R2 | NDVI | R1 | R2 | NDVI |
| 8 | 21 | 0.142 | 0.285 | 0.334 | 0.176 | 0.244 | 0.163 | 0.223 | 0.307 | 0.157 | 0.297 | 0.396 | 0.142 |
| 8 | 25 | 0.103 | 0.228 | 0.379 | 0.121 | 0.185 | 0.208 | 0.121 | 0.241 | 0.333 | 0.185 | 0.291 | 0.223 |
| 8 | 27 | 0.084 | 0.214 | 0.437 | 0.105 | 0.178 | 0.259 | 0.095 | 0.232 | 0.417 | 0.162 | 0.283 | 0.272 |
| 8 | 28 | 0.098 | 0.249 | 0.437 | 0.128 | 0.211 | 0.243 | 0.126 | 0.262 | 0.353 | 0.205 | 0.333 | 0.239 |

**Goodwell**

| Mn | Da | P&M | | | ExoAtmo | | | DOS | | | No Path | | |
|---|---|---|---|---|---|---|---|---|---|---|---|---|---|
| | | R1 | R2 | NDVI | R1 | R2 | NDVI | R1 | R2 | NDVI | R1 | R2 | NDVI |
| 5 | 29 | 0.074 | 0.244 | 0.536 | 0.089 | 0.198 | 0.378 | 0.086 | 0.251 | 0.491 | 0.141 | 0.296 | 0.356 |
| 5 | 30 | 0.070 | 0.233 | 0.540 | 0.093 | 0.193 | 0.349 | 0.077 | 0.224 | 0.487 | 0.283 | 0.440 | 0.217 |
| 6 | 5 | 0.107 | 0.230 | 0.364 | 0.116 | 0.188 | 0.236 | 0.133 | 0.241 | 0.290 | 0.176 | 0.283 | 0.233 |
| 6 | 6 | 0.095 | 0.211 | 0.381 | 0.107 | 0.178 | 0.248 | 0.108 | 0.204 | 0.309 | 0.151 | 0.257 | 0.260 |
| 6 | 13 | 0.114 | 0.259 | 0.387 | 0.122 | 0.210 | 0.264 | 0.122 | 0.256 | 0.354 | 0.185 | 0.302 | 0.241 |
| 6 | 15 | 0.106 | 0.289 | 0.463 | 0.119 | 0.236 | 0.329 | 0.093 | 0.219 | 0.405 | 0.187 | 0.335 | 0.284 |
| 6 | 16 | 0.090 | 0.292 | 0.529 | 0.115 | 0.240 | 0.352 | 0.069 | 0.163 | 0.404 | 0.190 | 0.353 | 0.300 |
| 6 | 23 | 0.089 | 0.222 | 0.427 | 0.106 | 0.187 | 0.279 | 0.108 | 0.219 | 0.341 | 0.156 | 0.276 | 0.277 |
| 6 | 24 | 0.093 | 0.228 | 0.421 | 0.115 | 0.194 | 0.254 | 0.116 | 0.230 | 0.329 | 0.174 | 0.284 | 0.239 |
| 6 | 26 | 0.082 | 0.258 | 0.517 | 0.132 | 0.216 | 0.242 | 0.087 | 0.220 | 0.431 | 0.276 | 0.404 | 0.188 |
| 6 | 28 | 0.142 | 0.285 | 0.334 | 0.158 | 0.234 | 0.195 | 0.173 | 0.275 | 0.228 | 0.236 | 0.344 | 0.186 |
| 7 | 10 | 0.098 | 0.233 | 0.406 | 0.119 | 0.198 | 0.248 | 0.112 | 0.193 | 0.264 | 0.179 | 0.286 | 0.230 |
| 8 | 12 | 0.088 | 0.187 | 0.363 | 0.128 | 0.169 | 0.141 | 0.060 | 0.072 | 0.097 | 0.209 | 0.267 | 0.121 |
| 8 | 16 | 0.119 | 0.221 | 0.301 | 0.133 | 0.181 | 0.152 | 0.105 | 0.216 | 0.347 | 0.199 | 0.268 | 0.147 |
| 8 | 26 | 0.091 | 0.207 | 0.388 | 0.109 | 0.173 | 0.229 | 0.105 | 0.208 | 0.332 | 0.155 | 0.246 | 0.227 |
| 8 | 28 | 0.112 | 0.229 | 0.345 | 0.152 | 0.203 | 0.142 | 0.155 | 0.247 | 0.227 | 0.244 | 0.326 | 0.143 |
| 9 | 9 | 0.120 | 0.242 | 0.338 | 0.133 | 0.183 | 0.157 | 0.146 | 0.249 | 0.260 | 0.232 | 0.310 | 0.144 |
| 9 | 12 | 0.100 | 0.211 | 0.359 | 0.134 | 0.182 | 0.152 | 0.137 | 0.215 | 0.221 | 0.215 | 0.286 | 0.142 |

| | | P&M | | | ExoAtmo | | | DOS | | | No Path | | |
|---|---|---|---|---|---|---|---|---|---|---|---|---|---|
| Mn | Da | R1 | R2 | NDVI | R1 | R2 | NDVI | R1 | R2 | NDVI | R1 | R2 | NDVI |

**Marena**

| Mn | Da | R1 | R2 | NDVI | R1 | R2 | NDVI | R1 | R2 | NDVI | R1 | R2 | NDVI |
|---|---|---|---|---|---|---|---|---|---|---|---|---|---|
| 3 | 15 | 0.148 | 0.304 | 0.346 | 0.187 | 0.236 | 0.114 | 0.187 | 0.306 | 0.240 | 0.351 | 0.376 | 0.034 |
| 3 | 31 | 0.140 | 0.328 | 0.400 | 0.188 | 0.258 | 0.157 | 0.165 | 0.316 | 0.313 | 0.342 | 0.409 | 0.089 |
| 4 | 1 | 0.114 | 0.248 | 0.368 | 0.143 | 0.200 | 0.164 | 0.146 | 0.251 | 0.265 | 0.237 | 0.305 | 0.125 |
| 4 | 7 | 0.164 | 0.441 | 0.458 | 0.241 | 0.335 | 0.164 | 0.266 | 0.433 | 0.238 | 0.494 | 0.570 | 0.071 |
| 5 | 15 | 0.036 | 0.250 | 0.750 | 0.065 | 0.210 | 0.527 | 0.044 | 0.256 | 0.708 | 0.098 | 0.316 | 0.525 |
| 5 | 18 | 0.084 | 0.491 | 0.707 | 0.156 | 0.375 | 0.412 | 0.115 | 0.577 | 0.667 | 0.294 | 0.673 | 0.392 |
| 5 | 20 | 0.060 | 0.317 | 0.681 | 0.092 | 0.257 | 0.473 | 0.058 | 0.343 | 0.712 | 0.141 | 0.391 | 0.471 |
| 5 | 30 | 0.038 | 0.249 | 0.732 | 0.061 | 0.204 | 0.538 | 0.049 | 0.288 | 0.709 | 0.095 | 0.327 | 0.551 |
| 6 | 6 | 0.044 | 0.248 | 0.698 | 0.070 | 0.206 | 0.495 | 0.052 | 0.277 | 0.683 | 0.101 | 0.321 | 0.521 |
| 6 | 13 | 0.058 | 0.322 | 0.693 | 0.094 | 0.263 | 0.471 | 0.071 | 0.370 | 0.679 | 0.144 | 0.423 | 0.491 |
| 6 | 25 | 0.054 | 0.238 | 0.632 | 0.082 | 0.202 | 0.423 | 0.072 | 0.226 | 0.516 | 0.123 | 0.307 | 0.429 |
| 6 | 26 | 0.045 | 0.248 | 0.692 | 0.085 | 0.211 | 0.427 | 0.067 | 0.242 | 0.564 | 0.136 | 0.330 | 0.417 |
| 6 | 27 | 0.117 | 0.422 | 0.566 | 0.185 | 0.334 | 0.286 | 0.184 | 0.485 | 0.451 | 0.334 | 0.607 | 0.290 |
| 6 | 30 | 0.045 | 0.237 | 0.680 | 0.073 | 0.197 | 0.459 | 0.048 | 0.265 | 0.693 | 0.108 | 0.306 | 0.476 |
| 7 | 8 | 0.054 | 0.242 | 0.636 | 0.081 | 0.202 | 0.428 | 0.045 | 0.255 | 0.699 | 0.119 | 0.297 | 0.427 |
| 7 | 17 | 0.052 | 0.197 | 0.581 | 0.073 | 0.166 | 0.391 | 0.061 | 0.218 | 0.562 | 0.106 | 0.254 | 0.412 |
| 7 | 18 | 0.056 | 0.197 | 0.558 | 0.076 | 0.167 | 0.372 | 0.065 | 0.211 | 0.531 | 0.113 | 0.258 | 0.390 |
| 7 | 19 | 0.049 | 0.214 | 0.624 | 0.078 | 0.182 | 0.403 | 0.071 | 0.203 | 0.482 | 0.118 | 0.282 | 0.409 |
| 7 | 27 | 0.069 | 0.243 | 0.555 | 0.094 | 0.204 | 0.369 | 0.086 | 0.236 | 0.465 | 0.144 | 0.309 | 0.364 |
| 7 | 28 | 0.086 | 0.259 | 0.501 | 0.118 | 0.220 | 0.302 | 0.111 | 0.395 | 0.561 | 0.190 | 0.348 | 0.292 |
| 8 | 8 | 0.058 | 0.312 | 0.688 | 0.109 | 0.251 | 0.395 | 0.118 | 0.360 | 0.506 | 0.181 | 0.422 | 0.400 |
| 8 | 16 | 0.078 | 0.320 | 0.608 | 0.127 | 0.254 | 0.333 | 0.094 | 0.348 | 0.576 | 0.215 | 0.412 | 0.313 |
| 8 | 21 | 0.081 | 0.255 | 0.519 | 0.121 | 0.218 | 0.288 | 0.125 | 0.261 | 0.354 | 0.199 | 0.352 | 0.278 |
| 8 | 22 | 0.117 | 0.282 | 0.414 | 0.164 | 0.244 | 0.195 | 0.153 | 0.256 | 0.253 | 0.287 | 0.417 | 0.184 |
| 8 | 25 | 0.048 | 0.232 | 0.655 | 0.087 | 0.188 | 0.370 | 0.066 | 0.249 | 0.583 | 0.133 | 0.302 | 0.389 |

| | | P&M | | | ExoAtmo | | | DOS | | | No Path | | |
|---|---|---|---|---|---|---|---|---|---|---|---|---|---|
| Mn | Da | R1 | R2 | NDVI | R1 | R2 | NDVI | R1 | R2 | NDVI | R1 | R2 | NDVI |
| 8 | 26 | 0.046 | 0.198 | 0.620 | 0.072 | 0.163 | 0.384 | 0.047 | 0.203 | 0.623 | 0.106 | 0.250 | 0.406 |
| 8 | 27 | 0.038 | 0.182 | 0.658 | 0.066 | 0.153 | 0.398 | 0.032 | 0.186 | 0.707 | 0.100 | 0.238 | 0.410 |

**Wister**

| | | | | | | | | | | | | | |
|---|---|---|---|---|---|---|---|---|---|---|---|---|---|
| 2 | 13 | 0.101 | 0.246 | 0.418 | 0.119 | 0.184 | 0.213 | 0.118 | 0.242 | 0.344 | 0.212 | 0.274 | 0.127 |
| 3 | 10 | 0.066 | 0.192 | 0.485 | 0.088 | 0.155 | 0.274 | 0.066 | 0.194 | 0.492 | 0.143 | 0.226 | 0.224 |
| 3 | 15 | 0.130 | 0.410 | 0.518 | 0.203 | 0.304 | 0.199 | 0.222 | 0.434 | 0.323 | 0.422 | 0.517 | 0.101 |
| 3 | 21 | 0.074 | 0.252 | 0.546 | 0.120 | 0.218 | 0.288 | 0.095 | 0.203 | 0.363 | 0.195 | 0.319 | 0.240 |
| 3 | 31 | 0.128 | 0.479 | 0.580 | 0.206 | 0.357 | 0.268 | 0.201 | 0.500 | 0.426 | 0.417 | 0.610 | 0.188 |
| 4 | 12 | 0.059 | 0.256 | 0.624 | 0.080 | 0.209 | 0.447 | 0.048 | 0.240 | 0.664 | 0.121 | 0.302 | 0.428 |
| 5 | 15 | 0.035 | 0.282 | 0.777 | 0.060 | 0.232 | 0.587 | 0.034 | 0.295 | 0.795 | 0.091 | 0.361 | 0.599 |
| 5 | 20 | 0.062 | 0.423 | 0.743 | 0.107 | 0.335 | 0.515 | 0.080 | 0.479 | 0.715 | 0.174 | 0.532 | 0.508 |
| 5 | 21 | 0.052 | 0.343 | 0.738 | 0.082 | 0.277 | 0.545 | 0.047 | 0.377 | 0.780 | 0.124 | 0.424 | 0.547 |
| 5 | 31 | 0.043 | 0.283 | 0.735 | 0.066 | 0.232 | 0.559 | 0.049 | 0.325 | 0.737 | 0.100 | 0.370 | 0.575 |
| 6 | 7 | 0.047 | 0.278 | 0.711 | 0.069 | 0.228 | 0.533 | 0.053 | 0.320 | 0.715 | 0.102 | 0.364 | 0.563 |
| 6 | 24 | 0.046 | 0.257 | 0.698 | 0.066 | 0.213 | 0.525 | 0.067 | 0.287 | 0.622 | 0.097 | 0.323 | 0.537 |
| 6 | 25 | 0.050 | 0.243 | 0.661 | 0.073 | 0.204 | 0.470 | 0.058 | 0.236 | 0.607 | 0.110 | 0.324 | 0.492 |
| 6 | 29 | 0.077 | 0.392 | 0.670 | 0.127 | 0.313 | 0.424 | 0.122 | 0.451 | 0.575 | 0.214 | 0.515 | 0.413 |
| 7 | 18 | 0.058 | 0.230 | 0.596 | 0.077 | 0.191 | 0.425 | 0.063 | 0.256 | 0.604 | 0.114 | 0.307 | 0.457 |
| 7 | 19 | 0.051 | 0.240 | 0.651 | 0.074 | 0.201 | 0.463 | 0.062 | 0.235 | 0.582 | 0.111 | 0.321 | 0.486 |
| 7 | 27 | 0.065 | 0.258 | 0.597 | 0.086 | 0.215 | 0.428 | 0.070 | 0.250 | 0.563 | 0.129 | 0.326 | 0.432 |
| 7 | 28 | 0.123 | 0.319 | 0.442 | 0.141 | 0.263 | 0.304 | 0.141 | 0.457 | 0.530 | 0.221 | 0.409 | 0.298 |
| 8 | 27 | 0.080 | 0.232 | 0.487 | 0.098 | 0.187 | 0.314 | 0.078 | 0.246 | 0.518 | 0.153 | 0.304 | 0.329 |
| 8 | 28 | 0.075 | 0.231 | 0.512 | 0.097 | 0.191 | 0.326 | 0.067 | 0.228 | 0.548 | 0.152 | 0.307 | 0.337 |
| 9 | 13 | 0.087 | 0.233 | 0.455 | 0.110 | 0.187 | 0.260 | 0.115 | 0.246 | 0.363 | 0.184 | 0.314 | 0.260 |

| Mn | Da | $T_{b4}$ (K) | $T_{b5}$ (K) | $T_s$ (°C) | Air Temperature (°C) | | Relative Humidity (%) | | Average Wind | Total Solar Rad. | Potential ET | |
|---|---|---|---|---|---|---|---|---|---|---|---|---|
| | | | | | | | | | | | PMon | Harg |
| | | | | | Max | Min | Max | Min | Spd. (m s$^{-1}$) | (MJ m$^{-2}$ d$^{-1}$) | (mm d$^{-1}$) | (mm d$^{-1}$) |

*(header: Based on Daily Observations)*

**Apache**

| Mn | Da | $T_{b4}$ | $T_{b5}$ | $T_s$ | Max | Min | Max | Min | Spd. | Total | PMon | Harg |
|---|---|---|---|---|---|---|---|---|---|---|---|---|
| 2 | 13 | 285.2 | 285.2 | 15.0 | 13.7 | -7.3 | 76 | 17 | 2.68 | 18.19 | 2.5 | 2.0 |
| 3 | 10 | 288.9 | 288.6 | 19.5 | 18.3 | -2.3 | 95 | 23 | 2.01 | 21.89 | 2.7 | 3.1 |
| 3 | 15 | 288.8 | 288.2 | 19.8 | 21.3 | 7.7 | 92 | 29 | 4.34 | 22.09 | 4.1 | 3.3 |
| 3 | 21 | 293.9 | 293.1 | 25.6 | 20.7 | 4.7 | 65 | 20 | 3.00 | 24.18 | 5.2 | 3.5 |
| 3 | 31 | 291.8 | 291.2 | 23.1 | 22.3 | 1.7 | 80 | 24 | 4.34 | 25.08 | 4.7 | 4.2 |
| 4 | 1 | 295.2 | 294.6 | 26.4 | 26.3 | 7.3 | 79 | 25 | 5.01 | 24.88 | 5.4 | 4.7 |
| 4 | 12 | 290.2 | 289.3 | 22.1 | 19.7 | 4.3 | 86 | 28 | 4.65 | 26.58 | 4.8 | 3.8 |
| 5 | 15 | 298.2 | 296.7 | 31.3 | 27.3 | 14.0 | 99 | 42 | 3.00 | 28.48 | 5.4 | 5.3 |
| 5 | 18 | 294.9 | 292.9 | 29.1 | 28.7 | 16.0 | 100 | 52 | 2.01 | 26.48 | 4.9 | 5.4 |
| 5 | 20 | 297.9 | 296.5 | 30.9 | 27.3 | 13.7 | 94 | 46 | 2.32 | 28.58 | 5.4 | 5.4 |
| 5 | 21 | 296.3 | 294.2 | 30.5 | 28.7 | 13.3 | 89 | 45 | 3.00 | 27.48 | 5.5 | 5.8 |
| 5 | 30 | 302.7 | 300.8 | 36.6 | 33.0 | 17.7 | 100 | 45 | 1.34 | 27.28 | 4.9 | 6.5 |
| 5 | 31 | 301.9 | 299.6 | 36.7 | 33.0 | 19.0 | 100 | 46 | 2.01 | 29.48 | 5.6 | 6.4 |
| 6 | 5 | 302.8 | 300.3 | 37.8 | 35.7 | 21.7 | 96 | 48 | 4.65 | 27.28 | 6.5 | 6.8 |
| 6 | 8 | 307.9 | 305.6 | 42.9 | 38.3 | 24.7 | 93 | 33 | 3.67 | 28.28 | 7.2 | 7.2 |
| 6 | 26 | 304.1 | 300.0 | 42.6 | 39.3 | 24.0 | 79 | 34 | 2.68 | 28.78 | 7.6 | 7.6 |
| 6 | 27 | 308.2 | 304.9 | 45.1 | 44.0 | 24.0 | 83 | 22 | 3.98 | 28.58 | 9.1 | 9.2 |
| 6 | 30 | 304.1 | 301.6 | 39.4 | 37.3 | 21.3 | 87 | 37 | 2.68 | 27.98 | 7.0 | 7.4 |
| 7 | 6 | 300.5 | 296.9 | 37.8 | 34.7 | 20.0 | 91 | 49 | 3.67 | 25.68 | 6.5 | 6.7 |
| 7 | 18 | 303.1 | 300.7 | 38.3 | 37.3 | 23.3 | 83 | 31 | 3.35 | 27.98 | 7.4 | 6.9 |
| 7 | 19 | 303.5 | 301.1 | 38.6 | 36.3 | 22.7 | 81 | 27 | 5.01 | 28.48 | 8.8 | 6.7 |
| 7 | 20 | 297.7 | 293.4 | 36.8 | 36.3 | 24.0 | 75 | 34 | 5.01 | 27.68 | 8.4 | 6.5 |
| 7 | 27 | 301.4 | 299.0 | 36.2 | 29.3 | 15.0 | 93 | 32 | 2.68 | 29.08 | 6.4 | 5.7 |
| 8 | 9 | 304.7 | 302.5 | 39.2 | 34.0 | 18.7 | 96 | 33 | 3.00 | 27.48 | 6.4 | 6.3 |
| 8 | 13 | 302.8 | 298.0 | 43.0 | 38.0 | 23.0 | 78 | 27 | 3.67 | 25.48 | 7.9 | 6.7 |

345

| | | $T_{b4}$ (K) | $T_{b5}$ (K) | $T_s$ (°C) | Based on Daily Observations | | | | | | Potential ET | |
|---|---|---|---|---|---|---|---|---|---|---|---|---|
| | | | | | Air | | Relative | | Average | Total | | |
| | | | | | Air Temperature (°C) | | Humidity (%) | | Wind | Solar Rad. | PMon | Harg |
| Mn | Da | | | | Max | Min | Max | Min | Spd. (m s$^{-1}$) | (MJ m$^{-2}$ d$^{-1}$) | (mm d$^{-1}$) | (mm d$^{-1}$) |
| 8 | 21 | 301.2 | 298.4 | 37.1 | 30.7 | 16.3 | 94 | 34 | 1.65 | 25.78 | 5.7 | 5.4 |
| 8 | 25 | 302.0 | 298.0 | 40.2 | 37.3 | 24.3 | 83 | 33 | 4.34 | 23.38 | 7.3 | 6.0 |
| 8 | 27 | 304.6 | 301.2 | 41.6 | 38.0 | 24.0 | 78 | 31 | 4.65 | 24.88 | 8.6 | 6.2 |
| 8 | 28 | 306.6 | 303.6 | 43.0 | 38.0 | 22.3 | 79 | 27 | 3.98 | 24.59 | 8.2 | 6.4 |

**Goodwell**

| Mn | Da | $T_{b4}$ (K) | $T_{b5}$ (K) | $T_s$ (°C) | Max | Min | Max | Min | Spd. (m s$^{-1}$) | (MJ m$^{-2}$ d$^{-1}$) | (mm d$^{-1}$) | (mm d$^{-1}$) |
|---|---|---|---|---|---|---|---|---|---|---|---|---|
| 5 | 29 | 303.2 | 301.6 | 36.3 | 32.0 | 13.0 | 98 | 20 | 3.00 | 30.88 | 6.4 | 6.8 |
| 5 | 30 | 305.9 | 303.9 | 39.9 | 35.3 | 15.3 | 82 | 22 | 4.34 | 30.68 | 7.8 | 7.5 |
| 6 | 5 | 307.7 | 305.4 | 42.5 | 37.0 | 19.7 | 78 | 19 | 3.98 | 30.88 | 8.5 | 7.5 |
| 6 | 6 | 308.4 | 306.6 | 42.3 | 36.0 | 16.0 | 98 | 30 | 3.98 | 29.08 | 7.2 | 7.7 |
| 6 | 13 | 308.9 | 307.5 | 41.7 | 39.7 | 20.3 | 74 | 13 | 5.68 | 30.98 | 10.5 | 8.3 |
| 6 | 15 | 310.9 | 310.2 | 42.2 | 39.7 | 20.7 | 85 | 7 | 7.64 | 31.18 | 11.1 | 8.3 |
| 6 | 16 | 311.9 | 311.2 | 43.3 | 40.0 | 22.0 | 84 | 6 | 7.02 | 32.18 | 12.1 | 8.2 |
| 6 | 23 | 306.4 | 304.1 | 41.3 | 32.0 | 17.3 | 94 | 30 | 4.34 | 29.18 | 7.2 | 6.4 |
| 6 | 24 | 308.6 | 305.6 | 44.7 | 37.7 | 17.7 | 82 | 17 | 3.67 | 28.78 | 8.7 | 8.0 |
| 6 | 26 | 309.6 | 307.3 | 44.5 | 39.3 | 17.7 | 82 | 20 | 3.67 | 31.08 | 9.1 | 8.5 |
| 6 | 28 | 309.4 | 306.7 | 45.0 | 38.0 | 17.7 | 74 | 18 | 3.00 | 28.48 | 8.1 | 8.1 |
| 7 | 10 | 308.6 | 305.7 | 44.5 | 36.0 | 16.7 | 91 | 16 | 4.65 | 30.28 | 8.3 | 7.5 |
| 8 | 12 | 306.5 | 302.8 | 44.3 | 37.0 | 19.3 | 74 | 22 | 5.99 | 27.78 | 10.1 | 6.9 |
| 8 | 16 | 304.8 | 302.7 | 39.1 | 35.0 | 14.3 | 84 | 24 | 3.67 | 26.88 | 6.7 | 6.8 |
| 8 | 26 | 307.4 | 305.8 | 40.9 | 38.0 | 21.0 | 66 | 17 | 3.67 | 26.28 | 8.6 | 6.5 |
| 8 | 28 | 302.2 | 297.8 | 41.5 | 35.0 | 21.7 | 76 | 35 | 4.34 | 24.88 | 8.0 | 5.6 |
| 9 | 9 | 298.0 | 296.5 | 30.9 | 30.7 | 13.3 | 97 | 38 | 3.67 | 23.79 | 5.1 | 5.1 |
| 9 | 12 | 300.3 | 298.0 | 35.1 | 32.7 | 18.3 | 87 | 33 | 7.02 | 22.99 | 7.3 | 4.9 |

| | | | | | Based on Daily Observations | | | | | | Potential ET | |
|---|---|---|---|---|---|---|---|---|---|---|---|---|
| | | | | | Air | | Relative | | Average | Total | PMon | Harg |
| | | $T_{b4}$ | $T_{b5}$ | $T_s$ | Air Temperature (°C) | | Humidity (%) | | Wind | Solar Rad. | | |
| Mn | Da | (K) | (K) | (°C) | Max | Min | Max | Min | Spd. (m s$^{-1}$) | (MJ m$^{-2}$ d$^{-1}$) | (mm d$^{-1}$) | (mm d$^{-1}$) |
| **Marena** | | | | | | | | | | | | |
| 3 | 15 | 289.4 | 288.5 | 21.4 | 20.3 | 8.3 | 85 | 24 | 3.67 | 21.59 | 4.4 | 3.0 |
| 3 | 31 | 291.2 | 290.2 | 23.3 | 22.7 | 1.3 | 80 | 23 | 4.34 | 24.18 | 4.6 | 4.2 |
| 4 | 1 | 296.0 | 295.1 | 27.6 | 27.3 | 5.7 | 85 | 25 | 3.67 | 23.98 | 5.0 | 4.9 |
| 4 | 7 | 288.0 | 286.9 | 20.2 | 19.0 | -1.0 | 92 | 29 | 4.65 | 24.88 | 4.3 | 3.8 |
| 5 | 15 | 298.4 | 296.8 | 31.6 | 27.7 | 14.3 | 100 | 41 | 2.01 | 29.18 | 5.4 | 5.3 |
| 5 | 18 | 297.0 | 295.5 | 30.0 | 28.0 | 16.3 | 100 | 48 | 1.34 | 28.18 | 5.1 | 5.2 |
| 5 | 20 | 298.1 | 297.1 | 30.2 | 27.3 | 13.3 | 89 | 43 | 2.01 | 29.18 | 5.5 | 5.4 |
| 5 | 30 | 302.1 | 300.4 | 35.7 | 33.0 | 17.3 | 100 | 49 | 0.00 | 28.58 | 5.1 | 6.6 |
| 6 | 6 | 297.5 | 295.4 | 31.8 | 30.0 | 19.0 | 100 | 65 | 2.01 | 22.89 | 4.3 | 5.5 |
| 6 | 13 | 301.5 | 299.6 | 35.4 | 33.7 | 23.0 | 100 | 50 | 4.65 | 29.18 | 6.2 | 5.9 |
| 6 | 25 | 306.9 | 303.8 | 43.4 | 39.7 | 21.0 | 87 | 25 | 3.35 | 29.08 | 7.9 | 8.2 |
| 6 | 26 | 304.7 | 302.1 | 40.2 | 37.0 | 22.3 | 85 | 24 | 2.01 | 30.08 | 7.2 | 7.2 |
| 6 | 27 | 301.2 | 297.9 | 38.0 | 39.0 | 22.3 | 85 | 37 | 2.68 | 28.78 | 7.5 | 7.8 |
| 6 | 30 | 303.7 | 300.9 | 39.7 | 36.3 | 20.7 | 95 | 37 | 1.65 | 28.78 | 6.5 | 7.2 |
| 7 | 8 | 301.9 | 299.6 | 36.8 | 31.0 | 19.3 | 88 | 31 | 2.68 | 29.08 | 6.9 | 5.7 |
| 7 | 17 | 301.5 | 298.6 | 37.5 | 34.0 | 21.7 | 98 | 46 | 1.65 | 19.99 | 4.2 | 6.2 |
| 7 | 18 | 302.8 | 299.8 | 39.2 | 37.0 | 23.0 | 99 | 34 | 3.35 | 27.48 | 6.9 | 6.9 |
| 7 | 19 | 303.5 | 300.9 | 39.0 | 36.0 | 25.3 | 72 | 32 | 5.01 | 28.68 | 8.8 | 6.1 |
| 7 | 27 | 298.0 | 296.3 | 31.6 | 28.0 | 16.0 | 92 | 37 | 2.32 | 28.58 | 5.7 | 5.2 |
| 7 | 28 | 298.6 | 296.5 | 32.8 | 28.7 | 16.3 | 87 | 41 | 2.01 | 27.98 | 5.5 | 5.3 |
| 8 | 8 | 299.9 | 297.4 | 35.1 | 32.0 | 18.0 | 100 | 50 | 2.32 | 25.88 | 5.1 | 5.8 |
| 8 | 16 | 301.8 | 299.5 | 36.6 | 33.7 | 16.0 | 78 | 25 | 1.34 | 26.68 | 5.7 | 6.3 |
| 8 | 21 | 298.7 | 296.7 | 33.0 | 28.7 | 16.7 | 96 | 43 | 1.34 | 25.88 | 5.3 | 4.8 |
| 8 | 22 | 297.9 | 295.4 | 33.3 | 30.3 | 16.3 | 93 | 42 | 1.65 | 25.38 | 5.2 | 5.2 |
| 8 | 25 | 300.0 | 296.8 | 36.7 | 36.0 | 22.3 | 98 | 41 | 3.35 | 23.08 | 5.7 | 5.9 |

| Mn | Da | $T_{b4}$ (K) | $T_{b5}$ (K) | $T_s$ (°C) | Air Temperature (°C) Max | Min | Relative Humidity (%) Max | Min | Average Wind Spd. (m s⁻¹) | Total Solar Rad. (MJ m⁻² d⁻¹) | PMon (mm d⁻¹) | Harg (mm d⁻¹) |
|---|---|---|---|---|---|---|---|---|---|---|---|---|
| | | | | | | | Based on Daily Observations | | | | Potential ET | |
| 8 | 26 | 302.0 | 298.5 | 39.2 | 37.3 | 24.7 | 86 | 38 | 4.34 | 22.09 | 6.5 | 5.8 |
| 8 | 27 | 303.5 | 300.4 | 40.1 | 38.0 | 23.7 | 85 | 31 | 3.98 | 24.78 | 7.9 | 6.2 |

**Wister**

| Mn | Da | $T_{b4}$ (K) | $T_{b5}$ (K) | $T_s$ (°C) | Max | Min | Max | Min | Spd. (m s⁻¹) | (MJ m⁻² d⁻¹) | PMon (mm d⁻¹) | Harg (mm d⁻¹) |
|---|---|---|---|---|---|---|---|---|---|---|---|---|
| 2 | 13 | 280.4 | 280.6 | 10.0 | 10.3 | -6.3 | 100 | 28 | 1.34 | 17.29 | 1.4 | 1.7 |
| 3 | 10 | 285.8 | 285.5 | 16.4 | 15.7 | -4.0 | 100 | 34 | 1.34 | 21.48 | 2.3 | 2.7 |
| 3 | 15 | 290.4 | 289.4 | 22.4 | 23.3 | 4.7 | 100 | 21 | 2.01 | 21.89 | 3.3 | 3.8 |
| 3 | 21 | 292.5 | 292.0 | 23.5 | 20.0 | 2.3 | 100 | 25 | 2.68 | 23.69 | 4.2 | 3.5 |
| 3 | 31 | 288.5 | 287.5 | 20.6 | 19.0 | -4.3 | 100 | 32 | 1.34 | 24.48 | 2.8 | 3.7 |
| 4 | 12 | 289.7 | 289.1 | 21.1 | 19.0 | 5.0 | 100 | 44 | 3.00 | 25.98 | 4.1 | 3.7 |
| 5 | 15 | 295.8 | 294.2 | 29.1 | 26.3 | 14.3 | 100 | 67 | 0.98 | 20.69 | 3.9 | 4.9 |
| 5 | 20 | 295.6 | 294.6 | 27.7 | 25.0 | 8.0 | 100 | 50 | 0.67 | 29.98 | 4.8 | 5.3 |
| 5 | 21 | 297.0 | 295.9 | 29.3 | 27.3 | 8.3 | 100 | 47 | 0.31 | 29.68 | 4.6 | 5.9 |
| 5 | 31 | 298.3 | 296.5 | 32.2 | 29.3 | 15.0 | 100 | 64 | 0.67 | 26.98 | 4.7 | 5.8 |
| 6 | 7 | 300.2 | 297.8 | 35.1 | 33.3 | 19.0 | 100 | 65 | 0.98 | 28.08 | 5.3 | 6.5 |
| 6 | 24 | 299.9 | 297.8 | 34.3 | 31.0 | 15.7 | 100 | 47 | 1.34 | 29.38 | 5.8 | 6.3 |
| 6 | 25 | 302.0 | 299.0 | 38.4 | 35.7 | 15.7 | 100 | 49 | 1.65 | 29.28 | 6.2 | 7.6 |
| 6 | 29 | 304.4 | 302.3 | 38.8 | 38.3 | 24.0 | 100 | 21 | 0.98 | 28.38 | 6.1 | 7.3 |
| 7 | 18 | 301.2 | 298.0 | 38.0 | 35.7 | 20.0 | 100 | 47 | 1.34 | 25.48 | 5.4 | 6.9 |
| 7 | 19 | 301.9 | 299.0 | 38.1 | 35.0 | 20.0 | 100 | 46 | 1.65 | 28.68 | 6.2 | 6.7 |
| 7 | 27 | 296.5 | 294.7 | 30.3 | 27.7 | 15.3 | 96 | 48 | 1.65 | 27.88 | 5.3 | 5.2 |
| 7 | 28 | 297.7 | 296.1 | 31.0 | 29.0 | 15.0 | 98 | 42 | 1.34 | 24.88 | 4.6 | 5.6 |
| 8 | 27 | 301.4 | 298.7 | 36.9 | 34.7 | 20.0 | 99 | 46 | 0.98 | 22.59 | 4.7 | 5.8 |
| 8 | 28 | 301.6 | 299.3 | 36.4 | 35.7 | 18.7 | 99 | 40 | 1.34 | 24.88 | 5.4 | 6.2 |
| 9 | 13 | 300.1 | 297.5 | 35.5 | 34.0 | 16.7 | 99 | 41 | 1.34 | 21.59 | 4.3 | 5.5 |

| | | Days Since Rain | Days Since Rain > 10 mm | | At Time of Over-Pass | | |
|---|---|---|---|---|---|---|---|
| Mn | Da | | | | Air Temp. (°C) | Relative Humidity (%) | Vapor Pressure (kPa) |

**Apache**

| Mn | Da | Days Since Rain | Days Since Rain > 10 mm | Air Temp. (°C) | Relative Humidity (%) | Vapor Pressure (kPa) |
|---|---|---|---|---|---|---|
| 2 | 13 | 3 | 44 | 13.2 | 17 | 0.26 |
| 3 | 10 | 1 | 2 | 17.8 | 30 | 0.61 |
| 3 | 15 | 2 | 7 | 19.1 | 35 | 0.77 |
| 3 | 21 | 8 | 13 | 19.9 | 21 | 0.49 |
| 3 | 31 | 5 | 23 | 21.5 | 28 | 0.72 |
| 4 | 1 | 6 | 24 | 25.5 | 29 | 0.95 |
| 4 | 12 | 1 | 1 | 19.4 | 32 | 0.72 |
| 5 | 15 | 1 | 13 | 27.0 | 43 | 1.53 |
| 5 | 18 | 4 | 16 | 27.2 | 53 | 1.91 |
| 5 | 20 | 6 | 18 | 26.8 | 48 | 1.69 |
| 5 | 21 | 7 | 19 | 27.8 | 47 | 1.75 |
| 5 | 30 | 0 | 6 | 32.8 | 48 | 2.39 |
| 5 | 31 | 1 | 7 | 32.3 | 53 | 2.56 |
| 6 | 5 | 6 | 12 | 34.4 | 53 | 2.88 |
| 6 | 8 | 9 | 15 | 38.2 | 36 | 2.41 |
| 6 | 26 | 1 | 15 | 38.6 | 40 | 2.74 |
| 6 | 27 | 2 | 16 | 42.6 | 35 | 2.96 |
| 6 | 30 | 0 | 1 | 36.8 | 43 | 2.67 |
| 7 | 6 | 0 | 7 | 33.8 | 49 | 2.58 |
| 7 | 18 | 2 | 2 | 36.3 | 33 | 1.99 |
| 7 | 19 | 3 | 3 | 36.2 | 30 | 1.80 |
| 7 | 20 | 4 | 4 | 36.1 | 37 | 2.21 |
| 7 | 27 | 1 | 11 | 29.2 | 35 | 1.42 |
| 8 | 9 | 5 | 24 | 32.9 | 36 | 1.80 |
| 8 | 13 | 9 | 28 | 37.5 | 27 | 1.74 |

| Mn | Da | Days Since Rain | Days Since Rain > 10 mm | | At Time of Over-Pass | | |
|---|---|---|---|---|---|---|---|
| | | | | | Air Temp. (°C) | Relative Humidity (%) | Vapor Pressure (kPa) |
| 8 | 21 | 1 | 4 | | 30.3 | 35 | 1.51 |
| 8 | 25 | 5 | 8 | | 36.1 | 39 | 2.33 |
| 8 | 27 | 7 | 10 | | 37.0 | 36 | 2.26 |
| 8 | 28 | 8 | 11 | | 37.0 | 28 | 1.76 |

**Goodwell**

| Mn | Da | Days Since Rain | Days Since Rain > 10 mm | | Air Temp. (°C) | Relative Humidity (%) | Vapor Pressure (kPa) |
|---|---|---|---|---|---|---|---|
| 5 | 29 | 4 | 4 | | 31.3 | 23 | 1.05 |
| 5 | 30 | 5 | 5 | | 35.1 | 27 | 1.53 |
| 6 | 5 | 3 | 11 | | 35.8 | 27 | 1.59 |
| 6 | 6 | 4 | 12 | | 35.8 | 30 | 1.76 |
| 6 | 13 | 2 | 3 | | 39.3 | 13 | 0.92 |
| 6 | 15 | 4 | 5 | | 39.3 | 7 | 0.50 |
| 6 | 16 | 5 | 6 | | 40.0 | 7 | 0.52 |
| 6 | 23 | 1 | 13 | | 32.0 | 31 | 1.47 |
| 6 | 24 | 2 | 14 | | 36.9 | 19 | 1.19 |
| 6 | 26 | 4 | 16 | | 38.4 | 22 | 1.49 |
| 6 | 28 | 6 | 18 | | 37.8 | 20 | 1.31 |
| 7 | 10 | 7 | 30 | | 35.0 | 19 | 1.07 |
| 8 | 12 | 1 | 63 | | 36.5 | 23 | 1.41 |
| 8 | 16 | 2 | 2 | | 34.9 | 26 | 1.45 |
| 8 | 26 | 2 | 2 | | 36.9 | 21 | 1.31 |
| 8 | 28 | 4 | 4 | | 34.6 | 36 | 1.98 |
| 9 | 9 | 1 | 16 | | 29.1 | 48 | 1.94 |
| 9 | 12 | 4 | 19 | | 31.7 | 34 | 1.59 |

|  |  | Days Since Rain | Days Since Rain > 10 mm |  | At Time of Over-Pass | | |
|---|---|---|---|---|---|---|---|
| Mn | Da |  |  |  | Air Temp. (°C) | Relative Humidity (%) | Vapor Pressure (kPa) |

**Marena**

| Mn | Da | Days Since Rain | Days Since Rain > 10 mm | Air Temp. (°C) | Relative Humidity (%) | Vapor Pressure (kPa) |
|---|---|---|---|---|---|---|
| 3 | 15 | 5 | 7 | 19.6 | 26 | 0.59 |
| 3 | 31 | 4 | 5 | 21.7 | 26 | 0.68 |
| 4 | 1 | 5 | 6 | 26.5 | 27 | 0.94 |
| 4 | 7 | 2 | 12 | 17.3 | 32 | 0.63 |
| 5 | 15 | 1 | 13 | 27.7 | 42 | 1.56 |
| 5 | 18 | 4 | 16 | 27.4 | 52 | 1.90 |
| 5 | 20 | 6 | 18 | 26.8 | 45 | 1.58 |
| 5 | 30 | 1 | 1 | 32.6 | 52 | 2.56 |
| 6 | 6 | 0 | 8 | 29.7 | 69 | 2.88 |
| 6 | 13 | 3 | 15 | 32.6 | 56 | 2.76 |
| 6 | 25 | 2 | 27 | 39.6 | 26 | 1.88 |
| 6 | 26 | 3 | 28 | 36.5 | 26 | 1.59 |
| 6 | 27 | 4 | 29 | 38.1 | 42 | 2.80 |
| 6 | 30 | 1 | 32 | 35.7 | 42 | 2.46 |
| 7 | 8 | 7 | 40 | 30.4 | 34 | 1.48 |
| 7 | 17 | 0 | 1 | 33.8 | 46 | 2.42 |
| 7 | 18 | 1 | 2 | 36.4 | 39 | 2.37 |
| 7 | 19 | 2 | 3 | 35.6 | 34 | 1.98 |
| 7 | 27 | 1 | 2 | 27.6 | 40 | 1.48 |
| 7 | 28 | 2 | 3 | 28.4 | 42 | 1.63 |
| 8 | 8 | 3 | 4 | 30.9 | 53 | 2.37 |
| 8 | 16 | 11 | 12 | 31.8 | 32 | 1.50 |
| 8 | 21 | 1 | 1 | 28.4 | 44 | 1.70 |
| 8 | 22 | 2 | 2 | 30.0 | 47 | 2.00 |
| 8 | 25 | 5 | 5 | 34.2 | 49 | 2.64 |

| Mn | Da | Days Since Rain | Days Since Rain > 10 mm | At Time of Over-Pass Air Temp. ($^{o}$C) | Relative Humidity (%) | Vapor Pressure (kPa) |
|---|---|---|---|---|---|---|
| 8 | 26 | 6 | 6 | 37.0 | 39 | 2.45 |
| 8 | 27 | 7 | 7 | 37.2 | 35 | 2.22 |

**Wister**

| Mn | Da | Days Since Rain | Days Since Rain > 10 mm | Air Temp. ($^{o}$C) | Relative Humidity (%) | Vapor Pressure (kPa) |
|---|---|---|---|---|---|---|
| 2 | 13 | 1 | 18 | 10.2 | 31 | 0.39 |
| 3 | 10 | 0 | 2 | 15.6 | 34 | 0.60 |
| 3 | 15 | 2 | 7 | 21.4 | 23 | 0.59 |
| 3 | 21 | 1 | 13 | 19.9 | 27 | 0.63 |
| 3 | 31 | 4 | 5 | 18.5 | 35 | 0.75 |
| 4 | 12 | 1 | 1 | 18.6 | 45 | 0.97 |
| 5 | 15 | 1 | 2 | 26.1 | 67 | 2.27 |
| 5 | 20 | 4 | 7 | 24.2 | 54 | 1.63 |
| 5 | 21 | 5 | 8 | 27.2 | 49 | 1.77 |
| 5 | 31 | 0 | 2 | 29.0 | 66 | 2.65 |
| 6 | 7 | 1 | 9 | 32.6 | 68 | 3.35 |
| 6 | 24 | 1 | 15 | 30.5 | 49 | 2.14 |
| 6 | 25 | 2 | 16 | 34.8 | 50 | 2.78 |
| 6 | 29 | 6 | 20 | 36.8 | 28 | 1.74 |
| 7 | 18 | 3 | 12 | 34.2 | 61 | 3.28 |
| 7 | 19 | 4 | 13 | 34.3 | 52 | 2.81 |
| 7 | 27 | 1 | 1 | 27.3 | 49 | 1.78 |
| 7 | 28 | 2 | 2 | 27.8 | 43 | 1.61 |
| 8 | 27 | 2 | 7 | 34.2 | 47 | 2.53 |
| 8 | 28 | 3 | 8 | 34.7 | 42 | 2.33 |
| 9 | 13 | 4 | 13 | 32.6 | 45 | 2.21 |

# Appendix J

## Summary Satellite and Meteorological Data Used in the State-Wide Comparison

## Including Correlation Coefficients Between Mesonet and Satellite Data

## on a Per Image Basis

Below is a definition of column headings for the tables that follow:

| Column Heading | Definition |
|---|---|
| Date | Month/Day |
| Time | Hour:Minute of the satellite overpass (GMT) |
| N | Number of observations |
| Stat | Summary statistic for the observations |
|   Max | Maximum value on the given date |
|   Min | Minimum value on the given date |
|   Avg | Average of all observations |
|   STD | Standard deviation of all observations |

From Daily Observations:

*Air Temperature ($^oC$):*

| | |
|---|---|
|   Max | Maximum daily air temperature |
|   Min | Minimum daily air temperature |

*Relative Humidity (%):*

| | |
|---|---|
|   Max | Maximum daily relative humidity |
|   Min | Minimum daily relative humidity |

| | |
|---|---|
| Average Wind Speed | Average daily wind speed (m s$^{-1}$) |

Potential ET:

| | |
|---|---|
|   PMon | Calculated from the Penman-Monteith equation (mm d$^{-1}$) |
|   Harg | Calculated from the Hargreaves equation (mm d$^{-1}$ ) |

At Time of Over-Pass:

| | |
|---|---|
|   RH | Relative humidity at the time of satellite over pass (%) |
|   AirTemp. | 1.5 m air temperature at the time of satellite over pass ($^oC$) |
|   Vapor Pres | Calculated vapor pressure at the time of satellite over pass (kPa) |

| | |
|---|---|
| R1 | Exoatmospheric reflectance in channel 1 |
| R2 | Exoatmospheric reflectance in channel 2 |
| NDVI | Normalized Difference Vegetation Index based on exoatmospheric reflectance |
| SAVI | Soil Adjusted Vegetation Index based on exoatmospheric reflectance (L = 0.5) |
| $T_{b4}$ | Brightness temperature from channel 4 (K) |
| $T_{b5}$ | Brightness temperature from channel 5 (K) |
| $T_s$ | AVHRR derived surface temperature ($^oC$) |
| $T_{b4} - T_{b5}$ | Difference in channel 4 and 5 brightness temperatures (K) |

354

| Date | Time (GMT) | N | Stat | Air Temperature (°C) | | Relative Humidity (%) | | Average Wind Speed (m s⁻¹) | Potential ET PMon mm d⁻¹ | Harg mm d⁻¹ | RH % | Air Temp (°C) | Vapor Pres (kPa) |
|---|---|---|---|---|---|---|---|---|---|---|---|---|---|
| | | | | Max | Min | Max | Min | | | | | | |
| 03/16 | 22:45 | 23 | Max | 24.0 | 8.7 | 100 | 35 | 4.70 | 5.0 | 4.0 | 38 | 23.7 | 0.927 |
| | | | Min | 21.0 | 0.3 | 60 | 20 | 1.20 | 3.3 | 3.2 | 21 | 20.0 | 0.600 |
| | | | Avg | 22.4 | 3.5 | 85 | 26 | 2.90 | 4.1 | 3.7 | 30 | 21.8 | 0.775 |
| | | | STD | 0.9 | 2.2 | 12 | 4 | 1.04 | 0.5 | 0.2 | 5 | 1.0 | 0.102 |
| 4/12 | 22:21 | 55 | Max | 22.7 | 6.7 | 100 | 44 | 7.64 | 5.5 | 4.4 | 51 | 22.5 | 0.974 |
| | | | Min | 14.7 | 3.0 | 73 | 18 | 1.69 | 2.8 | 2.9 | 20 | 14.7 | 0.437 |
| | | | Avg | 19.6 | 4.9 | 86 | 29 | 4.51 | 4.4 | 3.8 | 34 | 19.2 | 0.749 |
| | | | STD | 1.6 | 1.0 | 6 | 6 | 1.06 | 0.5 | 0.3 | 7 | 1.8 | 0.121 |
| 5/20 | 22:58 | 59 | Max | 29.7 | 16.0 | 100 | 48 | 5.01 | 6.0 | 6.1 | 49 | 28.7 | 1.690 |
| | | | Min | 24.7 | 8.0 | 83 | 35 | 0.97 | 4.6 | 4.8 | 36 | 23.6 | 1.221 |
| | | | Avg | 27.0 | 12.3 | 95 | 41 | 2.16 | 5.2 | 5.4 | 43 | 26.4 | 1.482 |
| | | | STD | 1.2 | 1.9 | 5 | 3 | 0.76 | 0.3 | 0.3 | 3 | 1.1 | 0.112 |
| 5/30 | 22:36 | 39 | Max | 37.0 | 20.7 | 100 | 63 | 3.98 | 7.2 | 7.6 | 67 | 36.0 | 3.012 |
| | | | Min | 29.7 | 15.3 | 93 | 29 | 0.31 | 3.9 | 5.1 | 30 | 28.4 | 1.678 |
| | | | Avg | 32.5 | 17.6 | 99 | 47 | 1.33 | 5.2 | 6.4 | 50 | 32.0 | 2.336 |
| | | | STD | 1.9 | 1.5 | 1 | 10 | 0.67 | 0.7 | 0.5 | 9 | 1.9 | 0.290 |
| 06/05 | 22:51 | 26 | Max | 36.0 | 23.7 | 100 | 62 | 5.09 | 6.6 | 6.7 | 74 | 34.6 | 3.274 |
| | | | Min | 30.7 | 18.3 | 91 | 49 | 0.97 | 4.8 | 5.2 | 51 | 29.9 | 2.478 |
| | | | Avg | 32.8 | 20.9 | 97 | 57 | 3.09 | 5.7 | 6.0 | 60 | 32.2 | 2.871 |
| | | | STD | 1.5 | 1.4 | 3 | 4 | 0.98 | 0.5 | 0.4 | 5 | 1.3 | 0.203 |
| 06/13 | 23:06 | 53 | Max | 38.3 | 24.7 | 100 | 61 | 8.67 | 9.7 | 7.4 | 63 | 37.5 | 3.016 |
| | | | Min | 30.7 | 21.0 | 81 | 32 | 1.94 | 5.7 | 4.8 | 34 | 30.1 | 1.940 |

356

| | | | | From Daily Observations | | | | | Potential ET | | At Time of Over-Pass | | |
| | Time | | | Air Temperature (°C) | | Relative Humidity (%) | | Average Wind Speed | PMon | Harg | RH | Air | Vapor |
| Date | (GMT) | N | Stat | Max | Min | Max | Min | (m s⁻¹) | mm d⁻¹ | mm d⁻¹ | % | Temp (°C) | Pres (kPa) |
|---|---|---|---|---|---|---|---|---|---|---|---|---|---|
| 06/13 | 23:06 | 53 | Avg | 33.5 | 22.9 | 91 | 48 | 4.84 | 7.1 | 5.9 | 51 | 32.9 | 2.543 |
| | | | STD | 2.0 | 0.8 | 5 | 8 | 1.30 | 1.0 | 0.7 | 9 | 2.0 | 0.256 |
| 06/30 | 22:58 | 70 | Max | 41.0 | 25.3 | 100 | 62 | 4.12 | 8.0 | 8.5 | 71 | 40.8 | 3.574 |
| | | | Min | 32.7 | 16.3 | 50 | 20 | 0.97 | 4.9 | 5.8 | 26 | 28.4 | 2.002 |
| | | | Avg | 36.4 | 21.6 | 78 | 25 | 2.24 | 6.4 | 7.1 | 44 | 35.7 | 2.580 |
| | | | STD | 1.6 | 1.5 | 131 | 124 | 0.63 | 0.5 | 0.6 | 8 | 2.0 | 0.297 |
| 07/18 | 22:38 | 40 | Max | 38.7 | 26.3 | 100 | 53 | 4.12 | 9.4 | 7.7 | 57 | 38.7 | 2.989 |
| | | | Min | 33.7 | 20.0 | 69 | 20 | 1.34 | 5.6 | 5.5 | 21 | 32.9 | 1.363 |
| | | | Avg | 36.2 | 23.3 | 90 | 39 | 2.62 | 6.9 | 6.6 | 42 | 35.5 | 2.430 |
| | | | STD | 1.4 | 1.3 | 7 | 8 | 0.71 | 0.8 | 0.5 | 8 | 1.4 | 0.364 |
| 07/19 | 22:25 | 72 | Max | 40.3 | 26.3 | 100 | 57 | 7.64 | 12.1 | 8.0 | 64 | 39.6 | 3.313 |
| | | | Min | 32.3 | 20.3 | 61 | 18 | 0.97 | 5.7 | 5.1 | 19 | 32.2 | 1.294 |
| | | | Avg | 35.9 | 23.7 | 83 | 37 | 3.61 | 7.9 | 6.3 | 40 | 35.3 | 2.223 |
| | | | STD | 2.0 | 1.3 | 10 | 10 | 1.43 | 1.6 | 0.7 | 11 | 2.0 | 0.466 |
| 08/27 | 22:49 | 99 | Max | 43.3 | 27.0 | 100 | 66 | 6.51 | 11.7 | 7.4 | 71 | 41.6 | 3.284 |
| | | | Min | 31.3 | | | | 0.31 | 4.4 | 4.4 | 19 | 30.5 | 1.527 |
| | | | Avg | 36.6 | 23.3 | 74 | 30 | 3.41 | 7.2 | 5.7 | 44 | 35.4 | 2.432 |
| | | | STD | 3.0 | 5.5 | 110 | 105 | 1.37 | 1.9 | 0.8 | 13 | 2.8 | 0.448 |
| ALL | | 537 | Max | 43.3 | 27.0 | 100 | 66 | 8.67 | 12.1 | 8.5 | 74 | 41.6 | 3.574 |
| | | | Min | 14.7 | 0.3 | 56 | 17 | 0.31 | 2.8 | 2.9 | 19 | 14.7 | 0.437 |
| | | | Avg | 32.2 | 18.7 | 90 | 40 | 3.15 | 6.3 | 5.8 | 43 | 31.5 | 2.098 |
| | | | STD | 6.0 | 7.0 | 9 | 11 | 1.47 | 1.6 | 1.1 | 11 | 5.9 | 0.724 |

| Date | Time (GMT) | N | Stat | R1 | R2 | NDVI | SAVI | $T_{b4}$ | $T_{b5}$ | $T_s$ | $T_{b4}$-$T_{b5}$ |
|---|---|---|---|---|---|---|---|---|---|---|---|
| 03/16 | 22:45 | 23 | Max | 0.184 | 0.295 | 0.404 | 0.277 | 294.0 | 293.6 | 24.8 | 1.20 |
| | | | Min | 0.115 | 0.142 | 0.105 | 0.054 | 285.2 | 284.0 | 17.6 | 0.20 |
| | | | Avg | 0.138 | 0.208 | 0.200 | 0.124 | 290.7 | 290.1 | 21.9 | 0.57 |
| | | | STD | 0.015 | 0.033 | 0.066 | 0.047 | 2.6 | 2.8 | 2.3 | 0.27 |
| 4/12 | 22:21 | 55 | Max | 0.146 | 0.313 | 0.554 | 0.371 | 295.4 | 294.4 | 27.3 | 1.20 |
| | | | Min | 0.059 | 0.135 | 0.112 | 0.059 | 285.6 | 284.5 | 17.7 | 0.40 |
| | | | Avg | 0.097 | 0.190 | 0.321 | 0.176 | 290.8 | 289.9 | 22.6 | 0.87 |
| | | | STD | 0.019 | 0.043 | 0.090 | 0.060 | 1.9 | 2.0 | 1.9 | 0.18 |
| 5/20 | 22:58 | 59 | Max | 0.150 | 0.313 | 0.559 | 0.361 | 301.2 | 299.4 | 34.9 | 3.30 |
| | | | Min | 0.074 | 0.171 | 0.233 | 0.131 | 294.1 | 290.8 | 27.5 | 0.70 |
| | | | Avg | 0.102 | 0.248 | 0.411 | 0.255 | 297.8 | 296.5 | 30.4 | 1.27 |
| | | | STD | 0.014 | 0.039 | 0.092 | 0.068 | 1.6 | 1.7 | 1.9 | 0.47 |
| 5/30 | 22:36 | 39 | Max | 0.109 | 0.240 | 0.620 | 0.331 | 307.8 | 306.0 | 41.9 | 2.60 |
| | | | Min | 0.053 | 0.155 | 0.351 | 0.183 | 298.7 | 297.3 | 31.6 | 1.30 |
| | | | Avg | 0.072 | 0.200 | 0.469 | 0.248 | 302.0 | 300.3 | 35.6 | 1.73 |
| | | | STD | 0.012 | 0.019 | 0.074 | 0.041 | 2.4 | 2.2 | 2.8 | 0.28 |
| 06/05 | 22:51 | 26 | Max | 0.121 | 0.298 | 0.479 | 0.318 | 301.9 | 299.5 | 37.4 | 2.70 |
| | | | Min | 0.089 | 0.224 | 0.361 | 0.222 | 296.4 | 294.0 | 31.4 | 2.10 |
| | | | Avg | 0.101 | 0.250 | 0.424 | 0.262 | 299.7 | 297.3 | 34.7 | 2.39 |
| | | | STD | 0.007 | 0.020 | 0.030 | 0.025 | 1.6 | 1.6 | 1.7 | 0.14 |
| 06/13 | 23:06 | 53 | Max | 0.161 | 0.319 | 0.497 | 0.319 | 307.8 | 304.9 | 43.9 | 2.90 |
| | | | Min | 0.079 | 0.154 | 0.120 | 0.073 | 296.6 | 294.0 | 32.2 | 1.70 |

| Date | Time (GMT) | N | Stat | R1 | R2 | NDVI | SAVI | $T_{b4}$ | $T_{b5}$ | $T_s$ | $T_{b4}-T_{b5}$ |
|---|---|---|---|---|---|---|---|---|---|---|---|
| 06/13 | 23:06 | 53 | Avg | 0.112 | 0.236 | 0.351 | 0.217 | 301.4 | 299.2 | 36.1 | 2.23 |
| | | | STD | 0.018 | 0.036 | 0.101 | 0.068 | 2.6 | 2.6 | 2.7 | 0.27 |
| 06/30 | 22:58 | 70 | Max | 0.147 | 0.257 | 0.547 | 0.305 | 310.2 | 308.0 | 47.0 | 4.05 |
| | | | Min | 0.066 | 0.121 | 0.148 | 0.089 | 297.0 | 294.3 | 32.5 | 1.74 |
| | | | Avg | 0.093 | 0.205 | 0.378 | 0.211 | 303.0 | 300.2 | 38.9 | 2.81 |
| | | | STD | 0.018 | 0.024 | 0.100 | 0.058 | 3.0 | 3.0 | 3.1 | 0.43 |
| 07/18 | 22:38 | 40 | Max | 0.127 | 0.264 | 0.561 | 0.282 | 308.1 | 304.9 | 44.9 | 3.40 |
| | | | Min | 0.055 | 0.149 | 0.318 | 0.175 | 302.0 | 298.8 | 35.9 | 1.90 |
| | | | Avg | 0.081 | 0.198 | 0.422 | 0.224 | 303.5 | 300.8 | 38.9 | 2.64 |
| | | | STD | 0.018 | 0.023 | 0.062 | 0.027 | 1.5 | 1.3 | 2.1 | 0.37 |
| 07/19 | 22:25 | 72 | Max | 0.149 | 0.244 | 0.589 | 0.300 | 306.7 | 303.4 | 45.6 | 4.40 |
| | | | Min | 0.050 | 0.159 | 0.157 | 0.089 | 297.7 | 294.9 | 33.2 | 1.90 |
| | | | Avg | 0.087 | 0.204 | 0.412 | 0.223 | 302.6 | 299.9 | 38.4 | 2.75 |
| | | | STD | 0.025 | 0.021 | 0.118 | 0.057 | 2.1 | 1.6 | 3.3 | 0.66 |
| 08/27 | 22:49 | 99 | Max | 0.192 | 0.299 | 0.561 | 0.307 | 308.5 | 305.2 | 45.8 | 4.57 |
| | | | Min | 0.063 | 0.138 | 0.125 | 0.062 | 297.6 | 295.4 | 32.1 | 1.77 |
| | | | Avg | 0.091 | 0.177 | 0.326 | 0.169 | 302.6 | 299.8 | 38.5 | 2.81 |
| | | | STD | 0.022 | 0.023 | 0.108 | 0.054 | 3.0 | 2.5 | 4.2 | 0.64 |
| ALL | | 537 | Max | 0.192 | 0.319 | 0.620 | 0.371 | 310.2 | 308.0 | 47.0 | 4.57 |
| | | | Min | 0.050 | 0.121 | 0.105 | 0.054 | 285.2 | 284.0 | 17.6 | -0.20 |
| | | | Avg | 0.095 | 0.208 | 0.372 | 0.209 | 300.2 | 298.0 | 34.7 | 2.16 |
| | | | STD | 0.023 | 0.037 | 0.111 | 0.065 | 4.8 | 4.2 | 6.4 | 0.89 |

| Remotely Sensed Data | Image Date | From Daily Observations | | | | | Potential ET | | At Time of Over-Pass | | |
|---|---|---|---|---|---|---|---|---|---|---|---|
| | | Air Temperature (°C) | | Relative Humidity (%) | | Wind Speed | PMon | Harg | Relative | Air | Vapor |
| | | Max | Min | Max | Min | (m s⁻¹) | mm d⁻¹ | mm d⁻¹ | Humidity | Temp | Pres |

Correlation Coefficient Between Data Listed In Column 1 and the Data Listed In the Column Headings

| Remotely Sensed Data | Image Date | Max | Min | Max | Min | Wind Speed (m s⁻¹) | PMon | Harg | RH | Air Temp | Vapor Pres |
|---|---|---|---|---|---|---|---|---|---|---|---|
| NDVI | 03/16 | -0.366 | 0.049 | 0.039 | 0.348 | 0.089 | -0.227 | -0.234 | 0.454 | -0.362 | 0.351 |
| NDVI | 04/12 | 0.220 | -0.175 | 0.443 | 0.415 | -0.486 | -0.264 | 0.252 | 0.191 | 0.245 | 0.437 |
| NDVI | 05/20 | -0.569 | -0.593 | 0.316 | 0.180 | -0.767 | -0.625 | -0.165 | 0.310 | -0.574 | -0.172 |
| NDVI | 05/30 | -0.599 | -0.424 | -0.092 | 0.646 | -0.508 | -0.449 | -0.501 | 0.667 | -0.602 | 0.562 |
| NDVI | 06/05 | -0.412 | -0.555 | -0.177 | 0.413 | 0.037 | -0.187 | -0.165 | 0.205 | -0.371 | -0.139 |
| NDVI | 06/13 | -0.730 | 0.324 | 0.188 | 0.671 | -0.562 | -0.665 | -0.774 | 0.641 | -0.715 | 0.417 |
| NDVI | 06/30 | -0.314 | 0.473 | 0.094 | 0.113 | -0.500 | -0.460 | -0.454 | 0.362 | -0.317 | 0.287 |
| NDVI | 07/18 | -0.255 | 0.080 | 0.444 | 0.648 | -0.665 | -0.682 | -0.260 | 0.599 | -0.287 | 0.640 |
| NDVI | 07/19 | -0.751 | 0.269 | 0.711 | 0.870 | -0.784 | -0.855 | -0.744 | 0.865 | -0.784 | 0.842 |
| NDVI | 08/27 | -0.785 | -0.193 | 0.014 | 0.038 | -0.578 | -0.749 | -0.783 | 0.811 | -0.780 | 0.750 |
| NDVI | All | 0.025 | 0.185 | 0.490 | 0.610 | -0.533 | -0.286 | 0.048 | 0.594 | 0.035 | 0.421 |
| R1 | 03/16 | -0.277 | 0.284 | -0.154 | 0.420 | 0.196 | 0.138 | -0.412 | 0.249 | -0.115 | 0.255 |
| R1 | 04/12 | 0.228 | -0.462 | -0.133 | -0.701 | 0.564 | 0.463 | 0.285 | -0.613 | 0.211 | -0.660 |
| R1 | 05/20 | 0.359 | 0.238 | -0.312 | -0.226 | 0.451 | 0.456 | 0.192 | -0.330 | 0.374 | -0.003 |
| R1 | 05/30 | 0.443 | 0.329 | -0.195 | -0.443 | 0.327 | 0.308 | 0.362 | -0.474 | 0.416 | -0.407 |
| R1 | 06/05 | -0.198 | -0.108 | 0.294 | 0.114 | -0.387 | -0.211 | -0.147 | 0.315 | -0.268 | 0.051 |
| R1 | 06/13 | 0.570 | -0.071 | -0.051 | -0.445 | 0.332 | 0.419 | 0.553 | -0.423 | 0.519 | -0.226 |
| R1 | 06/30 | 0.399 | -0.448 | 0.107 | 0.084 | 0.527 | 0.505 | 0.521 | -0.479 | 0.391 | -0.391 |
| R1 | 07/18 | 0.347 | -0.030 | -0.604 | -0.690 | 0.749 | 0.782 | 0.310 | -0.710 | 0.429 | -0.719 |
| R1 | 07/19 | 0.731 | -0.284 | -0.691 | -0.872 | 0.782 | 0.828 | 0.732 | -0.863 | 0.770 | -0.839 |
| R1 | 08/27 | 0.700 | 0.138 | 0.032 | 0.005 | 0.476 | 0.633 | 0.732 | -0.698 | 0.692 | -0.635 |
| R1 | All | -0.122 | -0.272 | -0.305 | -0.444 | 0.450 | 0.171 | -0.050 | -0.463 | -0.124 | -0.417 |

| Remotely Sensed Data | Image Date | From Daily Observations | | | | | Potential ET | | At Time of Over-Pass | | |
|---|---|---|---|---|---|---|---|---|---|---|---|
| | | Air Temperature (°C) | | Relative Humidity (%) | | Wind Speed (m s$^{-1}$) | PMon mm d$^{-1}$ | Harg mm d$^{-1}$ | Relative Humidity | Air Temp | Vapor Pres |
| | | Max | Min | Max | Min | | | | | | |

Correlation Coefficient Between Data Listed In Column 1 and the Data Listed In the Column Headings

| | | | | | | | | | | | |
|---|---|---|---|---|---|---|---|---|---|---|---|
| R2 | 03/16 | -0.529 | 0.224 | -0.082 | 0.585 | 0.229 | -0.101 | -0.486 | 0.575 | -0.427 | 0.474 |
| R2 | 04/12 | 0.389 | -0.562 | 0.262 | -0.260 | 0.110 | 0.180 | 0.470 | -0.368 | 0.395 | -0.196 |
| R2 | 05/20 | -0.492 | -0.621 | 0.173 | 0.025 | -0.688 | -0.478 | -0.075 | 0.115 | -0.484 | -0.278 |
| R2 | 05/30 | -0.375 | -0.249 | -0.420 | 0.492 | -0.388 | -0.341 | -0.322 | 0.477 | -0.421 | 0.409 |
| R2 | 06/05 | -0.553 | -0.609 | 0.097 | 0.479 | -0.303 | -0.363 | -0.281 | 0.457 | -0.579 | -0.093 |
| R2 | 06/13 | -0.511 | 0.385 | 0.215 | 0.539 | -0.498 | -0.556 | -0.587 | 0.516 | -0.539 | 0.373 |
| R2 | 06/30 | 0.019 | 0.197 | 0.315 | 0.316 | -0.173 | -0.110 | -0.053 | -0.050 | 0.006 | -0.047 |
| R2 | 07/18 | 0.267 | 0.106 | -0.569 | -0.419 | 0.535 | 0.544 | 0.171 | -0.507 | 0.364 | -0.488 |
| R2 | 07/19 | 0.005 | 0.057 | -0.085 | -0.109 | 0.116 | 0.017 | -0.013 | -0.101 | 0.023 | -0.101 |
| R2 | 08/27 | -0.188 | -0.086 | 0.092 | 0.091 | -0.193 | -0.232 | -0.139 | 0.233 | -0.195 | 0.228 |
| R2 | All | -0.155 | -0.121 | 0.257 | 0.255 | -0.128 | -0.172 | -0.013 | 0.210 | -0.144 | 0.005 |
| | | | | | | | | | | | |
| SAVI | 03/16 | -0.420 | 0.087 | 0.008 | 0.412 | 0.134 | -0.200 | -0.298 | 0.496 | -0.397 | 0.387 |
| SAVI | 04/12 | 0.301 | -0.352 | 0.391 | 0.158 | -0.254 | -0.096 | 0.359 | -0.028 | 0.320 | 0.201 |
| SAVI | 05/20 | -0.564 | -0.627 | 0.280 | 0.125 | -0.771 | -0.599 | -0.139 | 0.247 | -0.564 | -0.223 |
| SAVI | 05/30 | -0.578 | -0.403 | -0.195 | 0.666 | -0.512 | -0.463 | -0.486 | 0.675 | -0.596 | 0.577 |
| SAVI | 06/05 | -0.529 | -0.648 | -0.066 | 0.491 | -0.122 | -0.295 | -0.240 | 0.347 | -0.515 | -0.137 |
| SAVI | 06/13 | -0.714 | 0.358 | 0.205 | 0.674 | -0.579 | -0.674 | -0.768 | 0.643 | -0.708 | 0.428 |
| SAVI | 06/30 | -0.250 | 0.433 | 0.155 | 0.171 | -0.460 | -0.405 | -0.382 | 0.280 | -0.255 | 0.222 |
| SAVI | 07/18 | -0.128 | 0.183 | 0.088 | 0.411 | -0.336 | -0.368 | -0.204 | 0.313 | -0.111 | 0.352 |
| SAVI | 07/19 | -0.705 | 0.295 | 0.629 | 0.785 | -0.696 | -0.795 | -0.713 | 0.781 | -0.732 | 0.759 |
| SAVI | 08/27 | -0.744 | -0.185 | 0.039 | 0.061 | -0.553 | -0.718 | -0.735 | 0.776 | -0.742 | 0.718 |
| SAVI | All | -0.038 | 0.103 | 0.469 | 0.569 | -0.459 | -0.282 | 0.035 | 0.541 | -0.026 | 0.329 |

| Remotely Sensed Data | Image Date | From Daily Observations | | | | | Potential ET | | At Time of Over-Pass | | |
| | | Air Temperature (°C) | | Relative Humidity (%) | | Wind Speed | PMon | Harg | Relative | Air | Vapor |
| | | Max | Min | Max | Min | $(m\ s^{-1})$ | $mm\ d^{-1}$ | $mm\ d^{-1}$ | Humidity | Temp | Pres |
|---|---|---|---|---|---|---|---|---|---|---|---|
| | | | | | Correlation Coefficient Between Data Listed In Column 1 and the Data Listed In the Column Headings | | | | | | |
| T4-T5 | 03/16 | -0.156 | 0.473 | -0.503 | -0.168 | -0.320 | 0.094 | -0.330 | -0.341 | 0.078 | -0.381 |
| T4-T5 | 04/12 | -0.457 | -0.060 | -0.174 | -0.127 | 0.354 | -0.138 | -0.416 | 0.165 | -0.471 | -0.165 |
| T4-T5 | 05/20 | 0.584 | 0.382 | -0.165 | -0.319 | 0.699 | 0.558 | 0.314 | -0.433 | 0.582 | 0.061 |
| T4-T5 | 05/30 | 0.571 | 0.184 | 0.412 | -0.592 | 0.448 | 0.509 | 0.595 | -0.617 | 0.580 | -0.514 |
| T4-T5 | 06/05 | 0.069 | 0.054 | 0.088 | -0.222 | 0.219 | 0.006 | 0.062 | -0.216 | 0.070 | -0.176 |
| T4-T5 | 06/13 | 0.078 | -0.160 | 0.163 | 0.024 | -0.222 | -0.069 | 0.099 | 0.032 | 0.060 | 0.081 |
| T4-T5 | 06/30 | -0.093 | 0.051 | -0.008 | -0.007 | -0.356 | -0.222 | -0.092 | -0.139 | -0.046 | -0.221 |
| T4-T5 | 07/18 | 0.469 | -0.361 | -0.216 | -0.745 | 0.505 | 0.615 | 0.583 | -0.628 | 0.519 | -0.570 |
| T4-T5 | 07/19 | 0.775 | -0.379 | -0.612 | -0.810 | 0.656 | 0.808 | 0.802 | -0.809 | 0.817 | -0.773 |
| T4-T5 | 08/27 | 0.856 | 0.208 | 0.026 | 0.001 | 0.709 | 0.843 | 0.841 | -0.886 | 0.858 | -0.806 |
| T4-T5 | All | 0.870 | 0.818 | -0.310 | -0.043 | 0.148 | 0.780 | 0.740 | -0.046 | 0.867 | 0.549 |
| Ts | 03/16 | 0.524 | -0.365 | 0.427 | -0.167 | -0.400 | -0.480 | 0.516 | -0.152 | 0.549 | 0.063 |
| Ts | 04/12 | 0.811 | -0.473 | 0.386 | -0.238 | -0.238 | 0.496 | 0.832 | -0.493 | 0.812 | -0.035 |
| Ts | 05/20 | 0.604 | 0.349 | -0.168 | -0.166 | 0.460 | 0.410 | 0.380 | -0.291 | 0.599 | 0.214 |
| Ts | 05/30 | 0.767 | 0.465 | 0.387 | -0.730 | 0.656 | 0.553 | 0.682 | -0.810 | 0.764 | -0.680 |
| Ts | 06/05 | 0.571 | 0.472 | -0.254 | -0.714 | 0.703 | 0.641 | 0.385 | -0.790 | 0.586 | -0.276 |
| Ts | 06/13 | 0.863 | -0.164 | -0.379 | -0.848 | 0.625 | 0.829 | 0.858 | -0.830 | 0.869 | -0.595 |
| Ts | 06/30 | 0.492 | -0.381 | 0.169 | 0.142 | 0.446 | 0.624 | 0.588 | -0.642 | 0.591 | -0.431 |
| Ts | 07/18 | 0.504 | -0.281 | -0.457 | -0.798 | 0.622 | 0.795 | 0.564 | -0.791 | 0.585 | -0.756 |
| Ts | 07/19 | 0.783 | -0.325 | -0.736 | -0.893 | 0.756 | 0.860 | 0.786 | -0.894 | 0.824 | -0.866 |
| Ts | 08/27 | 0.910 | 0.206 | 0.023 | 0.002 | 0.794 | 0.924 | 0.881 | -0.946 | 0.902 | -0.885 |
| Ts | All | 0.949 | 0.857 | -0.177 | 0.012 | 0.061 | 0.801 | 0.873 | -0.027 | 0.952 | 0.605 |

VITA

Edward MacDonald Barnes

Candidate for the Degree of

Doctor of Philosophy

Thesis: ESTIMATION OF EVAPOTRANSPIRATION USING ADVANCED VERY HIGH RESOLUTION RADIOMETER (AVHRR) DATA

Major Field: Biosystems Engineering

Biographical:

Education: Graduated from Brevard High School, Brevard, North Carolina in May 1983; received Bachelor of Science and Master of Science degrees in Biological and Agricultural Engineering from North Carolina State University in May 1988 and May 1990, respectively. Completed the requirements for the Doctor of Philosophy degree with a major in Biosystems Engineering at Oklahoma State University in May 1996.

Experience: Employed as a Biochemicals Research Field Assistant for PPG Industries in Oxford, North Carolina during the summer of 1987; worked as a Graduate Research Assistant in the department of Biological and Agricultural Engineering at North Carolina State University, 1988 to 1990; served as an Extension Engineer in the Department of Biosystems Engineering at Oklahoma State University, 1990 to 1992; USDA National Needs Fellow in the Department of Biosystems at Oklahoma State University, 1992 to 1995.

Professional Memberships: ASAE